Mullen, Christopher Andrew (2020) *Linearly polarised pion photoproduction on the deuteron.* PhD thesis.

https://theses.gla.ac.uk/80265/

Enlighten: Theses
https://theses.gla.ac.uk/
research-enlighten@glasgow.ac.uk

Linearly Polarised Pion Photoproduction on the Deuteron

Christopher Andrew Mullen

Submitted in fulfilment of the requirements for the

Degree of Doctor of Philosophy

School of Physics and Astronomy

College of Science and Engineering

University of Glasgow

March 9, 2020

Abstract

Measurements of the linear polarisation asymmetry in pion photoproduction on both the proton and neutron have been performed with a liquid deuterium target using the Mainzer Microtron and Crystal Ball detector at the Johannes Gutenberg Universität in Mainz. These results, particularly the π^0n channel, provide current models attempting to describe the nucleon resonance spectrum and properties with essential constraints. Measurements on the neutron are essential to determine isospin amplitudes of the nucleon resonance spectrum. The experiment featured a photon beam polarised through coherent bremsstrahlung of a $1.5\,\text{GeV}$ electron beam on an aligned diamond radiator. The target was cryogenic liquid deuterium cooled to $23\,\text{K}$. Detection of the produced π^0s was achieved through their dominant decay to two photons which were subsequently recorded in high density scintillating crystal calorimeters, known as the Crystal Ball and TAPS. The same detectors were used to determine the direction of the recoiling proton or neutron while thin plastic scintillator was used to distinguish between the two nucleons. Results on the proton are consistent with previous measurements and predictions from groups performing partial wave analysis to determine the resonance properties. Results on the neutron are measured for the first time in this energy regime spanning the first and second resonance regions and favour the SAID partial wave analysis solution.

Contents

List of Tables

List of Figures

Declaration

The work in this thesis is based on research carried out at the Nuclear Physics Group, School of Physics and Astronomy, University of Glasgow, UK. No part of this thesis has been submitted elsewhere for any other degree or qualification and it is all my own work unless referenced to the contrary in the text.

Chapter 1

Introduction

Quantum Chromodynamics, QCD, is the theory describing the strong interaction the force carrier for which is the gluon, which binds quarks into particles like the proton and neutron. QCD describes the interaction of these gluons and quarks as a quantum field theory. These particles are referred to as hadrons and split into two subcategories, baryons and mesons, which are constructed from 3 constituent valence quarks and 2 constituent valence quarks respectively bound into a colourless state. At high energies, perturbation theory allows us to perform calculations. However, as the QCD coupling constant is not actually a constant but increases asymptotically as the distance of the interaction increases, we cannot perform calculations using perturbation theory on the size of the baryons and mesons. The internal structure of these particles are instead described by a series of phenomenological models which rely heavily on experimental data for guidance.

In any theory or model that attempts to describe the natural world the building blocks of the macroscopic world, the proton and the neutron, must play an important role. Current models do not fully describe the excitation spectrum of such nucleons, which can be related to their internal dynamics and constituents. In fact, even the lowest lying isospin-1/2 state, the famous Roper resonance, is not well understood.

The nucleon excitation spectrum may be explored experimentally via scattering reactions, such as pion scattering or pion photoproduction. Pion photoproduction is dependent on the spin states of the photon beam as well as the initial and final (or recoil) state nucleon. This results

in so-called polarisation observables which are accessible by experiments incorporating these degrees of polarisation i.e. beam, target and recoil nucleon spin polarisation. These polarisation observables can be related to bilinear combinations of complex production amplitudes that make up the transition matrix for the reaction. Measurements of such polarisation observables are necessary for models which use partial wave analysis to establish resonance properties. A global program of experiments is being performed to determine these polarisation observables and establish the nucleon resonance spectrum.

The Crystal Ball detector has been installed at the Mainzer Microtron (MAMI) facility in Mainz, Germany for the purpose of measuring polarisation observables in pion photoproduction. The facility uses a polarised photon beam with the energy of the beam determined by the Glasgow Tagger. The Crystal Ball detector in combination with the TAPS spectrometer provide an angular coverage of 96% of 4π. This allows a wide range of pion production energies and angles to be measured.

This work presents measurements of the photon beam asymmetry Σ from a liquid deuterium target for the reaction channels $\gamma p \rightarrow p\pi^0$ and $\gamma n \rightarrow n\pi^0$ over a photon beam energy range of 400-700 MeV in chapter 8. These results provide essential data to constrain partial wave analyses. In particular, the neutron channel is the first data in the world at this energy region. Measurements of pion photoproduction neutron channels are essential to determine the isospin couplings of N* and Δ resonances and as a test of isospin symmetry breaking.

1.1 Hadrons and QCD

The discovery of the neutron in 1932 [1] with a very similar mass to the proton, discovered 13 years prior [2], naturally lead to the hypothesis that they were the same type of particle, the nucleon [3]. However, the different charge for each particle required the introduction of the quantum number isospin to distinguish them with the isospin projection taking the value of $\frac{1}{2}$ for the proton and $-\frac{1}{2}$ for the neutron [4]. The discovery of many more particles in the resulting decades led to the introduction of further quantum numbers to describe the properties of hadrons. The strangely long lifetimes of particles such as the Kaon produced the strangeness
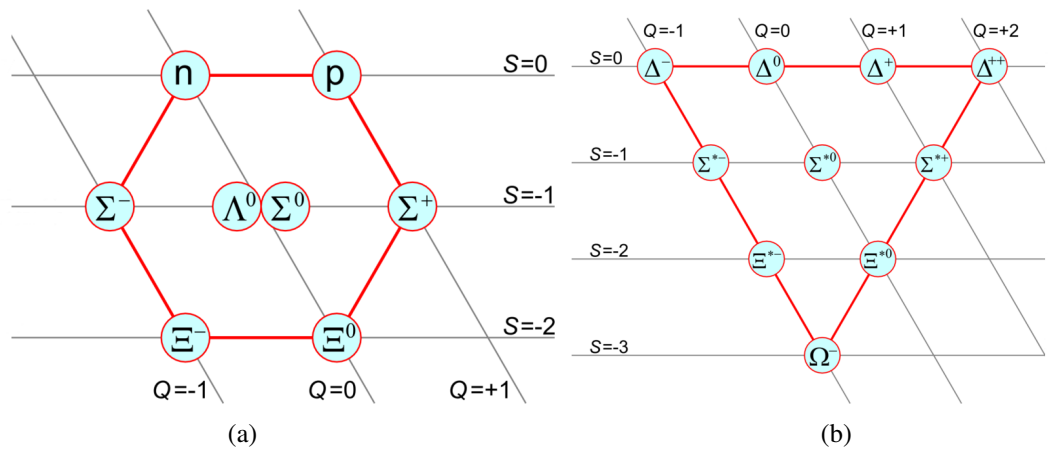
Figure 1.1: The $1/2^+$ baryon octet and the $3/2^+$ baryon decuplet. Images from Wikimedia Commons.

quantum number (S) to describe the number of strange quarks present [5,6]. The baryon quantum number (B) was used to distinguish mesons, 2 quark states with B=0, from baryons, 3 quark states with B=1. Initially the hypercharge quantum number(Y) was described as the sum of the strange and baryon numbers. It was also used to relate the electric charge to the third component of isospin. From this array of quantum numbers both Gell-Mann and Ne'eman devised the Eight-fold way system for classifying hadrons into baryons and mesons [7, 8]. Particles of the same total angular momentum and parity were grouped into multiplets of similar masses and properties. This led to the postulation of several new particles in order to complete these structures. Most notably the Ω^- baryon was predicted in 1962 by Gell-Mann and subsequently discovered through experiment in 1964 with very similar properties to the prediction [9]. The multiplets for the ground state baryons and mesons are shown in Figures 1.1 and 1.2 respectively.

The baryons are grouped into isospin $\frac{1}{2}$ and isospin $\frac{3}{2}$ multiplets and the mesons into spin-parity nonets such as the $J^P=0^-$ pseudoscalars and $J^P=1^-$ vector mesons. Naturally, the organisation of particles by this Eightfold Way led to the conclusion that they were composed of constituents. The SU(3) symmetry of the observed states implied that there was 3 such constituents required to describe the multiplets of observed baryons and mesons. These constituents, dubbed quarks by Gell-Mann after a line from James Joyce's Finnegans Wake [10], were labelled up (u), down (d) and strange (s). A summary of their properties are shown in Table 1.1.
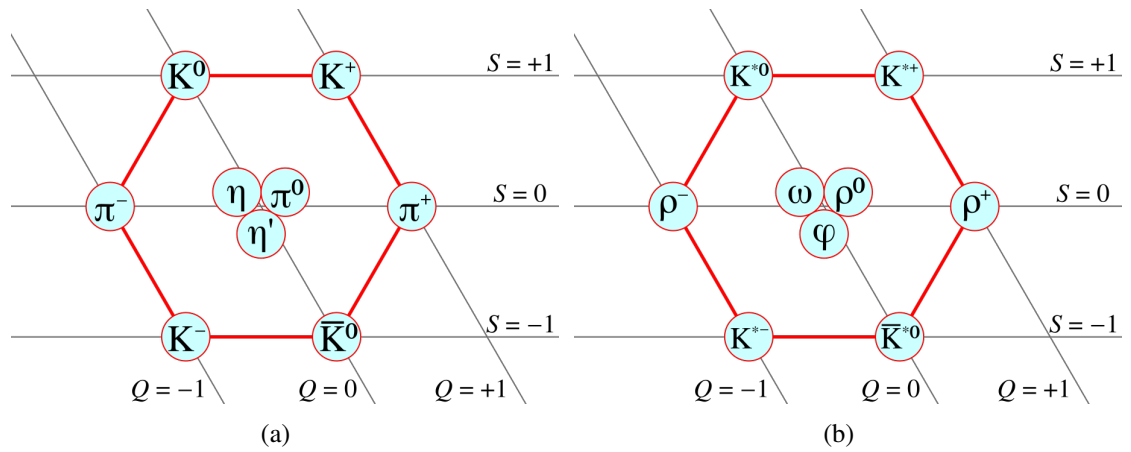
Figure 1.2: The $J^P = 0^-$ pseudoscalar and 1^- vector meson nonets. Images from Wikimedia Commons.

Flavour	Mass(MeV/c^2)	Q	B	S	I	I$_3$	J^P
u	2.2	$\frac{2}{3}$e	1/3	0	1/2	+1/2	$\frac{1}{2}^+$
d	4.7	$-\frac{1}{3}$e	1/3	0	1/2	-1/2	$\frac{1}{2}^+$
s	95	$-\frac{1}{3}$e	1/3	-1	0	0	$\frac{1}{2}^+$

Table 1.1: A summary of the properties of the three lightest quarks.

Mesons, the simplest bound objects, are described as consisting of a quarks and anti-quark pair. The baryons contain three quarks such as the proton with quark content *uud* and the neutron with *ddu*. It was not evident at the time whether quarks were real objects or simply a convenient mathematical representation. The first indication of their actual existence arose from deep inelastic electron-proton scattering [11] as these results were indicative of point-like scattering centres present within the proton.

One problem with this picture was the existence of several states such as the Δ^{++} which seemingly violated the Fermi exclusion principle. Since the spin $\frac{3}{2}$ Δ^{++} consisted of three spin $\frac{1}{2}$ u quarks with spins aligned then each quark would occupy the same state and hence violate the Fermi exclusion principle. To resolve this a new property of quarks was proposed by Greenberg [12] called colour. This new property had three states: red, blue and green. A quark could be in any one of these states with antiquarks possessing an anticolour state. All baryons and mesons have a net zero resultant colour charge. The overall colour neutral nature of all free particles leads to an interesting consequence, confinement [13]. There are no free quarks as they are always confined in a colourless bound state.

Unlike the SU(3) flavour symmetry, the SU(3) colour symmetry is an exact symmetry. From Noether's theorem [14], there must be a conserved current and charge associated with this symmetry. The force between quarks is mediated via spin-1 particles, the gluons. This is analogous to quantum electrodynamics, QED, in which the spin-1 mediating particle is the photon. However, there are significant differences between the theories which manifest in a variety of ways. QED obeys U(1) group gauge symmetry which forbids self-interaction of the force carriers in this theory [15]. As QCD obeys SU(3) group gauge symmetry, and consequently the gluons carry colour charge themselves, self interacting force carriers are possible. That is to say that gluons can and do interact with each other whereas photons do not [16]. As such, exotic states may be constructed from only gluons [17, 18].

The eight massless, colour charged gluons of the theory derive from the SU(3) group. There are 8, not 9, since the linear combination of red anti-red + blue anti-blue + green anti-green would be non-interacting [19]. The other eight arise from the different linearly independent combinations available from the 3x3 unitary matrices with determinant 1 which describes the colour charge gluons and hence the symmetry of the strong force.

A hadron is composed of valence quarks and a sea of $q\bar{q}$ pairs and virtual gluons. Recent experiments have shown that the sea accounts for around 2/3 of the total spin and half of the momentum of the nucleon [20]. The interaction between the valence quarks and this sea account for the vast majority of the mass of a hadron [21]. The summed bare mass of the valence quarks of the proton are less than 10 MeV as shown in Table 1.1. The valence quarks are dressed by this interaction with the sea to give the total mass of the proton of approximately 938 MeV.

The QCD Lagrangian is described by:

$$L_{QCD} = \sum_f \bar{q}_f [i\gamma_\mu(\partial^\mu + igA^\mu) - m_f]q_f - \frac{1}{2}Tr(F_{\mu\nu}F^{\mu\nu}) \quad (1.1)$$

where $F_{\mu\nu}$ is the field strength tensor, q_f are the quark fields, m_f are the quark masses, A are the gluon fields and g is the gauge coupling. A significant difference between QCD and QED is the change with energy of the coupling constant, g. Figure 1.3 depicts this. As is shown, the QED coupling constant varies by as little as $5\text{x}10^{-5}$ over the 200 GeV energy range. In contrast,

(a) The QED coupling constant

(b) The QCD coupling constant
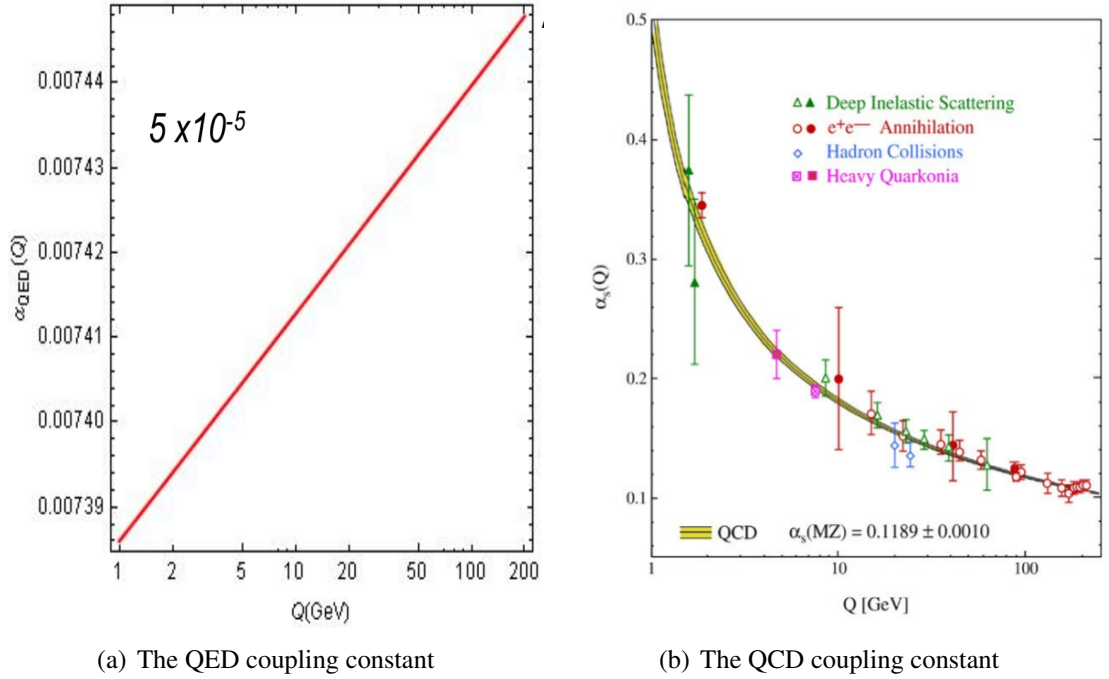
Figure 1.3: A comparison of the QED and QCD coupling constants over an energy range of 200 GeV [22].

the QCD coupling constant changes significantly over the same region. As shown by Politzer, Gross and Wilczek in 1973, for which they subsequently won the Nobel prize in 2004 [23, 24], the coupling runs with the 4-momentum transfer squared, Q^2:

$$g^2(Q^2) = \frac{4\pi}{\beta_0 ln(\frac{Q^2}{\Lambda_{QCD}^2})} \qquad (1.2)$$

where β_0 is a renormalization constant which is greater than 0 and Λ_{QCD} is the QCD scale, the value at which the coupling constant diverges, and is approximately 220 MeV. This momentum dependent coupling translates directly into a coupling which depends strongly on separation. That is to say, the interaction increases significantly as the separation grows. In fact, the coupling is massive in comparison to QED before we even reach the radius of the proton and leads to confinement of quarks within hadrons. As perturbation theory relies upon being able to neglect higher order contributions with coefficients of the coupling constant to a power and we cannot make this approximation in the low energy regime then perturbation theory fails on the scale of a few GeV. We, therefore, cannot perform ab initio calculations on the scale of baryons and mesons with perturbation theory.

1.2 QCD in the Non-Perturbative Regime

Typically, attempts to describe QCD in the non-perturbative regime can be divided into two groups. Phenomenological approaches use observed properties of QCD to constrain models while CPU intensive attempts to calculate QCD from first principles are becoming increasingly successful. These include lattice QCD in which Feynman integrals are computed on a finite 4-D Euclidean lattice; Dyson-Schwinger equations in which a truncated set of the equations of motion for quantum field theory are computed; or models such as the constituent quark model which uses dressed quarks as degrees of freedom to describe QCD bound states.

1.2.1 First Principle Approaches to QCD

Lattice QCD

Lattice QCD was first proposed by Wilson [25] in 1974 where he described a method of computing QCD on a finite 4-dimensional Euclidean lattice using Feynman path integrals. Gluons act as links between lattice sites containing quarks. In order to calculate any properties, the value of this lattice spacing must be chosen as well as the quark masses and coupling strength. Ideally, realistic quark masses and a very small lattice spacing should be used. However, the smaller the lattice spacing with the same lattice size results in an increase in the number of links and hence path integrals to be determined. Typically, lattice sizes of less than 1 fm are used corresponding to the size of a hadron.

Such calculations have been performed on supercomputers and have produced promising results. There has been a good agreement with experimental values observed for the masses of lighter hadrons [26]. Figure 1.4 shows the masses of different hadrons reproduced successfully for a variety of lattice QCD methods.

Dyson-Schwinger Equations

From the field equations of a quantum field theory one can derive a set of coupled integral equations relating the Green's functions. This infinite set of equations are known as the Dyson-Schwinger equations [28]. These are the equations of motion of the field theory and solving
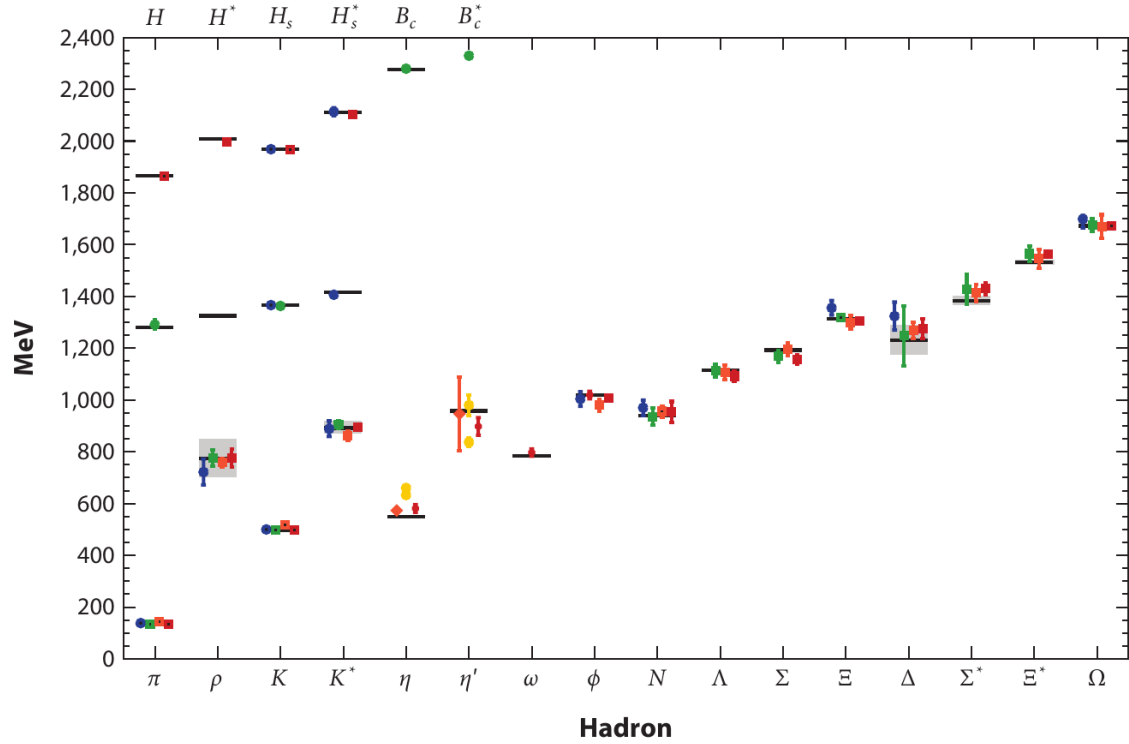
Figure 1.4: A spectrum of hadron masses reproduced from lattice QCD. Cirles, squares and diamonds represent staggered, Wilson and chiral sea quark methods respectively. The black dots represent masses which have been input into the calculations to fix parameters. The differing colours show increasing number of ensembles(lattice space and sea quark mass) from red to blue via orange yellow and green. Experimental values are denoted by the horizontal bars with grey boxes for the widths. The b-flavoured meson masses have been adjusted by 4000 MeV. Taken from [27]
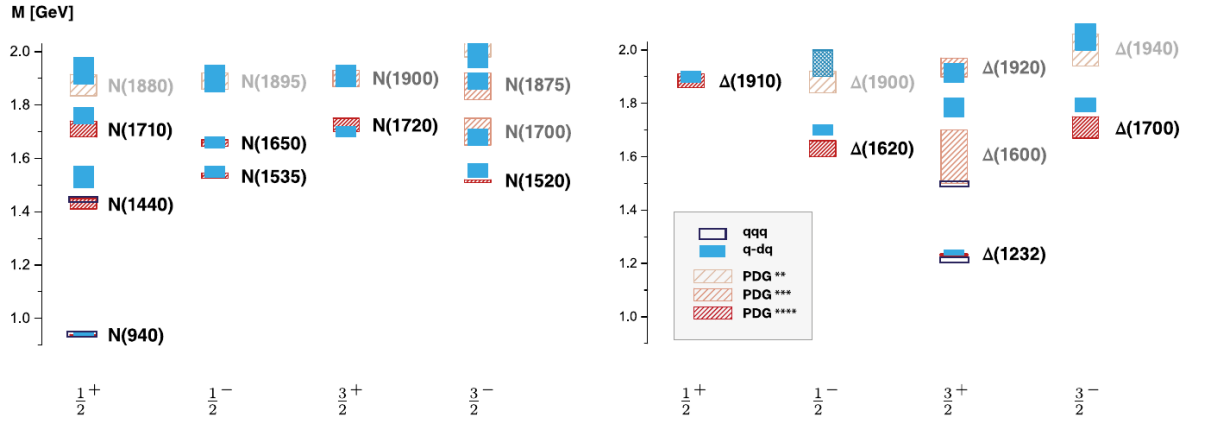
Figure 1.5: Experimental values of nucleon and Δ baryon resonances from the Particle Data Group are compared to predictions from dyson-schwinger equation calculations. Taken from [30]

these would produce a solution to the theory. However, the infinite set cannot be calculated so they are truncated. This truncated set are known as the n-point Green's functions and using these functions has produced results consistent with experiment for the form factors of the nucleon [29]. A more recent notable result from the use of Dyson-Schwinger equations has shown good agreement for the nucleon and Δ baryon spectrum states as shown in Figure 1.5 [30].

1.2.2 Phenomenological Models

MIT Bag Model

In the MIT Bag model [31] a bag of quarks interact via gluon exchange within a specified region. A boundary condition is imposed such that the quark wave function is zero outside this bag and quarks are kept inside the bag by an external pressure. Any resultant hadron produced must exist as a colour neutral/singlet state. This model has had some success at low energy, <2GeV, and low total angular momentum [32]. Extensions to this model have allowed a successful fit to πN scattering amplitudes at low energy [33].

Constituent Quark Model

As described in Section 1.1 the bare quark masses are significantly smaller than the composite mass of any hadron. The valence quarks of any such object interact with the QCD vacuum and
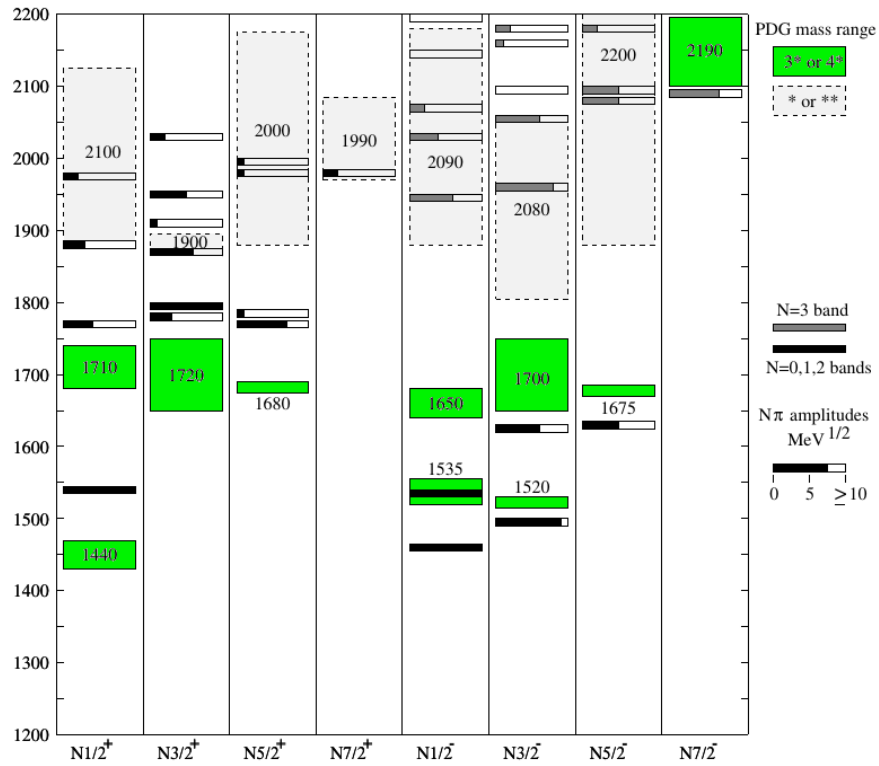
Figure 1.6: A comparison of the nucleon excitation spectrum for I=1/2 between the measured values taken from the Particle Data Group(boxes) and the predicted values from the constituent quark model(lines). Taken from [38]

generate an effective mass via spontaneous chiral symmetry breaking. The constituent quark model [34–36] uses these dressed quarks as its degrees of freedom to describe QCD bound states. This model predicts the nucleon resonance spectrum quite well [37] as shown in Figure 1.6.

However, it predicts many more resonances than have been observed experimentally. Another issue with this model is that it does not predict the Roper resonance, the lowest lying $\frac{1}{2}^+$ state with the observed mass. An extension to this model reduces the degrees of freedom by grouping two quarks together inside hadrons [39, 40]. This diquark model predicts fewer resonances but the short range force between quarks is not expected to be strong enough for these diquark objects to form [41, 42].

1.3   N* and Δ Resonances

The nucleon can be excited into a series of resonant states. Determining the complete excitation spectrum of this composite system would allow us to understand its internal structure and determine its degrees of freedom. Quark model predictions of this spectrum accurately describe the majority of low mass states. However, they also predict many more higher mass states which have not been discovered experimentally, so called missing resonances [37]. Missing resonances could be hidden due to the broad decay widths of neighbouring states or they could selectively decay via different, currently unmeasured, reaction channels. Alternatively they may not exist and the quark model requires another restriction on the degrees of freedom to accurately describe the spectrum. Figure 1.7 illuminates the the differences between quark model predicted baryon resonances and experimental discoveries. These missing resonances remain an outstanding question in the field of baryon spectroscopy.

Early measurements of the nucleon excitation spectrum primarily were provided by scattering charged pions off the proton [44]. Analysis of the final state decay angle distributions allow separation of intermediate resonances of different spin-parity into partial wave amplitudes. However, some resonances may couple very weakly to πN and are therefore hidden to pion scattering. This led to the introduction of experiments using photon beams with proton targets and measuring many different final states. However, the relative cross section between γN reactions and πN is of the order of 10^{-3} requiring high beam currents for the experiments. A significant advantage of the switch to photon beams is the ability to polarise the beam. Combined with polarised targets this leads to a collection of polarisation observables [45] providing additional sensitivity to the production amplitudes which contain the resonance response. This leads to potentially greater sensitivity to resonances with weak coupling as their interference with dominant states can be more evident in particular combinations of polarisation.

The latest Particle Data Group(PDG) summary [46] of the nucleon resonance spectrum is shown in Table 1.2. To unambiguously disentangle the contributions of differing partial waves requires precise measurements of a range of polarisation observables which has not yet been achieved experimentally. The quest to accurately determine the nucleon excitation spectrum
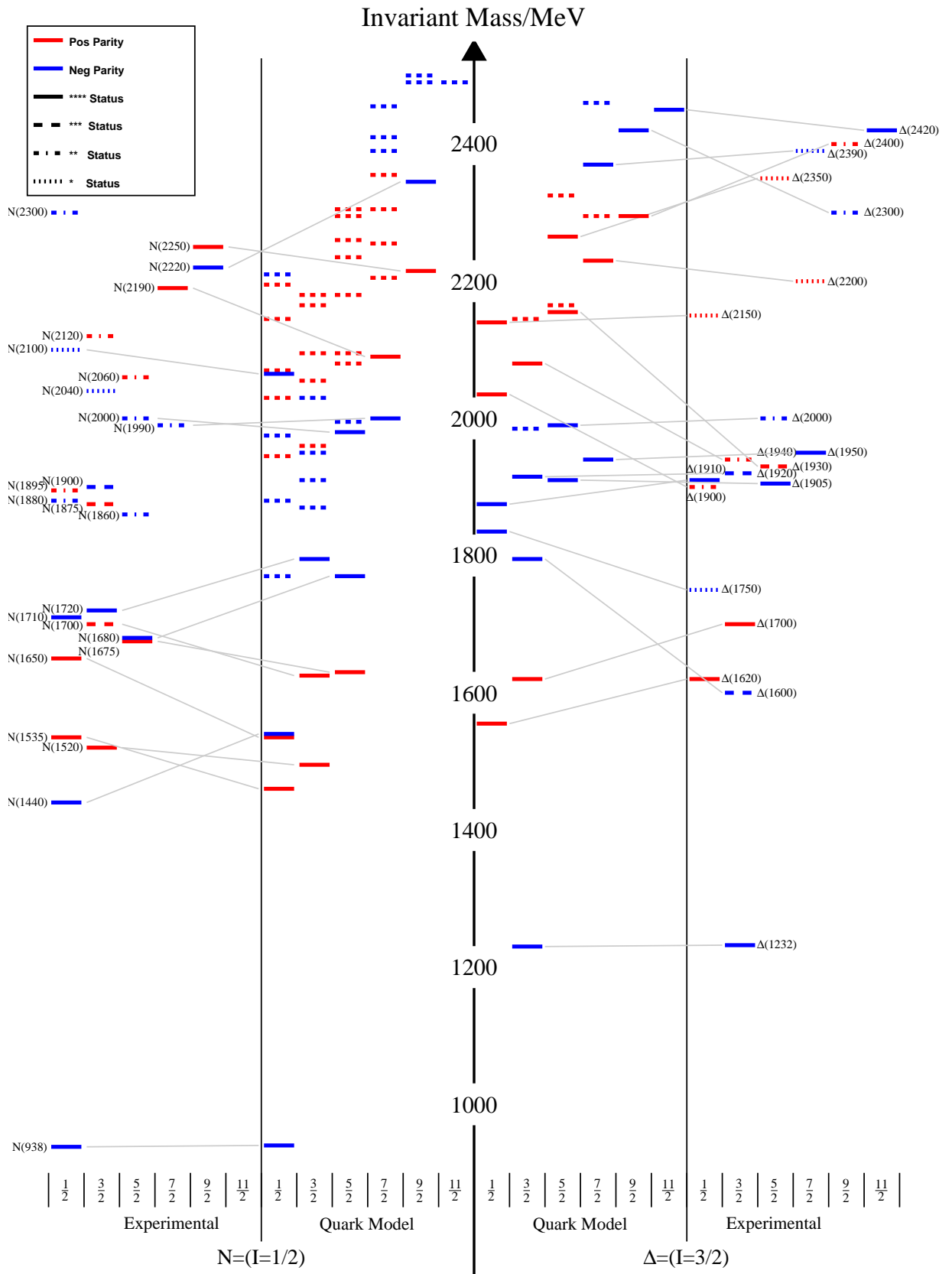
Figure 1.7: A comparison of measured baryon resonances to those predicted from quark model. The gray lines joining two states match the experimentally measured state to the quark model prediction. Dashed lines in the Quark model indicate there is no experimental designation for this state. Taken from [43].

N*	J^P	$L_{2I2J}(p\pi)$	Status	Δ^*	J^P	$L_{2I2J}(p\pi)$	Status
N(938)	$1/2^+$	P_{11}	****	Δ(1232)	$3/2^+$	P_{33}	****
N(1440)	$1/2^+$	P_{11}	****	Δ(1600)	$3/2^+$	P_{33}	****
N(1520)	$3/2^-$	D_{13}	****	Δ(1620)	$1/2^-$	S_{31}	****
N(1535)	$1/2^-$	S_{11}	****	Δ(1700)	$3/2^-$	D_{33}	****
N(1650)	$1/2^-$	S_{11}	****	Δ(1750)	$1/2^+$	P_{31}	*
N(1675)	$5/2^-$	D_{15}	****	Δ(1900)	$1/2^-$	S_{31}	***
N(1680)	$5/2^+$	F_{15}	****	Δ(1905)	$5/2^+$	F_{35}	****
N(1700)	$3/2^-$	D_{13}	***	Δ(1910)	$1/2^+$	P_{31}	****
N(1710)	$1/2^+$	P_{11}	****	Δ(1920)	$3/2^+$	P_{33}	***
N(1720)	$3/2^+$	P_{13}	****	Δ(1930)	$5/2^-$	D_{35}	***
N(1860)	$5/2^+$	F_{15}	**	Δ(1940)	$3/2^-$	D_{33}	**
N(1875)	$3/2^-$	D_{13}	***	Δ(1950)	$7/2^+$	F_{37}	****
N(1880)	$1/2^+$	P_{11}	***	Δ(2000)	$5/2^+$	F_{35}	**
N(1895)	$1/2^-$	S_{11}	****	Δ(2150)	$1/2^-$	S_{31}	*
N(1900)	$3/2^+$	P_{13}	****	Δ(2200)	$7/2^-$	G_{37}	***
N(1990)	$7/2^+$	F_{17}	**	Δ(2300)	$9/2^+$	H_{39}	**
N(2000)	$5/2^+$	F_{15}	**	Δ(2350)	$5/2^-$	D_{35}	*
N(2040)	$3/2^+$	P_{13}	*	Δ(2390)	$7/2^+$	F_{37}	*
N(2060)	$5/2^-$	D_{15}	***	Δ(2400)	$9/2^-$	G_{39}	**
N(2100)	$1/2^+$	P_{11}	***	Δ(2420)	$11/2^+$	$H_{3,11}$	****
N(2120)	$3/2^-$	D_{13}	***	Δ(2750)	$13/2^-$	$I_{3,13}$	**
N(2190)	$7/2^-$	G_{17}	****	Δ(2950)	$15/2^+$	$K_{3,15}$	**
N(2220)	$9/2^+$	H_{19}	****				
N(2250)	$9/2^-$	G_{19}	****				
N(2300)	$1/2^+$	P_{11}	**				
N(2570)	$5/2^-$	D_{15}	**				
N(2600)	$11/2^-$	$I_{1,11}$	***				
N(2700)	$13/2^+$	$K_{1,13}$	**				

Table 1.2: A summary of the N* and Δ resonances from the Particle Data Group [46]. There is significant experimental evidence for all four star resonances while the evidence for the existence of one star resonances is poor.

is part of a global programme of measurements to map out these polarisation observables in order to uniquely identify all contributing states and determine whether the missing resonance problem requires a review of the degrees of freedom of quark models.

Chapter 2

Meson Photoproduction

Pion and photon beams are used to probe nuclear targets in order to understand the resonant spectrum of the nucleon and determine the electric and magnetic couplings of individual resonances. In the past, pion beams have provided most of our understanding of the nucleon excitation spectrum [47–50]. However, a pion probe is limited as some states do not couple strongly to pions. Photoproduction provides an opportunity to excite and investigate the properties of resonances which may have been missed by pion beam experiments.

2.1   Scattering Formalism

Meson photoproduction can be described by a plane wave scattering reaction [51, 52]. An incoming plane wave representing the photon beam scatters off a scattering centre in the target producing a scattered wave containing information on the nature of the target. In terms of a particle reaction, knowledge of the momentum and spin polarisation of the initial state of the beam, target and the final state particles are required to fully determine the reaction amplitudes. The scattered wave is composed of many different reaction processes which can be disentangled into partial waves to determine the contributing reaction mechanisms.
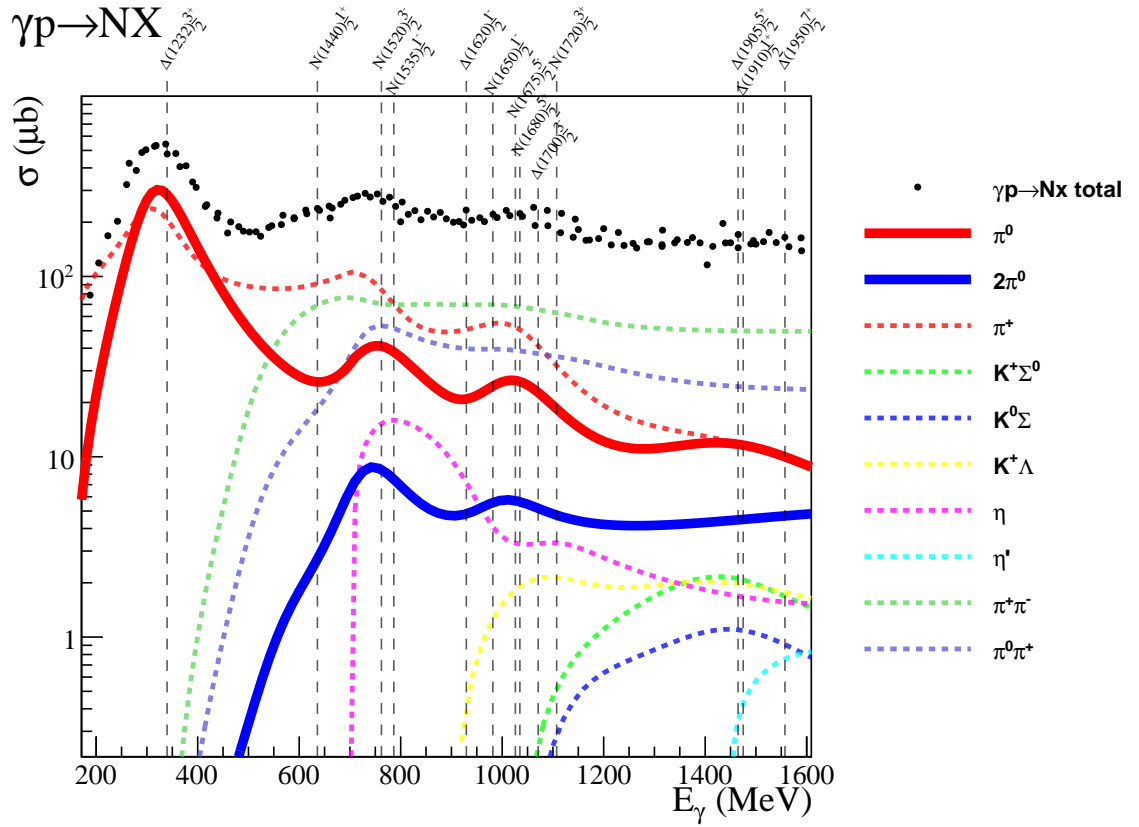
Figure 2.1: Cross section of different contributing hadronic photoproduction processes. Four star N* and Δ resonances from the PDG are indicated at the beam energy corresponding to the centre of mass energy required to reach their invariant mass in a fixed-target experiment. Taken from [43]

2.1.1 Reaction Mechanisms

A nucleon photoproduction reaction has many different possible final states as illustrated in Figure 2.1. Additional channels become possible with increasing photon beam energy such as the η meson final states. Each process has a different cross section associated with it. This is proportional to the probability that the interaction between the target and the beam will result in this particular state. The total cross section is the sum of all possible reactions from the photoproduction process including both the elastic and inelastic processes. The total cross section for $\gamma p \rightarrow NX$ is shown in Figure 2.1 [53–55]. Several resonances regions can be easily identified via peaks in the total cross section. However, many others are broad, overlapping and show up more prominently in different final states than others. Identifying all resonances from the total cross section alone is not possible and instead the decay products must be analysed to determine the

contributions of different states.

2.1.2 Scattering Formalism

The probability for some initial state $|i\rangle$ to transform into some final state $|f\rangle$ is described by the scattering matrix for the reaction. For pseudoscalar meson photoproduction, such as the case of $\gamma p \rightarrow p\pi^0$, this can be written as:

$$S_{fi} = \langle f|S|i\rangle = \frac{1}{(2\pi)^2}\delta^4(p_{N'} + p_m - p_N - p_\gamma)\sqrt{\frac{M_N^2}{4E_{N'}E_mE_NE_\gamma}} \cdot iT_{fi} \quad (2.1)$$

where p_i are the four momenta of each of the particles in the reaction; p_γ for the photon, p_N for the nucleon target, p_m for the meson and $p_{N'}$ for the final state nucleon. E_i are the energies for each of these particles. M_N is the mass of the nucleon target. The factor T_{fi} is the transition matrix containing the Lorentz invariant terms describing the transition from $|i\rangle$ to $|f\rangle$.

The transition matrix is related to the photon polarisation vector, ε_μ, via:

$$T_{fi} = \varepsilon_\mu J_\mu^{fi} \quad (2.2)$$

where J_μ^{fi} is the nucleon electromagnetic current. The transition matrix is also related to the differential cross section via:

$$\frac{d\sigma}{d\Sigma} = \frac{p_m}{p_\gamma}\sum\left|\frac{M_N}{4\pi W}T_{fi}\right|^2 \quad (2.3)$$

with the summation over all the nucleon and photon spin states.

Different reaction mechanisms contribute to the final state of photoproduction experiments. They are summarised in Figure 2.2 for the case of π^0 photoproduction. The resonant s-channel production is the reaction of interest for investigating nucleon excited states. The Born and vector meson terms exhibit a well understood and smooth trend across the energy range and are designated as background [56, 57].

(a) Born S-Channel

(b) Born T-Channel

(c) Born U-Channel

(d) Vector Meson Exchange

(e) Resonant S-Channel

(f) Resonant U-Channel
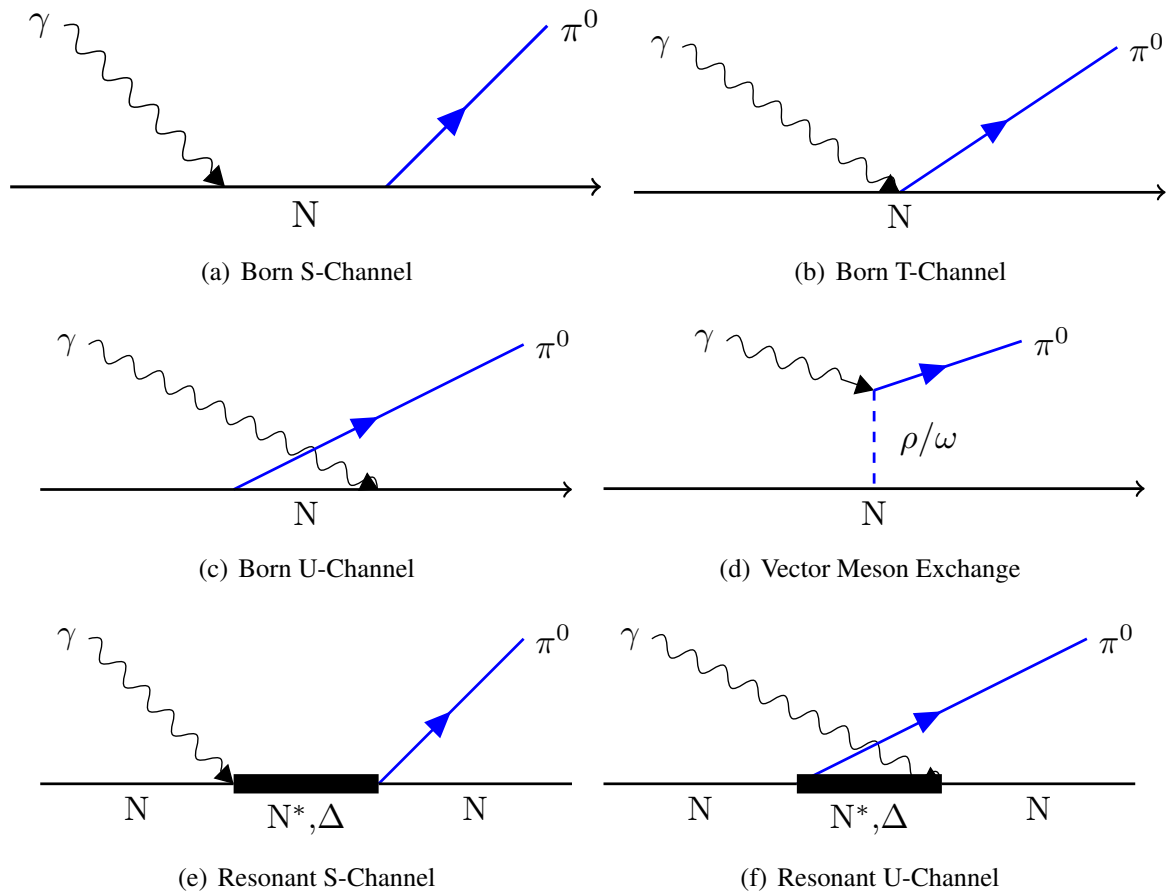
Figure 2.2: Processes that produce a single π^0 via a photoproduction reaction. Taken from [43].

(a) No spin flip   (b) Anti-parallel spin flip   (c) Parallel spin flip   (d) Double spin flip
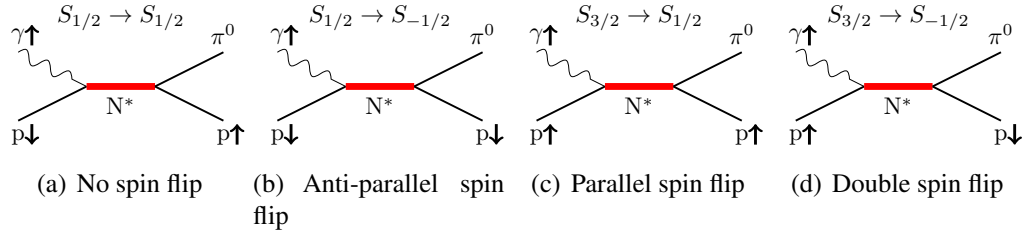
Figure 2.3: The four different spin flip helicity reactions. The spins are indicated by arrows beside the particles. The proton is a fermion with spin $\pm\frac{1}{2}$. The photon is a boson with spin ± 1. Taken from [43].

2.1.3   Photoproduction Amplitudes

In a photoproduction reaction the nucleon can take one of two spin states either aligned parallel or anti-parallel to the relative angular momentum. The photon has both an electric and magnetic component which results in four types of multipole to describe the coupling of the photon to the nucleon in the reaction. These four are E_{l+} E_{l-} M_{l+} M_{l+} with some relative angular momentum l.

The different possible orientations for the photon polarisation, target nucleon spin alignment and final state nucleon spin alignment result in 8 combinations and hence 8 amplitudes. Through parity and rotational invariance this can be reduced to 4 combinations. These four are shown in Figure 2.3 where the different s-channel diagrams represent a no spin flip N, an anti-parallel spin flip S_A, a parallel spin flip S_P and a double spin flip D. These correspond to four helicity amplitudes which can be expressed in terms of Legendre polynomials and the electric and magnetic multipoles [58, 59].

$$
\begin{aligned}
N &= \frac{1}{\sqrt{2}}\cos\left(\frac{\theta}{2}\right)\sum_{l=0}^{\infty}[(l+2)E_{l+}+lM_{l+}+lE_{(l+1)-}-(l+2)M_{(l+1)-}](P_l' - P_{l+1}') \\
S_A &= \frac{1}{\sqrt{2}}\sin\left(\frac{\theta}{2}\right)\sum_{l=0}^{\infty}[(l+2)E_{l+}+lM_{l+}-lE_{(l+1)-}+(l+2)M_{(l+1)-}](P_l' + P_{l+1}') \\
S_P &= \frac{1}{\sqrt{2}}\cos\left(\frac{\theta}{2}\right)\sin(\theta)\sum_{l=1}^{\infty}[E_{l+}-M_{l+}-E_{(l+1)-}-M_{(l+1)-}](P_l'' - P_{l+1}'') \\
D &= \frac{1}{\sqrt{2}}\sin\left(\frac{\theta}{2}\right)\sin(\theta)\sum_{l=1}^{\infty}[E_{l+}-M_{l+}+E_{(l+1)-}+M_{(l+1)-}](P_l'' + P_{l+1}'')
\end{aligned}
\tag{2.4}
$$

P' and P'' represent the first and second derivatives of the Legendre polynomials respectively

and are functions of $\cos\theta$ only. The total cross section can be calculated from these amplitudes via:

$$\sigma = N^2 + S_A^2 + S_P^2 + D^2 \tag{2.5}$$

Alternatively the spin flip amplitudes may be expressed as four complex transversity amplitudes giving a more natural link to the polarisation observables that can be measured in experiment [60].

$$
\begin{aligned}
b_1 &= \frac{1}{2}[(S_P + S_A) + i(N - D)] \\
b_2 &= \frac{1}{2}[(S_P + S_A) - i(N - D)] \\
b_3 &= \frac{1}{2}[(S_P - S_A) - i(N + D)] \\
b_4 &= \frac{1}{2}[(S_P - S_A) + i(N + D)]
\end{aligned}
\tag{2.6}
$$

Taking bilinear combinations of these amplitudes results in 16 polarisation observables that can be measured through experiments combining different combinations of polarised beam, target and recoil nucleon. The 16 polarisation observables are listed in Table 2.1 with the different combinations required to produce them. They are split into four categories. The single polarisation observables require no polarisation or just one of the beam, target or recoil nucleon to be polarised. The other three groupings are double polarisation observables requiring a combination of two polarisations at once. The beam-target set requires a polarised photon beam of either linear or circular polarisation and the nucleon target to be polarised. The beam-recoil require the photon beam polarised and the recoiling nucleon polarisation to be measured. The target recoil requires polarised target and measurement of the recoiling nucleon polarisation.

The polarisation observables are not independent. Relationships can be formed between several of them, reducing the number that need to be measured to provide an unambiguous solution and determine all the amplitudes [60–62]. The four single polarisation observables and four appropriately chosen double polarisation observables are one combination that if measured would allow prediction of all other observables [63, 64]. However, they would need to be accurately measured and the uncertainties associated with current measurements do not constrain the amplitudes sufficiently to provide a unique solution [65].

The observables can be linked to experimental polarisation observables by the differential

Observable	Helicity Representation	Transversity Representation	Experimental Conditions(B/T/R)	Observable Type
σ_0	$N^2 + S_A^2 + S_P^2 + D^2$	$b_1^2 + b_2^2 + b_3^2 + b_4^2$	-/-/-	Single
Σ	$2\mathrm{Re}(S_A^* S_P - ND^*)$	$b_1^2 + b_2^2 - b_3^2 - b_4^2$	P^L/-/-	Single
T	$2\mathrm{Im}(S_A N^* - S_P D^*)$	$b_1^2 - b_2^2 - b_3^2 + b_4^2$	-/P_y/-	Single
P	$2\mathrm{Im}(S_P N^* - S_A D^*)$	$b_1^2 - b_2^2 + b_3^2 - b_4^2$	-/-/σ'_y	Single
G	$-2\mathrm{Im}(S_A S_P^* + ND^*)$	$2\mathrm{Im}(b_1 b_3^* + b_2 b_4^*)$	P^L/P_z/-	Beam-Target
H	$-2\mathrm{Im}(S_A D^* + S_P N^*)$	$-2\mathrm{Re}(b_1 b_3^* - b_2 b_4^*)$	P^L/P_x/-	Beam-Target
E	$S_P^2 - S_1^2 - D^2 + N^2$	$-2\mathrm{Re}(b_1 b_3^* + b_2 b_4^*)$	P^C/P_z/-	Beam-Target
F	$2\mathrm{Re}(S_P D^* + S_A N^*)$	$2\mathrm{Im}(b_1 b_3^* - b_2 b_4^*)$	P^C/P_x/-	Beam-Target
O_x	$-2\mathrm{Im}(S_P D^* + S_A N^*)$	$-2\mathrm{Re}(b_1 b_4^* - b_2 b_3^*)$	P^L/-/σ'_x	Beam-Recoil
O_z	$-2\mathrm{Im}(S_P S_A^* + ND^*)$	$-2\mathrm{Im}(b_1 b_4^* + b_2 b_3^*)$	P^L/-/σ'_z	Beam-Recoil
C_x	$-2\mathrm{Re}(S_P N^* + S_A D^*)$	$2\mathrm{Im}(b_1 b_4^* - b_2 b_3^*)$	P^C/-/σ'_x	Beam-Recoil
C_z	$S_P^2 - S_A^2 - N^2 - D^2$	$-2\mathrm{Re}(b_1 b_4^* + b_2 b_3^*)$	P^C/-/σ'_z	Beam-Recoil
T_x	$2\mathrm{Re}(S_A S_P^* + ND^*)$	$2\mathrm{Re}(b_1 b_2^* - b_3 b_4^*)$	-/P_x/σ'_x	Target-Recoil
T_z	$2\mathrm{Re}(S_A N^* + S_P D^*)$	$2\mathrm{Im}(b_1 b_2^* - b_3 b_4^*)$	-/P_x/σ'_z	Target-Recoil
L_x	$2\mathrm{Re}(S_P N^* - S_A D^*)$	$2\mathrm{Im}(b_1 b_2^* + b_3 b_4^*)$	-/P_z/σ'_x	Target-Recoil
L_z	$S_A^2 + S_P^2 - N^2 - D^2$	$2\mathrm{Re}(b_1 b_2^* + b_3 b_4^*)$	-/P_z/σ'_z	Target-Recoil

Table 2.1: Single and double polarisation observables for pion photoproduction. The transversity and helicity amplitudes are shown for each observable. σ_0 is the unpolarised differential cross section. The experimental conditions required to measure the observable are shown with the format Beam/Target/Recoil. $P_{L,C}$ are the linear and circular polarisation respectively. $P_{x,y,z}$ and $\sigma'_{x,y,z}$ are the target and recoil nucleon polarisation for each of the respective axes.

cross section for pseudoscalar meson photoproduction [66]:

$$
\begin{aligned}
\frac{d\sigma}{d\Omega} = \frac{1}{2}\sigma_0 \big[& 1 - P^L \Sigma \cos 2\phi + P_x(P^C F + P^L H \sin 2\phi) \\
& + P_y(T - P^L P \cos 2\phi) + P_z(P^C E + P^L G \sin 2\phi) \\
& + \sigma'_x[P^C C'_x + P^L O'_x \sin 2\phi + P_x(T'_x - P^L L'_z \cos 2\phi) \\
& + P_y(P^L C'_z \sin 2\phi - P^C O'_z) + P_z(L'_x + P^L T'_z \cos 2\phi)] \\
& + \sigma'_y[P + P^L T \cos 2\phi + P_x(P^C G - P^L E \sin 2\phi) \\
& + P_y(\Sigma - P^L \cos 2\phi) + P_z(P^L F \sin 2\phi + P^C H)] \\
& + \sigma'_z[P^C C'_z + P^L O'_z \sin 2\phi + P_z(T'_z + P^L L'_x \cos 2\phi) \\
& + P_y(-P^L C'_x \sin 2\phi - P^L O'_z) + P_z(L'_z + P^L T'_z \cos 2\phi)] \big]
\end{aligned}
\tag{2.7}
$$

where $P_{x,y,z}$ is the degree of polarisation of the target and $\sigma'_{x,y,z}$ the polarisation axes of the recoiling nucleon respectively. σ_0 is the unpolarised differential cross section and the polarisation

observables are denoted by the colour red. P^L and P^C are the degree of linear and circular polar-isation respectively. This thesis presents measurement of the single polarisation observable Σ, the photon beam asymmetry, which represents the asymmetry between the polarisation plane of the photon beam and the production plane of the meson.

2.1.4 Resonance Contributions

A resonance produced via a photon beam has an electric and magnetic multipole associated with it which, along with the isospin, define its partial wave. In the photon beam energy regime of this work the $\Delta(1232)\frac{3}{2}^+$ (P_{33}) and $N^*(1520)\frac{3}{2}^-$ (D_{13}) are the most significant resonances for π^0 photoproduction. The partial waves for the P_{33} can be expressed in terms of the multipoles E_{1+} and M_{1+} and for the D_{13} resonance the M_{2-} and E_{2-}. For $\frac{d\sigma}{d\Omega}$ and Σ these partial waves can be described as a function of θ for each of the multipoles [67].

$$
\begin{aligned}
\left(\frac{d\sigma}{d\Omega}\right)_{E_{1+}} &= 9k_{E_{1+}}(1+\cos^2\theta) \\
\left(\frac{d\sigma}{d\Omega}\right)_{M_{1+}} &= k_{M_{1+}}(5-3\cos^2\theta) \\
\left(\frac{d\sigma}{d\Omega}\right)_{E_{2-}} &= k_{E_{2-}}(5-3\cos^2\theta) \\
\left(\frac{d\sigma}{d\Omega}\right)_{M_{2-}} &= 9k_{M_{2-}}(1+\cos^2\theta)
\end{aligned}
\tag{2.8}
$$

$$
\begin{aligned}
\check{\Sigma}_{E_{1+}} &= \left(\Sigma\frac{d\sigma}{d\Omega}\right)_{E_{1+}} = -9k_{E_{1+}}\sin^2\theta \\
\check{\Sigma}_{M_{1+}} &= \left(\Sigma\frac{d\sigma}{d\Omega}\right)_{M_{1+}} = 3k_{M_{1+}}\sin^2\theta \\
\check{\Sigma}_{E_{2-}} &= \left(\Sigma\frac{d\sigma}{d\Omega}\right)_{E_{2-}} = -3k_{E_{2-}}\sin^2\theta \\
\check{\Sigma}_{M_{2-}} &= \left(\Sigma\frac{d\sigma}{d\Omega}\right)_{M_{2-}} = 9k_{M_{2-}}\sin^2\theta
\end{aligned}
\tag{2.9}
$$

where k are coefficients unique to each partial wave. The amplitudes described in equation 2.4 are a function of energy as the contribution of each resonance varies with energy.

Isospin is not conserved in electromagnetic reactions. At the resonance production vertex

(a) π^0 reaction frame   (b) π^0 projection
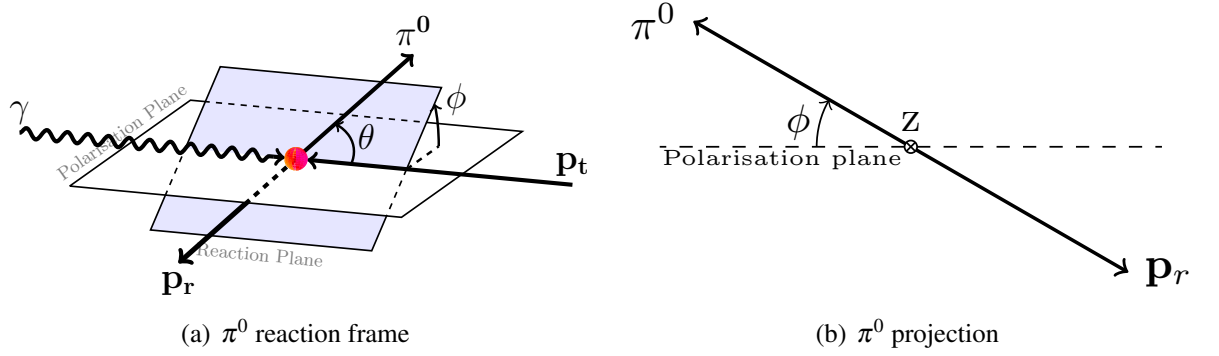
Figure 2.4: Pion photoproduction kinematics in the centre of mass frame. Taken from [43].

the photon can have both isoscalar(Δ I=0) and isovector(Δ I=0,$\pm$1) components which couple differently to resonances. For the four single pion photoproduction channels the amplitudes are given by linear combinations of the 3 isospin amplitudes [68]:

$$A(\gamma p \to \pi^+ n) = -\sqrt{\frac{1}{3}} A^{V3} + \sqrt{\frac{2}{3}} (A^{V1} - A^{S1})$$

$$A(\gamma p \to \pi^0 n) = \sqrt{\frac{2}{3}} A^{V3} + \sqrt{\frac{1}{3}} (A^{V1} - A^{S1})$$

$$A(\gamma n \to \pi^- n) = \sqrt{\frac{1}{3}} A^{V3} - \sqrt{\frac{2}{3}} (A^{V1} + A^{S1})$$

$$A(\gamma n \to \pi^0 n) = \sqrt{\frac{2}{3}} A^{V3} + \sqrt{\frac{1}{3}} (A^{V1} + A^{S1})$$

(2.10)

where $A^{V1,3}$ represent isovector amplitudes for a final state isospin of I=$\frac{1}{2}$ and I=$\frac{3}{2}$ respectively. A^{S1} is the I=$\frac{1}{2}$ final state isoscalar amplitude. In order to determine the full amplitude of the resonance photoproduction each of the 3 isospin amplitudes are required. Measurements of neutron channels are therefore essential. In principle, with 3 unknowns, one reaction is not required. However, it can be used to verify the other measurements or check for isospin symmetry breaking.

2.2 Single π^0 Photoproduction Reaction with Linear Polarisation

The centre of mass(COM) frame for single π^0 photoproduction is shown in Figure 2.4. In this

frame the nucleon and π^0 are produced back to back with equal and opposite momenta. The θ angle is defined as the angle between the beam axis and π^0 polar angle in the COM frame. ϕ is defined as the angle between the reaction plane of the π^0 and nucleon and the polarisation plane of the photon. Σ has a $\cos 2\phi$ dependence on the differential cross section:

$$\frac{d\sigma}{d\Omega}(\phi) = \left(\frac{d\sigma}{d\Omega}\right)_0 (1 + P^L \Sigma \cos(2\phi)) \tag{2.11}$$

Hence measuring the azimuthal (ϕ) dependence of the pion relative to the plane of linear polarisation allows one to determine Σ.

Chapter 3

Experimental Status

This chapter details previous measurements available for the channels and observables analysed in this thesis. Also included is a brief look at the application of such results by phenomenologists and prominent theoreticians and the differing methodologies used for Partial Wave Analysis of the data.

3.1 Previous Measurements

The photon beam asymmetry Σ for π^0 photoproduction measurements date back to 1964 [69]. This section details notable results in a similar photon beam energy regime to this work.

3.1.1 $\gamma \mathbf{p} \to \mathbf{p} \ \pi^0$

Mainz: A2

The Mainzer Microtron facility provided the majority of results which overlap with this work. Of particular note is the 2016 Gardner et al. [67] high statistics measurement covering the photon beam energy region of 320-650 MeV. Two results from Beck et al. [70, 71] provide coverage of 240-440 MeV. The Hornidge et al. [72] results cover the π^0 threshold from 147-180 MeV. Chapter 4 details the experimental facility at the A2 hall in Mainz. An electron beam is used to produce polarised photons via coherent Bremsstrahlung on a diamond radiator. The results by Gardner et al. and Hornidge used the same experimental setup as the current work but with a
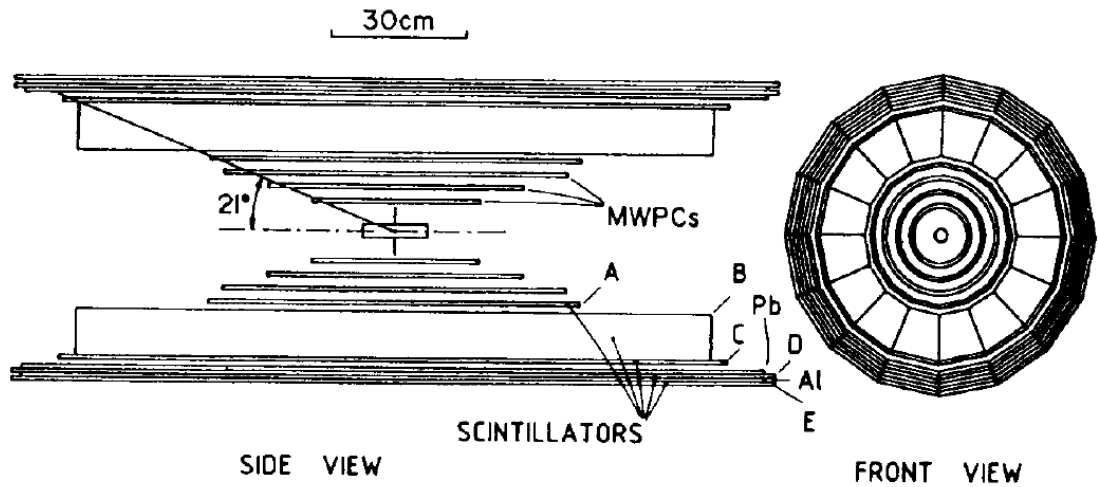
Figure 3.1: Schematic view of the DAPHNE detector. Taken from [73].

hydrogen target.

Prior to the upgrade to MAMI-C the electron beam energy was a maximum of 855 MeV and the Glasgow Tagger could tag photons up to 800 MeV. The first measurements by Beck et al. [70, 71] were taken with this energy and using the DAPHNE (Detecteur a grande Acceptance pour la physique PHotoNucleaire Experimentale) detector [73, 74] as shown in Figure 3.1. It was a multi-layered, segmented detector allowing measurements of the full 2π azimuthal range and a coverage of $21° < \theta < 159°$ of polar angle. This experiment provided measurements in the energy range of 270-420 MeV.

Additional measurements by Beck et al. [75] were obtained using the full TAPS array as shown in Figure 3.2. The polar angle coverage was increased to $12° < \theta < 170°$ by using this configuration. However, the azimuthal acceptance was reduced. The photon energy of these was increased slightly to cover the range $240 < E_\gamma < 420$ MeV. The results for Σ from these experiments are shown in Figure 3.3.

Measurements by Hornidge et al. [72] used the current setup at Mainz as detailed in Chapter 4. Results were obtained close to the π^0 threshold for 147-180 MeV and $-1 < \cos\theta < 1$ with a polarisation of photons between 50% and 70%. These are shown in Figure 3.4.

The most recent measurements by Gardner et al. [67] cover the gap between the first and second resonance region. An incident electron beam energy of 1508 MeV was used to produce results in a photon beam energy range of 320-650 MeV with $-1 < \cos\theta < 1$. The degree of polar-
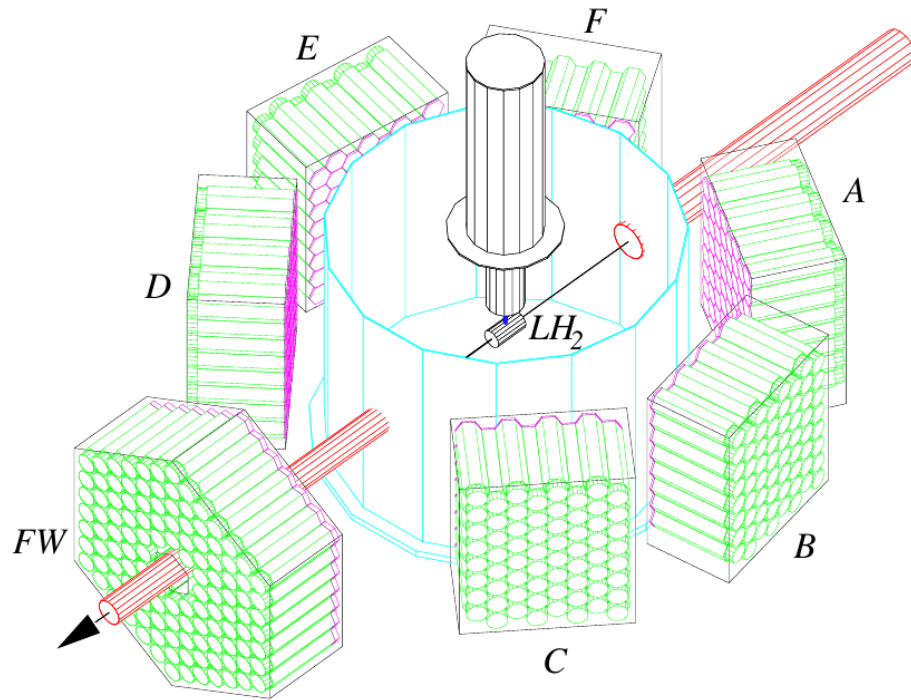
Figure 3.2: The arrangement of the TAPS BaF$_2$ detectors used in the A2 hall for the collection of data. Taken from [75]

isation ranged from 4% at 320 MeV to 53% at 630 MeV. The high statistical precision of these results and the photon energy overlap with the current work make them ideal for comparing with results on the quasi-free proton in Chapter 8. A selection of these results are shown in Figure 3.5.

GRAAL

GRAAL (GRenoble Anneau Accelerateur Laser) [82] produced highly polarised photons via Compton back scattering a laser off electrons from the European Synchrotron Radiation Facility (ESRF). An extremely high degree of polarisation of 98% was achieved with this configuration using a laser with two wavelengths of 514 nm and 351 nm and an electron beam of 6.03 GeV. Measurements for a large energy range of 550-1500 MeV were produced with 2π azimuthal angle range and polar angles of θ_{CM}=40-170° by Bartalini et al. [83]. A second measurement in the range 700-1500 MeV was performed by Di Salvo et al. [84] on a deuterium target with the results found to match the Bartalini results. A comparison of these two results in the region in which
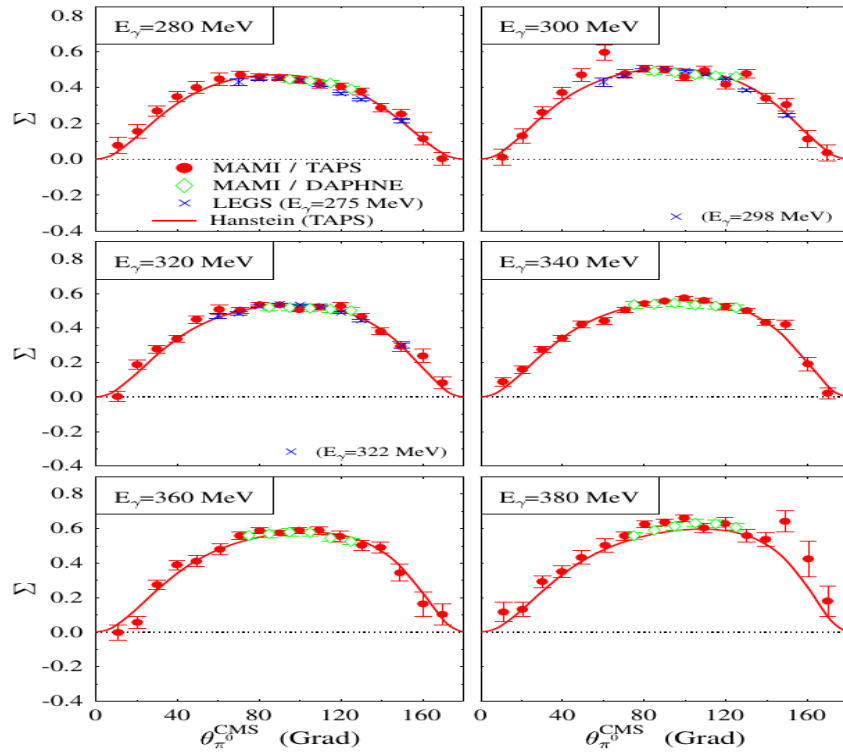
Figure 3.3: Results for the beam asymmetry Σ for the reaction $\gamma p \rightarrow \pi^0 p$ at MAMI for the TAPS and DAPHNE experiments at the A2 hall in Mainz. Results from the LEGS experiment are also shown. Red circles are the TAPS results [75], green diamonds are the DAPHNE [70] and blue crosses are from LEGS [76]. The data is plotted against a theoretical prediction from Hanstein [77, 78]. Taken from [75].
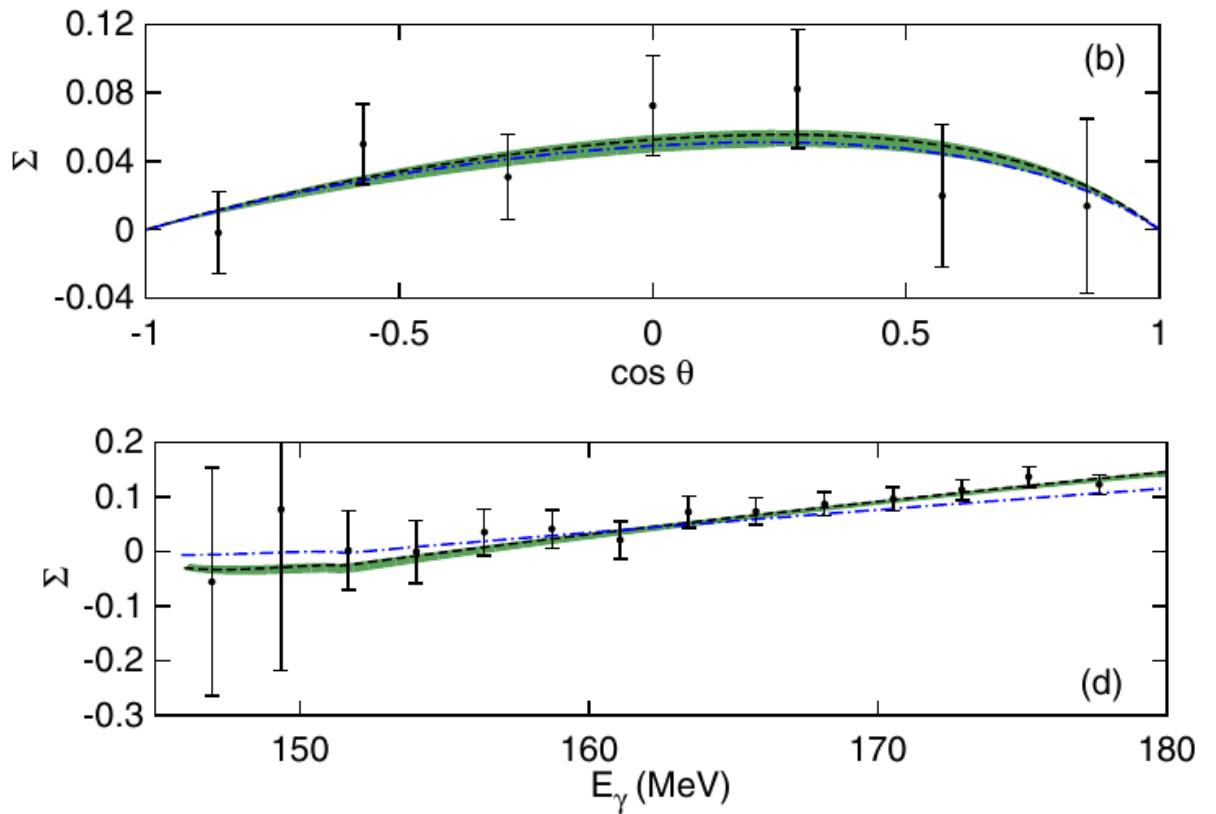
Figure 3.4: Results taken from Hornidge et al. [72] with the top figure showing photon beam asymmetry as a function of pion c.m. production angle with a beam energy of 163.4 MeV. The bottom figure shows the results across a range of beam energies for a fixed pion c.m. angle of 90°.
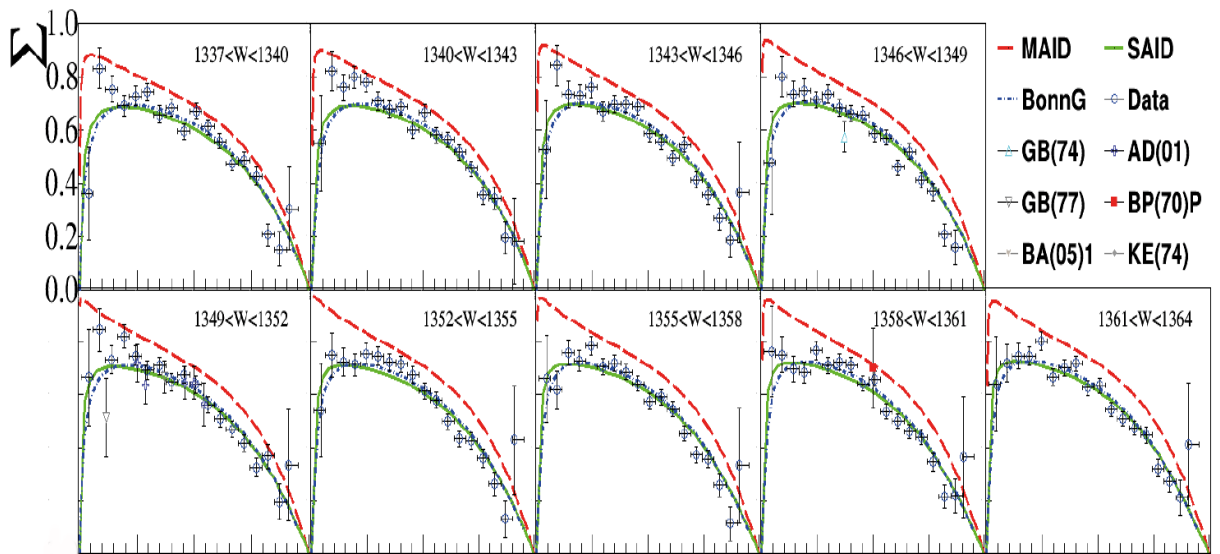
Figure 3.5: Beam asymmetry results from Gardner et al. [67] (blue open circles) for the c.m. energy range indicated on each plot from $\cos\theta$ -1 to 1. The PWA predictions are shown as coloured lines with SAID being green [79], MAID red [80] and Bonn-Gatchina blue (dashed) [81]. A few data points from older experiments are also plotted as indicated in the legend. W is the centre of mass energy of the reaction. Please see Gardner et al. for details.
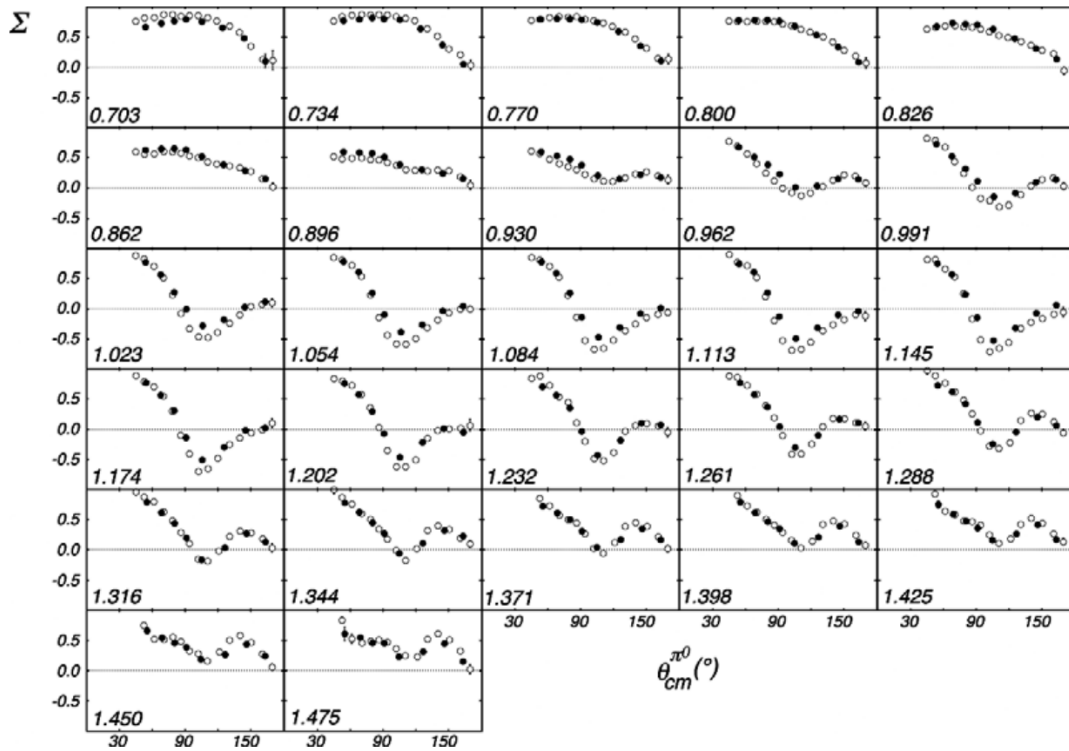
Figure 3.6: Comparison of the beam asymmetry Σ for results from Di Salvo et al. [84] on the deuteron(filled circles) with results from Bartalini et al. [83] on the proton(open circles). This is a comparison of the free proton results versus the bound proton in the deuteron. The behaviour of both results is the same. E is the photon beam energy. Taken from [84].

they overlap is shown in Figure 3.6.

Yerevan

In a similar manner to Mainz, the Yerevan experimental facility [85] used an electron beam of 3.5 GeV incident on a diamond target to produce linearly polarised photons. Measurements were taken by Adamian et al. [85] in the range 0.5-1.1 GeV in photon energy with a beam polarisation of 70% at 0.5 and 50% at 1.1 GeV and polar angle coverage of $85°<\theta_{\pi^0}<125°$. The detector set-up at Yerevan is shown in Figure 3.7 with the reduced angular acceptance due to the detectors being arranged as two arms. The results by Adamian et al. are shown in Figure 3.8.

CBELSA

The crystal barrel at ELSA (CBELSA) [86] experiment uses a coherent bremsstrahlung facility in the same manner as A2 at Mainz to produce linearly polarised photons. The ELSA contin-
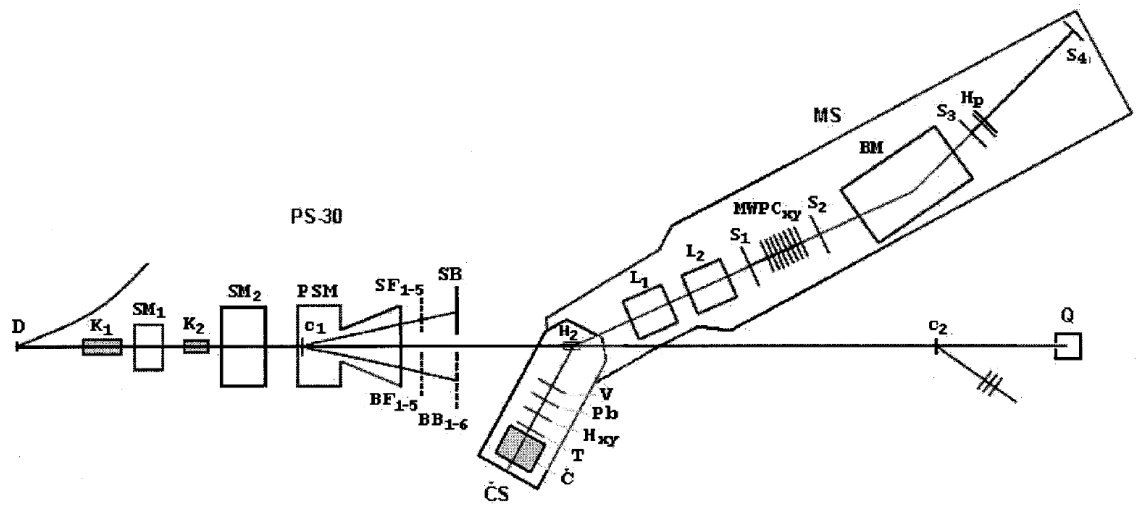
Figure 3.7: Schematic of the Yerevan detector system. Taken from [85]

uous wave electron accelerator provided an electron beam of 3.175 GeV to strike a diamond radiator and produce the polarised photons. A maximum degree of linear polarisation of 48% was achieved for the results discussed here. The configuration of the detectors for this experiment is shown in Figure 3.9. The crystal barrel was comprised of 1296 CsI crystals. TAPS consisted of 528 BaF$_2$ crystals and covered the polar angles of 5° to 30°. Two significant results from this experiment from Elsner et al. [88] and Sparks et al. [89] cover the photon beam energy range of 767 to 1680 MeV with polar angle acceptance of 6° to 168°. The results for these measurements are shown in Figures 3.10 and 3.11.

LEGS

Laser back-scattering was utilised at the Laser Electron Gamma Source (LEGS) at Brookhaven National Lab to produce photons with polarisation of greater than 80%. The National Synchrotron Light Source produced electrons of 2.6 GeV. Photons with energies ranging from 200-300 MeV were incident on the LH2 target as shown in Figure 3.12. The NaI detectors were used to detect the two photons from the decay of the π^0 and the recoil protons were measured using time of flight from tracking in the wire chambers and plastic scintillators. The results from this experiment are included in Figure 3.3, both from Blanpied et al. [76, 90].
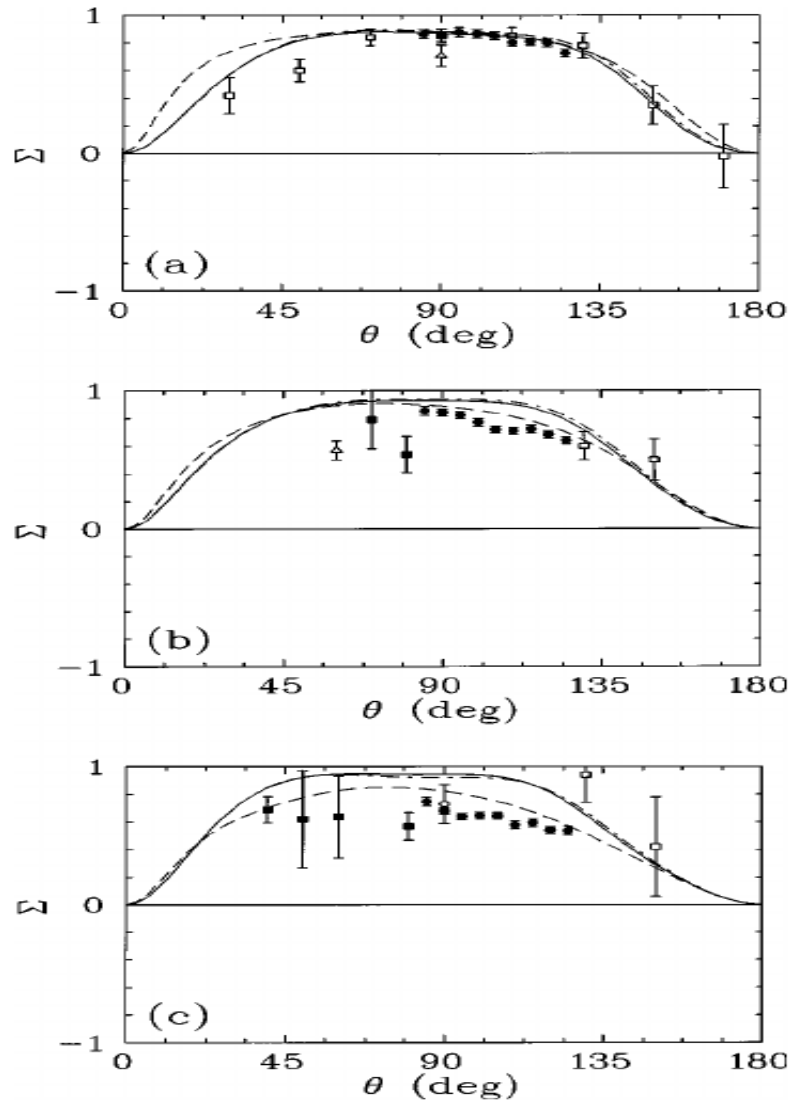
Figure 3.8: Angular dependence of the photon beam asymmetry Σ for beam energies of 700 MeV(top), 750 MeV(middle) and 800 MeV(bottom). Taken from [85].
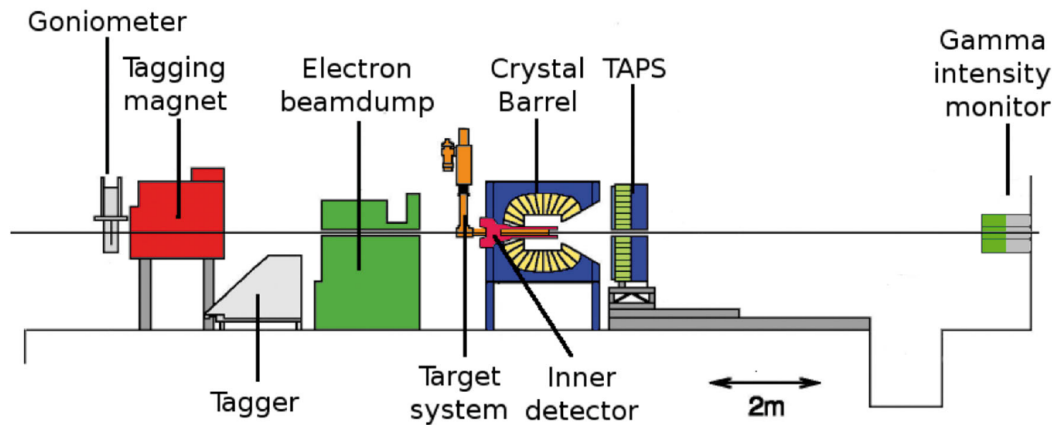
Figure 3.9: Representation of the CBELSA experiment. Taken from [87].
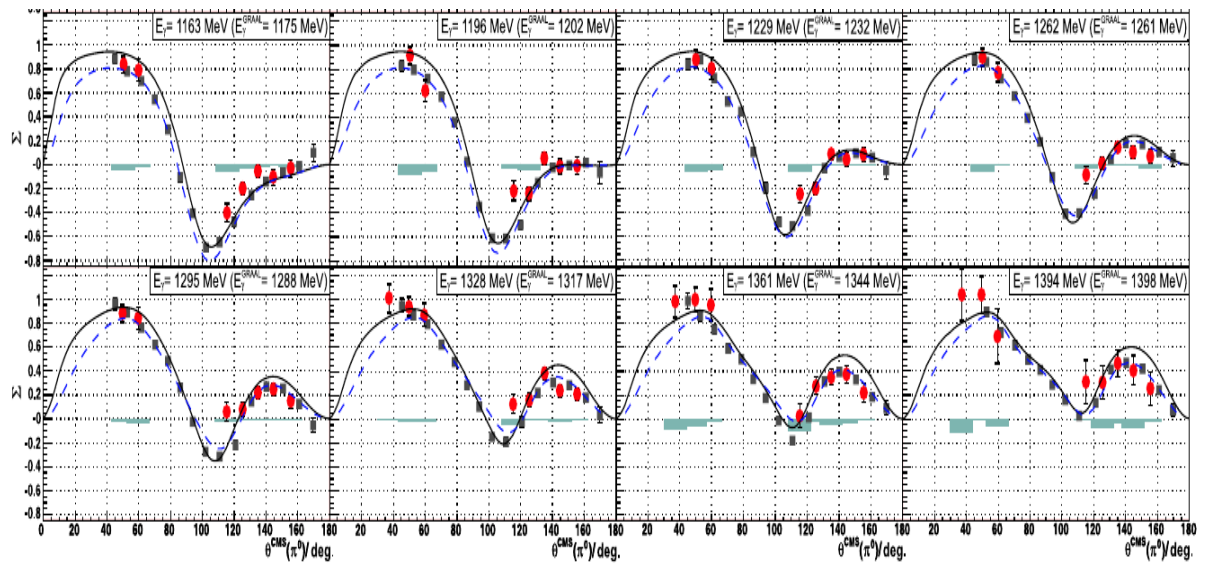
Figure 3.10: The beam asymmetry results for the data from Elsner et al. [88] (red circles). The MAID (full curve) and Bonn-Gatchina (dashed) partial wave analyses predictions are shown. Some data from GRAAL is also shown (boxes). Adapted from [88]
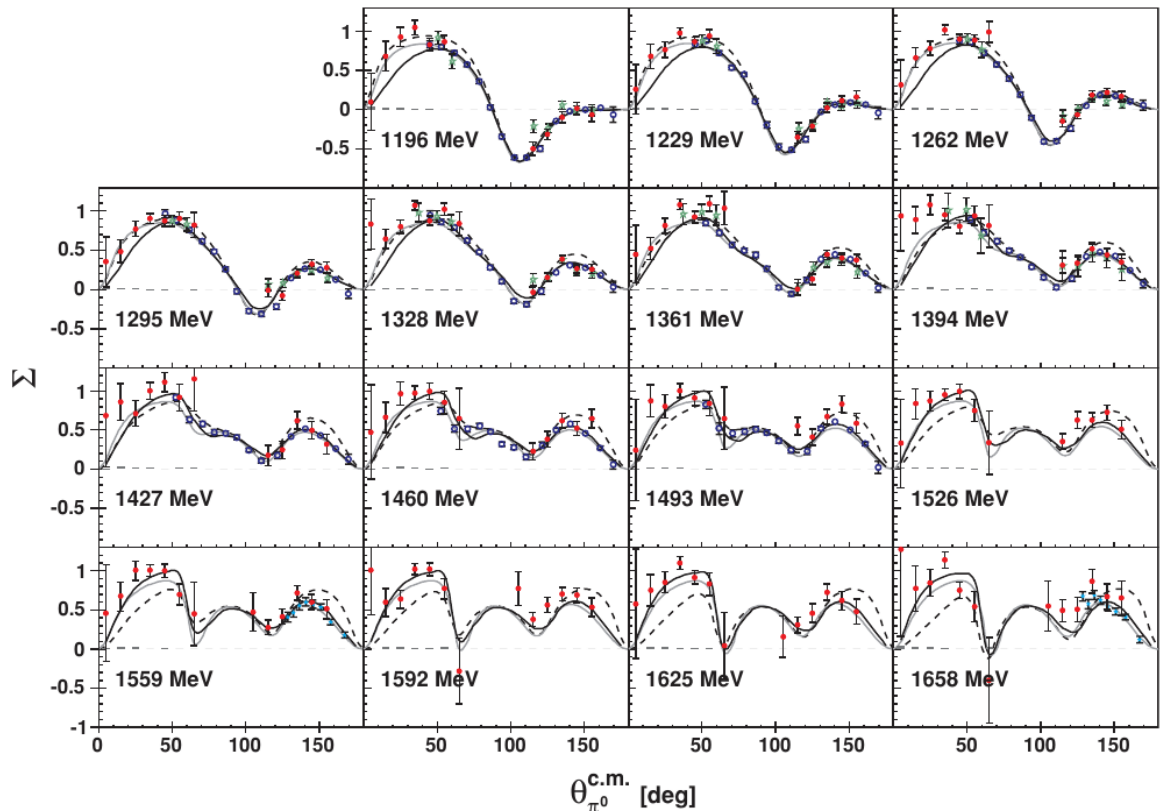
Figure 3.11: Σ measurements from Sparks et al. [89]. The data from CBELSA is denoted by filled red circles and a previous CBELSA analysis by the green stars. A comparison to GRAAL results, shown as open blue circles, is displayed. The solid black line is the Bonn-Gatchina partial wave analysis predictions, the solid grey is a prediction from SAID and the dashed black line is the MAID prediction. E is, once again, the photon beam energy. Taken from [89]
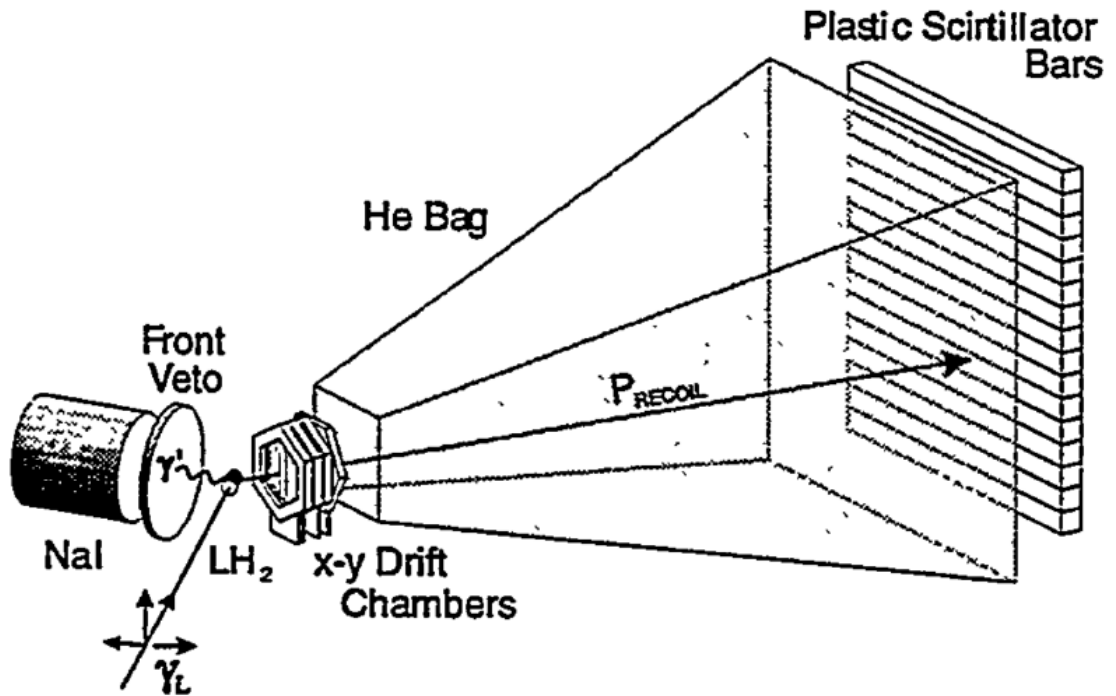
Figure 3.12: A schematic of the LEGS detector system. Taken from [76]

3.1.2 $\gamma\mathbf{D} \rightarrow \mathbf{n}\ \pi^0\ (p_{spec})$

GRAAL

The GRAAL facility provided the only significant results for the photon beam asymmetry for π^0 photoproduction off the neutron near the energy region of this work. Measurements were taken for photon beam energies between 700-1500 MeV and θ_{CM}=40-170° by Di Salvo et al [84]. The results are shown in Figure 3.13.

3.2   Partial Wave Analysis

To extract the properties of nucleon resonances from photoproduction data the world dataset of photoproduction experiments are analysed in terms of energy and angle with a partial wave analysis (PWA). The invariant mass dependence of the magnitude and phase of the extracted partial waves allow the resonance properties such as mass, width and couplings to be extracted. There are several active partial wave analysis projects and an overview of the 3 most influential is given here.
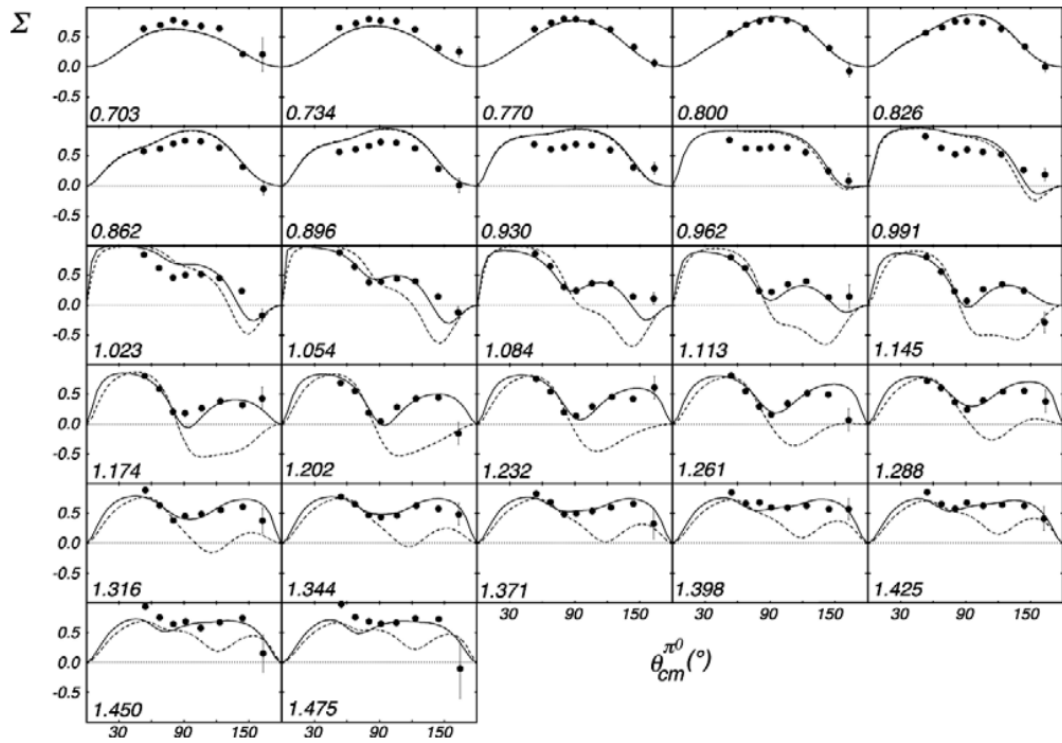
Figure 3.13: The Σ beam asymmetry for the reaction $\gamma n \to \pi^0 n$ from Di Salvo et al. [84] with two MAID predictions as the full and dashed lines. The data are the filled black circles. Taken from [84].

3.2.1   MAID

One such model is the Mainz unitary isobar model (MAID) [80, 91] which uses 4-star N* and Δ resonances below 2 GeV from the PDG [46] database to attempt to extract electromagnetic couplings from pion photoproduction data. It is well suited to predicting observables in pion photoproduction. The energy and width of each of the selected resonances are taken from the PDG database and a Breit-Wigner form was assumed for each. The non-resonant background is constructed from Born terms and t-channel vector-meson contributions. The resultant form of Breit-Wigner distributions coupled with non-resonant background terms is then fitted to the experimental data for polarisation observables and cross sections. For MAID a global fit across the entire energy range, 140-1610 MeV, is performed first to determine the phase of each multipole above the two pion threshold. Below this, the phase is constrained by the πN scattering phase. The energy range is then binned in 10 MeV bins for 140→460 MeV and 20 MeV bins for higher energy. Fits were performed for each bin using the phase determined from the prior, global, fit to find the best agreement while the multipole values were varied. The number of multipoles used for each fit varies. At energies >450 MeV all the multipoles up to F-wave were used while below this only the S and P-waves were varied and the $_{p,n}E_{2-}^{\frac{1}{2}}$ and $E_{2-}^{\frac{3}{2}}$. The model provides predictions across the entire COM energy regime for polarisation observables and cross sections for the π^0 photoproduction reaction channels considered in this work. However, the MAID model has not been updated since 2007 and the limited data in the energy region concerned for neutron π^0 final state limits the accuracy of the predictions.

3.2.2   SAID

The SAID (Scattering Analysis Interactive Dial-in) [79, 92] partial wave analysis differs from the MAID fit method by not using the widths and energies of the resonances from the PDG database as inputs. The πN elastic data up to W=2.5 GeV is fitted to determine the πN amplitudes. Resonances are identified via a search for poles in the complex energy plane. These poles originate from fitting the observables on the real energy axis while imposing the two-body unitarity cuts. Similarly to MAID, an analytical form containing Born terms, terms dictating
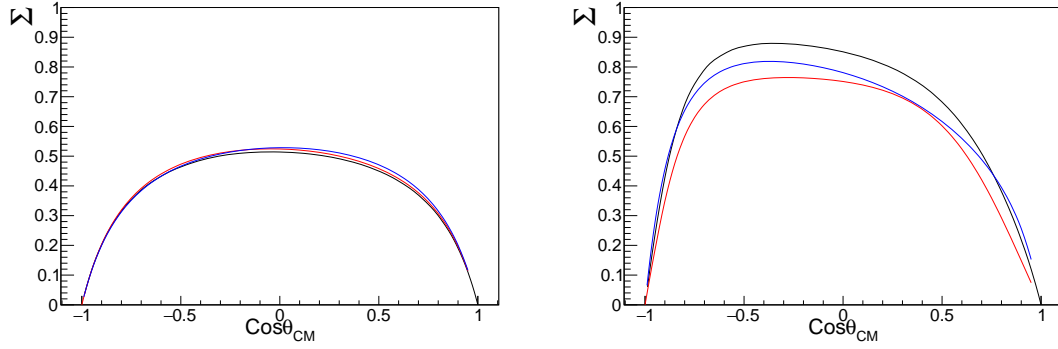
Figure 3.14: A comparison between the three different partial wave analysis predictions for the beam asymmetry, Σ, for the $\gamma p \rightarrow p\pi^0$ reaction channel. The left hand plot was created using a beam energy of 300 MeV to 320 MeV for the reaction and the right with 640 MeV to 660 MeV. The red curve represents the SAID, black the MAID and blue the BnGa PWA predictions.

the correct threshold behaviour and using Watsons theorem [93] below the two pion threshold can be used to parameterise the photoproduction multipoles. Above this threshold a unitary K-matrix approach is used. The resultant πN scattering matrix links structures found in the elastic scattering analysis with each multipole. Similarly to MAID, a global energy dependent fit is performed up to 2.5 GeV and narrowly binned single energy solution fits are performed using phase information from the energy dependent fit. The SAID model uses both πN scattering data from older experiments and new pion photoproduction data from as recently as 2015 [94].

3.2.3 Bonn-Gatchina

The Bonn-Gatchina (Bn-Ga) [81,95] partial wave analysis differs from SAID by using additional data from different reaction channels. It is a coupled channel fit using data from πN scattering and meson photoproduction channels and takes no input on resonance widths and energies from the PDG database. The low mass resonances are parameterised using a K-matrix approach. Above 2.2 GeV high mass resonances are described by multichannel Breit-Wigner amplitudes. Predictions for single π^0 photoproduction channels can be taken from this model from the latest fit BG2014-02 [87]. A comparison between the three different partial wave analysis predictions for the polarisation observable Σ is shown in Figure 3.14 for two different photon beam energies for the reaction channel $\gamma p \rightarrow p\pi^0$ and in Figure 3.15 for the $\gamma n \rightarrow n\pi^0$ reaction channel.
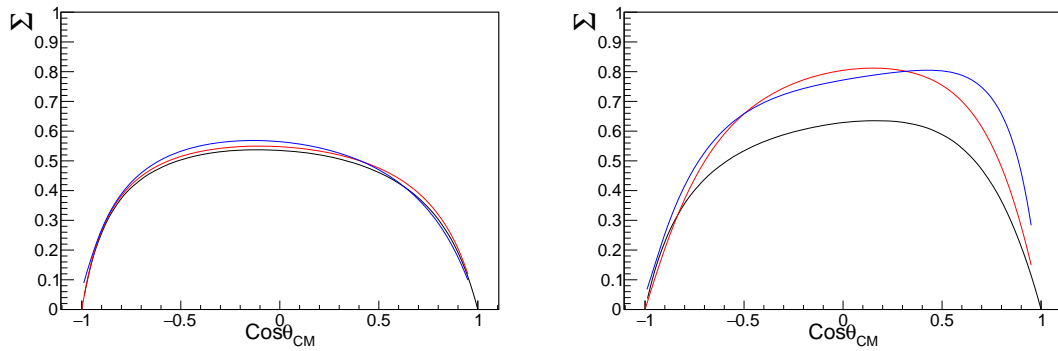
Figure 3.15: A comparison between the three different partial wave analysis predictions for the beam asymmetry, Σ, for the $\gamma n \rightarrow n\pi^0$ reaction channel. The left hand plot was created using a beam energy of 300 MeV to 320 MeV for the reaction and the right with 640 MeV to 660 MeV. The red curve represents the SAID, black the MAID and blue the BnGa PWA predictions.

Chapter 4

Experimental Facility

The experimental data for this work was collected in August and September 2016 in the A2 hall at the Mainzer Microtron(MAMI) facility situated at the Johannes Gutenberg Universität in Mainz, Germany. The main goal of this experiment was to obtain simultaneous measurements of polarisation observables for π meson photoproduction off both proton and neutron targets up to a beam energy of $E_\gamma \approx 1.5 \text{GeV}$. These measurements provide constraints on isospin production amplitudes and isospin symmetry breaking. A further goal was the investigation of the electromagnetic coupling of the d*(2380) hexaquark which has been analysed by Stephen Kay in [96]. The experiment also provided an opportunity to study the η meson photoproduction channels in a similar manner to the π meson. This chapter describes the accelerator infrastructure used at Mainz in Section 4.1 as well as features of the A2 experimental hall. The bremsstrahlung process used to produce the photon beam is discussed in Section 4.2 as are several of the detectors in Section 4.7, including the main Crystal Ball calorimeter, the liquid deuterium target, and configuration of the apparatus specific to this experiment.

4.1 Mainzer Microtron Electron Accelerator Facility

The Mainzer Microtron accelerates electrons to an energy of 1.5GeV before transporting them to the A2 hall where they radiate bremsstrahlung photons while passing through a thin metal foil. The beam from MAMI is considered a continuous wave electron beam. However, in reality it has

a very small separation between electron bunches which are below the experimental resolution so can be treated as a continuous wave source.

The initial beam was created by striking a GaAsP semi-conductor crystal with a circularly polarised Ti:Sapphire laser [97]. This produced a polarised electron beam which was accelerated by the injector linear accelerator to an energy of 3.5 MeV. The Ti:Sapphire laser passed through a Pockels cell which determines the helicity of the electron beam [98]. A Pockels cell is a birefringent material which, with the application of a voltage change, allows for a change in its birefringence proportional to the applied electric field. The birefringent axes of the Pockels cell were at $\pm 45°$ to the polarisation plane of the incident laser light. This introduced a $\pm \frac{\pi}{2}$ phase shift between the two axes, creating a circularly polarised laser beam. The dopant induced a strain in the photocathode crystal. This breaks the degeneracy in the valence band and leads to electrons with preferential spin being promoted to the conduction band via the use of the circularly polarised laser beam [99]. Inserting a wave plate upstream of the Pockels cell allowed the incident linear polarisation of the laser beam to be reversed, which changed the sign of the phase shift and, hence, flipped the helicity of the electron beam. The helicity of the beam was flipped at a frequency of 1 Hz.

MAMI consists of three racetrack microtrons and a harmonic double sided microtron to accelerate the electron beam. A schematic of the MAMI accelerator and the experimental halls it feeds can be found in Figure 4.1. This circularly polarised beam was ramped up through three racetrack microtrons. The racetrack microtrons (RTM) guide the electron beam through a linear accelerator multiple times [100]. This accelerator was situated between two magnets which cause the beam to recirculate, gaining energy and gradually increasing the orbit on each turn. In this manner, the energy of the electron beam was accelerated from 3.5 MeV up to 855 MeV when exiting the third racetrack microtron. Figure 4.2 shows a diagram of a racetrack microtron.

The last stage in accelerating the beam was a harmonic double sided microtron (HDSM) as shown in Figure 4.3. An HDSM is based upon the idea of higher order microtrons by Herminghaus who coined the term Polytrons to describe the many bending magnets systems [101]. The HDSM at MAMI consists of four dipole magnets and two linear accelerators. It allowed the beam energy to be increased to 1500 MeV while covering a much smaller area than a racetrack
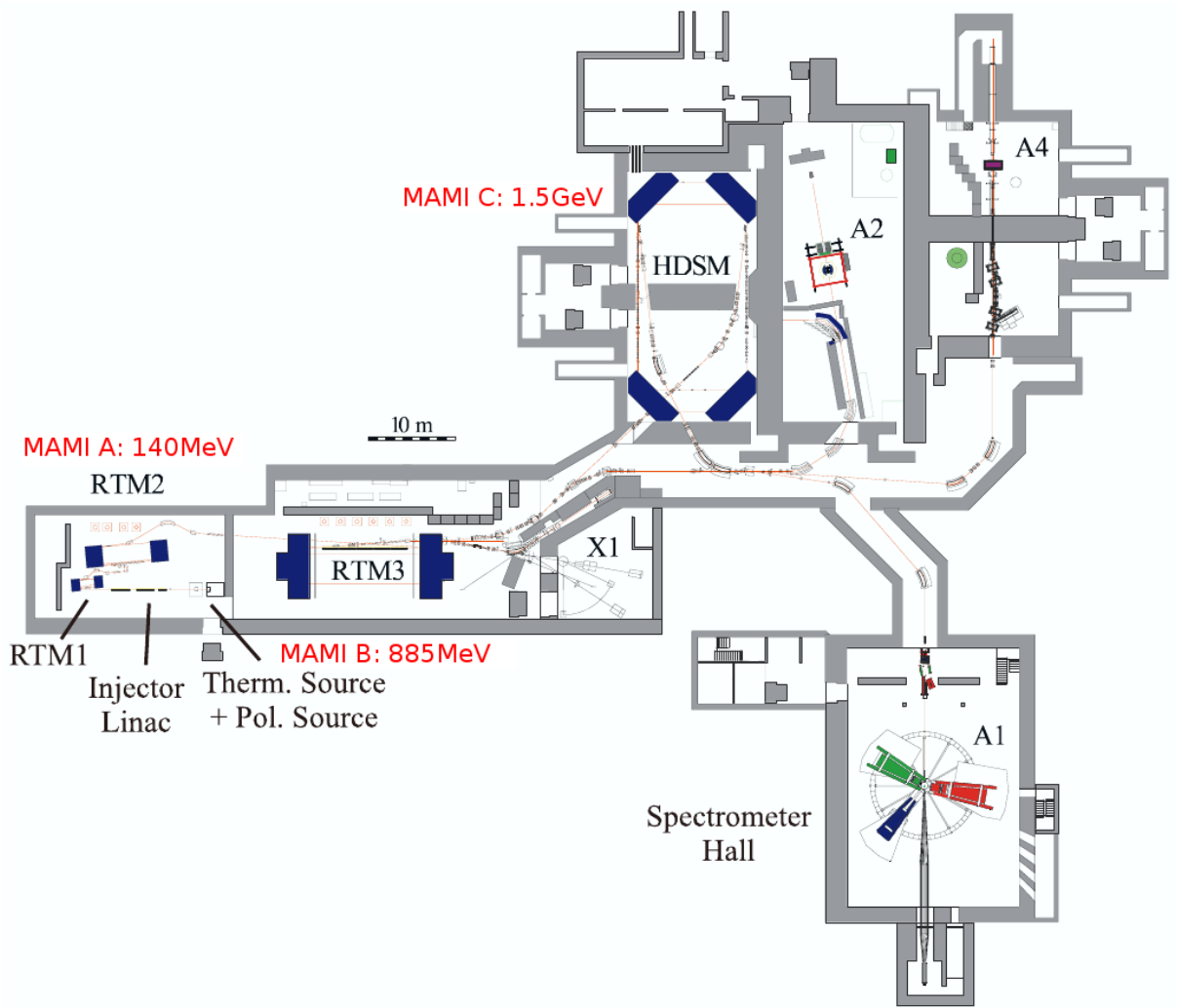
Figure 4.1: Floor plan of the MAMI accelerator facility showing the stages of acceleration and the experimental halls it provides beam for including the A2 experimental hall, where the data for this thesis was taken. Taken from [102].

microtron since each magnet only has to bend the beam 90° reducing the size of the magnet required. The acceleration of the electron beam is summarised in Table 4.1.

This circularly polarised $1.5\,\mathrm{GeV}$ beam entered the A2 hall as pictured in Figure 4.4 which shows a schematic of the main apparatus.

After acceleration, the electron beam was incident upon a thin metal radiator where circularly polarised photons were produced. Alternatively, by using an aligned diamond lattice radiator linearly polarised photons were also produced as outlined in Section 4.4. The Glasgow-Mainz Tagged Photon Spectrometer determines the energy of such photons by a momentum analysis of the recoil electron from the bremsstrahlung process.
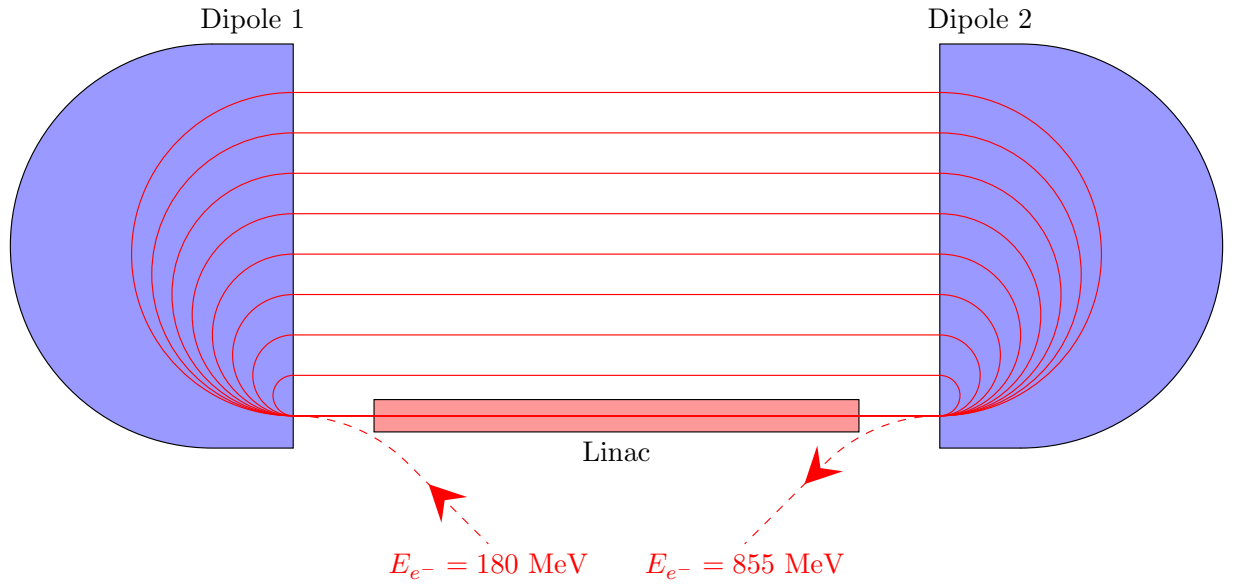
Figure 4.2: A racetrack microtron showing the dipole magnets in blue and the increasing orbital path in red. Taken from [43].
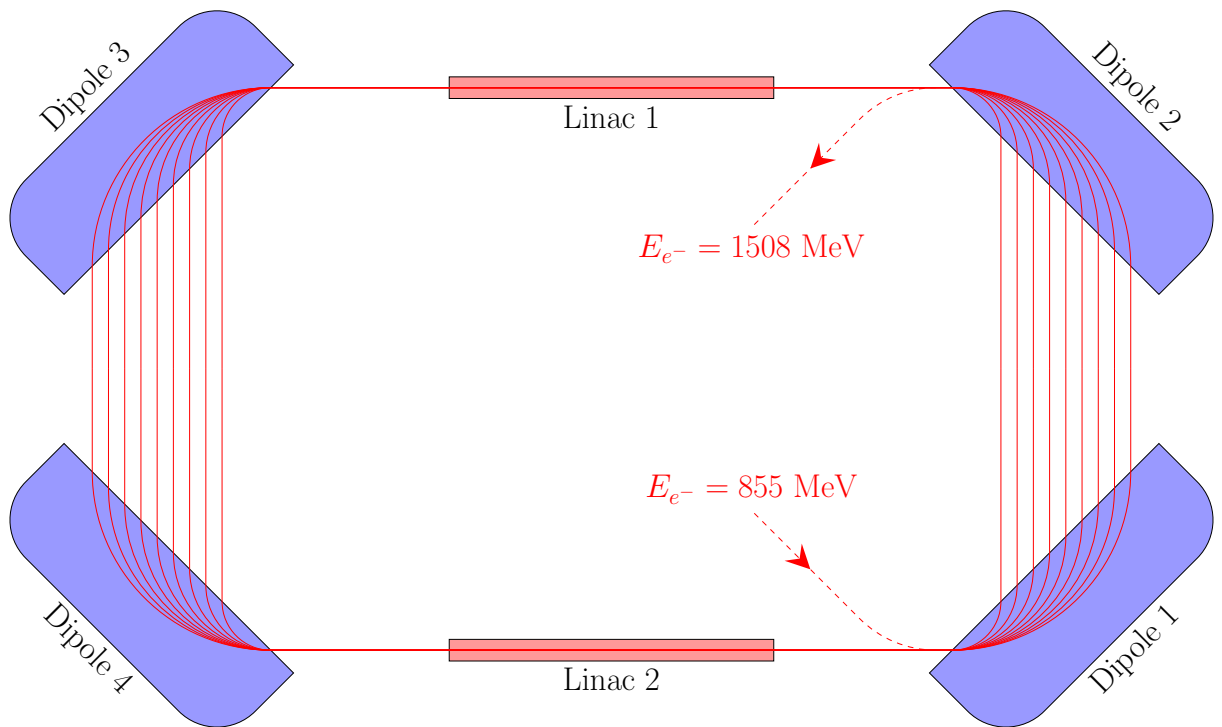
Figure 4.3: A Harmonic Double Sided Micrtotron(HDSM). The dipole magnets are situated at the corners in blue with the path of the beam shown in red. Taken from [43].
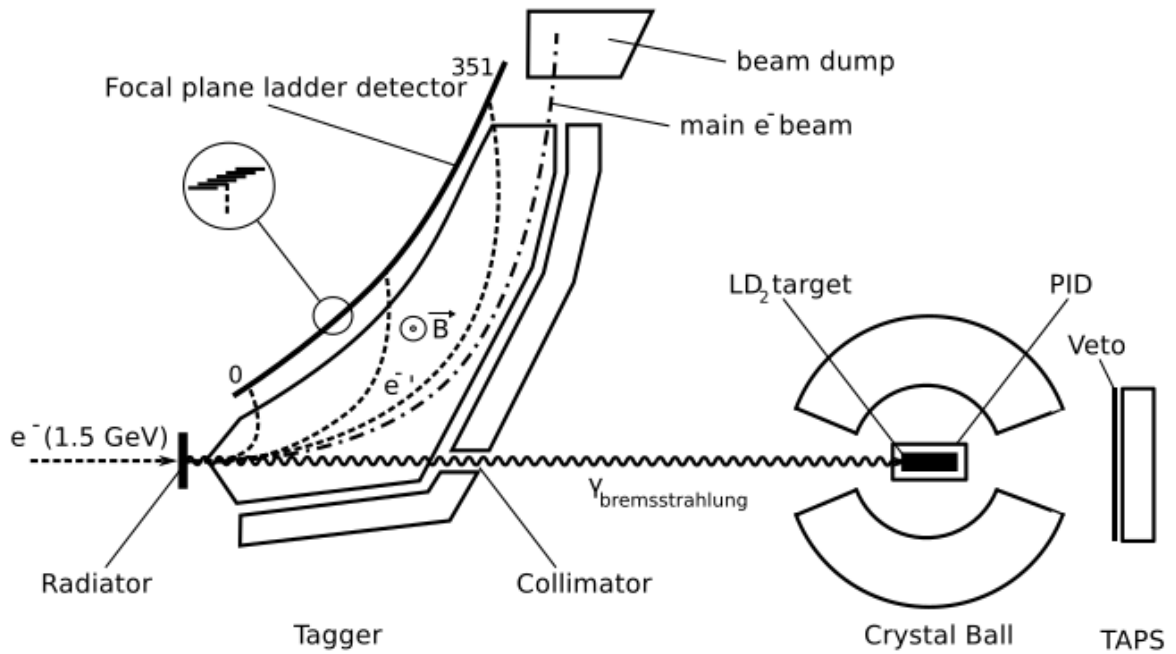
Figure 4.4: An overview of the experimental hall A2, detailing the Tagger, Crystal Ball and TAPS detectors. Taken from [103]

	Injection Energy (MeV)	Extraction Energy (MeV)	Magnetic Field (T)	ΔE per cycle (MeV)	N. Cycles
RTM1	3.97	14.75	0.103	0.599	18
RTM2	14.75	180	0.555	3.24	51
RTM3	180	855	1.284	7.5	90
HDSM	800	1508	1.53-0.95	16.58-13.66	43

Table 4.1: A summary of the accelerator properties at the Mainzer Microtron.

4.2 Production of Coherent Bremsstrahlung

The Mainzer Microtron produces an electron beam with a maximum energy of $\sim 1.5\,\text{GeV}$ which in turn produces a real photon beam by utilising the bremsstrahlung process. Bremsstrahlung or "breaking radiation" is a photon produced when a charged particle, in this case an electron, is deflected by the electromagnetic field of an atomic nucleus. The photon energy is directly related to the recoiling electron energy. By making a measurement of the electron energy in coincidence with an experimental trigger, the energy of the incident photon can be determined. In the general case of an amorphous radiator the incoming electron scatters in the electromagnetic field of an atomic nucleus in the material. Such a reaction has no preferred scattering plane and the resulting photons are therefore unpolarised. The flux of the produced photons as a function of energy follows a characteristic $\frac{1}{E_\gamma}$ distribution. For this experiment $12\,\mu\text{m}$ of Copper was used as an amorphous radiator.

In the special case of an electron beam incident on a material with a crystal lattice structure, preferential planes for momentum transfer are allowed, along the reciprocal lattice vectors producing polarised bremsstrahlung photons. A $30\,\mu\text{m}$ thick diamond radiator was used for this purpose. The relative orientation of the crystal to the incoming electron determines the allowed set of reciprocal lattice vectors and, hence, the available momentum transfers. This, in turn, constrains the plane of the photon's polarisation. The distribution for this bremsstrahlung process contains the characteristic $\frac{1}{E_\gamma}$ shape as given by the incoherent process and in addition polarisation peaks related to the reciprocal lattice vectors. A schematic comparison of the coherent and incoherent distributions is shown in Figure 4.5.

4.3 Goniometer

The selection of radiators in the A2 hall was facilitated by the use of a goniometer as pictured in Figure 4.6. This allows for the remote switching of radiators. There were four options for the goniometer: diamond, copper, Moeller coil and blank. For data taking the diamond or Moeller coil was used. The fine grain movements of the goniometer allowed for precise alignment of the diamond's lattice vectors with respect to the beam direction. The alignment procedure was
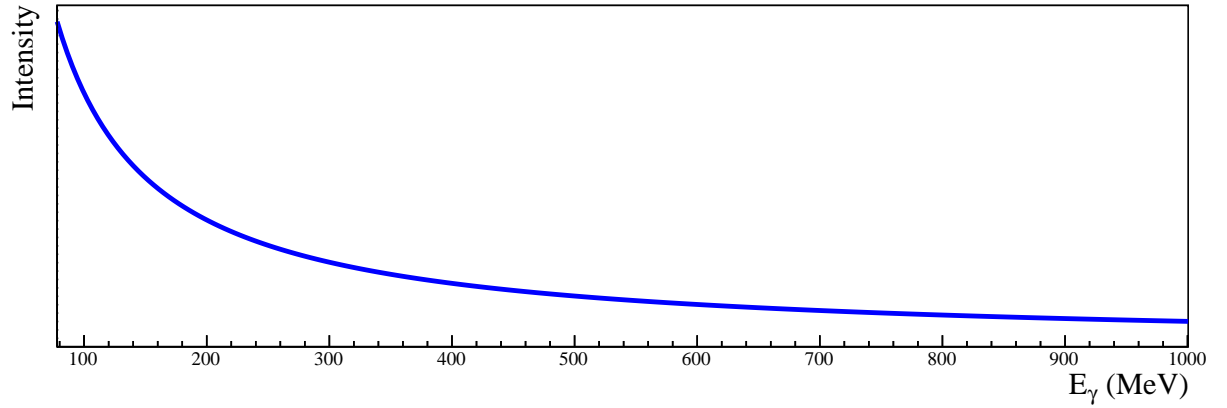
(a) Amorphous Bremsstrahlung
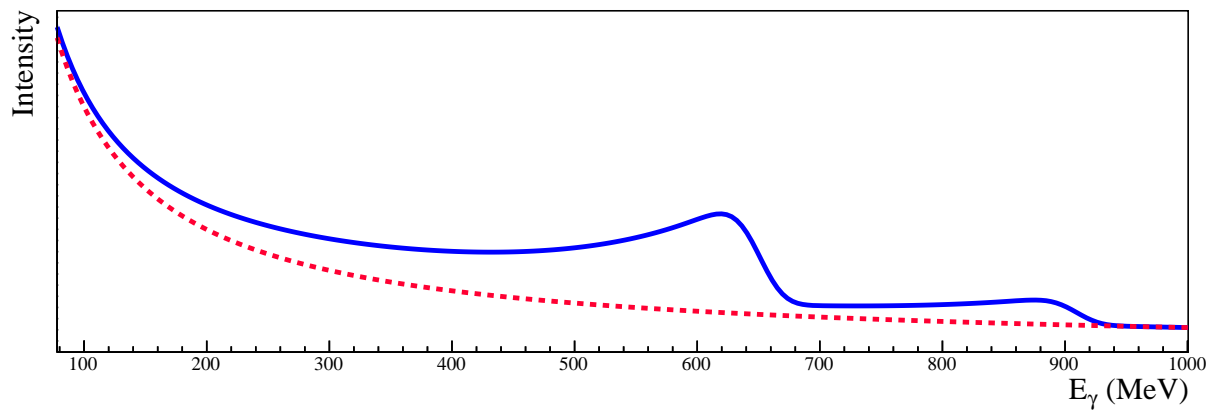
(b) Coherent Bremsstrahlung.

Figure 4.5: A comparison of the coherent(a) and incoherent(b) bremsstrahlung distributions showing the $\frac{1}{E_\gamma}$ shape of the incoherent process and polarisation peaks. Taken from [43].
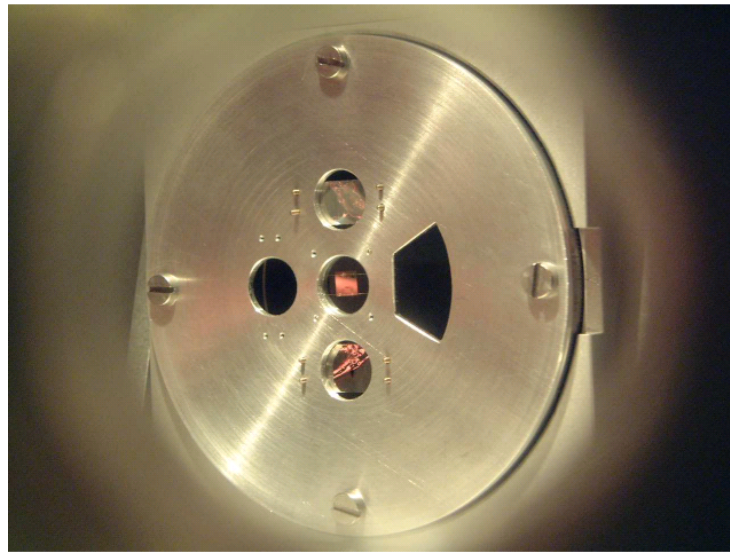
Figure 4.6: A Picture of the goniometer wheel used for setting the radiator. Taken from [104].

performed using the so-called "Stonehenge technique".

4.4 Stonehenge Technique

The relationship between the goniometer coordinate system and crystal lattice planes of the diamond must be determined in order to align the lattice planes with the electron beam to generate the desired polarisation spectrum. For this purpose, the Stonehenge technique [105] based on a method by Lohmann et al. [106] has been used at several experimental facilities including CLAS at Jefferson Lab and MAMI at Mainz. A scan is conducted as the goniometer is swept around a cone. A radial distribution of the coherent bremsstrahlung enhancement spectrum is built from this scan. The centre of the cone is moved and the scan repeated. These scans are repeated until a symmetrical spectrum is attained as shown in Figure 4.7. The symmetrical nature indicates alignment of the crystal lattice planes with the beam. The energy at which the coherent peaks, corresponding to different lattice planes, appear can be controlled by adjusting the angle between the beam and the desired lattice plane. The largest peak is produced via scattering off the $[0,2,2]$ and $[0,2,\bar{2}]$ planes of the crystal. The higher order planes also produce smaller coherent peaks at higher energies in the distribution. Linearly polarised photons are produced with linear polarisation perpendicular to the lattice plane. By rotating the goniometer azimuthally the
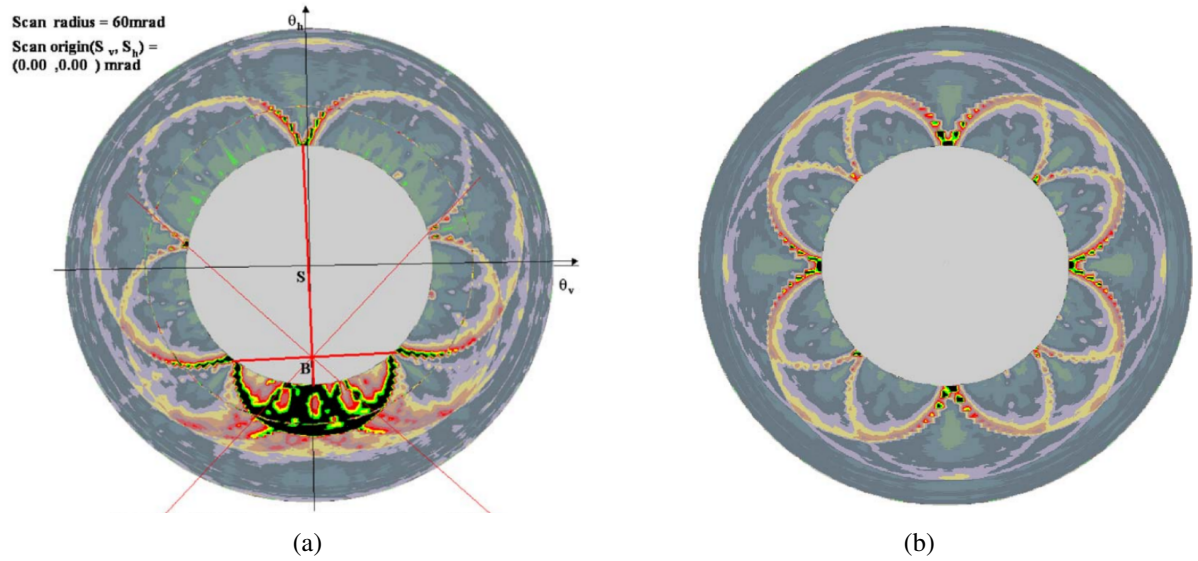
Figure 4.7: Colour intensity plots of radial distributions of goniometer scans. Left: Initial scan of the diamond. Right: Scan of the diamond after alignment with polarisation planes at ± 45. Taken from [105].

orientation of the linear polarisation can be controlled.

4.5   The Glasgow-Mainz Tagged Photon Spectrometer

The bremsstrahlung photons produced cover a range of energies. The energy of a particular photon interacting with the target was determined using the Glasgow Photon Tagging Spectrometer [107, 108] referred to as Tagger henceforth. The scattered electron was momentum analysed in the 1.9T magnetic field of the spectrometer as illustrated in Figure 4.8. The energy of the electron was inferred from its hit position in the tagger focal plane detector. The corresponding photon energy was then determined by subtracting the measured electron energy from the initial beam energy as:

$$E_\gamma = E_{beam} - E_{fp} \tag{4.1}$$

where E_γ is the photon energy, E_{beam} is the electron beam energy and E_{fp} is the energy of the electron detected in the focal plane detector (FPD).

The Tagger focal plane detector consisted of 353 plastic scintillators (EJ200), each with length 80 mm and thickness 2 mm. A variation of widths of 9-32 mm for each element was
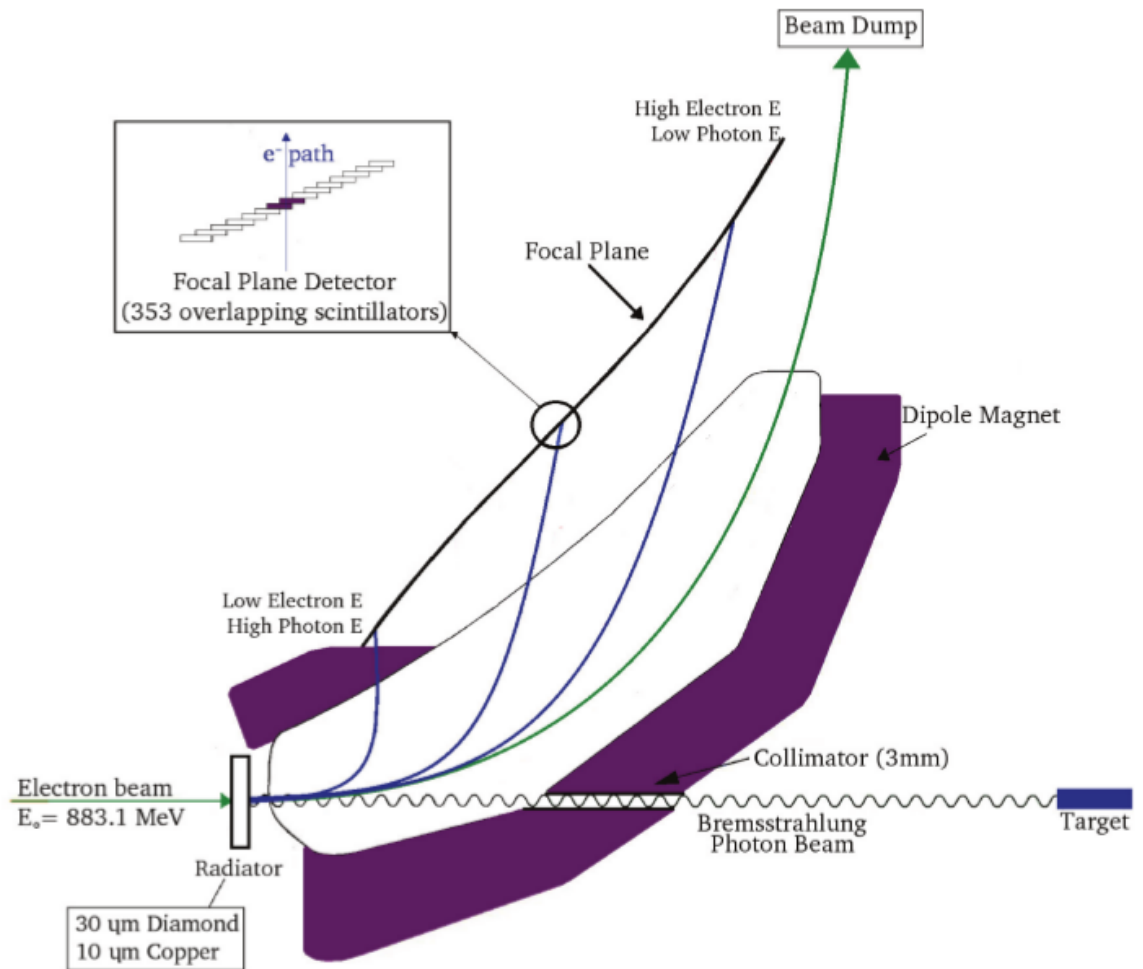
Figure 4.8: A schematic of the Glasgow-Mainz Tagged Photon Spectrometer(Tagger) illustrating its operation. Taken from [109]

(a) Focal Plane section

(b) FPD Plastic Scintillator
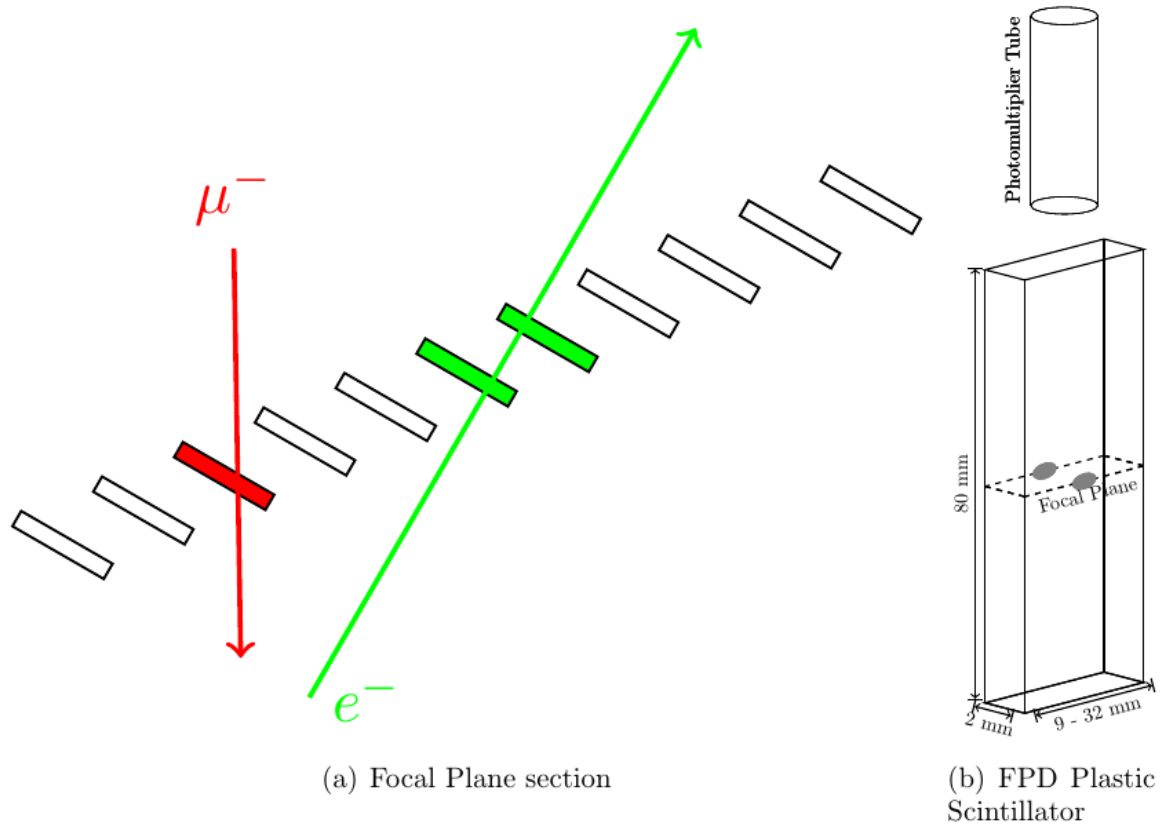
Figure 4.9: Left: An example of particles traversing the tagger focal plane. The electron creates a coincidence between two neighbouring detector elements resulting in a registered event. The muon only strikes one element and is not registered. Right: An example of one of the plastic scintillators forming the tagger focal plane with its corresponds PMT. Taken from [43]

used to ensure that each scintillator covered the same energy acceptance of around 4 MeV. Each scintillator was wrapped in aluminised mylar to ensure they were light-tight and to aid in the prevention of crosstalk. Every element overlapped with its neighbours defining a channel in the Tagger of which there are 352 in total. A coincidence hit of neighbouring elements in a channel yielded a measured electron. This coincidence significantly reduced the random background events. A schematic of the focal plane detector is shown in Figure 4.9. The scintillators were read out courtesy of Hamamatsu R1635 photomultiplier tubes (PMT). These PMTs were shielded from the magnetic field by a 0.7mm steel plate in between each one.

The Tagger covered approximately 5-93% of the initial electron beam energy with each individual detector element able to handle a maximum photon flux of up to 10^6 Hz. Due to broken channels and differences in efficiency of channels the energy spectra obtained experimentally

does not show the smooth variation of idealised bremsstrahlung shown in Figure 4.5. A coherent and an incoherent distribution obtained from experimental data are shown in Figure 4.10.

The experimental trigger was given a tagger timing gate for this experiment that resulted in around 20 coincidence photons per event. These false coincidence electrons correpond with a flat background in the timing spectra of the Tagger since many photons can be present during this timing window. A clear peak can be seen in the Tagger timing distribution in Figure 4.11. This corresponds to true event coincidences between the Crystal Ball detector, which makes the trigger, and the Tagger. The procedure for subtracting the flat random background will be discussed in sections 6.3.1 and 6.4. The timing resolution of the focal plane detectors has a full width at half maximum of 0.37-53 ns [108], significantly less than the peak in Figure 4.11 which is dominated by the trigger time.

Post radiator the photon beam was collimated before impinging on the target. A 3mm diameter Pb collimator was placed 2.5 m downstream from the radiator, and 8 m from the target, for this beamtime, to restrict the angular spread of bremsstrahlung photons to a narrow cone. This has the effect of preferentially selecting coherent bremsstrahlung as it is produced preferentially at smaller angles compared to the incoherent contribution and, hence, increased the degree of photon polarisation incident on the target.

4.6   Liquid Deuterium Target

The target used in this work was liquid deuterium contained in a 10 cm long cell of diameter 3 cm housed in a 125μm thick kapton cylinder and positioned in the centre of the Crystal Ball. A similar design is photographed in Figure 4.12 which was used for a previous beamtime. Liquid deuterium was supplied to the target via compressing and liquefying gaseous deuterium from a nearby storage tank. Hydrogen targets are filled in the same manner. The target was kept at a pressure of 1080 mBar and a temperature of 21 K ensuring a density of $\rho \approx 0.07 \, \mathrm{gcm}^{-3}$ for the target. These operating conditions were maintained throughout via the careful application of two 4 W heaters or adjusting the supply of liquid deuterium.
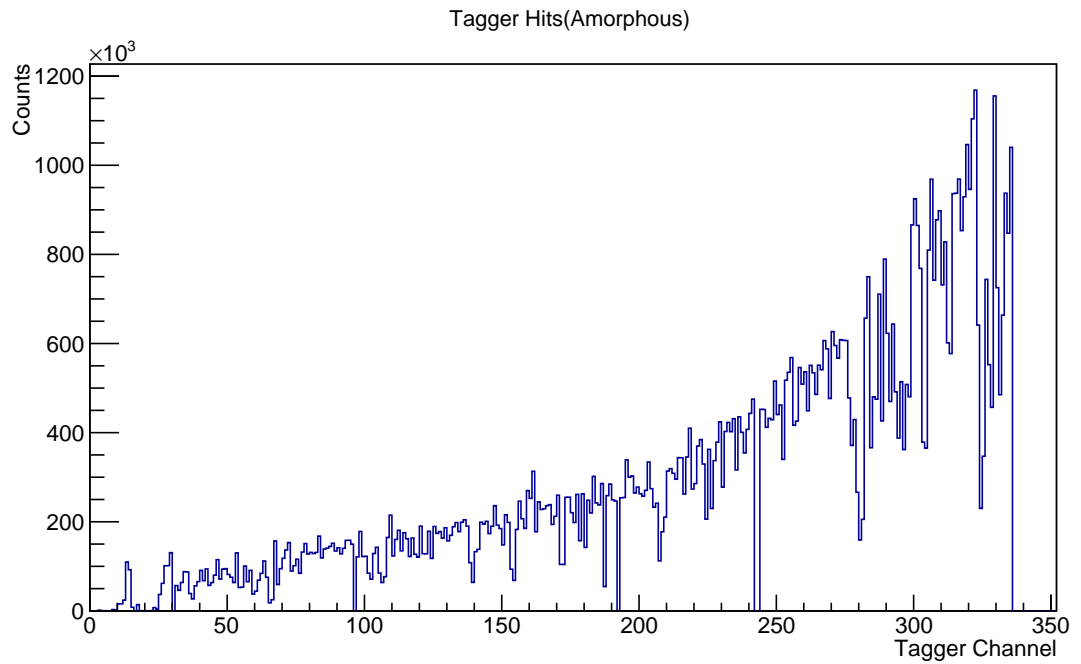
(a) Moeller Coil Bremsstrahlung
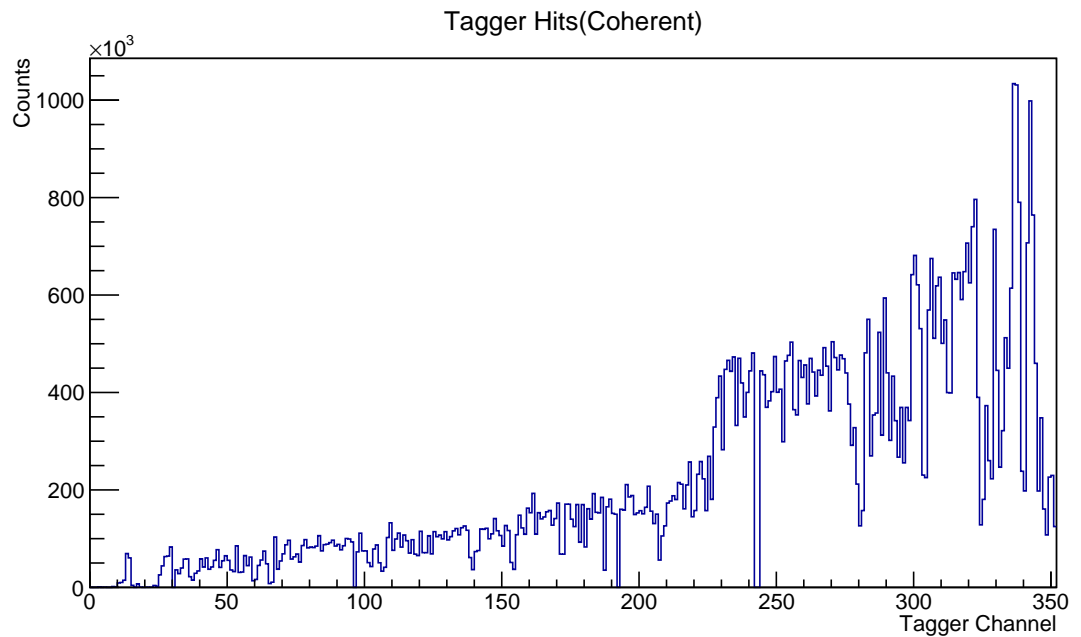
(b) Diamond Bremsstrahlung.

Figure 4.10: Moeller and diamond bremsstrahlung from production data. An edge can be clearly observed in the coherent spectra around channel 230 corresponding to enhancement from coherent bremsstrahlung on a diamond lattice vector. Note as the tagger channel numbering increases the beam energy decreases.
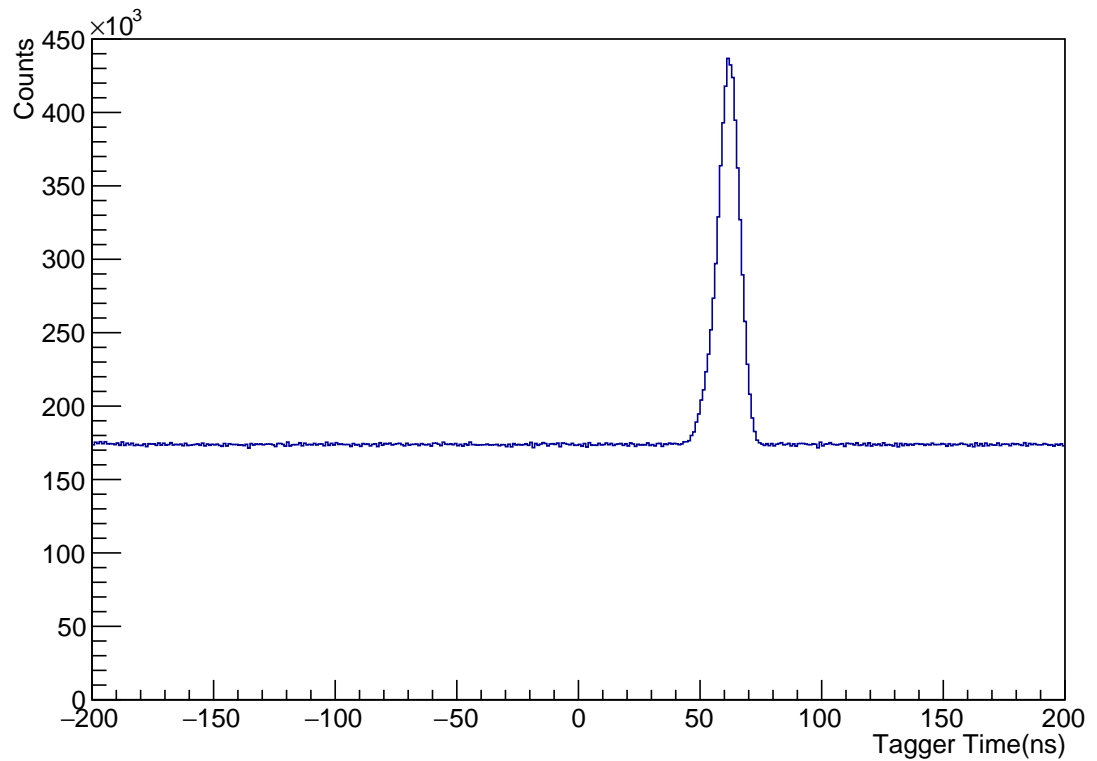
Figure 4.11: A plot of the tagger timing spectra showing the flat background underneath the coincidence peak of events of interest.

Figure 4.12: A photograph of a hydrogen target used for a previous experiment. This is very similar to the liquid deuterium filled target used for the work detailed here. Taken from [110].
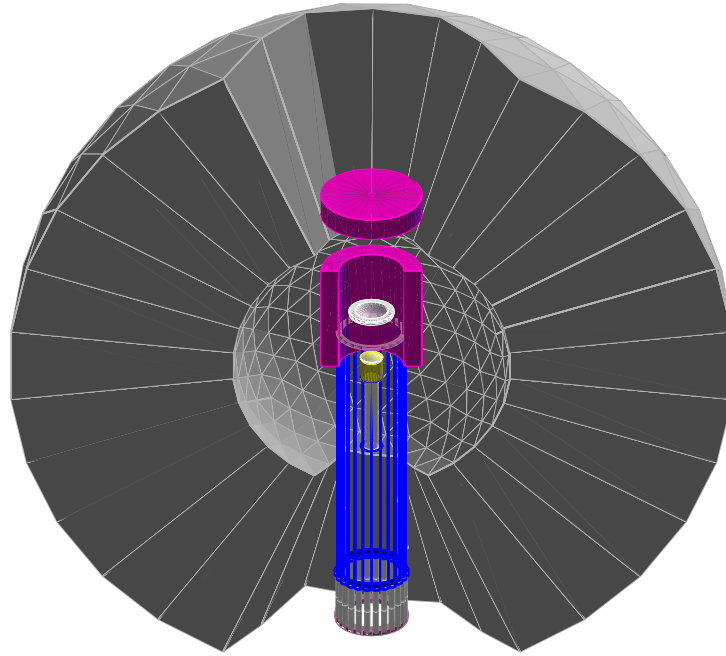
Figure 4.13: Inner view of the original Crystal Ball Polarimeter. The target is shown in yellow in the centre. The PID is in blue. The graphite scattering material is in purple and the grey is the calorimeter crystals. The PID is displaced downward for clarity.

4.7   Central Region Detectors

4.7.1   Crystal Ball Detector

The Crystal Ball photon calorimeter covers polar angles of 20-160° around the target and full azimuthal angle range with the exception of a 3.2mm gap where the top and bottom hemispheres of the ball meet. In combination with TAPS, the full detector system covers nearly 96% of 4π.

The Crystal Ball is composed of 672 thallium doped sodium iodide (NaI(Tl)) crystals as depicted in Figure 4.13. These are arranged in the form of an icosahedron, a regular polyhedron composed of twenty faces with an entry and exit for the beamline. Each crystal is a truncated triangular pyramid of length 40.6cm, corresponding to 15.7 radiation lengths, with 5.1cm sides at the top and 12.7 cm sides at the bottom of the pyramid as shown in Figure 4.14. The crys-
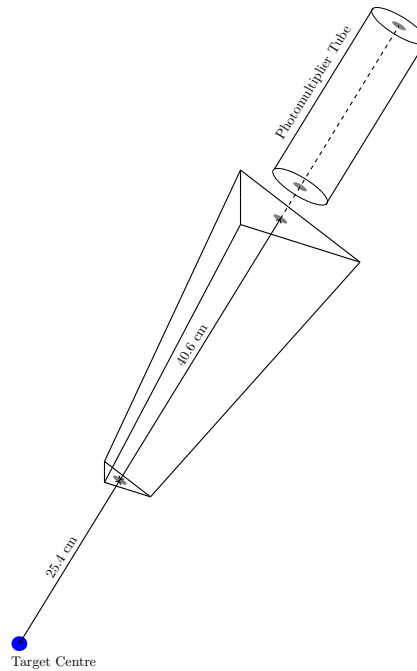
Figure 4.14: A schematic of one of the Crystal Ball calorimeter NaI(Tl) crystals showing where the PMT would be attached

tals are optically isolated from each other by wrapping them in mylar and protected from the environment by splitting the ball into two hemispheres which are hermetically sealed. This is necessary due to the hygroscopic nature of the crystals. To form the icosahedron, each of the twenty faces is comprised of 4 minor triangles which are each composed of 9 crystals to make a total of 720 crystals. However, 48 of these are removed for the beamline resulting in 672 crystals. A detected particle can be spread across a number of neighbouring crystals. This collection of crystals is known as a cluster and the energy of the detected particle is the sum of the energies of the crystals in the cluster.

When a charged particle strikes the NaI crystal it interacts via Coulomb interactions, valence electrons in the crystal are excited and subsequently release low energy photons. As the particle traverses the scintillator more of these interactions occur. The PMT collects photons from these interactions and produces an electrical signal proportional to energy of the incident particle. A neutral particle, such as a photon, incident on the scintillator can interact via pair production, Compton scattering and the photoelectric effect. All of these mechanisms will produce a charged particle(or two) which will deposit energy in the crystal by producing low energy photons as above. A high energy photon will mostly interact via the pair production mechanism which

will create an electromagnetic shower in the crystal. A neutron can interact with the crystal via quasi-elastic scattering from a bound proton. The proton will be detected in the manner of a charged particle.

4.7.2   Particle Identification Detector

The current particle identification detector (PID), version 3, was specifically designed and built for the aforementioned experimental run period of August 2016. A more compact detector was required for this run to accommodate the graphite polarimeter. Full details on the construction of the PID can be found in the thesis of Stephen Kay [96].

The PID was comprised of a series of 24 EJ204 scintillator elements arranged in a barrel formation and individually wrapped. This version of the PID reduced the length of each element from 50 cm to 30 cm but maintained the same angular coverage in polar angle via the reduced radius. The barrel has an inner radius of 3.3 cm and, with each element being 4 mm thick, an outer radius of 3.7 cm. To allow construction of the barrel shape each element has a side angled at 15°. At the forward end of each scintillator a 45° angled cut was taken. An additional end piece of EJ204 scintillator of the same thickness was attached. This end piece allowed particles to be detected as low as $\approx 7^{\circ}$ in polar angle. The other end of each element was glued to a perspex lightguide and optically joined to a Hamamatsu H3164-10 PMT as shown in Figure 4.15.

The PID barrel was orientated around the beam axis. It provided charged particle identification before the nucleon reaches the graphite polarimeter. A technique referred to as $\frac{\Delta E}{E}$ is often used for the identification. Charged particles traversing the thin scintillator element will deposit a small amount of their energy, ΔE. The correlation between this ΔE and the energy deposited by the particle in the Crystal Ball photon calorimeter, E, is related to the particle species. Hits in the CB and PID were connected if they were sufficiently close in azimuthal angle. Charged pions and electrons deposit a similar amount of energy as they are effectively minimum ionising particles, while protons, due to their larger mass, deposit significantly more. The higher proton energy can be clearly observed in Figure 4.16. If, however, the charged particle is not stopped in the Crystal Ball the discrimination is not so clear. Charged pions of up to 250 MeV and protons of up to 425 MeV can be stopped by the crystal ball photon calorimeter. For the analysis
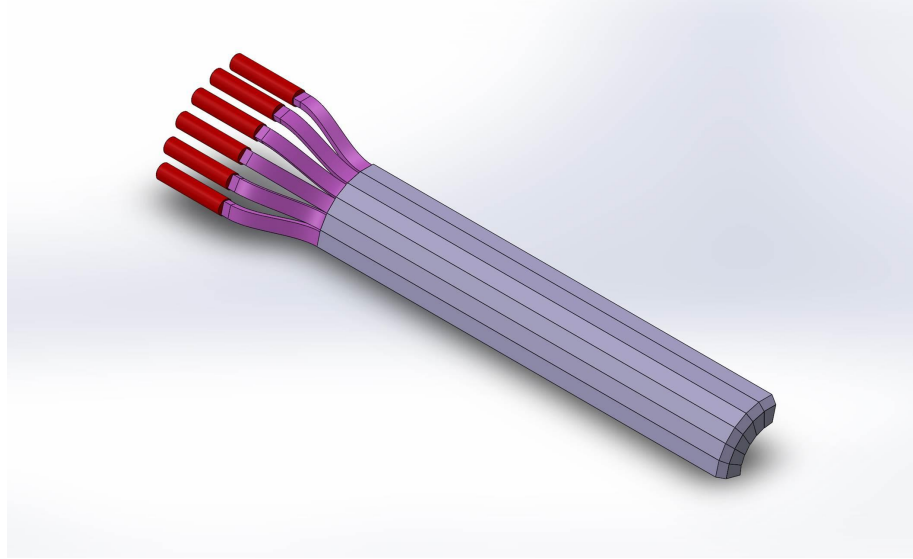
Figure 4.15: A CAD drawing of a portion of the PID elements. The grey colour on the right represents the scintillator elements, the red the PMTs and the magenta the lightguides.
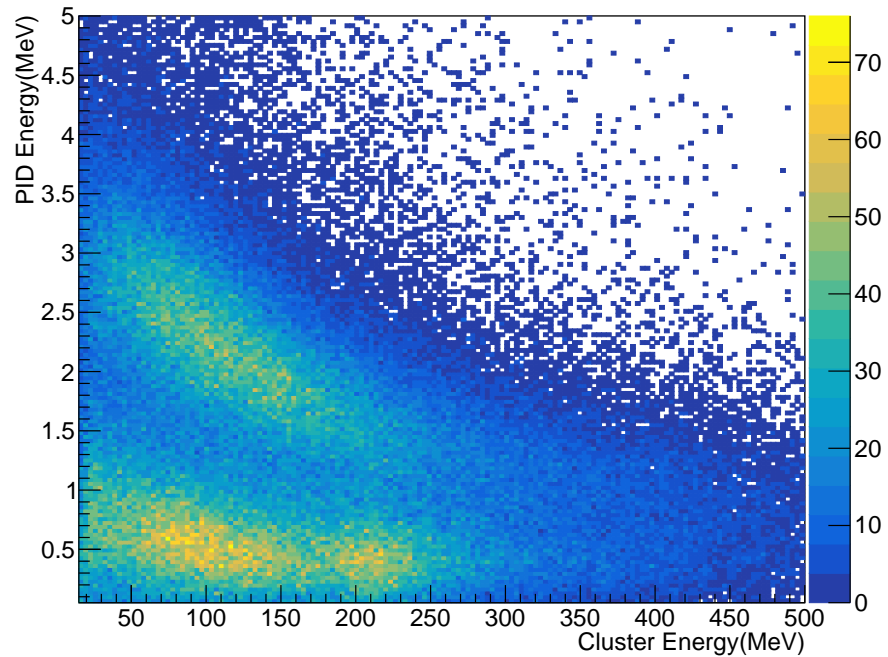
Figure 4.16: A comparison between the energy deposited in the crystal ball and the PID. Clear bands can be seen corresponding to charged pions, below 1 on the y axis, and to protons, above 1 at low cluster energy and decreasing toward higher cluster energy.
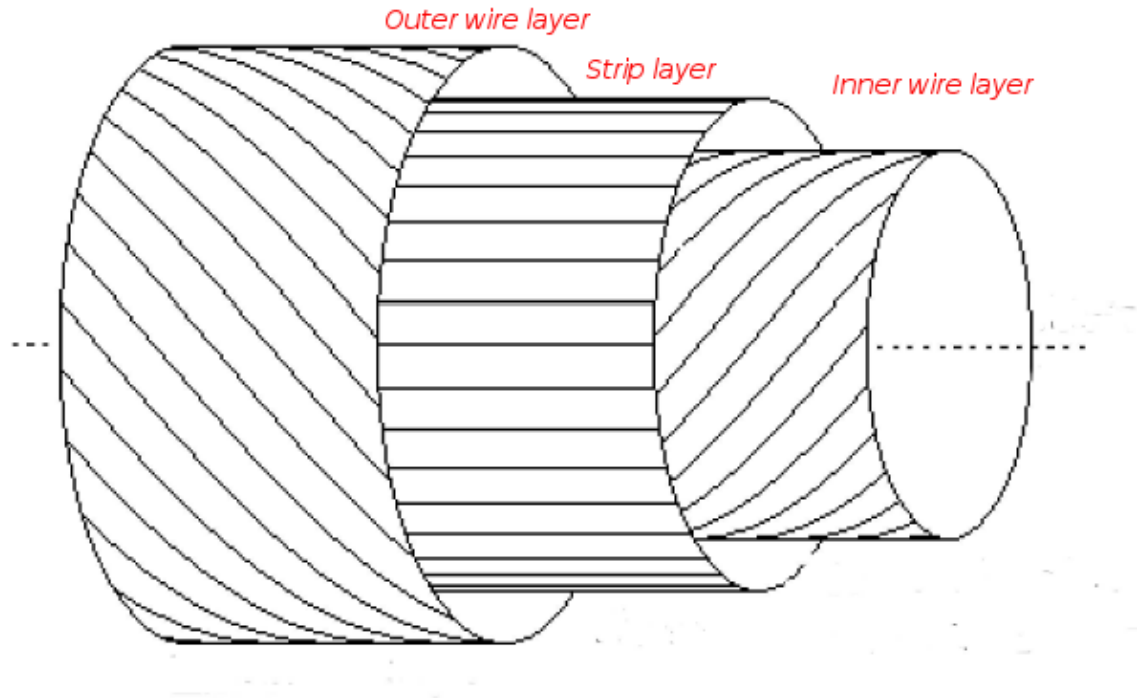
Figure 4.17: A drawing of one of the MWPCs showing the relative orientation of the wires to the strips. Taken from [96]

described in this thesis the PID information was handled differently for the different reaction channels and is described in the analysis chapter in Section 6.2.

4.7.3 Multi-Wire Proportional Chambers

Radially outwards from the graphite polarimeter there were two coaxial MWPCs each containing a layer of anode wires sandwiched between two layers of cathode strips and held at a potential difference with respect to each other. They allowed for the identification and tracking of charged particles. These were based on a design used for the DAPHNE experiment [73]. The cathode strips were wound at $\pm 45^{\circ}$ to the anode wires and hence 90° to each other as shown in Figure 4.17. For the specified beamtime the first wire chamber was held at an operating voltage of $2500\,\mathrm{V}$ and the second at $2550\,\mathrm{V}$. These were surrounded by a gas mixture of Argon, Ethane, Ethanol and Freon to allow ionization of charged particles passing through the chambers. The inner and an outer chamber were situated within the Crystal Ball detector surrounding the scattering material which encompasses the PID and target cell. These chambers covered 21° to 159° in polar angle and the full azimuthal range.
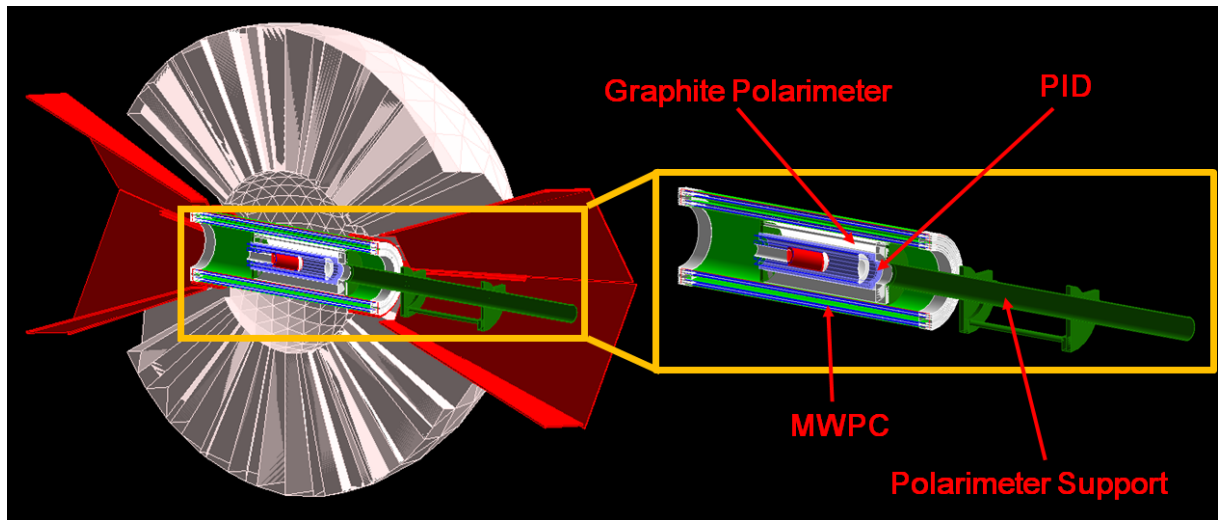
Figure 4.18: A image of the Geant4 simulation for the crystal ball detailing the positions of the PID, MWPCs, polarimeter and its support structures.

4.7.4   Graphite Polarimeter

The design of the graphite polarimeter was detailed in the proposal for this experiment [111] and followed on from the polarimeter used in a previous experiment [112]. This original polarimeter was designed to only measure protons while the latest polarimeter utilised both the PID and MWPCs to allow information from both recoiling protons and neutrons. It consisted of a 30 cm long graphite cylinder of inner radius 3.9 cm and outer radius 6.5 cm. There was also an end cap which was 2.6 cm thick and had a 2.4 cm radius hole removed to allow the beam to pass through. This was situated downstream of the target at the end of the main cylinder. A schematic of the polarimeter in the detector system can be viewed in Figure 4.18 while a CAD drawing is available in Figure 4.19.

4.8   Forward Region Detectors

4.8.1   Two Arm Photon Spectrometer (TAPS)

The TAPS array used for this experiment is a subset of the overall detector, with the other modules currently located at the Crystal Barrel experiment in Bonn. The TAPS detector at the crystal ball is an array of 366 BaF_2 crystals and inner rings consisting of 72 $PbWO_4$ crystals situated closer to the beamline for a total of 438 crystals. It covered the important downstream region
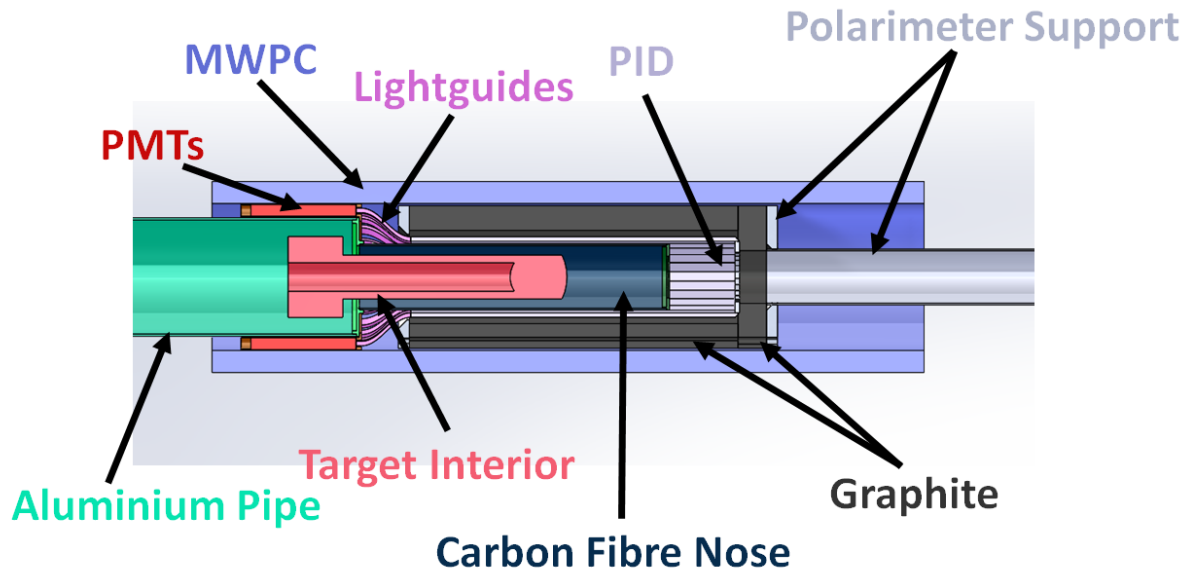
Figure 4.19: A CAD drawing of the recoil polarimeter detector system and target inside the crystal ball.

which is missed by the Crystal Ball due to the opening for the beam exit and it provided forward angular coverage of approximately 2-20° in the polar range. The crystal layout is depicted in Figure 4.20. Originally TAPS began with 384 BaF$_2$ crystals but to improve angular resolution and to allow for higher rate capabilities the 18 innermost crystals were each replaced by four PbWO$_4$ crystals.

The BaF$_2$ crystals are 25 cm long, corresponding to 12 radiation lengths, with a hexagonal face of diameter 5.9 cm. They have a fast scintillation component of 0.9 ns which can be used for time of flight measurements and a slow component of 650 ns which provides a better energy resolution. BaF$_2$ has a relatively fast timing component compared to NaI and some particle identification information can be gained from time of flight measurements, although this was not used in the current analysis. A schematic of a BaF$_2$ crystal is shown in Figure 4.21. The PbWO$_4$ crystals are 20cm long, corresponding to 22.5 radiation lengths, and have a trapezoidal shape so that four combine to give the hexagonal shape of the BaF$_2$ crystal they replaced. All the crystals are optically isolated from each other by wrapping the BaF$_2$ in 8 layers of 38 μm thick reflecting Teflon foil and one layer of 15 μm thick aluminium foil and the PbWO$_4$ in 70 μm thick reflector foil VME 2000 and 20 μm aluminium foil. Each BaF$_2$ is read out via a Hamamatsu R2059-01 PMT and each PbWO$_4$ by a Photonis XP1911 PMT. A visualisation of the detector
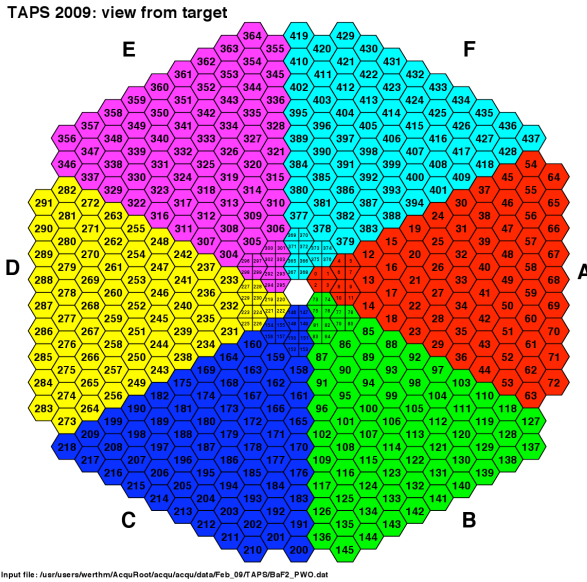
Figure 4.20: TAPS forward wall arrangement showing the numbering of the elements and the different sectors. The $PbWO_4$s are the quartered crystal situated nearest the centre of the detector.
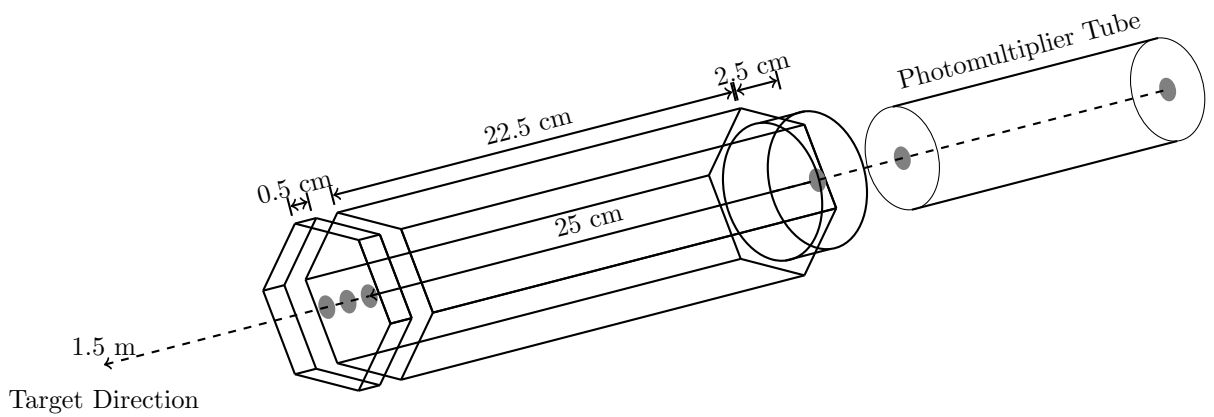
Figure 4.21: A schematic of a BaF_2 crystal used in TAPS detailing the position of the PMTs, the dimensions of the crystals. The Veto detector is shown sitting on the front face of the crystal. Taken from [43].
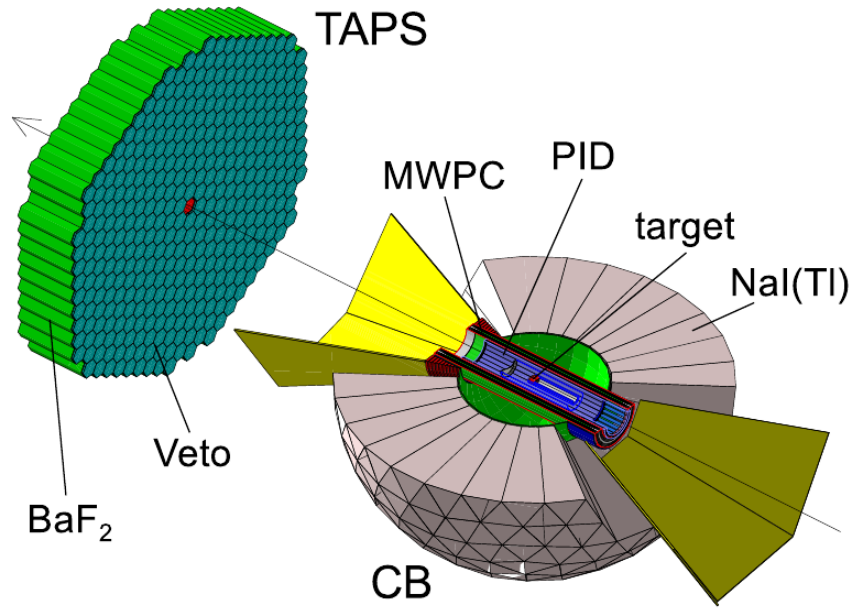
Figure 4.22: A Geant4 visualisation of the experimental setup with the CB cut in half to show the inner detectors.

configuration is shown in Figure 4.22

4.8.2   TAPS Veto Detectors

A charged particle veto detector was situated in front of each BaF_2 crystal and each grouping of four $PbWO_4$ crystals. This consisted of a $5\,mm$ thick layer of EJ-204 scintillator with the same hexagonal shape as the crystal beyond and was read out via BCF-92 wavelength shifting fibres to Hamamatsu H6568 multi-anode PMTs with 16 channels. This was used to separate charged particles from neutrals while a ΔE-E method, similar to the Crystal Ball PID detector, provided further PID information. A hit in the crystal with no corresponding hit in the veto gave classification of a particle as neutral. A schematic of the vetoes is shown in Figure 4.23. Note the differing numbering scheme from the crystals due to one veto covering four $PbWO_4$ crystals.
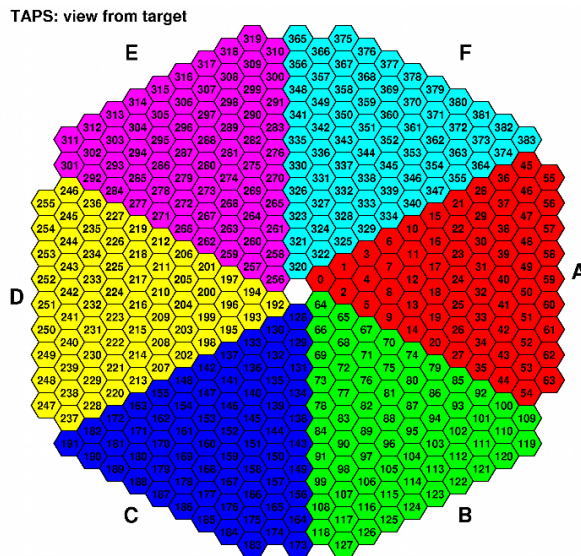
Figure 4.23: The Veto detector wall situated in front of TAPS. Note that the inner vetoes contain only one but cover four PbWO$_4$ crystals.

4.9 Data Acquisition

The data acquisition system used at the A2 hall experimental facility cannot record data continuously. This is due to the time taken for readout and digitisation of the data. A trigger is used to reduce the experimental rates to events of interest and subsequently allow a reasonable amount of dead time. For the particular experimental run under consideration a trigger to save an event was applied if the total energy sum in the CB was above 100 MeV and a multiplicity of 2+ was achieved. That is to say two or more particles detected and between them depositing more than 100 MeV in the Crystal Ball. A logic signal for the energy sum condition was created by passing the sum of all the elements in the CB to a discriminator. The energy sum trigger removed low energy backgrounds which were not able to produce the kinematics required for the pion photoproduction channels of interest. The multiplicity trigger condition required two clusters be detected within the CB and TAPS. This was chosen to allow the deuteron photodisintegration final state to be recorded. If any of these conditions were not met the signals would be dumped, the DAQ reset and prepared for the next event.

4.10   Simulations

A Geant4 simulation [113] of the detector geometry present in the A2 hall was used for a variety of different purposes in this body of work including simulation of signal and background channels and energy corrections. The Geant4 framework is a platform for simulating the passage of particles through matter using Monte Carlo methods. The A2 simulation contains all the detector geometries present in the A2 hall and was updated for this work to include the new PID, polarimeter and necessary support structures. Physics events, combinations of particles, to be simulated are created via an event generator. This results in information on each particle as well as the vertex of the interaction in the target being passed to the simulation. The passage of these particles through the detectors is tracked and the time of the hit and energy deposited is calculated using a database of known cross-sections of physical processes. Distributions of events were generated for reactions of interest and used as input to the A2 simulation. The detector response information was reconstructed and recorded. This was compared to the input generated distributions as shown in Figure 4.24. A good agreement was observed.
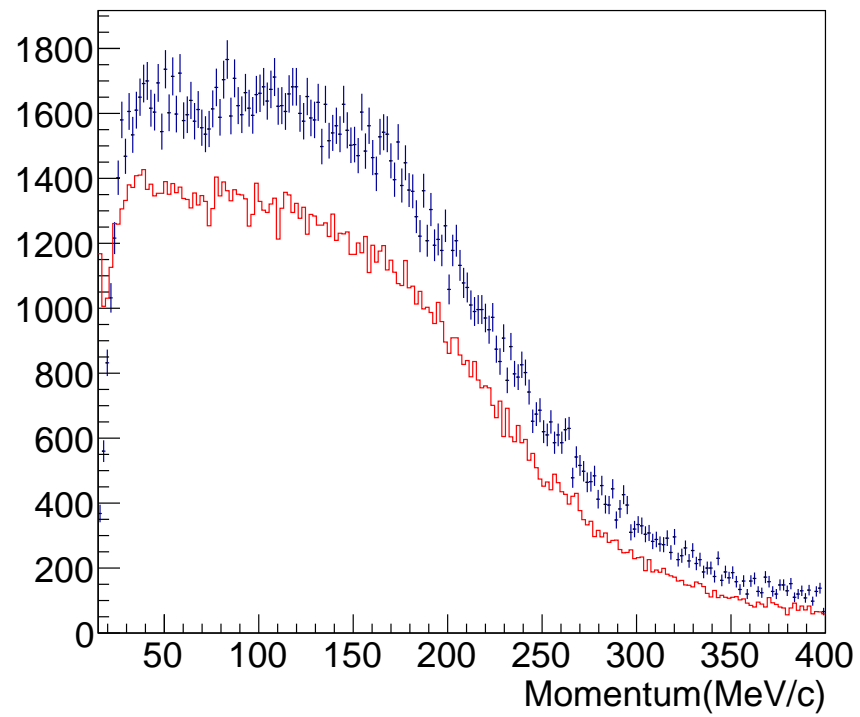
Figure 4.24: A distribution of generated proton momentum(blue) compared to the reconstructed momentum(red) after being processed by the A2 simulation.

Chapter 5

Calibrations

Calibrations of the various detectors present in the A2 hall were required to transform the digi-tised output signals into meaningful physical quantities. This chapter details the procedures for calibration of the detectors which I performed for the August and September 2016 beamtime. As many calibrations depend on clusters of crystals, Section 5.1 will first cover how clusters, corresponding to individual particles, are reconstructed in the calorimeters. In Sections 5.2 and 5.3 the methods of calibration of detectors for energy and time respectively will be presented. Finally, additional calibrations performed are given in subsection 5.4.

5.1 Clustering in the Crystal Calorimeters

5.1.1 Crystal Ball

Particles reconstructed from the crystal ball are formed using clusters of hits via an iterative process. A minimum threshold of around $2\,\text{MeV}$ for any struck crystal was applied to determine a hit and sorted by energy. The first cluster determination starts with the crystal with the highest energy deposit. For a cluster of hits, the struck crystal with the most energy is designated the centre of the event. Up to 15 neighbouring crystals can also be considered part of an event if they are above the $2\,\text{MeV}$ threshold. This forms our cluster for an event with the central cluster providing the timing signal and the energy coming from the sum of the energies deposited in the struck crystals in the cluster. 15 neighbours only are used as it has been determined that 98%

of the energy of a photon is distributed over this area. Occasionally a crystal separated from the main cluster is not included by the clustering algorithm. This is known as a split off cluster. To allow this split off cluster to be associated with the main cluster and, hence, reconstruct the full energy of the detected particle a predefined separation distance to add a cluster to the main cluster is afforded to the clustering algorithm. A 3 crystal separation was allowed for this in the crystal ball. After summation a total minimum energy threshold is applied to each cluster of 15 MeV. An impact position for a cluster can be estimated by determining the square root energy weighted mean:

$$r_{cl} = \frac{\sum\limits_{i=1}^{n}\sqrt{E_i} \cdot r_i}{\sum\limits_{i=1}^{n}\sqrt{E_i}} \tag{5.1}$$

where E_i is the energy of each of the individual crystals in the cluster and r_i are their centres of gravity. Each crystal can only participate in one cluster. The process described is repeated until no more clusters can be formed. Coincidences with the PID are assigned to designate clusters as having been created by charged particles. A correlation between the hit in the CB and the azimuthal angle given by the PID is determined. A cluster is said to be charged if the difference of these two is less than 15 degrees.

5.1.2 TAPS

For TAPS a similar method was used. An individual crystal threshold in the range of 3-5 MeV was used to reduce random backgrounds and determine a hit. The crystal with the most energy determines the centre of the event and gave the timing signal. All adjacent struck crystals were added to the cluster. The neighbours of these crystals were checked and added to the cluster if hit. No limit is placed on the number of elements present in a cluster. A cluster was identified when no more neighbouring elements were struck. The total energy was again the sum of the energies of the elements in the cluster but the estimated impact position was this time calculated

(a) CB Clustering. (b) TAPS Clustering.
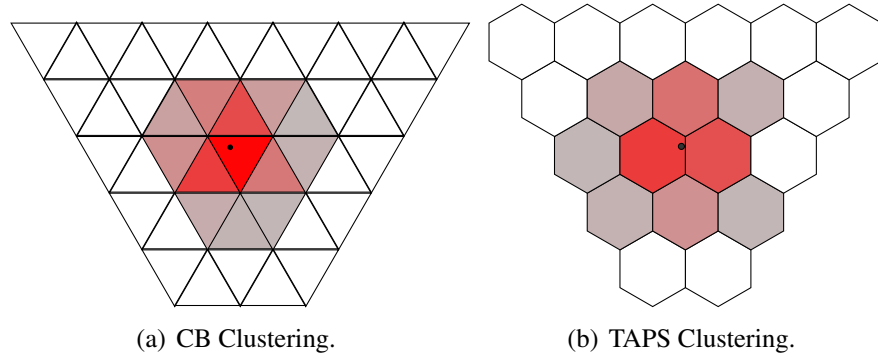
Figure 5.1: A potential cluster created in CB or TAPS. The black dot represents the location struck by the particle. The intensity of red describes the level energy deposited. Taken from [43].

using logarithmic weighting:

$$W_i = max \left[0.5 + log \dfrac{E_i}{\sum\limits_{i=1}^{n} E_i} \right] \tag{5.2}$$

$$r_{cl} = \dfrac{\sum\limits_{i=1}^{n} \sqrt{W_i} \cdot r_i}{\sum\limits_{i=1}^{n} \sqrt{W_i}} \tag{5.3}$$

A more detailed explanation can be found in [103]. A total minimum energy threshold of 20 MeV for each cluster was applied. The clustering of both detectors is illustrated in Figure 5.1.

TAPS is a forward detector wall and, hence, the individual elements do not point towards the target as is the case with the CB elements. A correction to the impact position had to be performed for photons due to this. The geometry of this is illustrated in Figure 5.2. The correction required to the x and y coordinates due to the shower depth was:

$$x' = x - x \left(\dfrac{s}{d} + 1 \right)^{-1} \tag{5.4}$$

$$y' = y - y \left(\dfrac{s}{d} + 1 \right)^{-1} \tag{5.5}$$
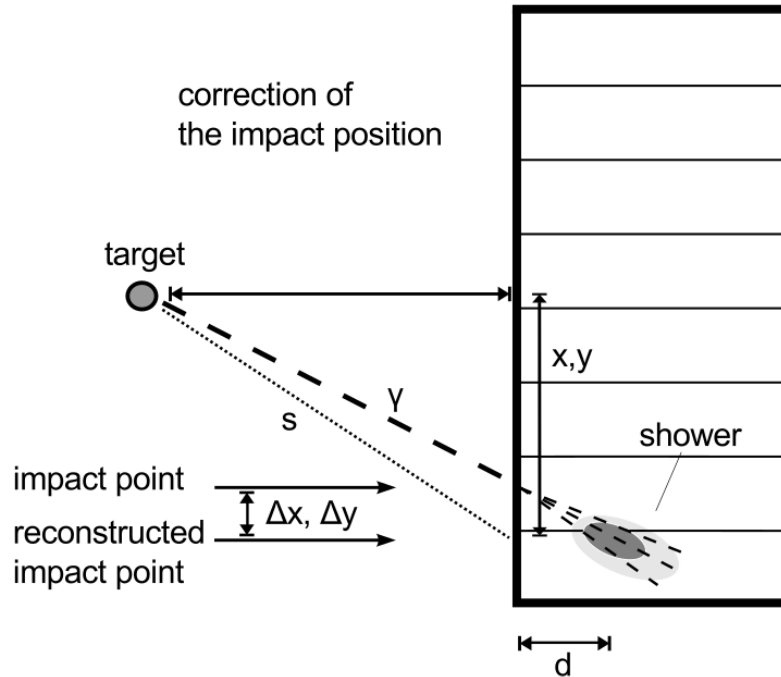
Figure 5.2: Correction to the impact position of particles in TAPS. Taken from [103].

$$d = X_0 \left(log \left[\frac{E_{cl}}{E_C} \right] + 1.2 \right)$$ (5.6)

where s is the particle flight path, E_{cl} is the energy of the cluster, E_C is the critical energy of BaF_2 and is 12.7 MeV and X_0 is the radiation length of 2.05 cm. Similarly to the CB and PID, each cluster in TAPS was checked for a coincidence with the veto detector in front of the element. The neighbouring elements veto detectors were also checked as it is possible that a charged particle may pass through these. If one or more veto hit was present, the cluster was determined to be charged.

5.2   Energy Calibrations

A charge to digital convertor, QDC, was used to convert electrical charge produced in PMTs by optical photons created in the scintillators, from energy deposited in the crystal when struck by a particle. As the charge collected is proportional to the energy deposited we form the following

equation:

$$E_{dep} = g \cdot (c - p) \tag{5.7}$$

where E_{dep} is the deposited energy in MeV, g is the conversion gain in MeV/channel, c is the QDC channel and p is the pedestal position which corresponds to the channel with zero energy. The majority of the energy calibrations discussed forthwith are concerned with determining the correct pedestal channel and conversion gain.

5.2.1 Crystal Ball Energy Calibrations

There were several stages required to fully calibrate the reconstructed energy of particles detected in the CB: a low energy calibration was performed before the beamtime to ensure each crystal contributes equally towards the energy based triggers; an iterative higher energy calibration was performed after the experimental data had been collected to accurately determine the response for detected photons; a further quadratic energy correction was required to compensate for the non-linear response of the CB over the full 20-1000 MeV range used in this experiment.

Low Energy Calibration

This calibration was performed by colleagues at the Johannes Guttenberg Universität. An alpha emitting ^{241}Am source was used for this calibration. These alpha particles were incident on ^{9}Be which decayed via a chain reaction to a metastable state of ^{12}C. This ^{12}C de-excited via monochromatic photons of energy 4.438 MeV.

$$\begin{aligned}
^{241}_{95}Am &\rightarrow ^{237}_{93}Np + \alpha, \\
^{9}Be + \alpha &\rightarrow ^{13}C^{*}, \\
^{13}C^{*} &\rightarrow ^{12}C^{*} + n \\
^{12}C^{*} &\rightarrow ^{12}C^{+}\gamma
\end{aligned} \tag{5.8}$$
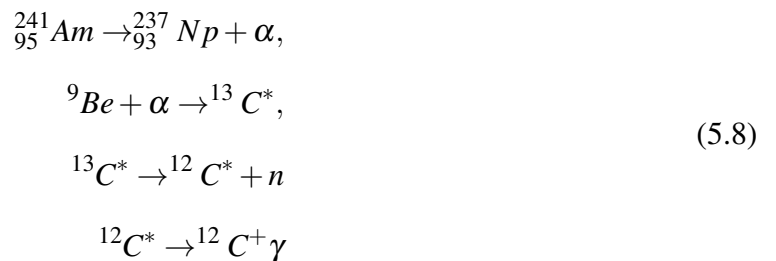
As this was a monochromatic source the gains of all the photomultipliers were set such that the peak from this beam was aligned in the ADC spectrum for all crystals. The spectrum for a single NaI(Tl) crystal is shown in Figure 5.3.
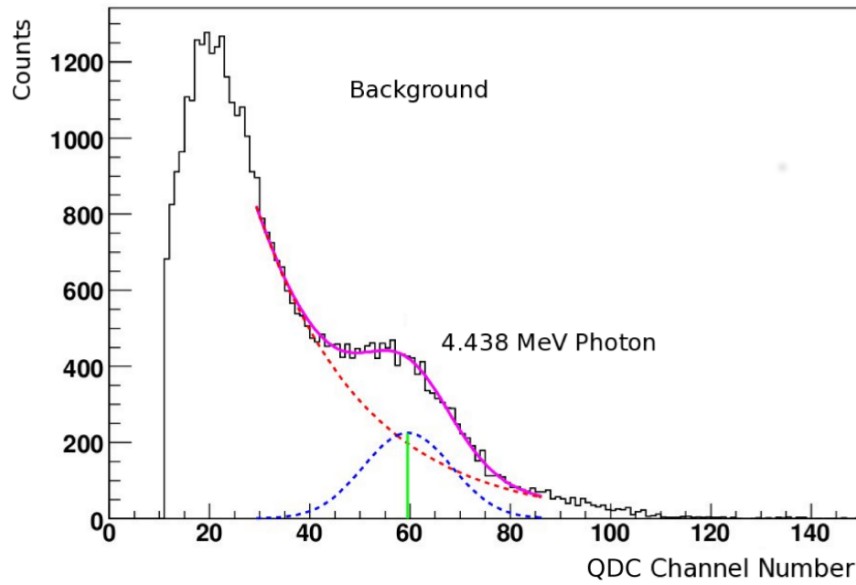
Figure 5.3: A QDC spectrum of a NaI,(Tl) crystal from an ^{241}Am/^{9}Be. The peak is fitted with a Gaussian, blue, and an exponential, red, to extract the position of the 4.438MeV photon peak. Taken from [110].

High Energy Calibration

A higher energy calibration was necessary due to the energies of the photons actually detected during the experiment being typically hundreds of MeV. The decay of a π^0-meson to two photons was used to calibrate the detector in this energy range by adjustng the crystal parameters to fix the invariant mass of two photons to peak at the π^0 mass. More specifically, when two photon clusters were identified a histogram corresponding to the highest energy crystal in each cluster was filled with the invariant mass of the two photons. The mean invariant mass of the two photons was calculated, for central element i, as:

$$\langle m_i \rangle = \sqrt{2\langle E_i \rangle \langle E_o \rangle (1 - \cos\langle \psi_{io} \rangle)} \tag{5.9}$$

where $\langle \psi_{io} \rangle$ is the mean opening angle of the two photons with one detected in element i. $\langle E_i \rangle$ is the mean photon energy of the central element i and $\langle E_o \rangle$ is the mean photon energy of the other elements. An example is shown in Figure 5.4. $\langle E_i \rangle$ is related to the integrated signal of the ADCs, $\langle I_i \rangle$, via:

$$\langle E_i \rangle = g_i \langle I_i \rangle \tag{5.10}$$
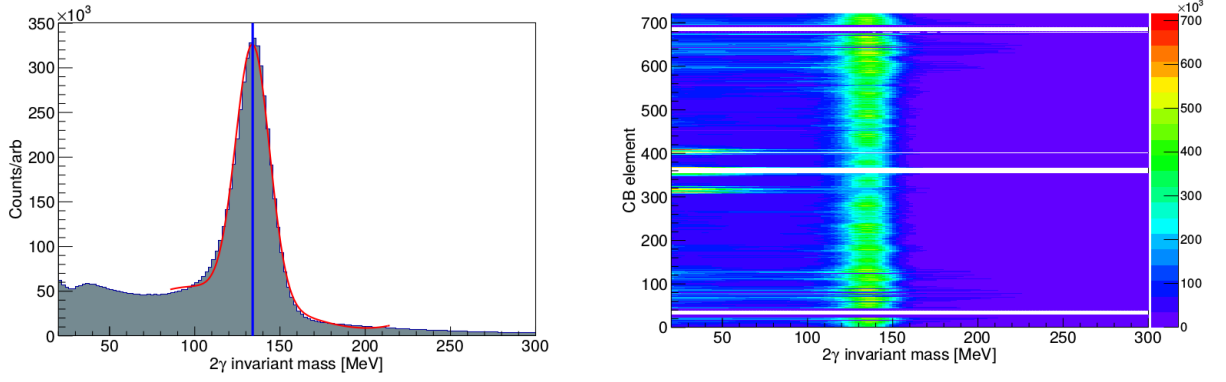
Figure 5.4: On the left an example fit to the 2 photon invariant for a single element is displayed. The plot on the right shows the invariant mass for every crystal ball element.

A new gain factor which moved the invariant mass closer to the π^0 mass was calculated using:

$$g_i^{'} = g_i \frac{m_{\pi^0}^2}{\langle m_i \rangle^2} \qquad (5.11)$$

where m_{π^0} is the physical pion mass and $\langle m_i \rangle$ was determined from a fit to the invariant mass(Figure 5.4) using a Gaussian plus polynomial function. An iterative process was necessary to determine the correct gains for every detector element since an alteration of gain in any particular high energy crystal effects all clusters and therefore invariant masses that it contributes to. The convergence of this calibration can be seen in Figure 5.5.

Quadratic Energy Calibration

A quadratic energy correction was necessary following the high energy calibration to account for energy dependent shower losses. These effects are corrected for at the π^0 mass by the high energy calibration. However, for higher cluster energies the relative weight of the energy losses are smaller and this leads to an overcorrection at higher masses. The idea behind this calibration was to determine the corrected energies, $E^{'}$, on both the π^0 and η mesons from the deposited energies, E, using a quadratic function of the form:

$$E^{'} = aE + bE^2 \qquad (5.12)$$
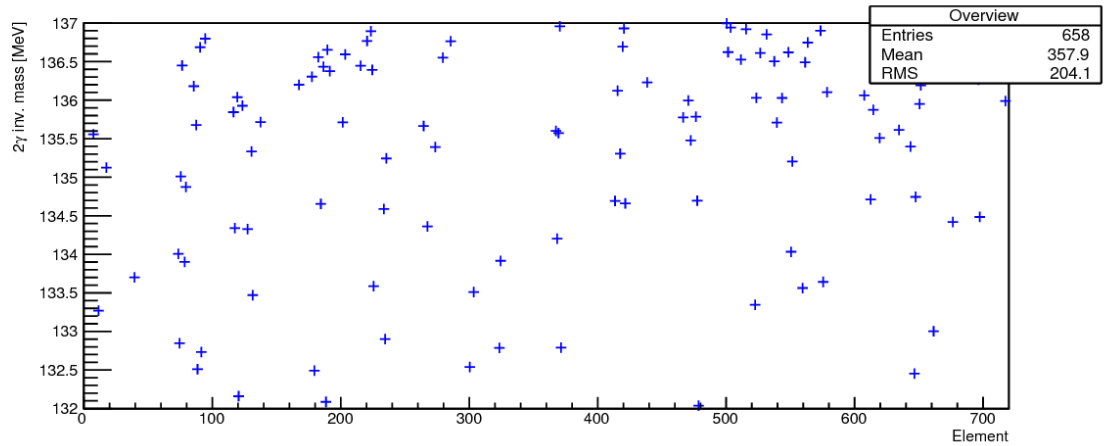
(a) The first iteration
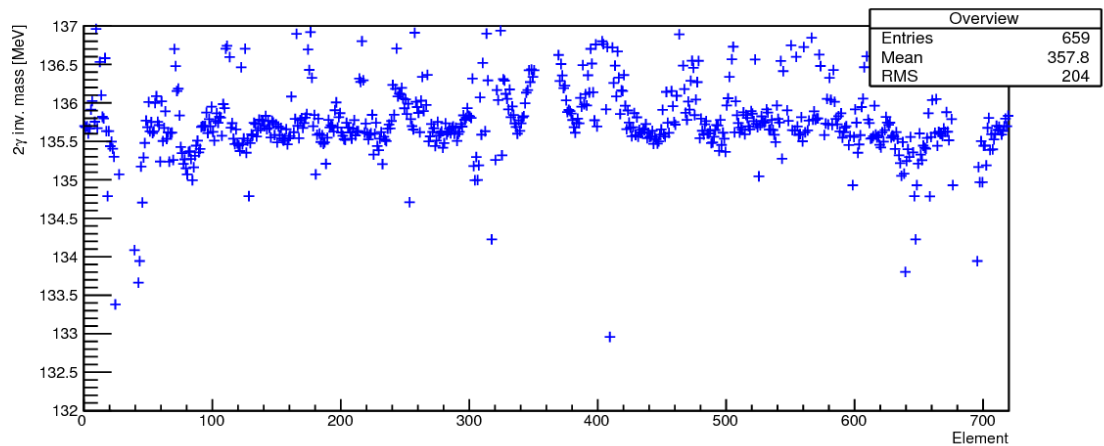
(b) Iteration 5
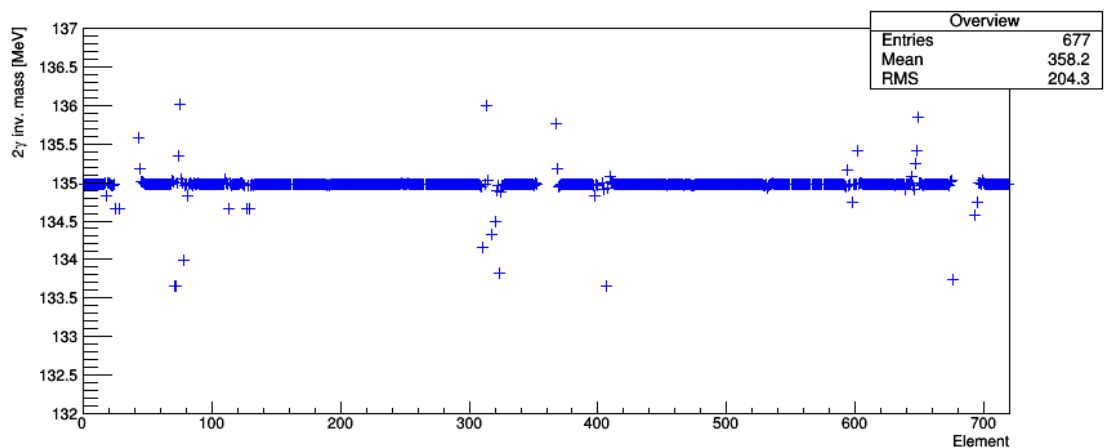
(c) Iteration 17

Figure 5.5: Showing three different iterations of the crystal ball energy calibration with crystal element versus mass reconstructed from two photon clusters. Sufficient convergence is achieved after 17 iterations.

where a and b are determined by again ensuring agreement between the mean invariant mass of the mesons detected and the physical mass:

$$\left\langle m'_{\pi^0} \right\rangle = \sqrt{2 \left\langle E'_{\pi^0} \right\rangle^2 (1 - \cos\left\langle \psi_{\pi^0} \right\rangle)} = m_{\pi^0} \qquad (5.13)$$

$$\left\langle m'_{\eta} \right\rangle = \sqrt{2 \left\langle E'_{\eta} \right\rangle^2 (1 - \cos\left\langle \psi_{\eta} \right\rangle)} = m_{\eta} \qquad (5.14)$$

where m_{π^0} and m_{η} are the physical masses of the mesons and $\left\langle m'_{\eta} \right\rangle$ and $\left\langle m'_{\pi^0} \right\rangle$ are the mean values of the invariant mass distributions. The mean energies of the photons from the η and π^0 mesons are represented by $\left\langle E'_{\eta} \right\rangle$ and $\left\langle E'_{\pi^0} \right\rangle$ and the mean opening angles by $\left\langle \psi_{\eta} \right\rangle$ and $\left\langle \psi_{\pi^0} \right\rangle$. For every detector element these correction parameters, a and b were determined under the assumption that the mean opening angles of the decay photons of the mesons do not change when applying the energy correction. An example of the spectra that were fitted is displayed in Figure 5.6. The calibrations resulted in an invariant mass resolution of 10.5 MeV for π^0 mesons as shown in Figure 5.7.

5.2.2 TAPS Energy Calibrations

For the TAPS detector a calibration was performed with cosmic-rays before data-taking. As with the CB detector a higher energy calibration was necessary post data gathering and a quadratic energy correction.

Low Energy Cosmic Rays Calibration

As the elements of the TAPS detector are aligned horizontally the trajectories of cosmic rays traversing the crystals and therefore the deposited energy were similar. Cosmic ray calibration measurements were taken shortly before the beamtime, shortly afterwards and during maintenance periods. The spectrum of cosmic radiation in each BaF_2 crystal was fitted with a Gaussian and exponential to determine the channel corresponding to the mean deposited energy of minimum ionising particles. The mean deposited energy in BaF_2 crystals was found to
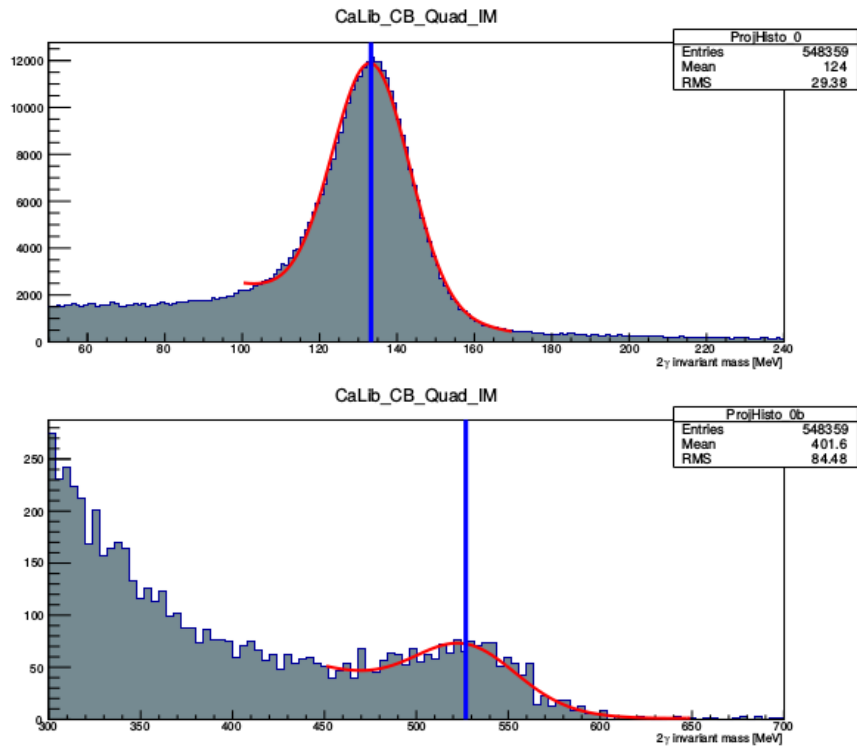
(a) The invariant mass fits for π^0 and η mesons in the crystal ball
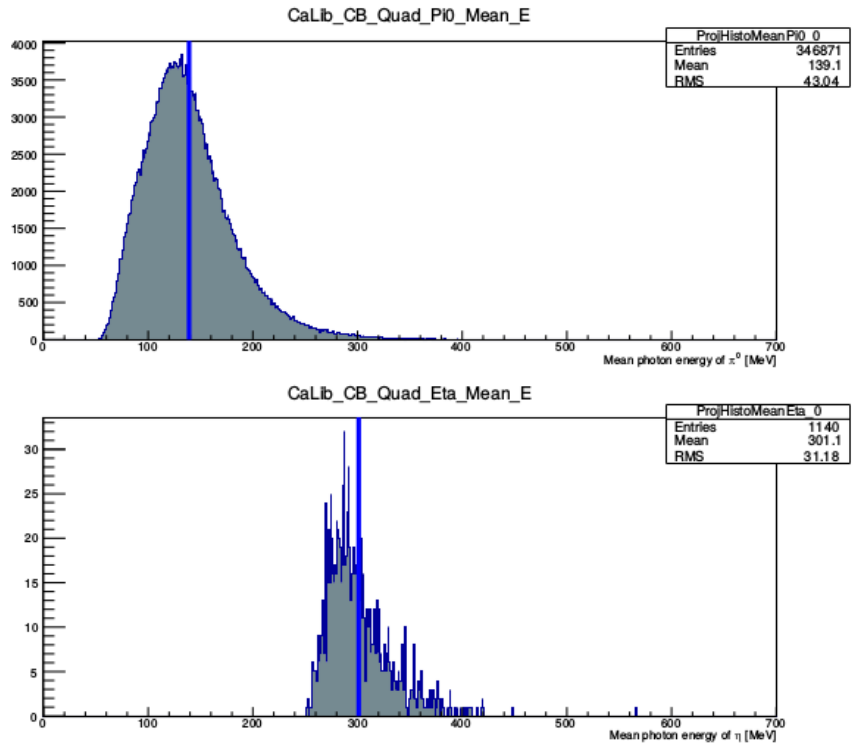
(b) The determination of the mean energy of the π^0 and η spectra.

Figure 5.6: The determination of both the mean positions of the η and π^0 mesons and the invariant mass of both is shown for a single crystal ball element. The statistics for the η meson is significantly smaller than the π^0.
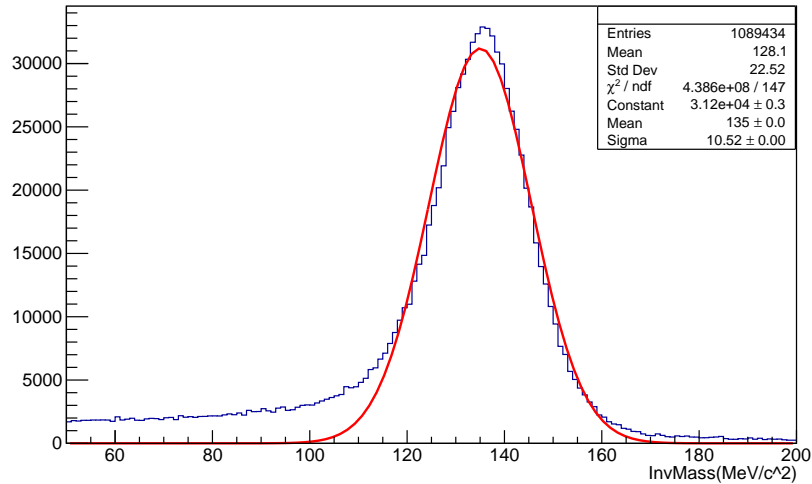
Figure 5.7: A fit to the invariant mass of a reconstructed pion with calibrations applied to determine the resolution. A resolution of 10.5 MeV was achieved.

be 37.7 MeV [114]. The pedestal position was also determined from this spectrum, and using equation 5.7 the conversion gain was calculated. A representative raw ADC spectrum is shown in Figure 5.8. In this manner a rough energy calibration was established before the beamtime by adjusting the voltages of the PMTs to normalise the gains of the individual elements.

High Energy Calibration

For the higher energy calibration of TAPS a similar method as for the CB was used. Due to the relatively small angular coverage of TAPS an insufficient number of events with both photons from the π^0 decay were recorded in TAPS to accurately determine an invariant mass peak position. This led to using one of the photons detected in the CB in combination with a TAPS photon cluster. The CB energy calibration was completed before the TAPS energy calibration.

Quadratic Energy Calibration

Once again the same method for the quadratic energy calibration as detailed in section 5.2.1 was used with the exception that for both the π^0 and η mesons, one photon was taken to be detected in the crystal ball.
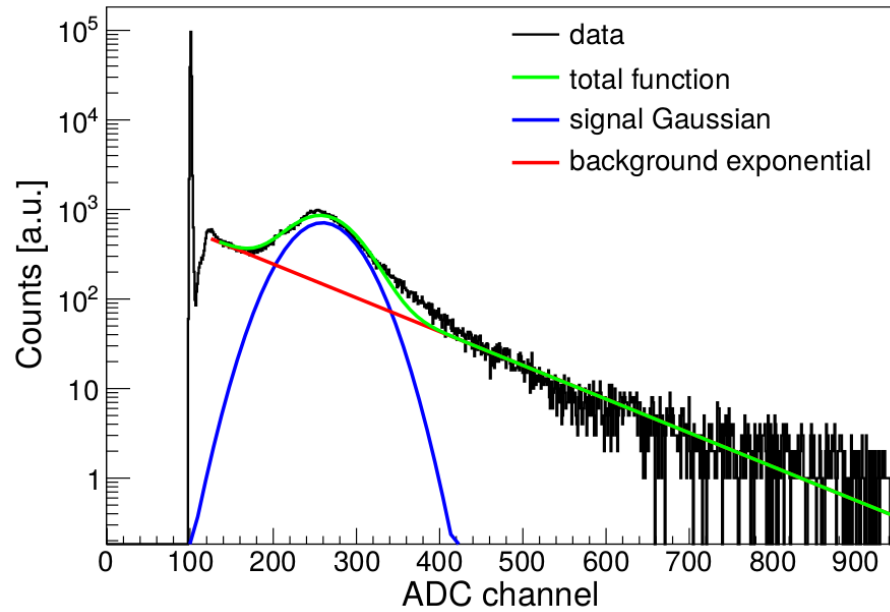
Figure 5.8: An ADC spectrum of a BaF$_2$ crystals obtained from cosmics data. The pedestal can be clearly observed around channel 100 and the cosmic ray peak at around channel 250. Taken from [103].

5.2.3 PID Energy Calibration

The following calibration was performed by collaborators at the University of Edinburgh. The reaction $\gamma n \rightarrow p \pi^-$ was used to provide PID detector responses that could be directly compared with simulation. Real experimental p π^- events were selected in the angular range of $35°$-$45°$ in θ using the over-constrained reaction kinematics. Simulated events for the same channel provided the actual energy deposited in both the CB and the PID. By comparing these values with the real experimental quantities, a conversion was determined between the two. First, the energy in the PID for real and simulated data was related to its corresponding CB energy. By then cutting events in terms of their CB energy, the corresponding PID energy for real and simulated data was compared and calibration parameters determined as illustrated in Figure 5.9. This was fitted with a function of the form given in equation 5.7 with the parameters determining the values of the gain and pedestal. This was performed separately for each of the PID elements. A typical fit for this method is shown in Figure 5.9. Arbitrary reference points distributed across the full deposition energy range are then taken in crystal ball energy. For each of these reference points the PID energy is then plotted against PID element. If there is not a smooth straight line
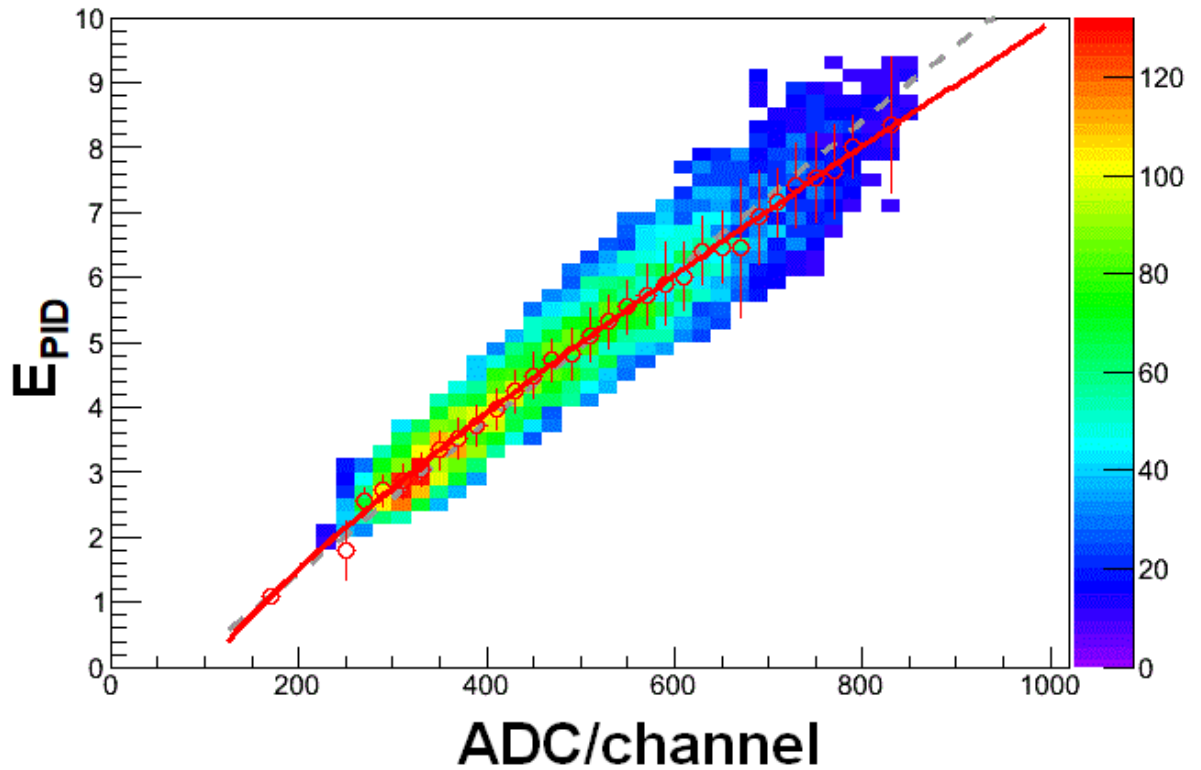
Figure 5.9: The calculated PID energy values as a function of ADC channel.

across element numbers then the procedure above is repeated until there is. One such plot is shown in Figure 5.10 for before and after the calibration.

5.2.4   TAPS Veto Energy Calibration

For the TAPS veto detectors, the pedestal positions were determined from the raw ADC spectra of the production data. The conversion gain was determined in a similar manner to the PID by comparing the energy deposition of charged particles from experimental data to simulated data. For this calibration events from the reaction $\gamma p \rightarrow p \pi^0$ were used. Simulated events from this channel were used to form histograms of energy deposited in TAPS versus the energy deposited in the Veto detector. These were also formed using the experimental data with the exception that the raw ADC spectra values were plotted for the energy deposited in the Veto detector. The deposited energy in TAPS was split into bins and the peak of the proton was fitted for a projection of the histogram for each bin for both simulated and production data. The values from the fits for simulated data were plotted against the fit values from experimental data. A
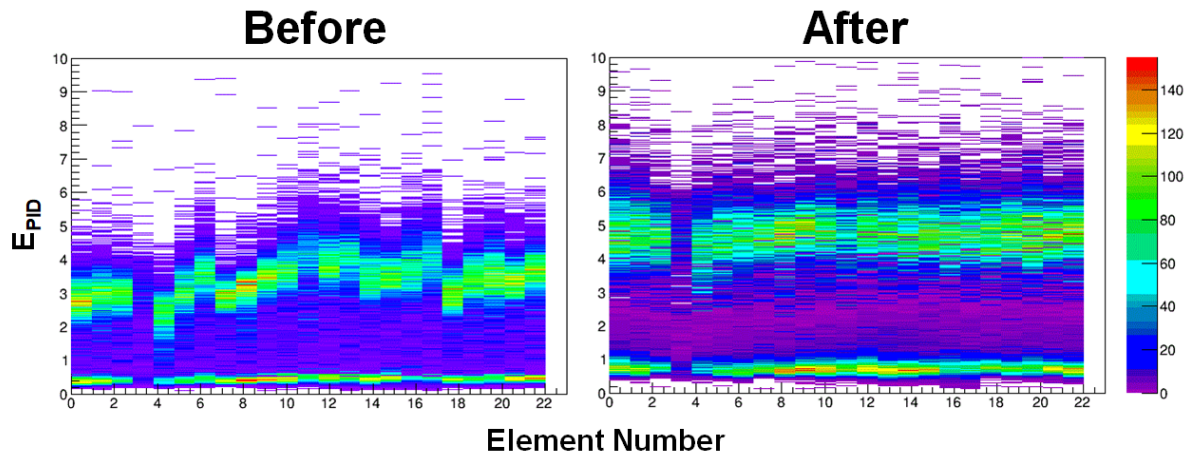
Figure 5.10: The PID energy for a given reference point plotted against the element. The left plot shows this before calibration of the PID iteratively and the right after such a calibration. Taken from [96].

linear function was applied to this and the conversion gain could be extracted from one of the fit parameters.

5.2.5 Tagger Electron Energy Calibration

The calibration of the electron energy in the Tagger focal plane detector is dependent upon the strength of the magnetic field of the dipole magnet and the electron beam energy. The energy of the electron beam remains at the same energy during a given beamtime and was considered a constant at 1508 MeV. The magnetic field strength was monitored using an nuclear magnetic resonance (NMR) probe measurement and was stable for the beamtime. The calibration was conducted with no radiator present. The electron beam was directed to the beam dump by adjusting the magnetic field strength. This was measured as 1.887 T with a beam energy of 1508 MeV for this experiment. Measurements were taken for seven different beam energies between 195-1308 MeV. The magnetic field strength was varied for each energy providing a number of reference points along the focal plane. A relationship between the incoming electron energies and tagger channels was determined via fitting these measurements and extrapolating to provide an energy calibration for every channel for the given beamtime assuming a uniform magnetic field. An uncertainty in the tagged photon energy of ± 0.5 MeV is associated with this

method.

5.3 Timing Calibrations

The detector timing signals were measured with time to digital converters (TDCs) and a relationship between the TDC channels, c, and the time was determined to be:

$$t = g \cdot (c - d) \tag{5.15}$$

where t is the time in ns, g is again the conversion gain and d is a start time offset of channels. The calibration determined these two parameters allowing conversion of the channels to the physical time. The offsets were adjusted so that the coincidence peak between the Tagger and CB was centred at zero. The detector TDCs can operate in either common start or stop mode. A common stop is when the individual TDC is started by the signal of its detector and stopped by the trigger. A common start is when they are started by the trigger and stopped individually. The tagger, crystal ball and PID are all common start with TAPS being common stop. An important note on these timing methods is, when dealing with time differences between detectors the trigger time must cancel as it experiences jittering effects which have an impact on the resolution. Due to the different timing methods the time difference was dependent on the detector and can be written as:

$$t = t_{det} - t_{trig} \tag{5.16}$$

for the Tagger, CB and PID detectors. For TAPS and the Veto detectors it was written as:

$$t = t_{trig} - t_{det} \tag{5.17}$$

The timing calibrations are pivotal in obtaining accurate time of flight measurements and determining tagger random coincidences.

5.3.1 Crystal Ball Timing Calibrations

There are three separate components to the timing calibration of the crystal ball. These are a time alignment calibration, a time walk calibration and a rise time calibration. The time walk calibration is necessary since the time when the signal passes above threshold is correlated with the energy deposited in the crystals. The crystal ball TDC conversion factors were all set to 117 ps/channel. It only remained to ascertain the offsets.

Time Alignment

The time alignment calibration determines the time difference distributions for all crystals in a cluster by using the highest energy element of a cluster as a reference signal. In this manner a distribution was formed for every crystal. By fitting these with Gaussians and determining the mean values, m_i, we can utilise the following relation to align the crystal ball TDC signals:

$$d_i' = d_i + \frac{m_i}{g_i} \tag{5.18}$$

where d_i' and d_i are the new and old offsets of the individual elements. Similarly to the energy calibration, this is an iterative process which aligns all of the time differences at zero. The convergence of this process is shown in Figure 5.11.

Time Walk Calibration

There is an energy dependence of the response time of an element, i.e. how long it takes to pass the threshold energy. Higher energy signals pass this threshold quicker than lower energy signals. This effect is referred to as time walk. To apply a correction for this time walk, a plot of energy against time for every detector element was created and a fit applied to describe the dependency. Once again, π^0 meson decays were used for this calibration. A cut around the expected missing mass for a $p\pi^0$ event and invariant mass for the π^0 was applied to suppress background. A sideband background subtraction was performed as described in Section 6.3.1 with a signal region of -25 to 25 ns and two background regions of -200 to -90 and 90 to 200 ns selected in the tagger timing spectrum. A cut of 110 to 160 MeV was applied to select the
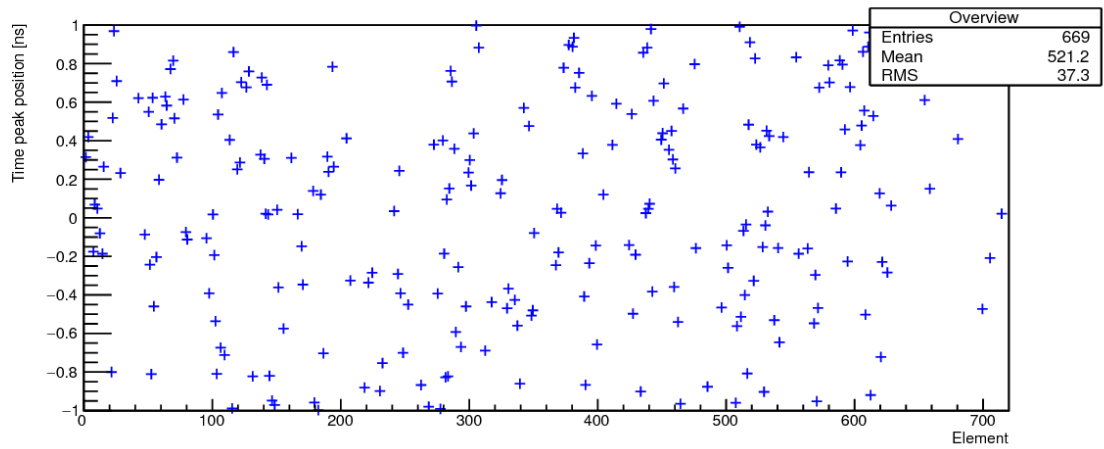
(a) The first iteration
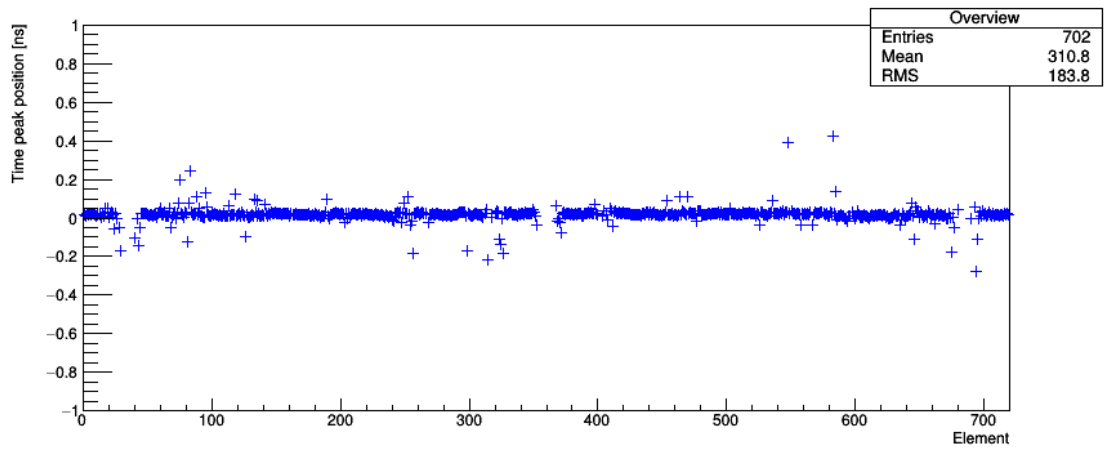
(b) Iteration 17

Figure 5.11: Showing two different iterations of the crystal ball time calibration with crystal element versus time peak position in ns. Sufficient convergence is achieved after 17 iterations.
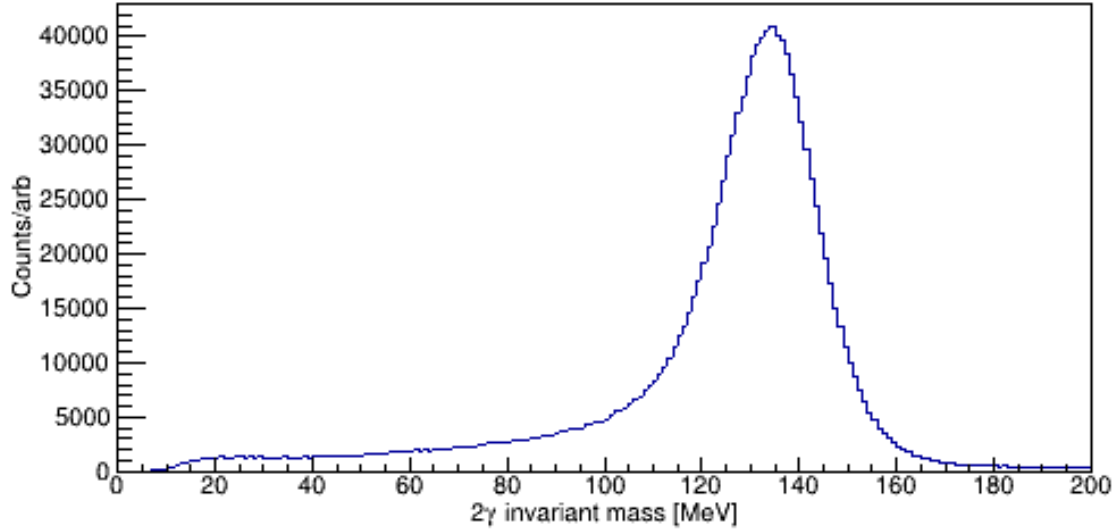
Figure 5.12: The invariant mass distribution of the combination of two photons with a peak at the π^0 mass.

135 MeV mass of a π^0 reconstructed from two photons. Figure 5.12 shows the invariant mass with the sideband subtraction applied. A missing mass cut was subsequently applied of -70 to 70 MeV. Figure 5.13 depicts the missing mass spectrum with both sideband subtraction and invariant mass cut applied. The distributions were fitted with a function of the form:

$$t(E_{dep}) = a + \frac{b}{(E_{dep} + c)^d} \tag{5.19}$$

with the tagger being used to provide relative timing to each detector element i.e. $t = t_{CB} - t_{tagger}$. An example fit is shown in Figure 5.14. The four parameters a,b,c and d were calculated for each distribution and applied to the detector times via:

$$t' = t - \left(a + \frac{b}{(E_{dep} + c)^d} \right) \tag{5.20}$$

Rise Time Calibration

The last timing calibration for the crystal ball involves rise time. The parameter a in equation 5.20 is the rise time. As there are insufficient statistics for some low cross section regions such as backward angles the aforementioned time walk fits can be poor. This results in shifted timing between the elements. By using a fit of the mean values of the relative times after the time walk
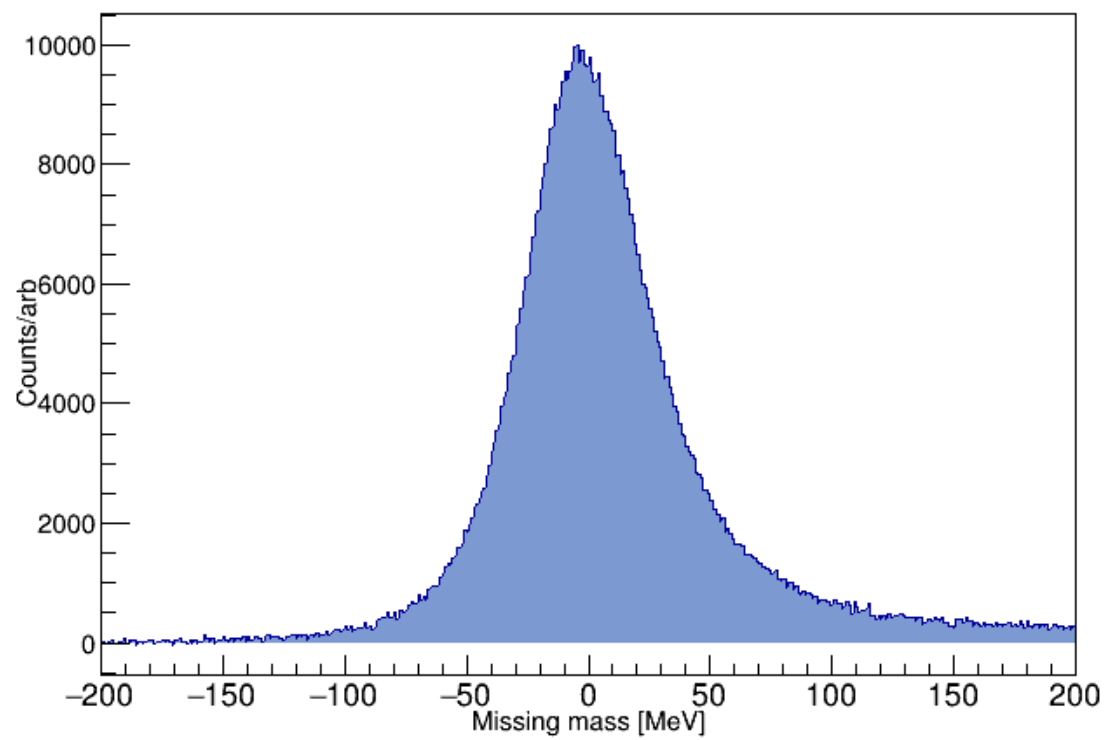
Figure 5.13: The missing mass distribution with tagger timing sideband subtraction and invariant mass cuts applied.
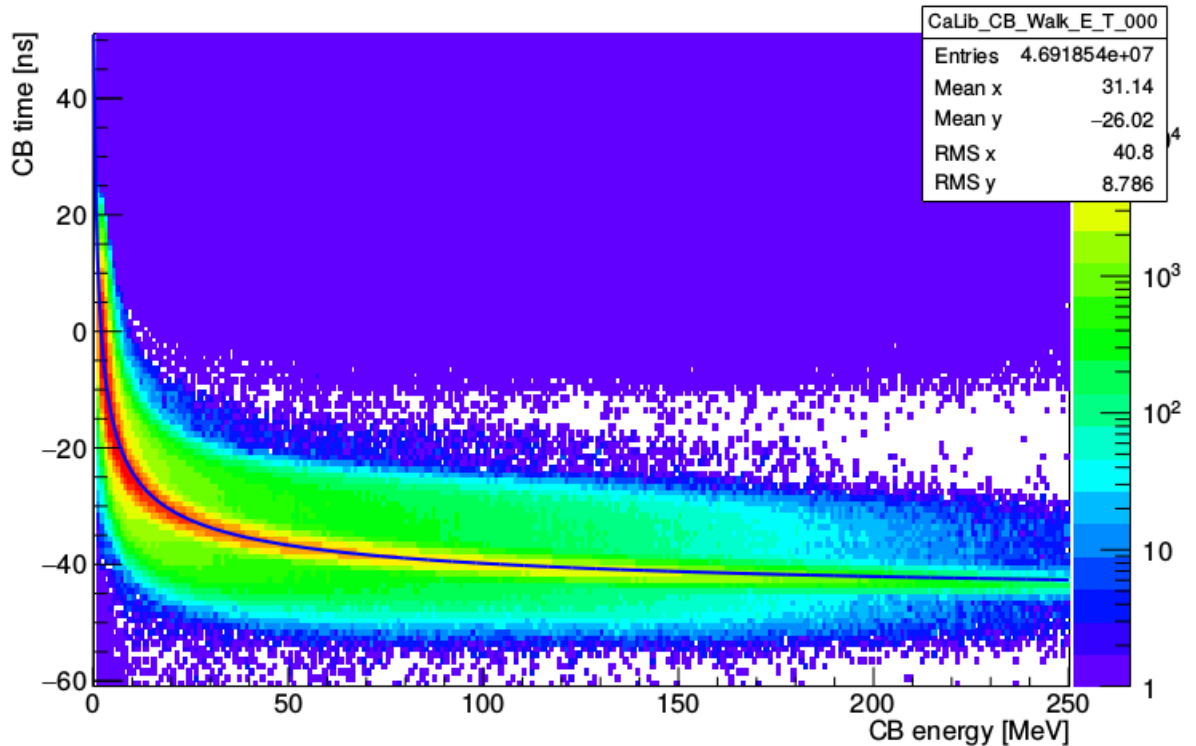
Figure 5.14: An example of a fit to the time walk. The deposited energy in the ball is plotted as a function of time. The time walk effect can be clearly observed.

correction has been performed, an improvement can be made and *a* can be adjusted until the elements are no longer shifted.

5.3.2 TAPS Timing Calibrations

A time walk calibration is not necessary for the TAPS TDCs as they used constant fraction discriminators which correct for the walk effect described previously. However, as they can be used for time of flight measurements due to the increased distance to the target than the crystal ball, an accurate timing calibration was warranted.

TDC Gain Calibration

The gains for the TDCs were obtained prior to the beamtime by using cabling with well known delays to retard the common stop signal of all the elements individually. TAPS measurements were then performed for increasing frequency of pedestal pulser. This pedestal position was determined for every TAPS measurement. A plot of the differences of these pulser pedestal

positions and the different delays were fitted and the gain determined from the slope of the fit. This process was repeated for all elements to give a gain for each.

TDC Offset Calibration

The remaining TAPS timing calibration is the TDC offset which is performed after the beamtime during the analysis phase. The same method was used as the time alignment calibration of the crystal ball. The time differences of elements in a cluster to the timing given by the central element were determined. These were fitted for each element and offsets obtained via equation 5.18. Again, it was performed iteratively until a convergence at zero was produced.

5.3.3 Tagger Timing Calibration

Similarly to the crystal ball, the conversion gain factors of the Tagger TDCs were fixed and so the calibration concerns only the offsets of the TDCs. A combination of a π^0 with a proton was selected by requesting two neutral clusters and a single charged cluster be present in the detectors. The time of the π^0 in TAPS was determined by taking the average time of any of the neutral clusters, assumed to be photons, present in the TAPS detector. An invariant mass cut of 120 to 150 MeV was applied to the reconstructed mass of the two neutral clusters to remove background and incorrect combinations. For every tagger channel the time difference of hits with respect to the time of the π^0 in TAPS was plotted as shown in Figure 5.15. Equation 5.18 was implemented again and new offsets were determined from the peaks in these distributions. The Tagger channels are independent of each other so a single iteration was sufficient.

5.3.4 PID Timing Alignment

The PID conversion gains are also fixed at 117 ps/channel so only the TDC offsets required adjustment. Events with two hits in separate PID elements were used and the time difference between these is plotted for the detector elements. For every detector element this spectra was fitted with a Gaussian and the offset value determined using equation 5.18. An example fit is shown in Figure 5.16. This was performed iteratively until the peak is aligned at zero for all
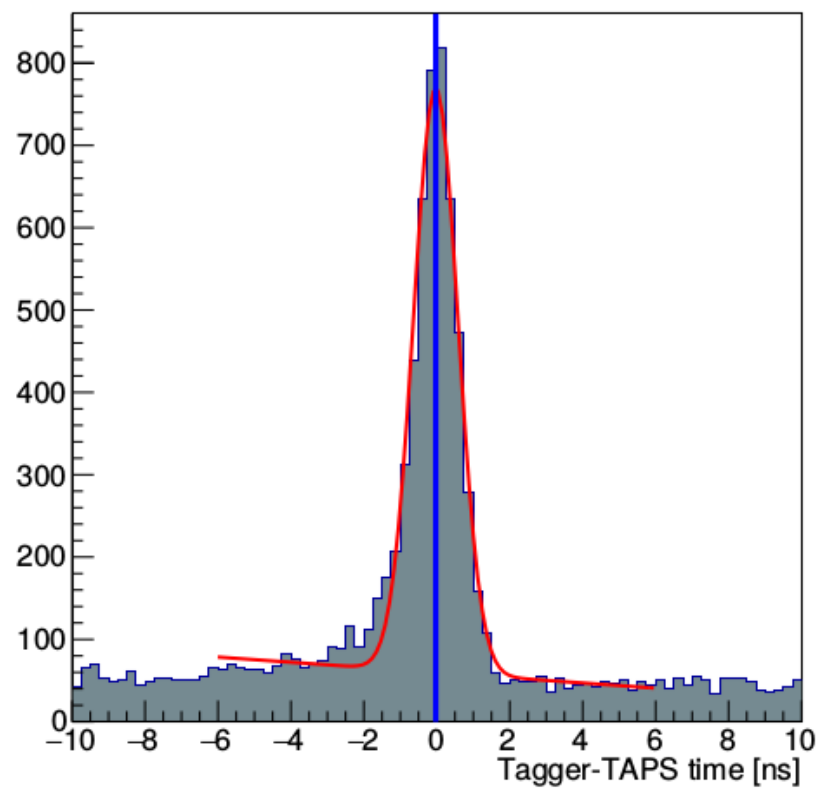
Figure 5.15: Fit of the coincidence timing between π^0 mesons detected in TAPS and hits in a tagger element.
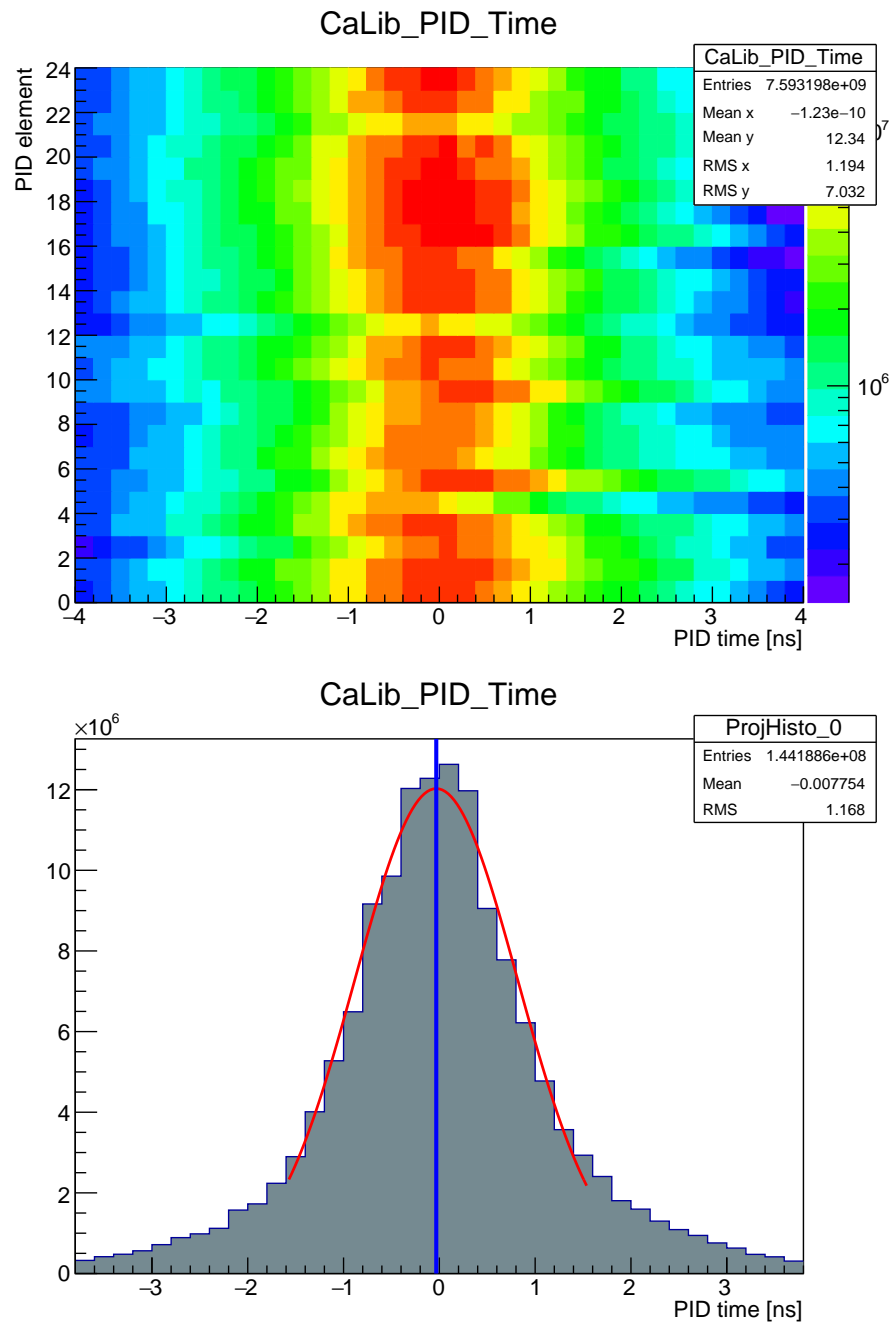
Figure 5.16: The lower plot shows a fit to the timing spectrum for a single PID element. In the plot above the alignment of all the elements can be seen.

elements.

5.3.5 TAPS Veto Timing Alignment

The Veto TDC gains were fixed at 50 ps/channel for all elements. The offsets were calibrated in the same manner as the PID using two charged hits, fitting the time difference spectrum and using equation 5.18 to determine the offset. This is performed iteratively until convergence around zero is achieved.

5.4 Additional Calibrations

5.4.1 PID-Crystal Ball Alignment

In order to identify charged particles the azimuthal angle of the PID scintillators has to be known in relation to the crystal ball. A charged particle passing through the PID and striking the crystal ball will have an azimuthal angle reconstructed in each of these detectors. By comparing the difference of these two, a charged event can be correlated with a cluster in the crystal ball. A new PID detector was installed for the August 2016 beamtime concerned in this work. The correlation for the new PID was determined using events with a single charged hit in the PID and a single cluster in the crystal ball. For each of the 24 scintillator elements this distribution was produced and a correlation peak was observed. This peak was fitted with a Gaussian to determine the azimuthal angle of each element. A fit of all of these extracted angles is then performed versus the PID element number. A linear fit was applied and the azimuthal angles for each element was extracted from the fit.

5.4.2 PID Light Attenuation Calibration

The following calibration was performed by Mikhail Bashkanov of the University of Edinburgh.

A particle will register a different amplitude of signal and hence energy depending on the location it struck along the length of the scintillator due to the PID having readout at one end via a PMT and the light attenuating as it travels the length to the PMT. To facilitate the calibration,

protons striking the PID were selected and E-ΔE histograms created for different angular bins. A function dependent on the energy deposited in the crystal ball and determined from Monte Carlo simulations was used to fit these histograms:

$$E_{PID} = f(E_{CB}) \tag{5.21}$$

The quantity $\frac{E_{PID}}{f(E_{CB})}$,sometimes referred to as droop factor, was determined for each angular bin and plotted against the length along the PID of that angular bin, L. L can be defined:

$$L = T_0 + V_0 + \frac{R_0}{\tan\theta} \tag{5.22}$$

where T_0 is the distance from the target centre to the lightguide, V_0 is the position of the event in the target along the z-axis, R_0 is the inner radius of the PID and θ is the polar angle. The plot of L versus the quantity $\frac{E_{PID}}{f(E_{CB})}$ was fitted with a straight line and the parameters above determined as shown in Figure 5.17. These parameters are tabulated in [96].

5.4.3   Linear Polarisation Calibration

A determination of the degree of linear polarisation of the incident photon beam for pion photoproduction experiments was required to reliably extract polarisation observables. Here the prescription detailed in [105] was followed. The polarisation of the beam is a product of the coherent bremsstrahlung reaction on a diamond radiator. The alignment of the internal crystal structure leads to coherent peak structures in the bremsstrahlung spectrum. The distribution of such structures can be highlighted by simply dividing the measured coherent, diamond spectrum by an incoherent, amorphous, spectrum to cancel the incoherent component of the diamond. This enhanced distribution, referred to as an enhancement spectrum from here on, was then fit to ascertain the degree of polarisation as a function of photon beam energy.

The position of the largest polarisation peak in terms of beam energy was tuned by making fine adjustments to the angle between the diamond and the electron beam. The strongest contributing reciprocal lattice vectors were fitted using a phenomenological fit intended to model
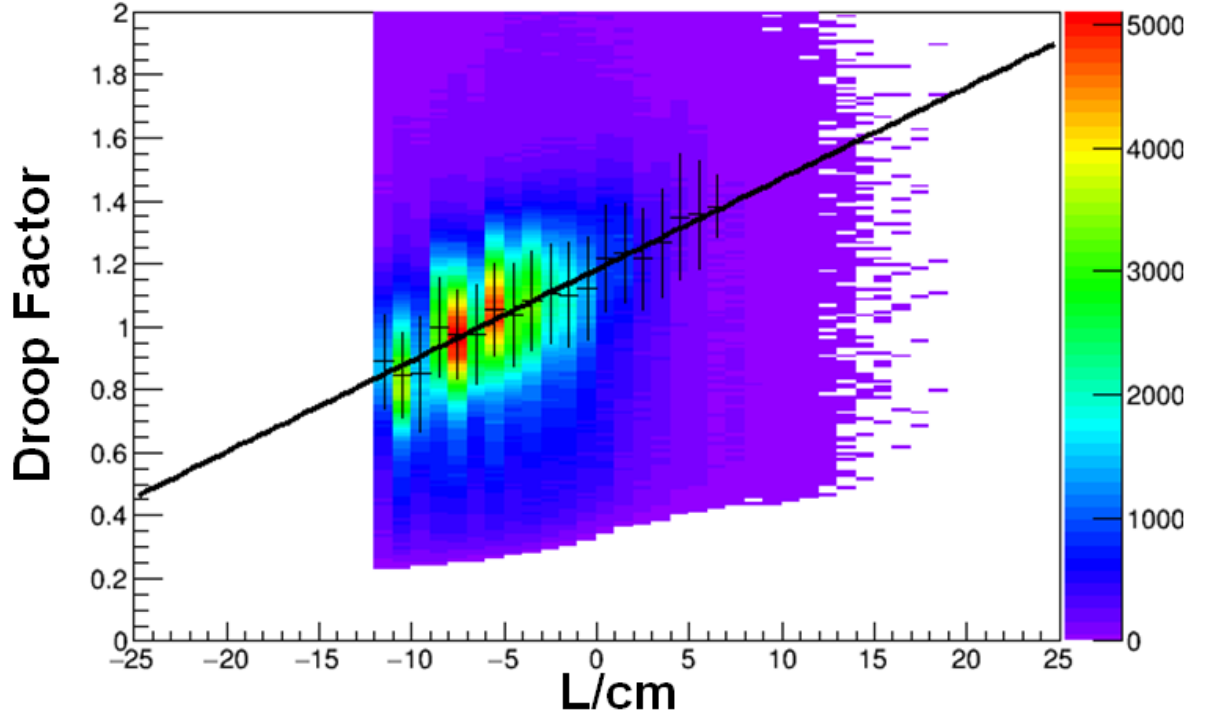
Figure 5.17: A plot of the quantity $\frac{E_{PID}}{f(E_{CB})}$ as a function of L with a fit to determine the attenuation factor.

the coherent contributions of these primary vectors. Each of the vectors were given five free fit parameters as illustrated in the enhancement spectrum shown in Figure 5.18. ϕ_r is the spread in θ_r, the opening angle of the collimator. These give the shape of the low energy side of the peak. ϕ is the distance from peak to θ. θ relates to the angle the beam makes with the lattice and is the point halfway down the edge. These two describe the shape of the sharp edge and I is the height of the peak maximum above the incoherent baseline. The enhancement spectrum was normalised by finding the five lowest consecutive bins and fixing their mean value to 1. The degree of linear polarisation was then extracted using equation 5.23.

$$P^s_{tot}(x,G,\theta,\sigma) = \frac{-\int_{\theta-3\sigma}^{\theta+3\sigma}\left\{e^{\frac{(\theta'-\theta)^2}{2\sigma^2}} \times \phi_{tot}(x,G,\theta') \times I_{coh}(x,G,\theta')\right\}d\theta'}{\int_{\theta-3\sigma}^{\theta+3\sigma}\left\{I_{total}(x,G,\theta') \times e^{\frac{(\theta'-\theta)^2}{2\sigma^2}}\right\}d\theta'} \tag{5.23}$$

where x is the photon energy, G represents the fitted lattice vector and σ is the Gaussian smearing of θ. I_{total} and I_{coh} refer to the intensities of the total bremsstrahlung distribution and
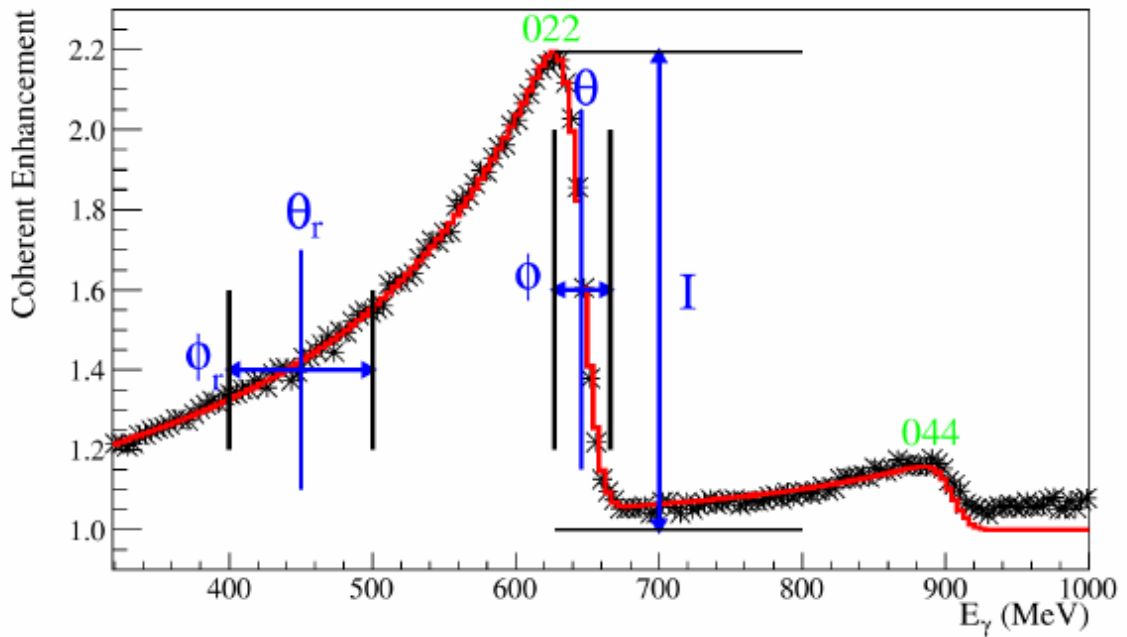
Figure 5.18: An enhancement plot with phenomenological fit in red and data in black. The five free fit parameters are in blue [115]. The lattice vectors for each peak are indicated in green.

the coherent distribution. The degree of linear polarisation with photon beam energy obtained via this method is shown in Figure 5.19. The polarisation was then assigned on an event by event basis given the photon beam energy for the event.

5.4.4   Linear Polarisation Uncertainty

The degree of linear polarisation discussed in Section 5.4.3 was obtained by dividing an experimental run using a diamond radiator from one with an amorphous radiator present. A baseline was chosen to normalise the spectrum so as to be able to determine the amount of enhancement provided by the diamond. The choice of the baseline is sensitive to the degree of linear polarisation as it is determined by a fit to the enhancement. The baseline was artificially adjusted by increments of 10% from the value used for the results presented here and the degree of polarisation extracted from fits to the new enhancement for each of these baselines. The results of this check are shown in Figure 5.20. At the polarisation peak position of 632 MeV an adjustment of 10% in either direction results in a 3% change in polarisation. At the peak of 54% this results in a percentage difference of 5% of the total. Larger discrepancies of the baseline are shown but
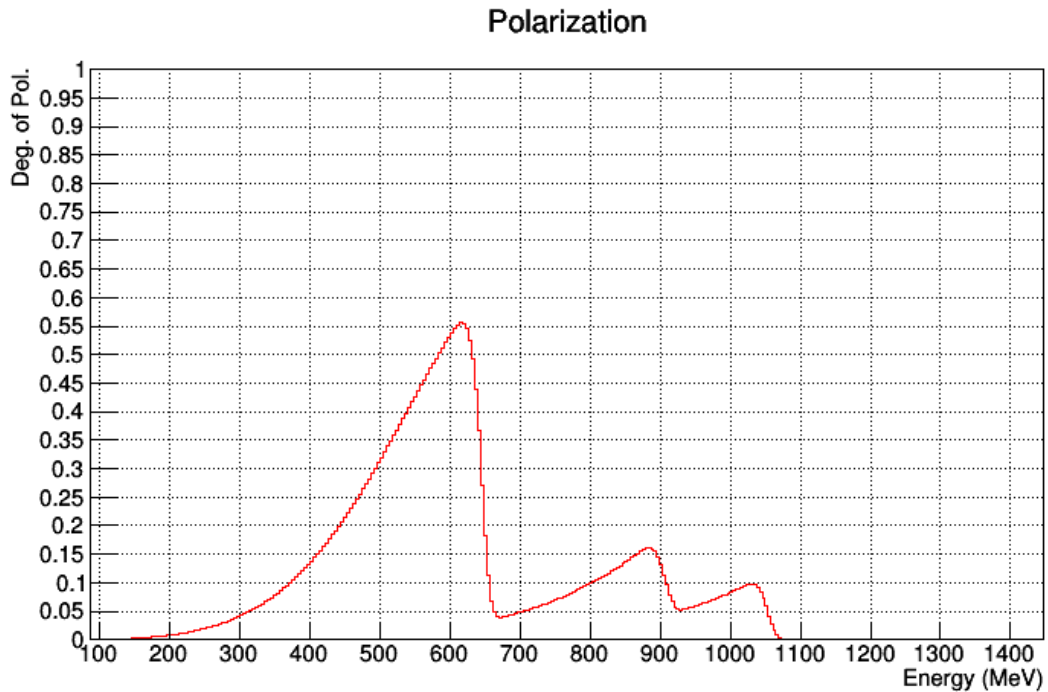
Figure 5.19: The distribution of the linear polarisation with photon beam energy for the beam-time showing a peak at 630 MeV of ~55%.

are unrealistic as would be more easily identifiable in the enhancement fits. The effect of this baseline change is more pronounced at lower polarisations as it determines the relative degree of polarisation from the enhancement fits. The higher order peak fluctuates to a larger degree than the main peak and so was not reliable enough to be used in this work. The quality of the fit to the enhancement provides another source of uncertainty to the linear polarisation. The systematic associated with this is estimated as 3% [116]. Some fits are shown in Figure 5.21.

In order to determine sources of uncertainty in the degree of linear polarisation an analytical calculation of the coherent bremsstrahlung was performed for a variety of different conditions. The known parameters for the beamtime were input to this calculation and the collimator radius varied. A change in collimator radius from 1.5 mm to 1.1 mm results in a sufficient change in the degree of polarisation to account for the discrepancy observed in the results with respect to Gardner et al as discussed in 7.5. This change is equivalent to a skewness of the collimator with respect to the beam momentum. Figure 5.22 shows the results of the analytical calculation for two different collimator sizes.

All the factors contributing to the uncertainty in the linear polarisation discussed in this
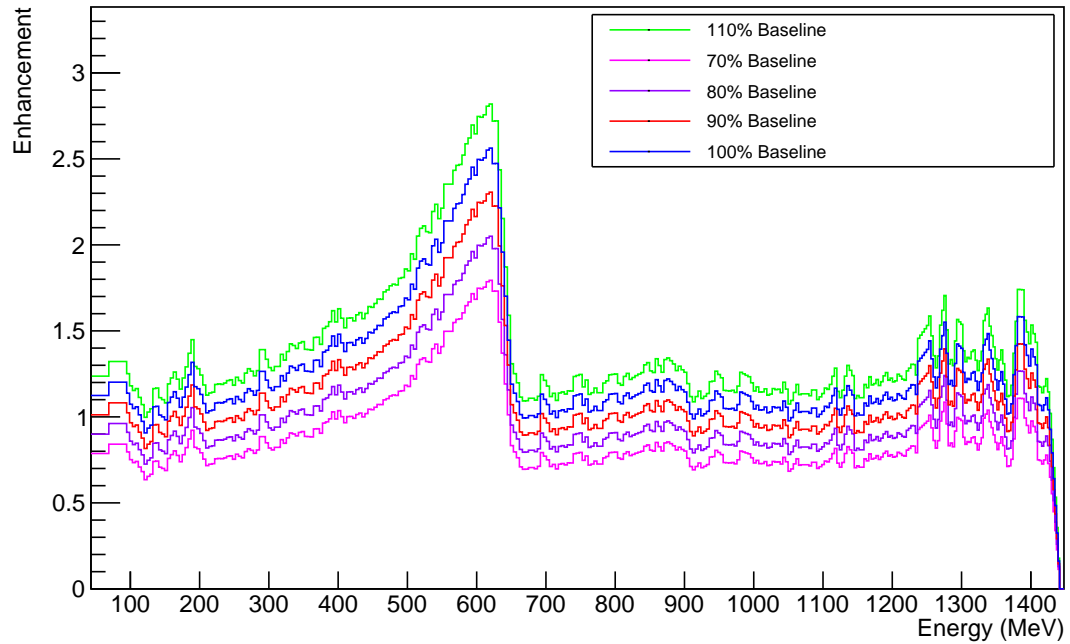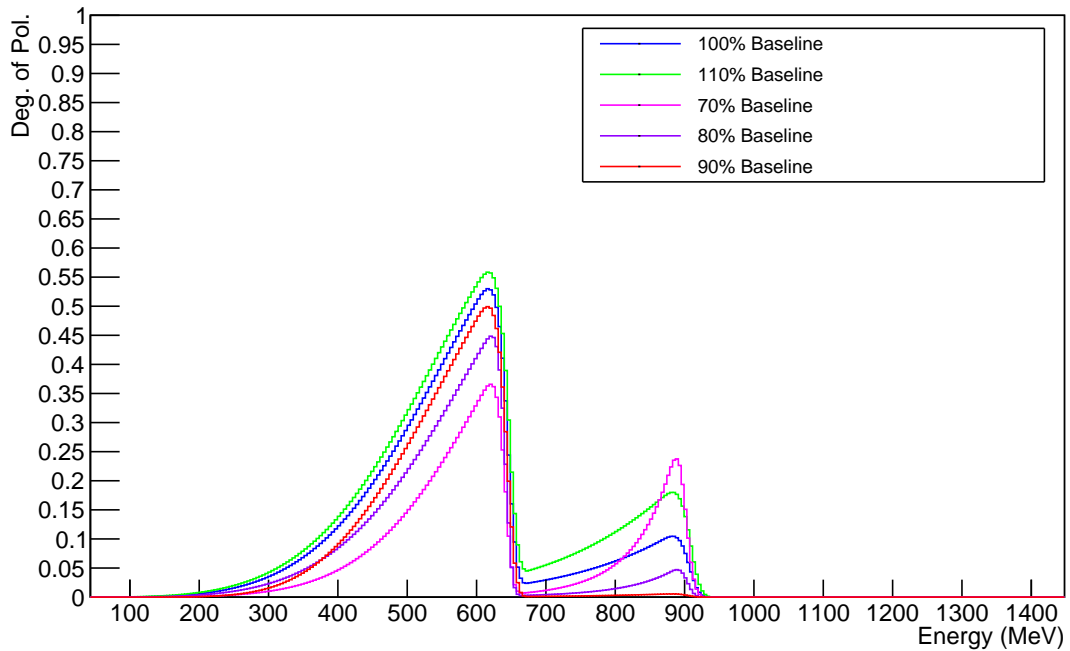
Figure 5.20: Alteration of the baseline in the enhancement(top). The degree of linear polarisation as a result of different changes to the baseline(bottom). The degree used in this work is listed as 100% and shown in blue. A change of 3% at the polarisation peak(630 MeV) is shown for a realistic change of $\pm$ 10% in the baseline.
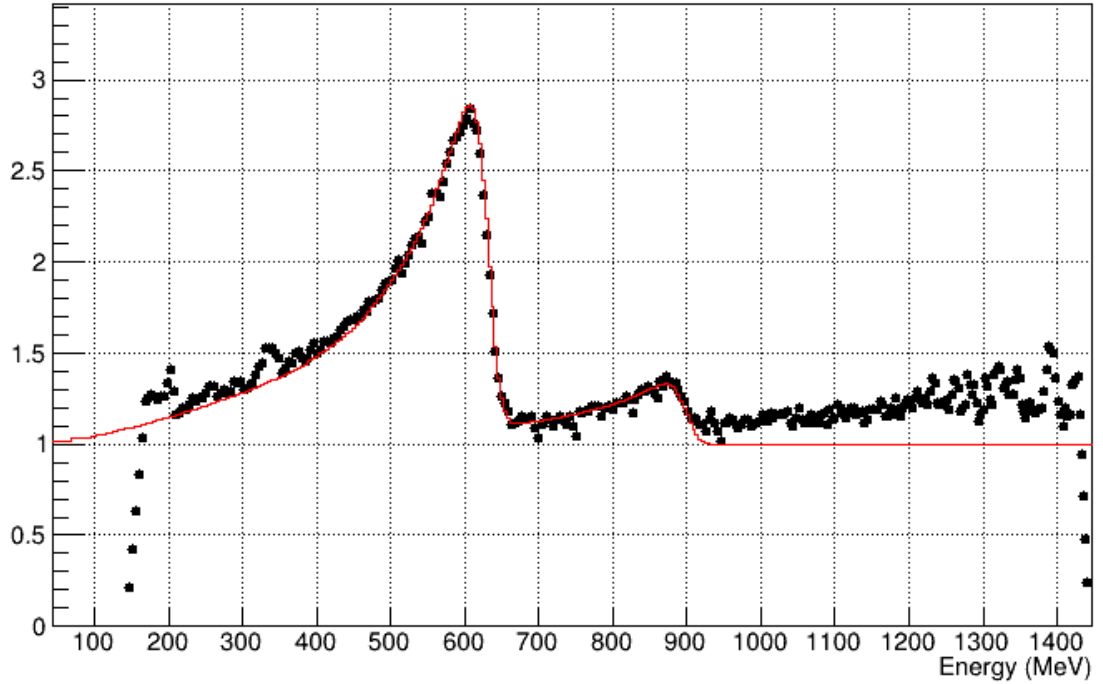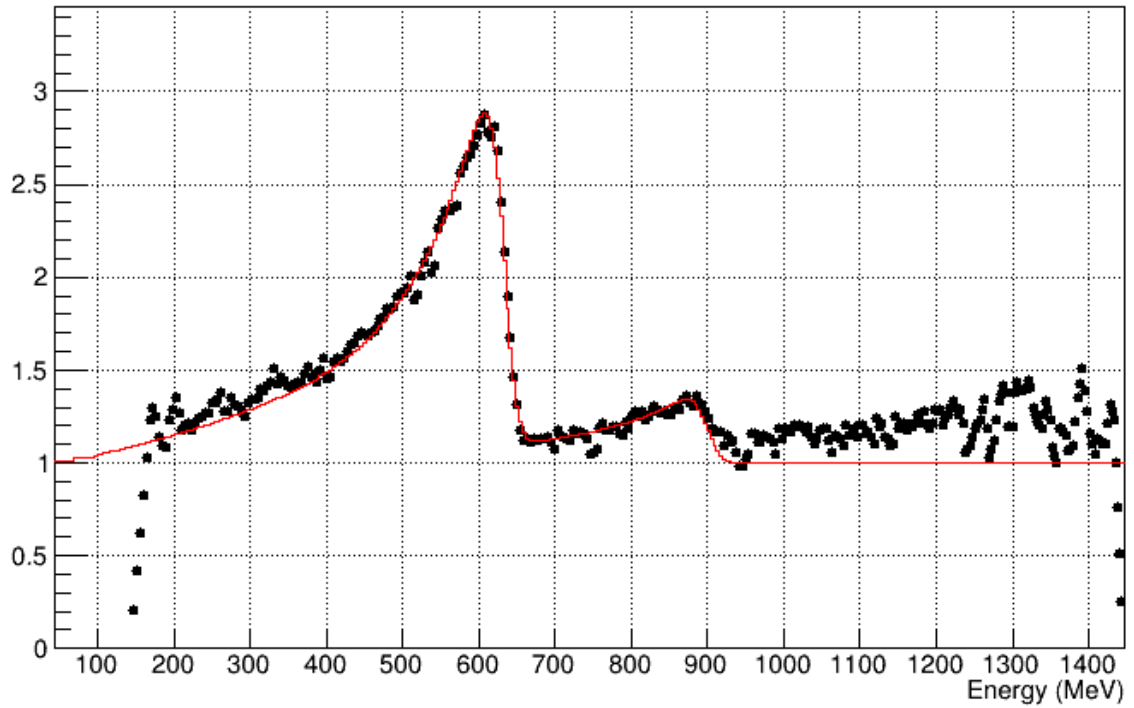
Figure 5.21: Examples of phenomenological fits to the enhancement showing the noisiness of the tagger at the lowest and highest energies.

Figure 5.22: An analytical bremsstrahlung calculation of the resultant photon beam polarisation for the conditions present at the A2 experimental facility. Two resultant enhancement and degree of linear polarisation plots for different sizes of collimator used. This corresponds to a skewness in the beam into the collimator. Parameters that could be altered in the calculation are listed with some typical values set.

section explain why the calibration of the degree of linear polarisation in Section 5.4.3 was off by around 10%. The correction factor applied to the results presented here accounts for these effects.

5.4.5   Circular Polarisation Determination

The resulting bremsstrahlung beam was also circularly polarised since the initial electron beam was longitudinally polarised. The degree of circular polarisation for a given photon, P_c, was calculated via [117]:

$$P_c = \frac{P_e E_\gamma (E_e + \frac{1}{3}(E_e - E_\gamma))}{E_e^2 + (E_e - E_\gamma)^2 - \frac{2}{3}E_e(E_e - E_\gamma)} \tag{5.24}$$

where P_e was the degree of longitudinal polarisation of the MAMI electron beam, E_e was the energy of the electron beam and E_γ was the energy of the produced photon.

P_e was determined using a Mott Polarimeter [118]. This device used the process of Mott scattering in which the asymmetry observed of an electron scattering from a gold foil into the $\pm$ $\hat{y}$ direction, polarised in the $\pm$ $\hat{x}$ direction is proportional to its degree of polarisation. That is to say, an asymmetry of electrons either side of the scattering plane for each helicity. The electron beam was rotated as it was initially polarised in the direction of its momentum. A Wien filter with specifically chosen fields was used for this purpose while not deflecting the beam. A Mott measurement was performed regularly throughout the beamtime and the results are detailed in Table 5.1. The degree of circular polarisation is shown in Figure 5.23.
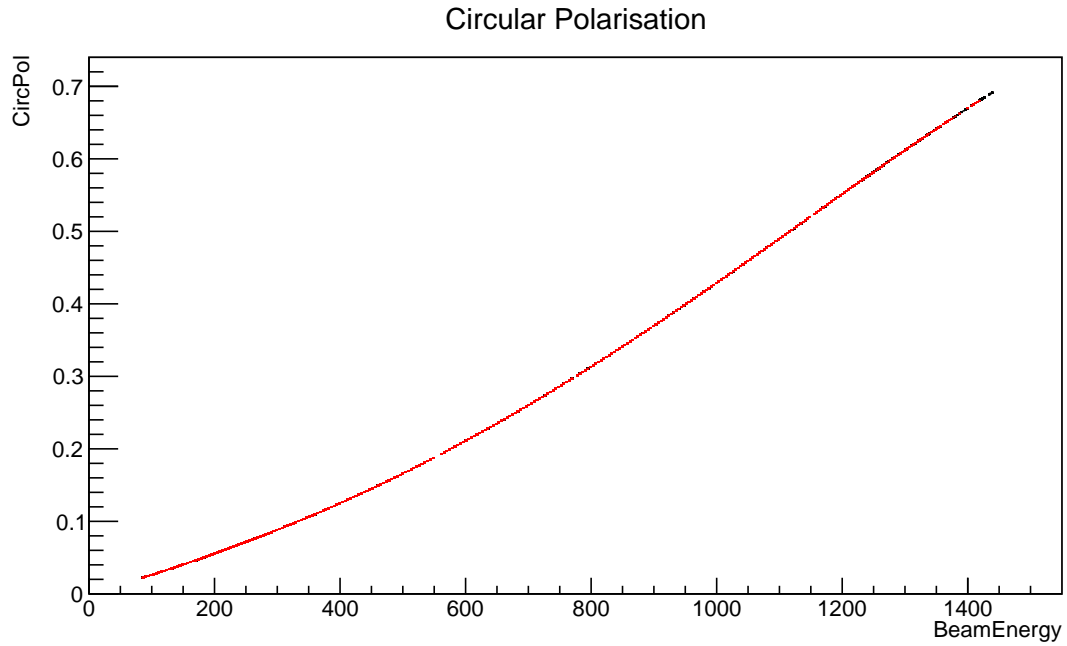
Figure 5.23: The circular polarisation for the range of beam energies for one electron beam polarisation measurement. Several missing tagger channels can be observed.

Date	P_e **With** $\frac{\lambda}{2}$ **plate(%)**	P_e **Without** $\frac{\lambda}{2}$ **plate(%)**
2/8/16	77.77±0.05	75.53±0.05
4/8/16	75.81±+0.05	76.79±0.05
6/8/16	75.85±0.05	76.64±0.06
8/8/16	76.20±0.05	77.06±0.05
10/8/16	76.49±0.05	77.30±0.05
12/8/16	77.01±0.06	77.72±0.05
19/8/16	77.50±0.06	77.68±0.06
22/8/16	77.53±0.07	77.20±0.08

Table 5.1: Table of the values of the mott measurements for the August 2016 beamtime. Note the half wave plate effectively flips the polarisation direction parallel and anti-parallel to the beam direction.

Chapter 6

Event Selection

This chapter details the analysis involved in determining single π^0 photoproduction events. The software packages used are describe in Section 6.1. The determination of candidate signal events given the reconstructed particles is explained in Section 6.2. A cuts-based analysis is detailed in Section 6.3 while a parallel analysis using the sPlots background subtraction method is covered in Section 6.4.

6.1 Software

Several software packages built on CERN ROOT [119] C++ libraries were used to analyse the data: AcquRoot [120], a framework designed for the A2 experimental hall detectors was used to read the raw signals from QDCs and TDCs and reconstruct particle 4-vectors as described in Chapter 5. GoAT(Generation of Analysis Trees) [121] is another A2 hall specific software package, which allowed faster processing and sorting of the data by skimming the dataset to select different channels and writing higher level particle information. The output files from GoAT, also in the form of ROOT trees, were subsequently analysed using the HaSpect [122] software package. The HaSpect software allowed for processing of large amounts of data quickly by utilising the CERN ROOT PROOF [123] framework. It allowed the construction of reaction observables and discriminatory variables associated with particles or reaction channels and provided an interface to the RooStats [124] implementation of the sPlot [125] fitting technique

detailed in Section 6.4.

6.2 Signal Determination

6.2.1 π^0p and π^0n Reaction Channels

The identification of the final states for the reaction channels, $\gamma D \rightarrow \pi^0 p(n_{spec})$ and $\gamma D \rightarrow \pi^0 n(p_{spec})$ was very similar. They both contain the same number of final state particles and as the π^0 decays to two photons and the low energy spectator nucleon did not typically have sufficient momentum to reach the calorimeters, only three particles were detected.

These final states were identified by first placing a restriction of 3 clusters registered in the calorimeters. Then to separate the proton channel a further requirement that one cluster must be charged was implemented by either having a coincidence with the PID or TAPS Veto detectors. Events that did not have such a coincidence were classed as production on neutrons. From this cluster selection an invariant mass for the two photon pair was constructed. For the detected neutron channel, where the neutron could not be distinguished from the two photons, the invariant mass was constructed for all three combinations of two particles. The invariant mass of a particle reconstructed from its two daughters was defined as:

$$M_{inv} = \sqrt{(\boldsymbol{p_1} + \boldsymbol{p_2})^2} = \sqrt{m_1^2 + m_2^2 + 2(E_1 E_2 - \vec{p_1} \cdot \vec{p_2})} \qquad (6.1)$$

where M_{inv} is the invariant mass, $\boldsymbol{p}_{1,2}$ is the 4-momentum of the particles and $\vec{p_{1,2}}$, $m_{1,2}$ and $E_{1,2}$ are the 3-momenta, mass and energy of the daughter particles respectively. For two photons with $m_\gamma = 0$ this simplifies to:

$$M_{inv} = \sqrt{2(E_1 E_2 - \vec{p_1} \cdot \vec{p_2})} \qquad (6.2)$$

For a π^0, the invariant mass will reconstruct to its mass of $\approx 135\,\text{MeV}$ within experimental resolutions. This is shown in Figure 6.1 for simulated data. The resulting π^0 4-vector then had its mass fixed to its known value by recalculating its momentum.
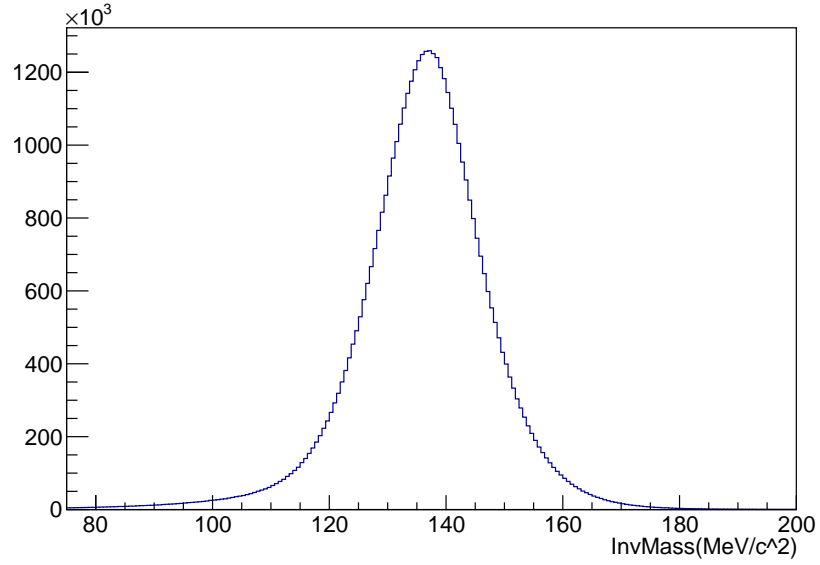
Figure 6.1: An invariant mass distribution from a reconstructed π^0 from two γ's for simulated data of the p π^0 reaction channel without cuts applied.

The identification of a π^0 allowed a missing 4-vector to be calculated from the 4-vectors of the beam, target and π^0. This was given by:

$$P_{missing} = \gamma_{beam} + D_{target} - P_{\pi^0} \tag{6.3}$$

γ_{beam} is the 4-vector for the beam photon detected in the tagger and associated with the event, D_{target} is the 4-vector of the deuterium target given by a stationary target with the mass of a deuteron and P_{π^0} is the 4-vector of the detected π^0. Calculating the mass of this 4-vector gave a peak at the mass of two nucleons corresponding to the spectator and participant with some extra energy from the Fermi momentum. The simulated spectra is shown in Figure 6.2.

The participant nucleon kinetic energy was calculated from the fully reconstructed 4-vector of the π^0, the beam energy, the polar and azimuthal angles of the participant nucleon and the masses of the target, spectator and participant. By defining the participant kinetic energy as T_P = E_P - m_P for the reaction γ D $\rightarrow \pi^0$ pn we can label one of the nucleons as the participant,
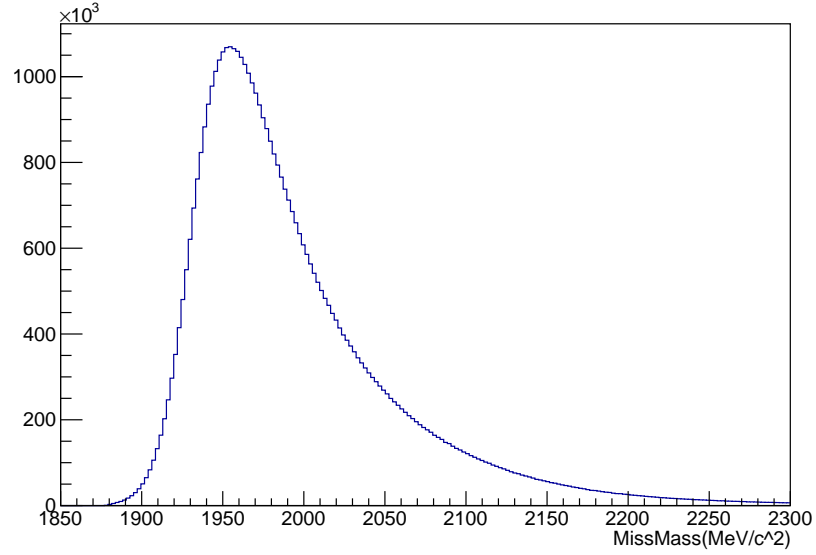
Figure 6.2: A missing mass distribution corresponding to the final state proton and neutron combination from simulated data of the p π^0 reaction channel.

denoted P, and the other as the spectator, denoted S. This allows the reaction to be written as:

$$\begin{pmatrix} E_\gamma \\ p_\gamma \end{pmatrix} + \begin{pmatrix} m_D \\ 0 \end{pmatrix} = \begin{pmatrix} E_{\pi^0} \\ p_{\pi^0} \end{pmatrix} + \begin{pmatrix} E_P \\ p_P \end{pmatrix} + \begin{pmatrix} E_S \\ p_S \end{pmatrix} \tag{6.4}$$

where E_X are the energies of each particle, p_X the momenta and m_X the masses. Using the measured polar and azimuthal angles of the participant the following parameters are defined:

$$a = p_{\pi^0,x} \sin\theta_P \cos\phi_P + p_{\pi^0,y} \sin\theta_P \sin\phi_P + (p_{\pi^0,z} - E_\gamma)\cos\theta_P \tag{6.5}$$

$$b = E_{\pi^0} - E_\gamma - m_d \tag{6.6}$$

$$c = (E_{\pi^0} + m_P - E_\gamma - m_d)^2 - (m_S^2 + p_{\pi^0}^2 + E_\gamma^2 - 2E_\gamma p_{\pi^0,z}) \tag{6.7}$$

The kinetic energy was detemined via:

$$T_P = \frac{-(bc - 2a^2 m_P) + \sqrt{(bc - 2a^2 m_P)^2 - c^2(b^2 - a^2)}}{2(b^2 - a^2)} \tag{6.8}$$
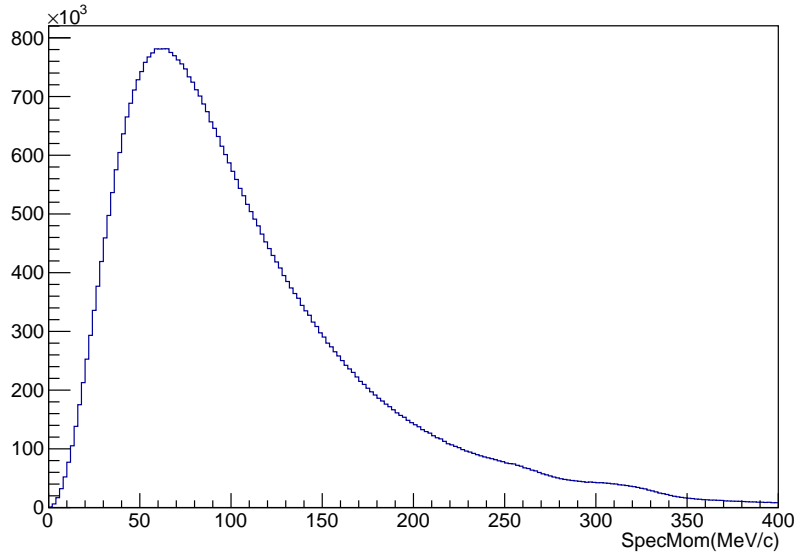
Figure 6.3: Spectator Momentum distribution corresponding to the undetected nucleon for p π^0 reaction channel from simulated data.

A more detailed analysis of this calculation can be found in [126].

The 4-vector of the participant nucleon was used to determine the spectators 4-vector via:

$$P_{spec} = \gamma_{beam} + D_{target} - P_{\pi^0} - P_{part} \tag{6.9}$$

where P_{spec} is the 4-vector of the spectator nucleon and P_{part} is the 4-vector of the detected participant nucleon. The momentum of the spectator was calculated and is shown in Figure 6.3, as this is simulated data this distribution is just the Fermi momentum distribution supplied in the event generator.

As the reactions were approximately two body, with a low momentum spectator, the π^0 and the participant nucleon were nearly coplanar in ϕ with some smearing from the Fermi motion. The coplanarity variable is introduced as:

$$\Delta\phi = \phi_{\pi^0} - (\phi_{part} - 180^\circ) \tag{6.10}$$

Here ϕ_{π^0} is the reconstructed azimuthal angle of the π^0 and ϕ_{part} for the participant nucleon. An example of simulated coplanarity for the $p\pi^0$ reaction is shown in Figure 6.4.

The detection of both the π^0 and the nucleon allowed the construction of the difference
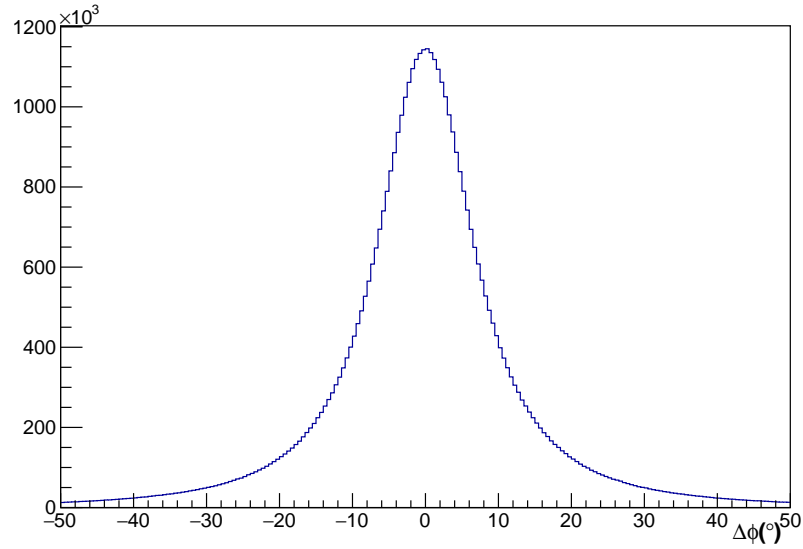
Figure 6.4: Coplanarity distribution for p π^0 reaction channel from simulated data. The signal gives a clear peak at 0°.

between the detected nucleon polar angle and nucleon polar angle reconstructed from the π^0 assuming a stationary nucleon target. This is referred to as the cone angle. A cone angle plot is shown in Figure 6.5. A peak at low angles shows where the reconstructed nucleon matches the detected nucleon and corresponds to the reactions of interest.

Finally the correct tagged photon was selected via the coincidence time between the π^0 in the calorimeter and the tagged photon was given by:

$$t_{\pi^0} = \frac{t_{\gamma_1} + t_{\gamma_2}}{2} - t_{tagger} \qquad (6.11)$$

where $t_{\gamma_{1,2}}$ are the times of the detected photons in the calorimeter and t_{tagger} is time of the electron detected in the tagger. If one photon was detected in TAPS and one in the CB then the TAPS time was taken as TAPS BaF2 crystals have better timing resolution. This timing distribution shows a distinct peak above a flat background corresponding to the tagger photon in coincidence with the detected particle in the calorimeter.
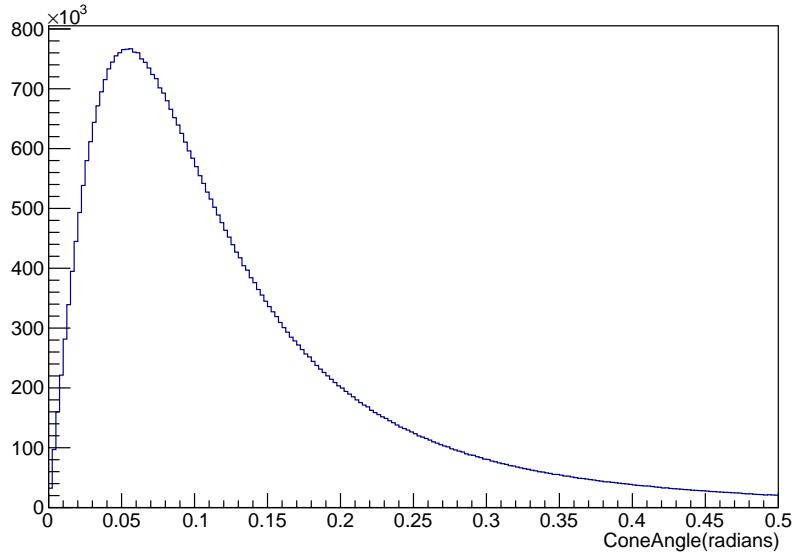
Figure 6.5: Cone Angle distribution for p π^0 reaction channel from simulated data.

6.3 Cuts-Based Analysis

To separate signal events from background a series of cuts to discriminatory variables was applied. The first cut is to remove background from the high rates in the photon tagger. A cut of -5<t_{π^0}<5 ns was applied as shown in Figure 6.8.The invariant mass region of 110 to 160 MeV/c^2 was selected by cuts to identify the π^0 in the reactions. The spectator momentum was used to select a region, less than 200 MeV/c where the participant-spectator model dominates as determined in [127]. Further cuts to cone angle, coplanarity, missing mass and spectator momentum were applied to isolate the signal region as seen in the simulation plots in Figures 6.1-6.5. The cuts were chosen using the distributions of simulated signal and background to maximise the signal to background ratio. A summary of these cuts is outlined in Table 6.1.

Variable	Cut Range	Units
Tagged Time	-5<t_{π^0}<5	ns
Coplanarity	-30<$\Delta\phi$<30	degrees
Missing Mass	1850<M_{miss}<2100	MeV/c^2
Cone Angle	0<θ_{Cone}<0.3	radians
Invariant Mass	110<M_{inv}<160	MeV/c^2
Spectator Momentum	0<P_{spec}<200	MeV/c

Table 6.1: A summary of the cuts applied to the data.

These discriminatory variables after cuts are shown in Figure 6.6 for the pπ^0 final state.

Channel	Percentage Contribution to background for $p\pi^0$	Percentage Contribution to background for $n\pi^0$
$p\eta$	0	0
$n\eta$	0	0
$p\gamma$	0.18	0
$n\gamma$	0.01	0.2
$p\pi^0\pi^0$	0.65	1.7
$n\pi^0\pi^0$	0.03	0.56
$p\pi^+\pi^-$	0	0
$n\pi^+\pi^-$	0	0
$p\pi^-\pi^0$	0.52	0.03
$n\pi^+\pi^0$	0.12	1.1
Total	1.51	3.6

Table 6.2: A table of the different backgrounds contributing after the cuts have been applied as a percentage of the signal remaining, as determined from simulations.

For the $n\pi^0$ final state Figure 6.7 shows the variables after cuts. In order to determine the effectiveness of the cuts in removing the background, a selection of background channels were simulated and propagated through the analysis chain. These channels are listed in Table 6.2 with the contribution of each as a percentage of the simulated signal and corrected for the respective cross-sections. A clean signal is obtained for both channels.

6.3.1   Sideband Background Subtraction

A random background of tagged photons remains after application of the coincidence cut. This background, present under the peak, derives from random electrons in the tagger and only one electron within the event time window will have been the one to produce the photon that interacted in the target. Under the assumption that these uncorrelated hits were uniform in time, this background was corrected for by subtraction of sideband events. Two regions in the timing spectra were selected to be representative of this background. These were -30 to -20 ns and 20 to 30 ns and will be referred to as the random intervals henceforth. In the further analysis histograms were filled with a weight of one for the prompt interval of -5 to 5 ns and a weight of -0.5 for both the random intervals. The number of signal entries, N_s per bin was therefore given by:

$$N_s = N_p - 0.5 N_r \qquad (6.12)$$

where N_p is the number of prompt entries and N_r is number of random entries. The regions selected for this are illustrated in Figure 6.8, after the application of the other cuts. The random
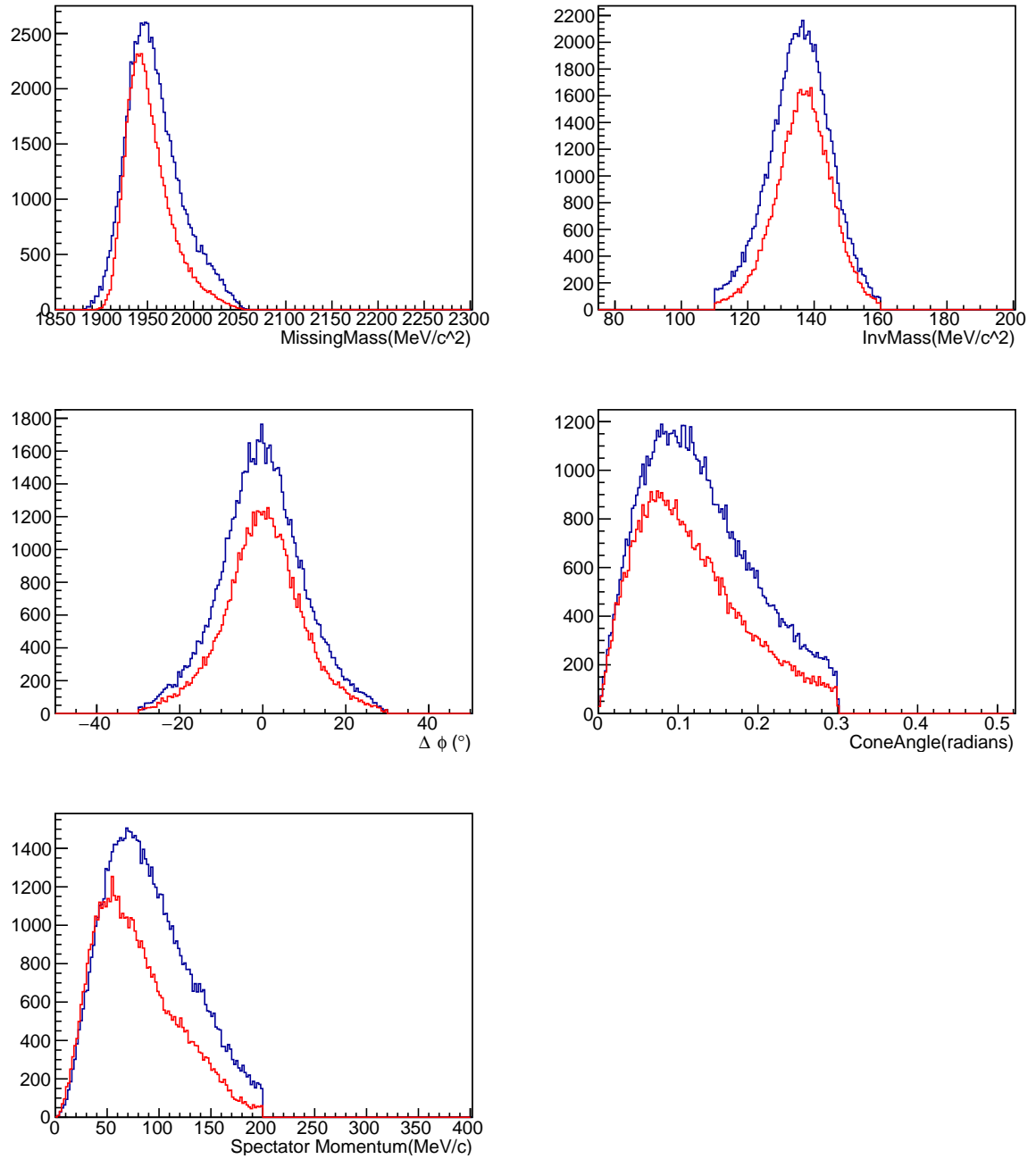
Figure 6.6: The discriminatory variables for the proton π^0 final state reaction channel with cuts applied and a sideband background subtraction performed as detailed in Section 6.3.1 for the experimental data in blue. The simulated data is shown in red with the same cuts applied.
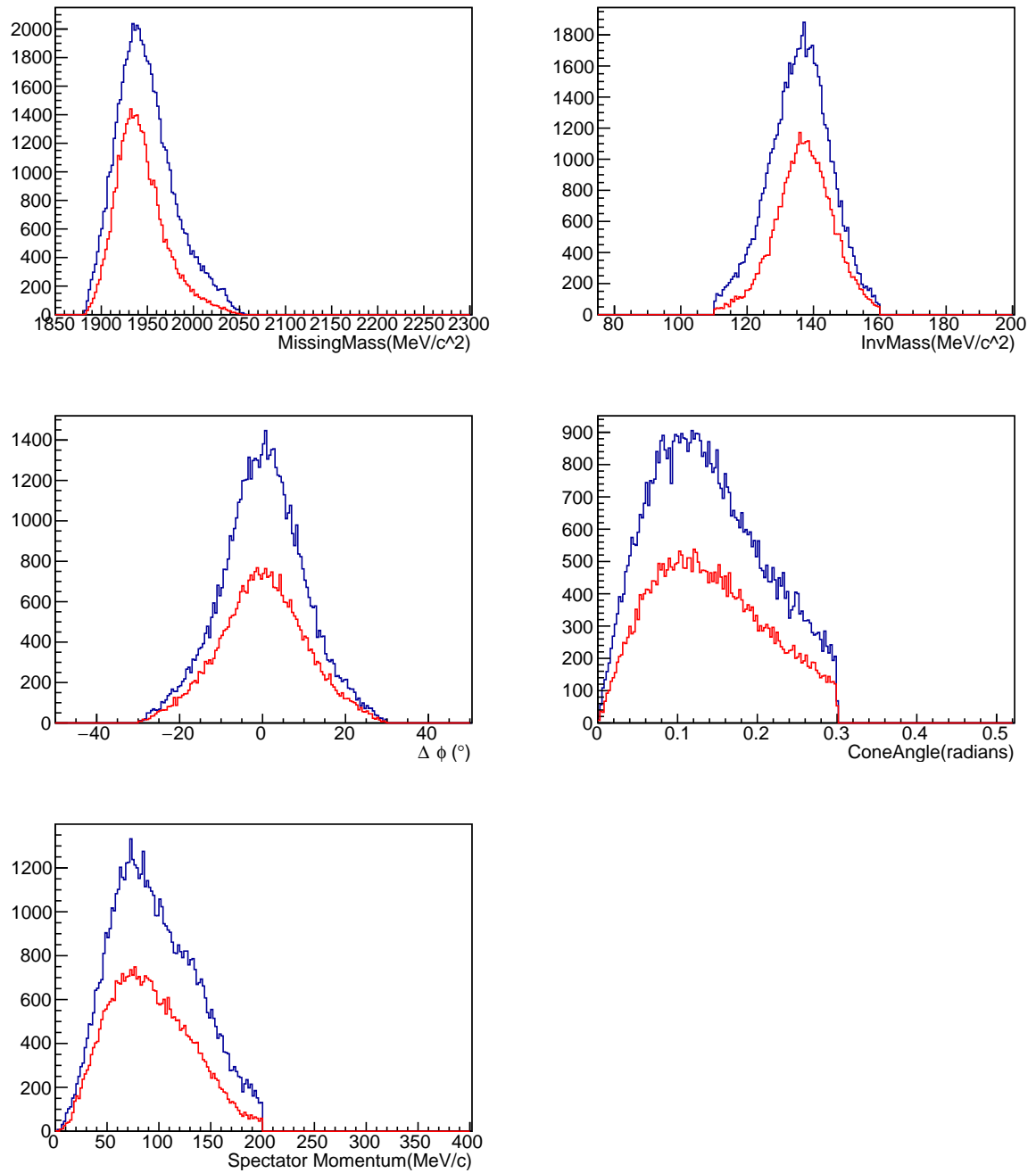
Figure 6.7: The discriminatory variables for the neutron π^0 final state reaction channel with cuts applied and a sideband background subtraction performed as detailed in Section 6.3.1 for the experimental data in blue. The simulated data is shown in red with the same cuts applied..
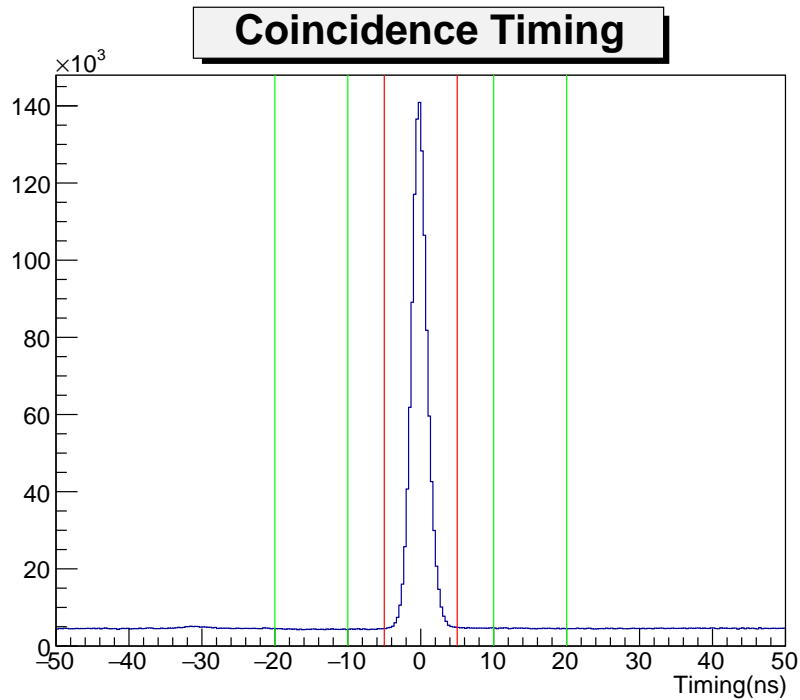
Figure 6.8: The coincidence timing between the photon hit in the tagger and the meson detected in the crystal ball or TAPS. A strong peak is observed corresponding to events of interest above a flat background corresponding to random photons in the tagger. The red lines indicate the selected prompt region for the cuts-based analysis and the random regions used for background subtraction are indicated by the green lines.

regions denoted by the green lines and the prompt by the red. After applying the cuts and subtracting the tagger random background the data gives essentially clean π^0 photoproduction events for further analysis.

6.4 sPlot Analysis

A cuts-based analysis requires a prominent peak to distinguish the signal from background; may leave a sizeable amount of background particularly underneath the peak; and may remove a sigificant fraction of signal events. A more optimised method is the sPlots technique which can be used to disentangle different event species such as signal and background using event-by-event weights, sWeights [125]. In this work, consecutive fits using these sWeights were performed. Initially a fit to the timing spectra to separate the random tagger events from prompt signal events was performed. A second fit was performed on the two photon invariant mass to

select final states with a π^0, with the signal weights from the timing fit. Finally, a fit of the coplanarity variable was performed after applying the weights produced from the previous fits to provide weights to select the single π^0, nucleon events.

6.4.1 sPlot Formalism

The sPlot technique aims to separate a dataset into the different sources of events. The variables associated with these events can be classed in one of two ways: a discriminatory variable is one in which the distribution of all event sources is known; a control variable in which some distributions are unknown and we are interested in. The technique aims to use the discriminatory variables to construct the distribution of the control variable for different sources of events. This assumes that the control and discriminatory variables are uncorrelated. In this analysis, a discriminatory variable would be invariant mass and a control variable would be the azimuthal angle, ϕ.

Let us consider the log-likelihood for a dataset in which several species of events are present:

$$\ln \mathscr{L} = \sum_{e=1}^{N} \ln \left\{ \sum_{i=1}^{N_s} N_i f_i(y_e, p) \right\} - \sum_{i=1}^{N_s} N_i \tag{6.13}$$

where N is the total number of events in the data sample, N_s is the number of species of events populating the data sample, N_i is the number of events expected on average for for the ith species, y is the set of discriminating variables, f_i is the probability density function(PDF) of discriminating variables for the ith species and $f_i(y_e)$ is the value the PDF takes for event, e, at y_e and p are the free parameters of the fit. The log likelihood is described by the yields of each of the species populating the data sample and the free parameters associated with the PDFs of the discriminating variables. The yields of each species of event can be determined by maximizing equation 6.13. The inverse of the covariance matrix is then given by the second derivative of $-\mathscr{L}$:

$$V_{nj}^{-1} = \frac{\partial^2 (\ln(-\mathscr{L}))}{\partial N_n \partial N_j} = \sum_{e=1}^{N} \frac{f_n(y_e, p) f_j(y_e, p)}{(\sum_{k=1}^{N_s} N_k f_k(y_e, p))^2} \tag{6.14}$$

If the control variable is uncorrelated with y, i.e. it does not belong to the set y, the appropriate weight to produce distributions corresponding to species n is the sWeight, which depends on the

fit covariance matrix:

$$
{}_sP_n(y_e, p) = \frac{\sum_{j=1}^{N_s} V_{nj} f_j(y_e, p)}{\sum_{k=1}^{N_s} N_k f_k(y_e, p)}
\tag{6.15}
$$

Using equation 6.15 it is possible to disentangle the dataset into its contributing sources. The sWeights are not probabilistic weights and hence are not restricted to the range 0 to 1. This method has two other properties worth noting: the sum of the species for a given event in each bin must be equal to one;

$$
\sum_{l=1}^{N_s} {}_sP_l(y_e, p) = 1
\tag{6.16}
$$

and the sum of the weighted events of a species is equal to the calculated yield of the species.

$$
\sum_{e=1}^{N} {}_sP_n(y_e, p) = N_n
\tag{6.17}
$$

In general the calculation of the sWeights is a two step process, first the free parameters in the species PDFs are determined from an extended maximum likelihood fit to all variables, then all free parameters apart from the species yields are held constant and a second fit is performed to determine the covariance matrix in equation 6.14.

6.4.2 Timing Fit

For each event all tagger photons were used to create possible sub-events of which at most one could correspond to an event with the correct tagger photon. The background sub-events were then subtracted using sWeights on an event-by-event basis. Prior to performing any of the fits a series of loose cuts were applied to the variables defined in Section 6.2 to skim the data. These cuts are detailed in Table 6.3.

Variable	Cut Range	Units
Tagged Time	$-80 < t_{\pi^0} < 20$	ns
Coplanarity	$-50 < \Delta\phi < 50$	degrees
Missing Mass	$1850 < M_{miss} < 2300$	MeV/c^2
Cone Angle	$0 < \theta_{Cone} < 0.5$	radians
Invariant Mass	$80 < M_{inv} < 200$	MeV/c^2

Table 6.3: A summary of the loose cuts applied to the data before the sPlots fits.

Probability distributions functions for both the signal and background were required to fit the

timing distribution. As the background was flat for all kinematic regions, a 1st order Chebychev polynomial was sufficient for describing its contribution. For the signal shape, a Gaussian PDF was used. Each distribution had some free parameters associated with it as shown in Figure 6.9. For the Gaussian the width and peak position were allowed to vary. The weights for each event were calculated using equation 6.15 and the signal distributions, corresponding to the correct photon in combination with the interaction in the target, were determined using these weights.

6.4.3 Two γ Invariant Mass Fit

To discriminate between signal events and events which do not have a π^0 present, or incorrect combination of the 3 neutral clusters in the case of the $n\pi^0$, a fit to the two γ invariant mass was used. Simulations of the final state of interest, either $p\pi^0$ or $n\pi^0$, were used to produce the signal PDFs. This PDF allowed flexibility through an offset in the fitting variable axis, a scaling of the PDF along the fitted variable axis and a Gaussian smearing that allowed for some additional convoluted resolution. A second order Chebychev polynomial was used to represent the background contribution. The sWeights calculated from the fit to timing spectra were applied to the data before the invariant mass fit was performed. An example fit for each final state channel is shown in Figure 6.10

The peak at the mass of a π^0 was clearly observed and a good separation of signal and background events obtained. The sWeights for each contribution were again calculated using 6.15.

6.4.4 Coplanarity Fit

At this stage we have an event sample with clean beam photon and a π^0. Next we must remove events from multi-pion production and that were produced on non-deuterium target material. To exclude these additional backgrounds within the timing coincidence window and having a reconstructed invariant mass of the π^0 mass, a fit to the coplanarity between the π^0 candidate and the nucleon was performed. The signal PDF was provided by simulations of the final state of interest. A second order polynomial was used for the background PDF. A fit of the coplanarity
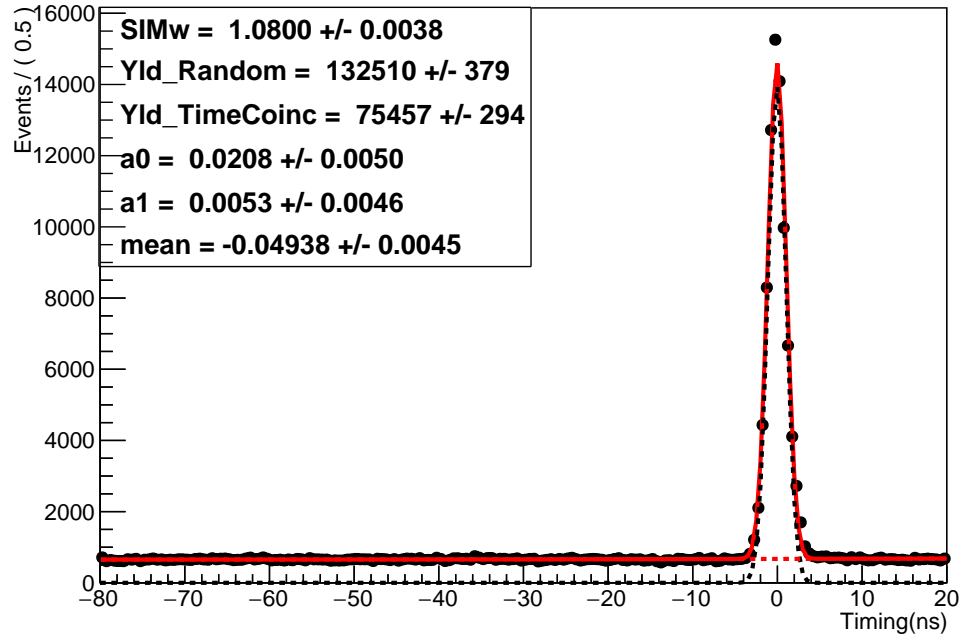
(a) Coincidence Timing Fit Proton Channel
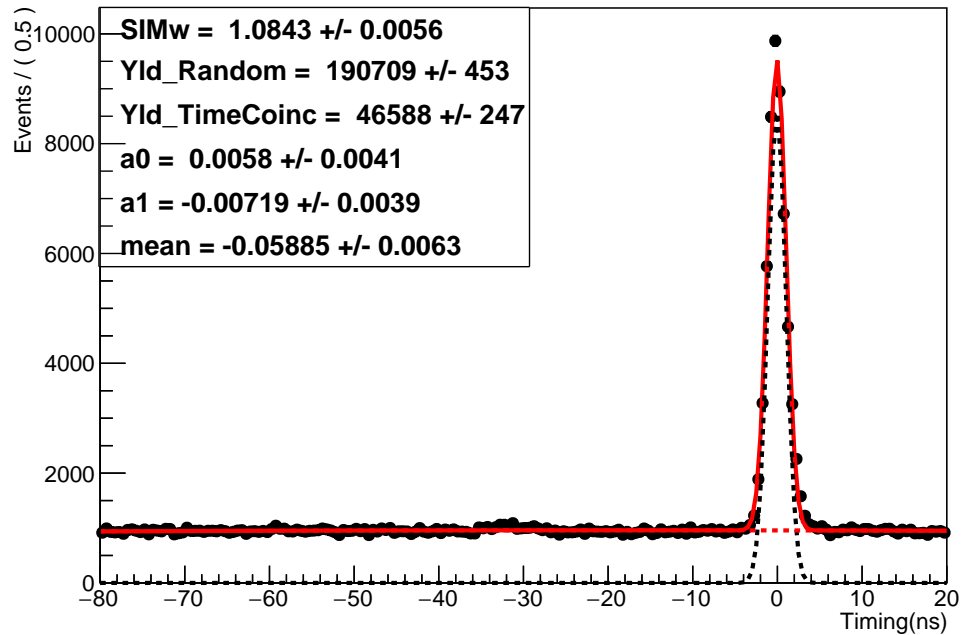
(b) Coincidence Timing Fit Neutron Channel

Figure 6.9: An sPlot fit of the coincidence timing for each final state reaction channel using a Gaussian signal shape, black dashed line, and a Chebychev polynomial, red dashed line, for the background shape. A good agreement with the production data, black dots, was reached as shown by the overall fit via the solid red line. The number of events determined by the fits for each species, random and signal(TimeCoinc), are listed in the statistics box. Parameters a0 and a1 are the coefficients of the Chebychev polynomial; mean and SIMw are the Gaussian mean and width; and Yld_Random and Yld_TimeCoinc are the summed yields of the background and peak respectively.
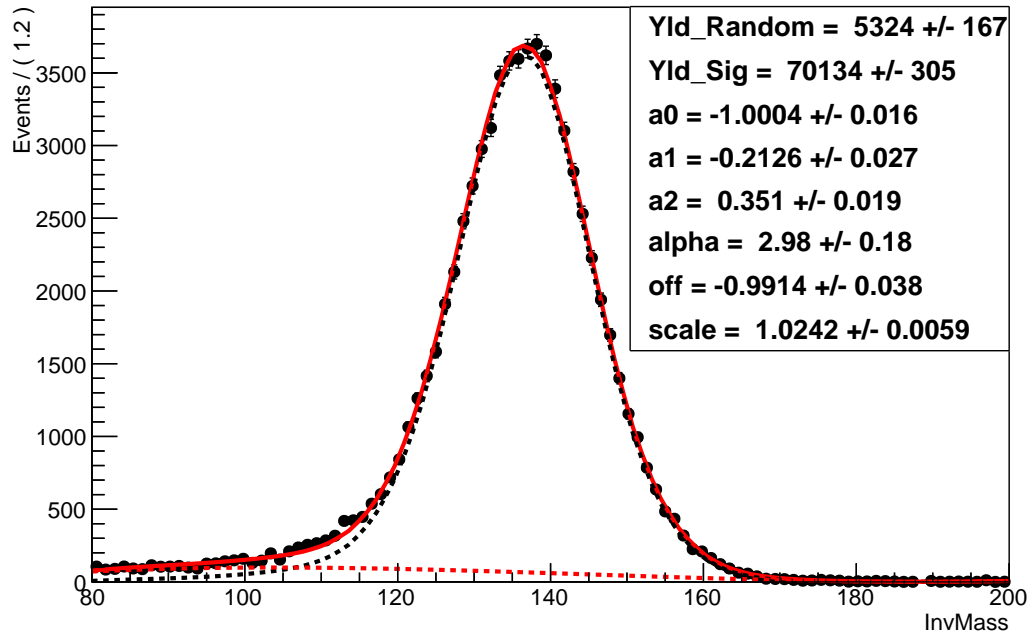
(a) Invariant Mass Fit Proton Channel

(b) Invariant Mass Fit Neutron Channel

Figure 6.10: An sPlots fit of the invariant mass of the meson for each final state reaction channel. The signal PDF shape was taken from simulations of the final state reaction channel. The background was provided by a Chebychev polynomial. A good agreement with the production data, black points, was obtained. Once again, the dashed black line is the signal shape, the dashed red line is the background shape and solid red line is the overall fit. Yld_Signal and Yld_Random are the summed yields of events with and without a π^0 present respectively. Parameters a0-a2 are the parameters of a second order Chebychev polynomial. Offset is a parameter describing any offset between the experimental data and the simulated data used to construct the signal PDF. The scale allows for a scale factor to be applied to the x-axis and alpha for a convolution with a gaussian width for the simulated data.

is shown in Figure 6.11.

The resultant discriminatory variables after the signal weights from the subsequent fits have been applied are shown in Figure 6.12 for the proton π^0 final state channel. For the nπ^0 final state Figure 6.13 shows the variables after signal weights have been applied.

Fit components for Coplanarity

Yld_Random = 6869 +/- 453
Yld_Sig = 63271 +/- 375
a0 = 0.045 +/- 0.014
a1 = -0.300000 +/- 0.00015
alpha = 0 +/- 11
off = -0.1276 +/- 0.029
scale = 0.904 +/- 0.045
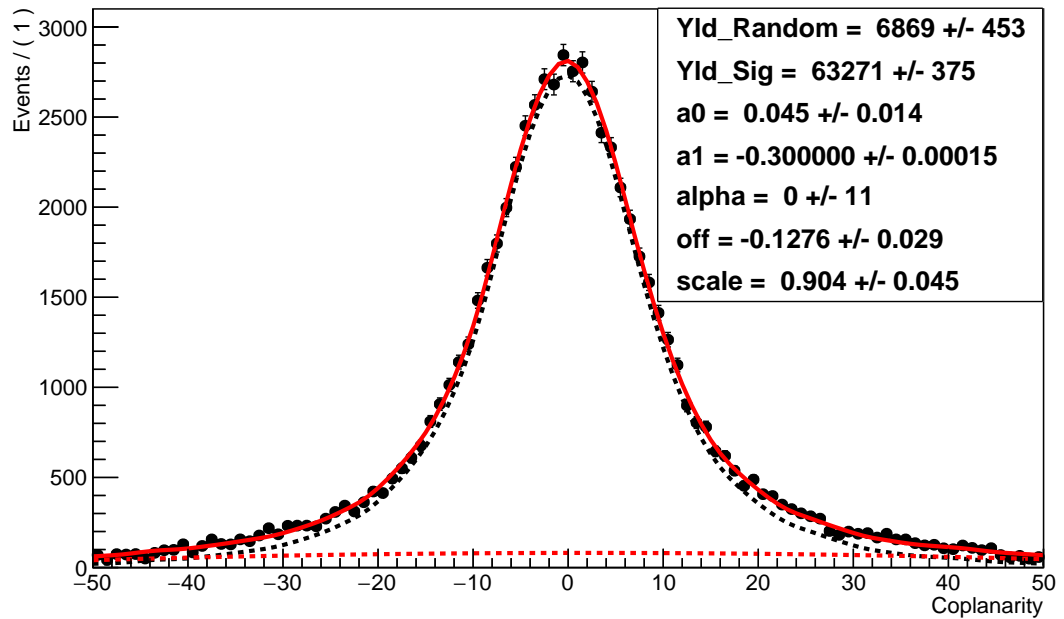
(a) Coplanarity Fit Proton Channel

Fit components for Coplanarity

Yld_Random = 4167 +/- 399
Yld_Sig = 38277 +/- 440
a0 = -0.0073 +/- 0.034
a1 = -0.300 +/- 0.21
alpha = 0.0 +/- 1.2
off = 0.084 +/- 0.066
scale = 1.118 +/- 0.020
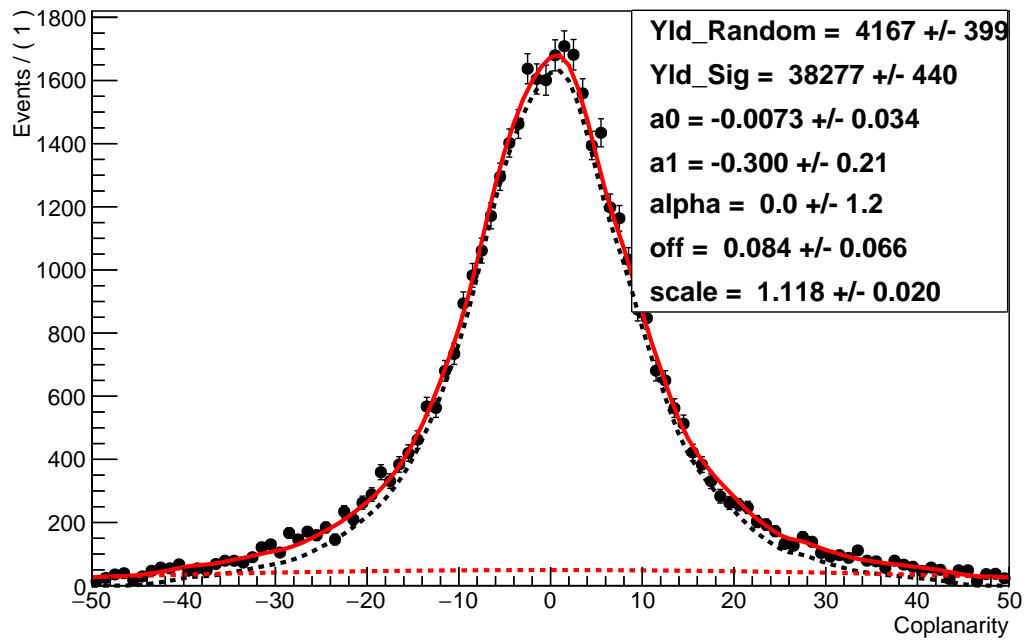
(b) Coplanarity Fit Neutron Channel

Figure 6.11: The final sPlots fit, to the Coplanarity variable, using the sWeights derived from the previous two fits. Once again, the dashed black line is the signal shape, the dashed red line is the background shape and solid red line is the overall fit. The signal shape is taken from simulations and the background modelled as a Chebychev polynomial. A good agreement with the data is clear. The parameters are the same as in 6.10.
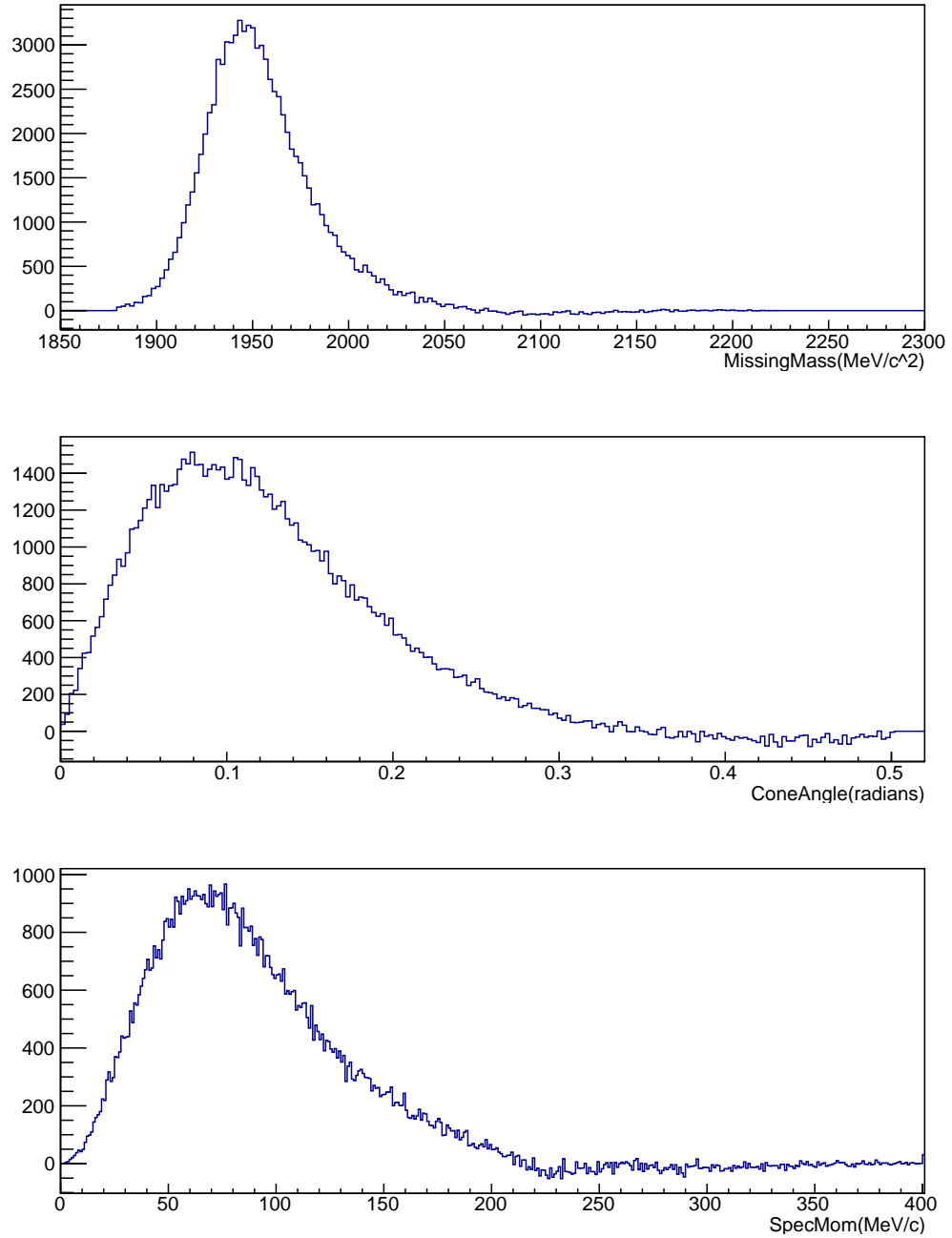
Figure 6.12: The discriminatory variables for the proton π^0 final state reaction channel with sWeights applied to experimental data.
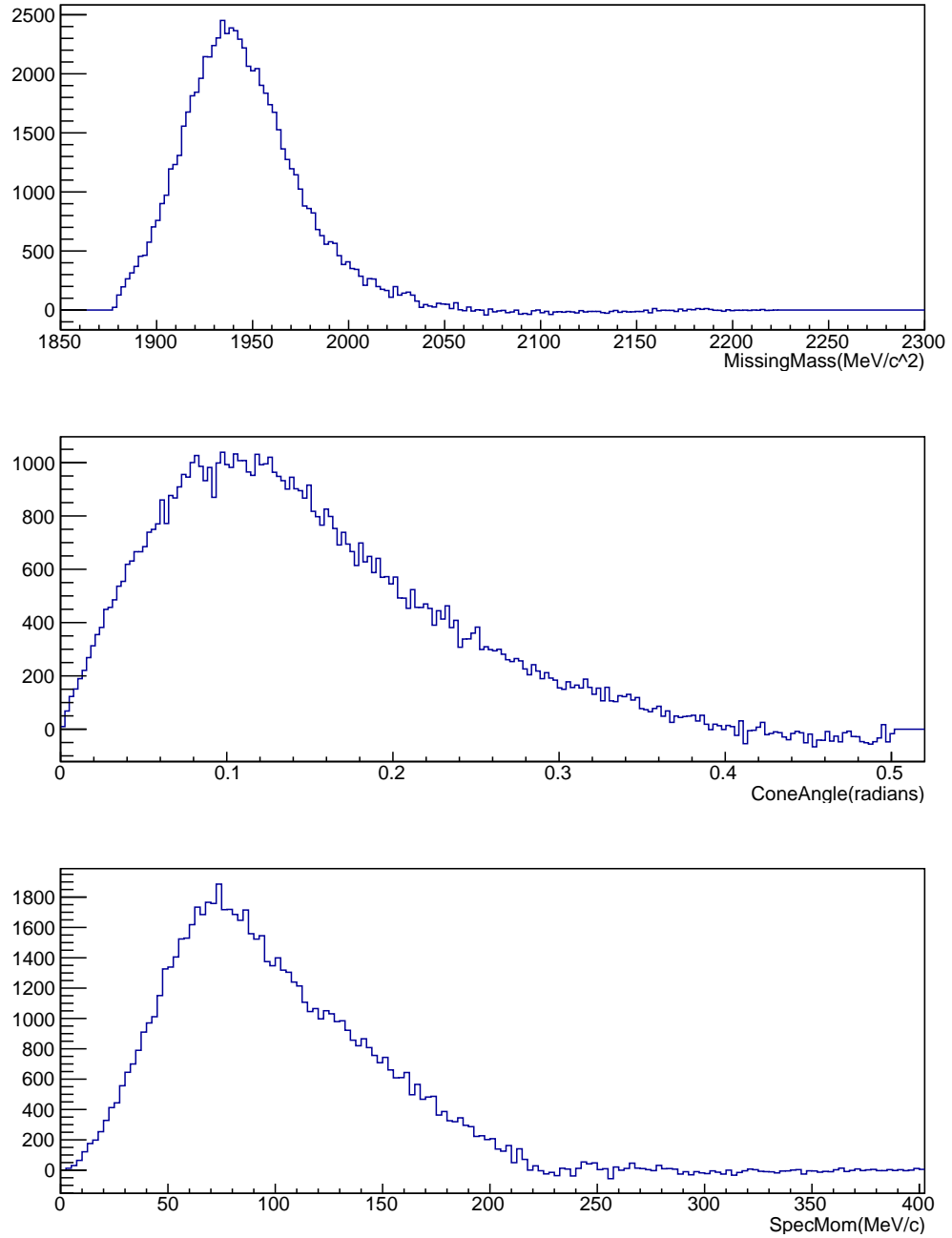
Figure 6.13: The discriminatory variables for the neutron π^0 final state reaction channel with sWeights applied to experimental data.

Chapter 7

Observable Extraction

7.1 Histogram Fit

The polarisation observable, Σ, sometimes referred to as the photon beam asymmetry, represents the effect of the polarisation of the beam on the excitation of the proton and its decay. Simplifying the total differential cross section by considering only a linearly polarised beam allows us to isolate the relationship between this linear polarisation and the azimuthal angular dependency of the produced meson as discussed in Section 2.2.

$$\frac{d\sigma}{d\Omega}(\phi) = \left(\frac{d\sigma}{d\Omega}\right)_0 \left(1 + P^L \Sigma \cos 2\phi\right) \tag{7.1}$$

where $\frac{d\sigma}{d\Omega}(\phi)$ is the total differential cross section, $\left(\frac{d\sigma}{d\Omega}\right)_0$ is the unpolarised differential cross section, P^L is the linear polarisation of the photon beam and ϕ is the azimuthal angle of the meson production plane relative to the plane of linear polarisation. Σ represents the sensitivity to polarisation. Due to the difficulties associated with reliably measuring cross sections stemming from accurate knowledge of detector acceptances, an asymmetry measurement is often performed to cancel any such effects. Measuring for two different polarisation planes perpendicular to each other and determining the azimuthal distribution allows an asymmetry to be formed. The data was taken with linear polarisation for angles of +45°, labelled +, and -45°, labelled -, to the

horizontal lab plane. These distributions are given by:

$$N_-(\phi) = A(\phi)F_- \left(1 + P_-^L \Sigma \cos(2(\phi - 45^\circ))\right) \tag{7.2}$$

$$N_+(\phi) = A(\phi)F_+ \left(1 + P_+^L \Sigma \cos(2(\phi + 45^\circ))\right) \tag{7.3}$$

where N_- is the yield for the -45° polarisation plane and N_+ for the +45° polarisation plane. $A(\phi)$ is the experimental acceptance, essentially the probability the event was detected and reconstructed and F is a term accounting for any difference in flux between the two settings. An asymmetry between these two can be described by:

$$\frac{N_-(\phi) - N_+(\phi)}{N_-(\phi) + N_+(\phi)} = \frac{A(\phi)\left(F_- - F_+ + F_- P_-^L \Sigma \cos(2(\phi - 45^\circ)) - F_+ P_+^L \Sigma \cos(2(\phi + 45^\circ))\right)}{A(\phi)\left(F_- + F_+ + F_- P_-^L \Sigma(cos2(\phi - 45^\circ)) + F_+ P_+^L \Sigma \cos(2(\phi + 45^\circ))\right)} \tag{7.4}$$

Cancelling the acceptance and applying $\cos(2(x - \frac{\pi}{2})) = -\cos 2x$ this simplifies to:

$$\frac{N_-(\phi) - N_+(\phi)}{N_-(\phi) + N_+(\phi)} = \frac{\left(F_- - F_+ - (F_- P_- + F_+ P_+^L)\Sigma \cos(2(\phi + 45^\circ))\right)}{\left(F_- + F_+ + (F_+ P_+^L - F_- P_-^L)\Sigma \cos(2(\phi + 45^\circ))\right)} \tag{7.5}$$

Under the assumption that the differences in flux and polarisation for each state are small:

$$\frac{N_-(\phi) - N_+(\phi)}{N_-(\phi) + N_+(\phi)} = \frac{F_- - F_+}{F_- + F_+} - \frac{(F_- P_- + F_+ P_+^L)\Sigma \cos(2(\phi + 45^\circ))}{(F_- + F_+)} \tag{7.6}$$

The following fit function was then used to extract Σ:

$$\frac{N_-(\phi) - N_+(\phi)}{N_-(\phi) + N_+(\phi)} = A + B \cos(2\phi + C) \tag{7.7}$$

where A accounts for an overall offset in the fluxes of the two different settings, B is the weighted mean of the polarisation multiplied by the observable Σ and C is a parameter that allows some freedom to account for the difference in diamond angle between the two settings which will likely not be exactly 90°. The average polarisation was determined from histogramming the polarisation for each kinematic bin and taking the mean value.

7.2   Extended Maximum Likelihood Fit

An extended maximum likelihood(EML) fit differs from a traditional maximum likelihood by allowing the normalisation of the probability density function to vary [128]. The maximum likelihood is described by:

$$\mathscr{L}(p) = \prod_{i=1}^{N} \frac{f(\tau_i : p)}{\int f(\tau_i : p)d\tau} \tag{7.8}$$

with probability function f, observables τ and parameters p. Here the experimental observable is the azimuthal angle ϕ i.e. $\tau = \phi$, the detector acceptance must also be considered in the probability density function. Including acceptance, the maximum likelihood becomes:

$$\mathscr{L}_{acc}(p) = \prod_{i=1}^{N} \frac{f(\tau_i : p)\eta(\tau_i)}{\int f(\tau_i : p)\eta(\tau_i)d\tau} \tag{7.9}$$

where η is the acceptance function of the detector. The normalisation factor for such a likelihood is given by the integral over the full observable space:

$$A(p) = \int f(\tau_i : p)\eta(\tau_i)d\tau \tag{7.10}$$

Now consider the extended maximum likelihood by modifying the maximum likelihood by a factor dictated by Poisson statistics:

$$\mathscr{L}_{acc}^{ext}(p) = \frac{A(p)^N}{N!}e^{-A(p)} \prod_{i=1}^{N} \frac{f(\tau_i : p)\eta(\tau_i)}{\int f(\tau_i : p)\eta(\tau_i)d\tau} \tag{7.11}$$

where N is the number of observed events. Taking the negative logarithm of this gives:

$$-\ln\mathscr{L}_{acc}^{ext}(p) \propto -\sum_{i}^{N} \ln f(\tau_i : p)\eta(\tau_i) + A(p) \tag{7.12}$$

Where we have dropped factors independent of p as they do not affect the position of the minima. Expanding further,

$$-\ln\mathscr{L}(p) = -\sum_{i}^{N} \ln f(\tau_i : p) - \sum_{i}^{N} \ln \eta(\tau_i) + A(p) \tag{7.13}$$

Hence we see we can also ignore the acceptance term in the likelihood sum as it is independent of p,

$$-\ln\mathcal{L}^{ext}_{acc}(p) \propto -\sum_{i}^{N} \ln f(\tau_i : p) + A(p) \qquad (7.14)$$

This quantity can then be minimised to determine parameters p. The acceptance function still contributes to the normalisation integral A(p). This integral can be approximated by summing the PDF over accepted simulated Monte Carlo events.

$$A(p) \approx \sum_{j}^{M} f(\tau_j : p) \qquad (7.15)$$

The use of weighted events modifies the log likelihood by:

$$-\ln\mathcal{L}^{ext}_{acc}(p) \propto -\sum_{i}^{N} w_i \ln f(\tau_i : p) + A(p) \qquad (7.16)$$

where w_i are weights used to distinguish signal from background. The following PDF was used for the meson ϕ distribution for both production data and Monte Carlo events on an event-by-event basis to extract the observable Σ:

$$1 + P_S P_L (D\cos(2\phi + E)) \qquad (7.17)$$

we can include additional experimental observables P_S for the polarisation state, ± 1, and P_L for the degree of linear polarisation of each event giving $\tau = \{\phi, P_S, P_L\}$. For the MC integral events P_S and P_L are given randomly to match the fluxes and polarisation degrees of the real data. This effectively corrects for second order systematic effects.

7.3   Comparison of Methods

Three different methods were used to extract the polarisation observable Σ. These were a cuts based event selection with a histogram χ^2 fit(CutsHist), an sPlot event selection with a histogram χ^2 fit(WeightsHist) and an sPlot based event selection with a maximum likelihood based fit(WeightsML).
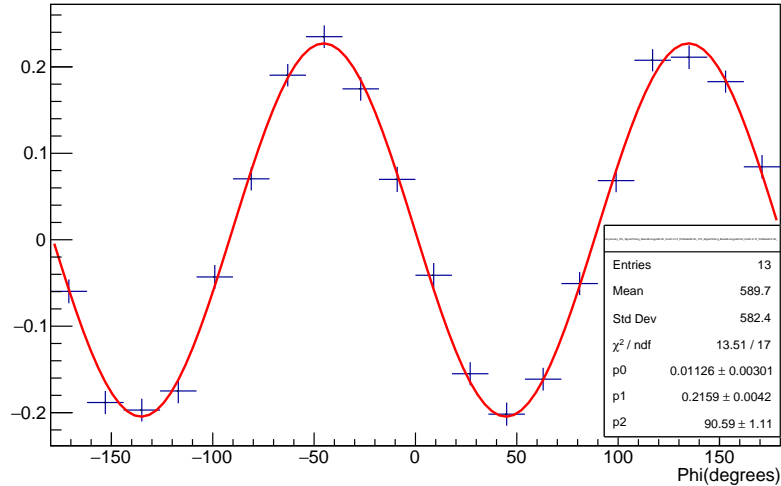
Figure 7.1: An example of a $\cos 2\phi$ fit to the histogram of an asymmetry of two different polarisation states.

The CutsHist analysis is the traditional method of applying cuts to discriminatory variables as outlined in Section 6.3. The observable was then extracted by filling histograms of phi for the two linear polarisation states forming an asymmetry in each histogram bin and fitting the resultant binned histogram with a $\cos 2\phi$ distribution as described in Section 7.1. An example histogram fit of a single bin is shown in Figure 7.1. The beam asymmetry observable, Σ, was extracted from the second fit parameter by dividing by the mean polarisation in the given bin.

The WeightsHist method uses the sPlots fitting technique from Section 6.4 to determine yields of signal and background in a distribution. First a fit was performed to subtract off random tagger photons before an invariant mass fit was conducted with the random photons subtracted. The product of the weights from the previous two fits allows isolation of the initial state photon in coincidence with the final state π^0. To remove background from events with more than just a nucleon a fit was performed to pion-nucleon coplanarity to provide the final event weights to subtract all backgrounds. An asymmetry was then formed for the two different linear polarisation states and the binned histogram of this fitted with a $\cos 2\phi$ distribution. In both cases of the histogram fits the CERN ROOT TH1::GetAsymmetry function was used which correctly propagates statistical uncertainties.

The WeightsML method differs from the WeightsHist by using the weights from the coplanarity fit to perform an unbinned EML fit to extract the observable as detailed in Section 7.2.
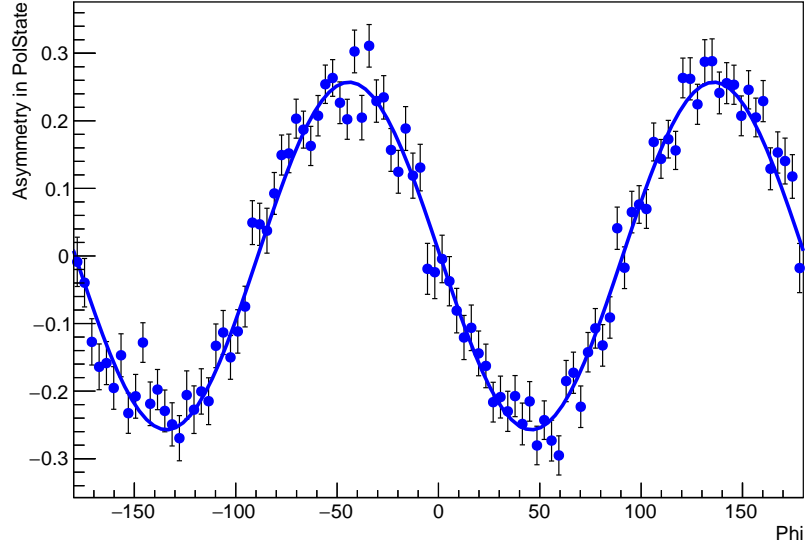
Figure 7.2: An example of an asymmetry of two different polarisation states produced from the results of an extended maximum likelihood fit.

The EML fit uses event by event polarisation and Monte Carlo simulation events to perform an acceptance correction. An example of an asymmetry produced from an EML fit to the data is shown in Figure 7.2. Note that the EML fit plot shows a larger asymmetry as the polarisation has been divided out of the amplitude.

Values of Σ extracted for each of these methods are shown in Figures 7.3 to 7.6 for the proton π^0 channel. A good agreement between all three methods is shown for a wide range of $\cos\theta$ and E_γ bins. The weighted methods are expected to be systematically higher than the cuts based results due to the event selection method removing all background beneath the signal peaks.

The fractional difference of each of the methods is calculated as follows:

$$\Delta\Sigma = \frac{\Sigma_1 - \Sigma_2}{\bar{\Sigma}} \tag{7.18}$$

where Σ_1 and Σ_2 represent the results of 2 of the three methods. $\bar{\Sigma}$ is the weighted mean of the two methods. The differences for the proton π^0 channel for WeightsHist and WeightsML are shown in Figures 7.7 to 7.10. The methods are in very good agreement with each other with the small fractional differences stemming from dilution to the binning in the histogram fit. Figures 7.11 to 7.14 show the differences between the WeightsHist and CutsHist methods for the $p\pi^0$

E$_\gamma$ (MeV)	Mean Fractional Difference Percentage(WeightsHist and WeightML)	Mean Fractional Difference Percentage(WeightsHist and CutsHist)
410	1.96	4.06
430	2.74	4.17
450	1.87	2.59
470	1.47	2.84
490	2.36	3.33
510	1.84	4.4
530	1.48	4.9
550	1.57	4.1
570	1.51	3.57
590	1.67	4.15
610	1.71	3.88
630	2.42	3.97
650	6.22	9.11
670	11.7	24.4
690	14.4	11.6
710	9.01	19.9

Table 7.1: A table of the mean fractional difference between the WeightsHist and CutsHist methods and the WeightsHist and WeightsML methods for each E$_\gamma$ bin for the pπ^0 channel.

channel. The fractional differences for the CutsHist and WeightsHist method show the effect of the different background subtraction methods. A table of the mean difference in each E$_\gamma$ bin is shown in Table 7.1. The CutsHist method has a small amount of background remaining under the discriminatory variable peaks, as discussed in Section 6.3, which result in this fractional difference.

Similarly for the neutron π^0 channel, the results for each of the three methods are shown in Figures 7.15 to 7.20. A good agreement is achieved between all methods and results are extracted to lower energies than the proton π^0 channel.

The difference between the WeightsHist and WeightsML methods are shown in Figures 7.21 to 7.26 and the difference between the WeightsHist and CutsHits are shown in Figures 7.27 to 7.32 with a little difference between any of the methods. The fractional difference between the two weights methods shows the effect of the histogram fit. The WeightedHist method results
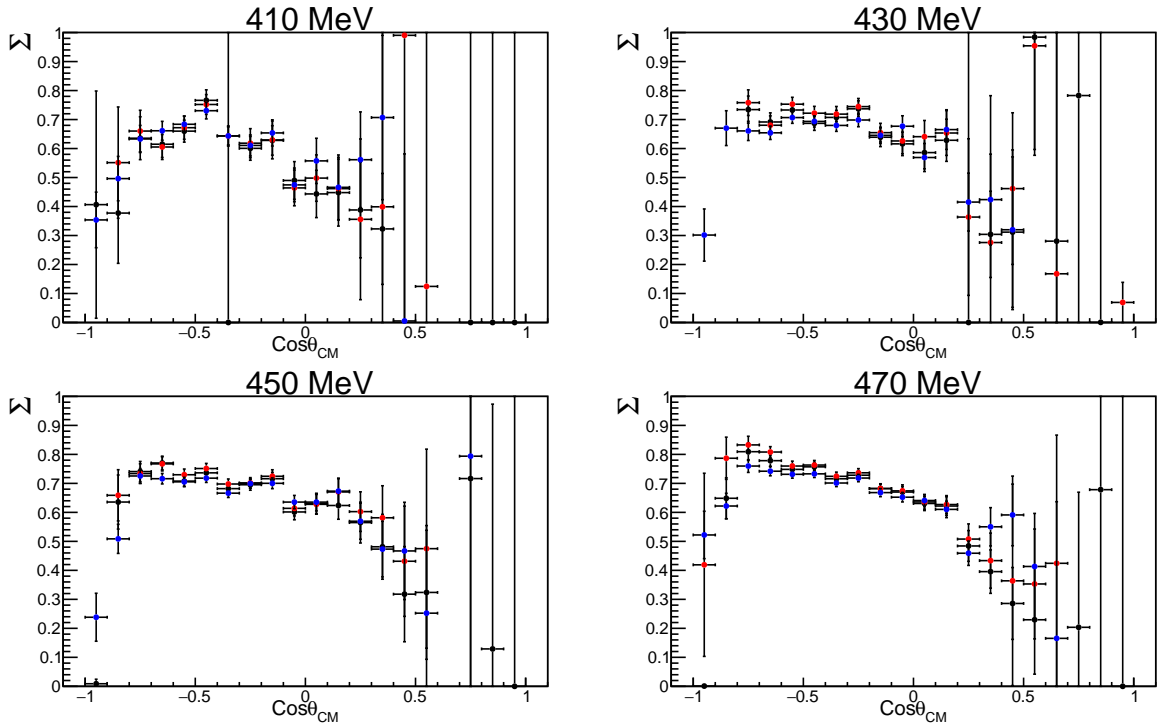
Figure 7.3: A comparison of the different event selection and observable extractions techniques used in this work for the $p\pi^0$ channel for E_γ bins of 410-470 MeV. The CutsHist analysis results are shown in blue. The WeightsHist method is represented by black and the WeightsML by red.

are diluted due to the binning chosen in ϕ for the histogram extraction. The WeightsML method experiences no binning effect. There is generally a very good agreement between these two methods. However, the WeightsML is a more robust extraction method in all cases whereas the WeightsHist fit fails in a few cases, in particular those regions where low statistics result in a failure from the χ^2 method. The mean fractional differences of 1.7-8.3% between the WeightsHist and CutsHist methods, as shown in Table 7.2, illustrates the effect of the small amount of background remaining under the peaks in the cuts-based method.

For this analysis, the WeightsML fit method is taken as the results to be compared with PWA predictions and previous data as it was free of effects from the binned fit and removed background under the discriminatory variable peaks. For the $p\pi^0$ channel the results in the region $\cos\theta$ -1 to 0.5 will be used for comparison due to the acceptance of low momenta protons in the detector. The cutoff value was determined from simulations.

Figure 7.4: A comparison of the different event selection and observable extractions techniques used in this work for the $p\pi^0$ channel for E_γ bins of 490-550 MeV. The CutsHist analysis results are shown in blue. The WeightsHist method is represented by black and the WeightsML by red.

Figure 7.5: A comparison of the different event selection and observable extractions techniques used in this work for the $p\pi^0$ channel for E_γ bins of 570-630 MeV. The CutsHist analysis results are shown in blue. The WeightsHist method is represented by black and the WeightsML by red.

Figure 7.6: A comparison of the different event selection and observable extractions techniques used in this work for the $p\pi^0$ channel for E_γ bins of 650-710 MeV. The CutsHist analysis results are shown in blue. The WeightsHist method is represented by black and the WeightsML by red.
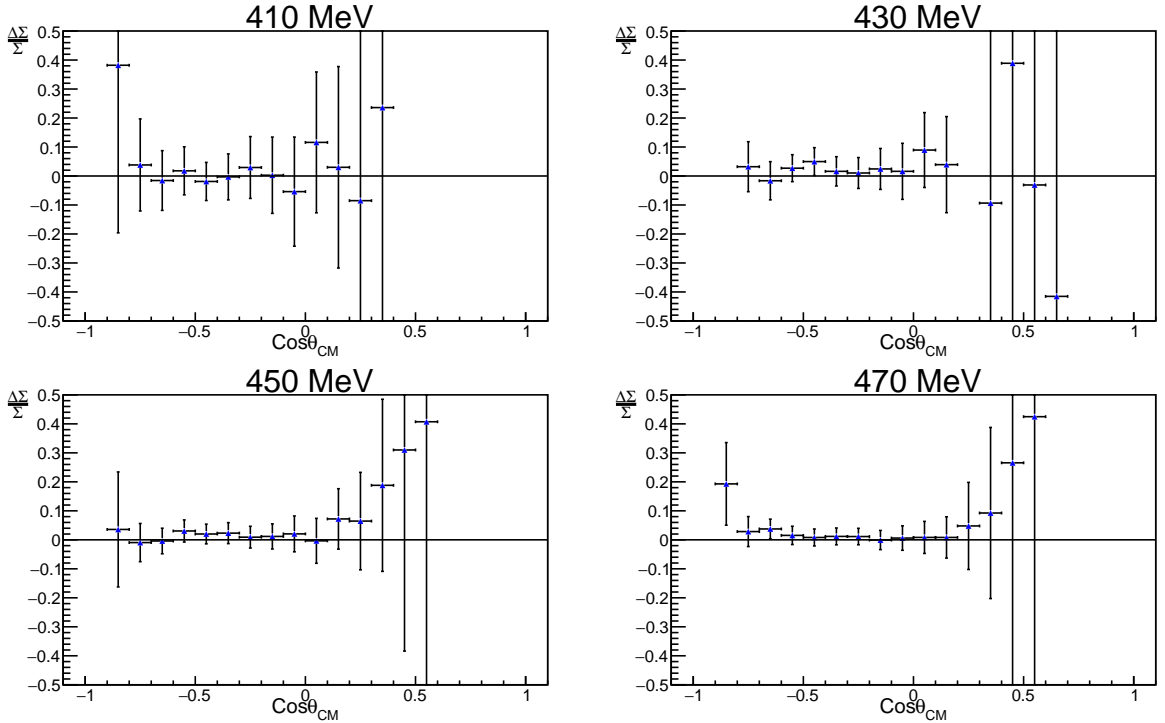
Figure 7.7: Systematic uncertainty from observable extraction method. The differences between the WeightsHist and WeightsML methods used for this analysis for the $p\pi^0$ channel for E_γ bins of 410-470 MeV. The difference between each method is divided by the weighted mean of the results of the two methods involved.

E_γ (MeV)	Mean Fractional Difference Percentage(WeightsHist and WeightML)	Mean Fractional Difference Percentage(WeightsHist and CutsHist)
250	62.77	82.8
270	38.32	25.5
290	23.39	29.7
310	9.53	8.34
330	8.67	1.57
350	2.2	3.20
370	3.84	4.36
390	5.34	3.1
410	3.21	2.76
430	3.14	2.06
450	2.69	2.43
470	1.84	2.47
490	2.42	2.91
510	1.89	2.78
530	1.54	1.56
550	3.02	3.48
570	2.1	1.72
590	2.82	2.32
610	2.35	1.99
630	3.31	5.04
650	6.41	10.78
670	48.74	37.88
690	20.45	26.72
710	8.9	34.36

Table 7.2: A table of the mean fractional difference between the WeightsHist and CutsHist methods and the WeightsHist and WeightsML methods for each E_γ bin for the $n\pi^0$ channel.

Figure 7.8: Systematic uncertainty from observable extraction method. The differences between the WeightsHist and WeightsML methods used for this analysis for the $p\pi^0$ channel for E_γ bins of 490-550 MeV. The difference between each method is divided by the weighted mean of the results of the two methods involved.

7.4   Final State Interactions

A consequence of using deuteron as a neutron target is the introduction of final state interactions(FSI) to both π^0 photoproduction reactions. The impulse approximation(IA), that the π^0 is produced from one of the nucleons such that one nucleon is considered the participant and the other the spectator playing no part in the process, is the dominant process however reactions with additional vertices can also contribute. The main such final state interaction involves a subsequent nucleon-nucleon scatter(NN-FSI), as pictured in Figure 7.33. A πN-FSI also occurs but does not contribute significantly above 200 MeV as discussed in [129]. The amplitude, M, for the reaction $\gamma d \rightarrow pn\pi^0$ according to [130] and [131] can be written as:

$$M = M_{a1} + M_{a2} + M_b \tag{7.19}$$

where M_{a1} is the spectator proton reaction, M_{a2} is the spectator neutron and M_b is a correction related to the NN-FSI reaction. A correction factor due to FSIs for the cross section is pictured

Figure 7.9: Systematic uncertainty from observable extraction method. The differences between the WeightsHist and WeightsML methods used for this analysis for the $p\pi^0$ channel for E_γ bins of 570-630 MeV. The difference between each method is divided by the weighted mean of the results of the two methods involved.

in Figure 7.34 for three different beam energies from previous Crystal Ball deuteron photopro-duction measurements [130]. We see that the FSI effects are significant, up to a factor of 2, at forward angles(<50°) and decrease with increasing beam energy. A detailed investigation of pion photoproduction on the deuteron [129], which gives similar results, explains why the deviations are much smaller at backward angles as being due to requiring regions where both nucleons have small momenta which requires high momentum components in the tail of the deuteron wave function.

The effect of FSI on polarisation observables is more difficult to ascertain due to lack of data to constrain the bare photoproduction amplitudes. The calculations of [129] deal with the inclusive case of production on both proton and neutron but give an indication of the likely size of corrections, which are significantly smaller than that of the cross sections and are shown in Figure 7.35

This model dependent correction has not been applied to the results here as we report only the experimental measurements of the reactions on the deuteron. It is left to the partial wave

Figure 7.10: Systematic uncertainty from observable extraction method. The differences between the WeightsHist and WeightsML methods used for this analysis for the $p\pi^0$ channel for E_γ bins of 650-710 MeV. The difference between each method is divided by the weighted mean of the results of the two methods involved.

analysis to account for such effects where they can apply their own models at the amplitude level.

7.5 Linear Polarisation Correction Factor

The beam linear polarisation calibration was cross checked using the SAID PWA predictions on $p\pi^0$. It was found that there was a significant discrepancy with the original calibrations of Section 5.4.3. This is shown in Figures 7.36 to 7.39. Section 5.4.4 outlines potential sources of this discrepancy. Detailed systematic checks were performed to understand the origin of this discrepancy ruling out background subtraction, while FSI effects do not give a significant shift across the full angular range as was observed in this analysis and is expected to decrease, rather than increase the asymmetries as was observed here [129]. The small systematic uncertainty for the SAID PWA predictions of 2% coupled with the large number of experimental measurements in this region which agree very well with SAID, give confidence to use the SAID parameterisa-
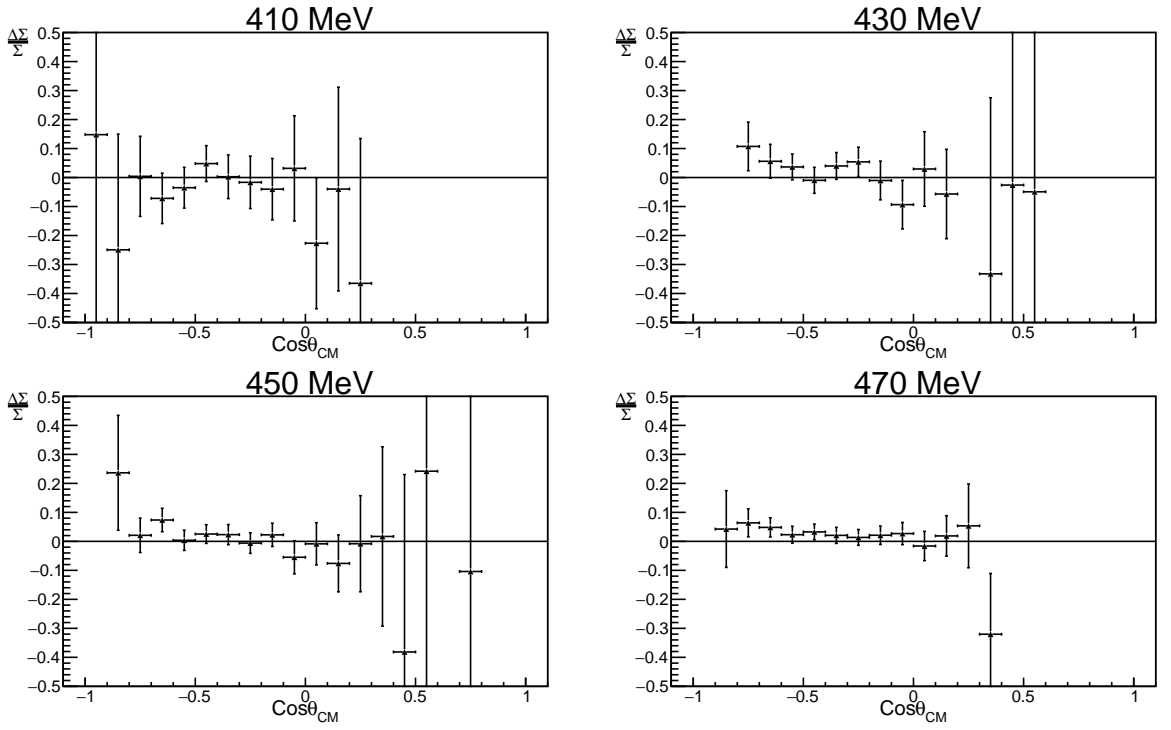
Figure 7.11: Systematic uncertainty from background extraction method. The differences between the WeightsHist and CutsHist methods used for this analysis for the $p\pi^0$ channel for E_γ bins of 410-470 MeV. The difference between each method is divided by the weighted mean of the results of the two methods involved.

tion to produce a correction factor to the linear polarisation.

A correction factor was calculated for each E_γ by taking the weighted mean of the ratio of the measurements to the SAID PWA predictions for a selected high statistical region of the measurements. The $\cos\theta_{CM}$ range of -0.45 to -0.05 was chosen for this purpose due to the large number of events in these bins for all energies and as the photon asymmetry does not vary considerably in this region. The weighted mean was calculated using the ratio of the extracted Σ to the SAID prediction, x_i for each $\cos\theta$ bin i, with associated uncertainty in the ratio σ_i:

$$\bar{x} = \frac{\sum\limits_{i=1}^{n} x_i \sigma_i^{-2}}{\sum\limits_{i=1}^{n} \sigma_i^{-2}} \tag{7.20}$$
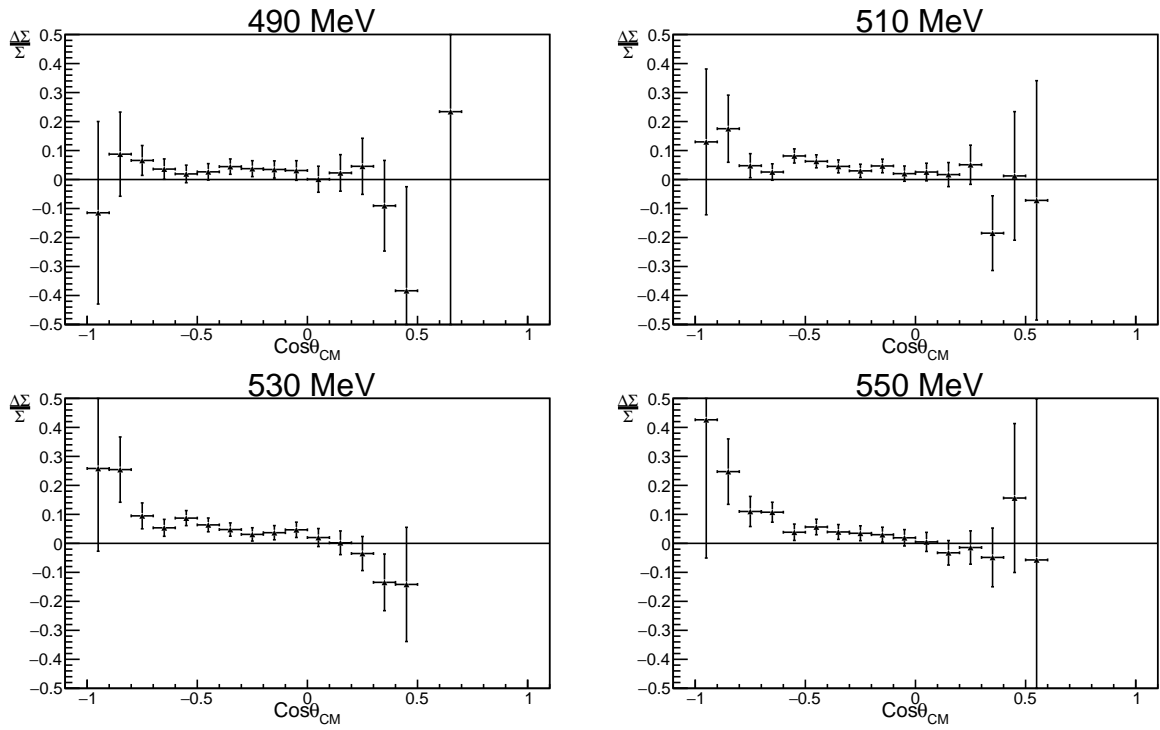
Figure 7.12: Systematic uncertainty from background extraction method. The differences between the WeightsHist and CutsHist methods used for this analysis for the $p\pi^0$ channel for E_γ bins of 490-550 MeV. The difference between each method is divided by the weighted mean of the results of the two methods involved.

with an uncertainty in the weighted mean of :

$$\sigma_{\bar{x}} = \sqrt{\frac{1}{\sum\limits_{i=1}^{n} \sigma_i^{-2}}} \qquad (7.21)$$

The applied correction factor for each E_γ bin is shown in Figure 7.40 with the linear polarisation on the same plot. The effect of the correction factor increases with energy up to 500 MeV and plateaus around 10% until the linear polarisation decreases again at the coherent edge at 630 MeV. These correction factors are applied to the neutron results in the energy region of 400 to 720 MeV as we do not measure sufficient proton statistics below this. No correction factor is applied to the results outside this range. Instead we assume the correction factor tends to one below 400 but estimate a systematic uncertainty of the average of the first three bins of the correction factor above 400 MeV of 5.5%. The application of the correction factor results in good agreement with partial wave analyses predictions within statistical and systematic uncer-
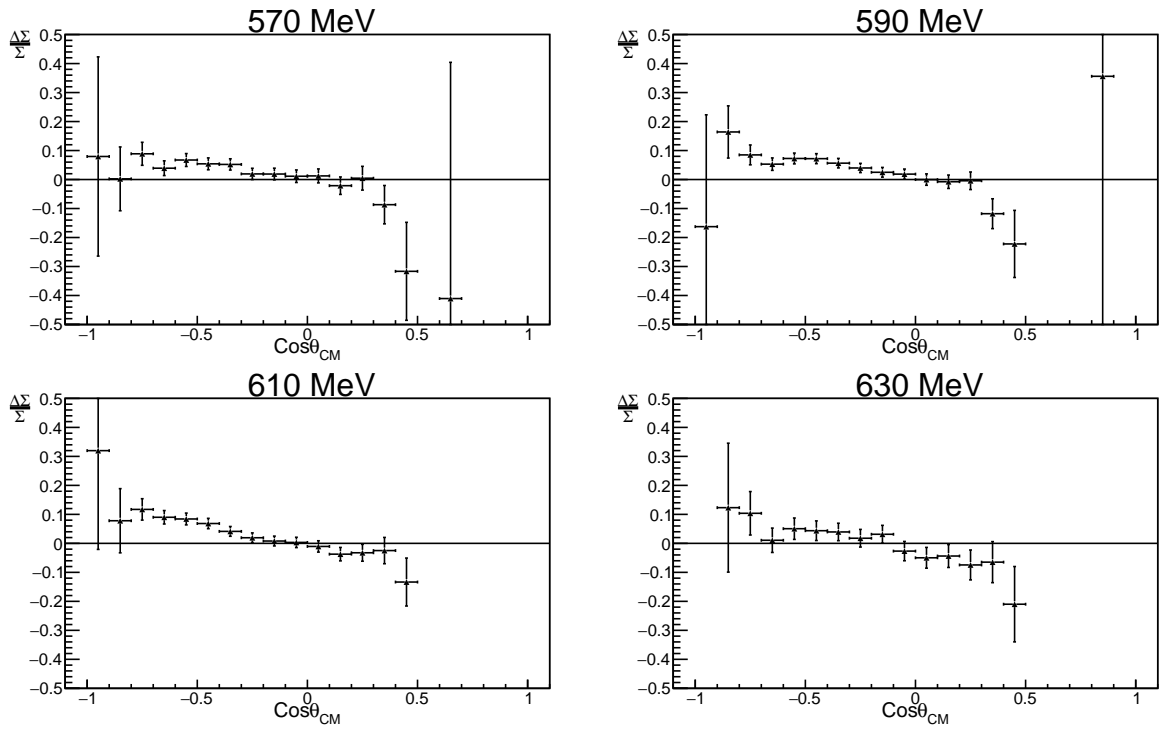
Figure 7.13: Systematic uncertainty from background extraction method. The differences between the WeightsHist and CutsHist methods used for this analysis for the $p\pi^0$ channel for E_γ bins of 570-630 MeV. The difference between each method is divided by the weighted mean of the results of the two methods involved.

tainties for both reaction channels. The correction factor and associated statistical uncertainty are tabulated in Table 7.3.

The correction factor required in the higher statistical bins ranging from 450 MeV to 630 MeV was generally 10% or greater. Taking into account the uncertainties from the fit to the polarisation peak of 5% and the uncertainties associated with the background subtraction method for each of these E_γ bins, of approximately 4-6%, does not provide a sufficient magnitude to explain the discrepancy. Furthermore, examining the region in cos theta from -0.45 to -0.05, where discrepancy between the different background subtraction methods is generally lower than the average of the E_γ bin, still exhibits a large discrepancy as in Figures 7.37 and 7.38. The 630 MeV and the 510 MeV bins in particular would require at least a doubling of the systematic uncertainty associated with the background subtraction method to be in agreement with both the SAID PWA predictions and previous measurements.
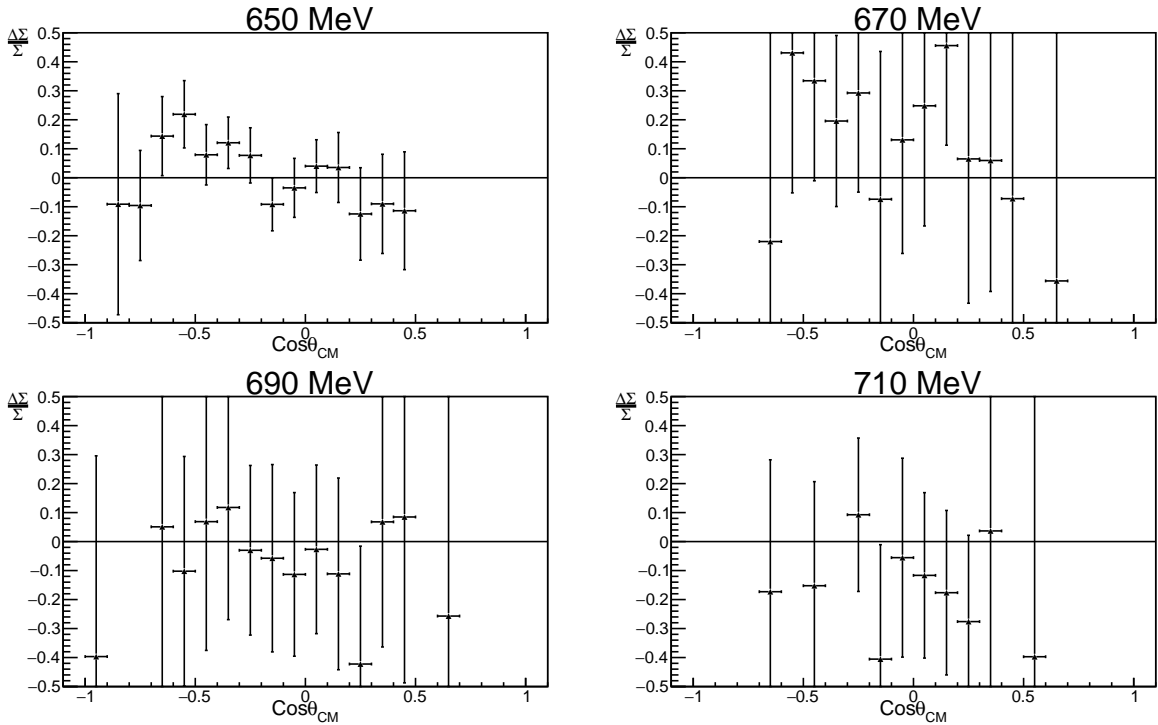
Figure 7.14: Systematic uncertainty from background extraction method. The differences between the WeightsHist and WeightsML methods used for this analysis for the $p\pi^0$ channel for E_γ bins of 650-710 MeV. The difference between each method is divided by the weighted mean of the results of the two methods involved.
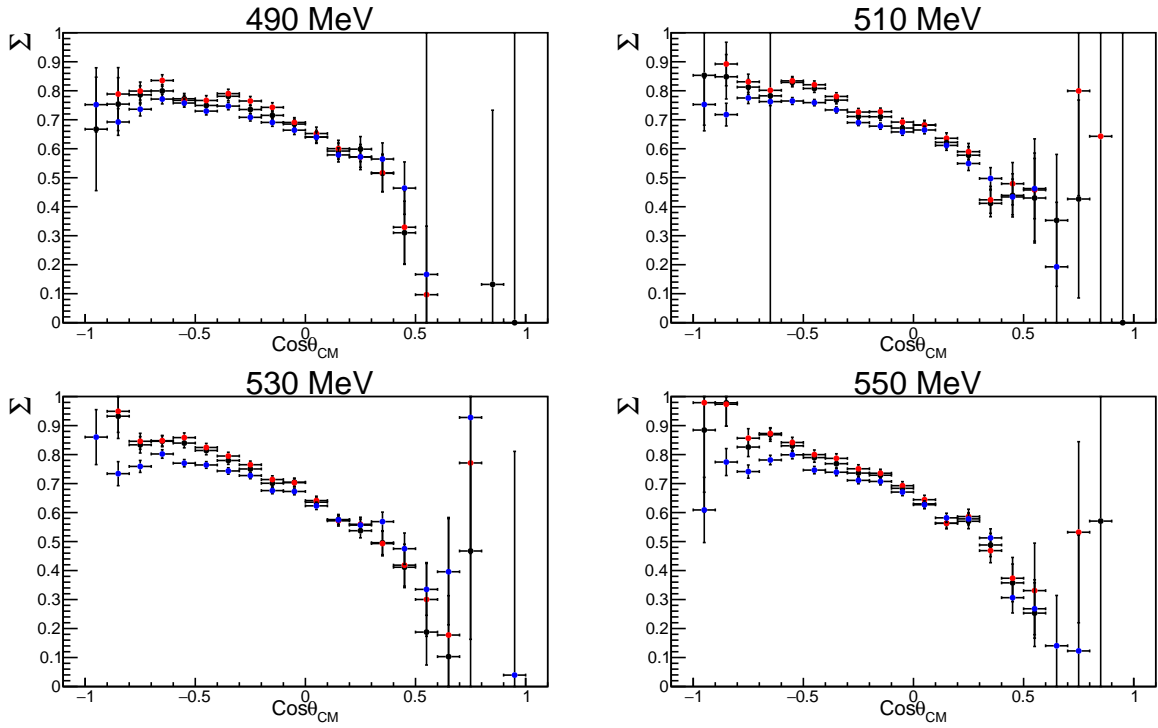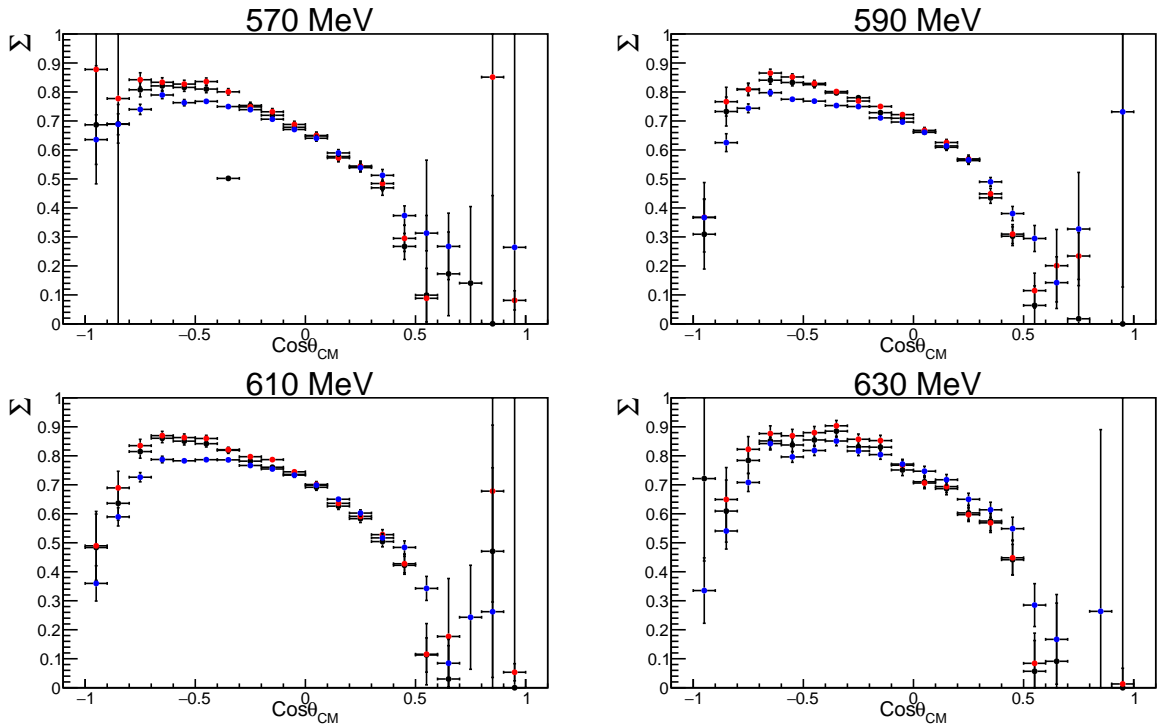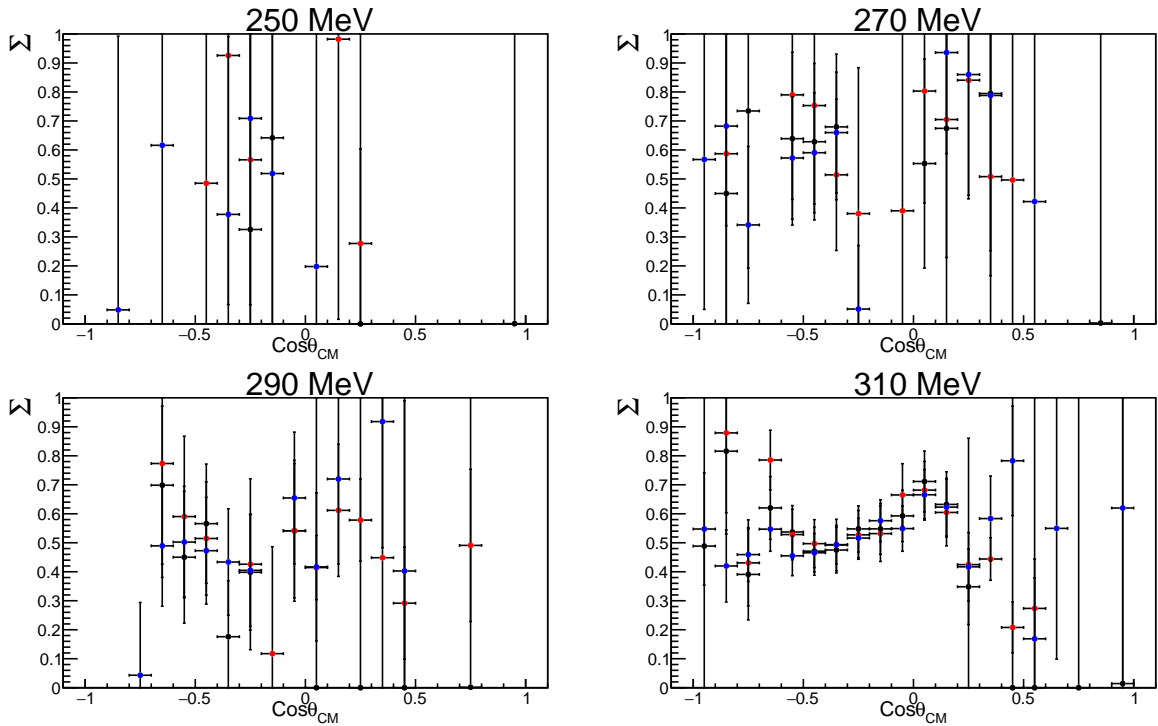

Figure 7.15: A comparison of the different event selection and observable extractions techniques used in this work for the $n\pi^0$ channel for E_γ bins of 250-310 MeV. The CutsHist analysis results are shown in blue. The WeightsHist method is represented by black and the WeightsML by red.
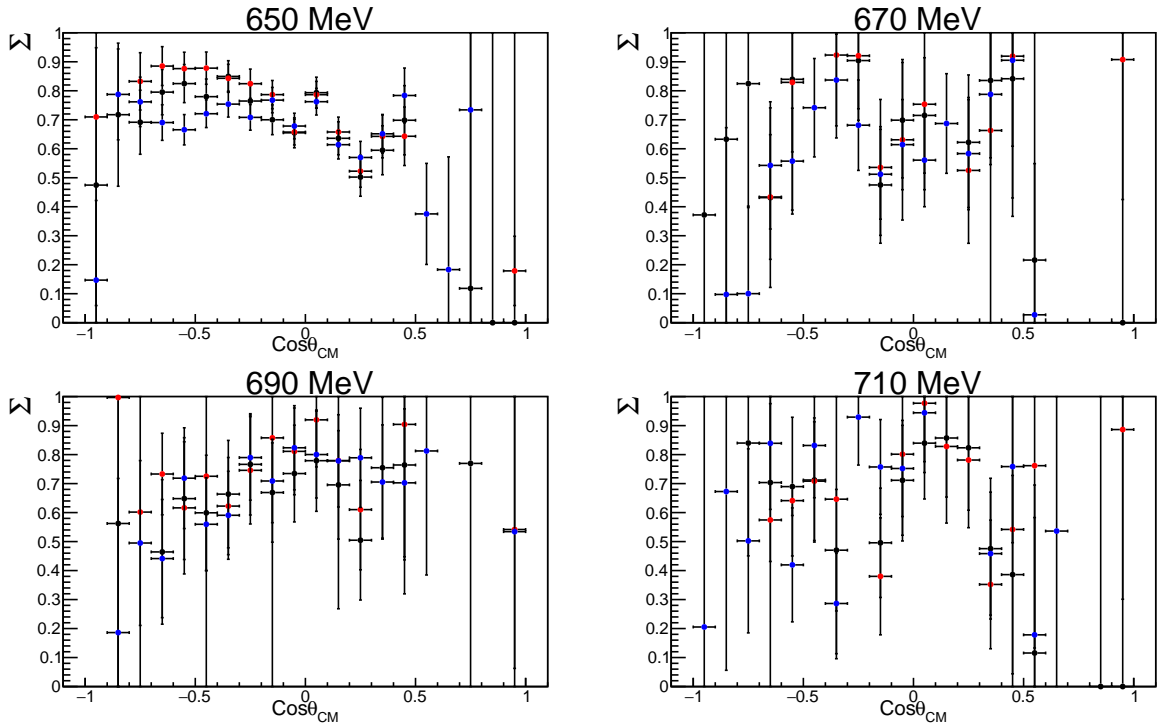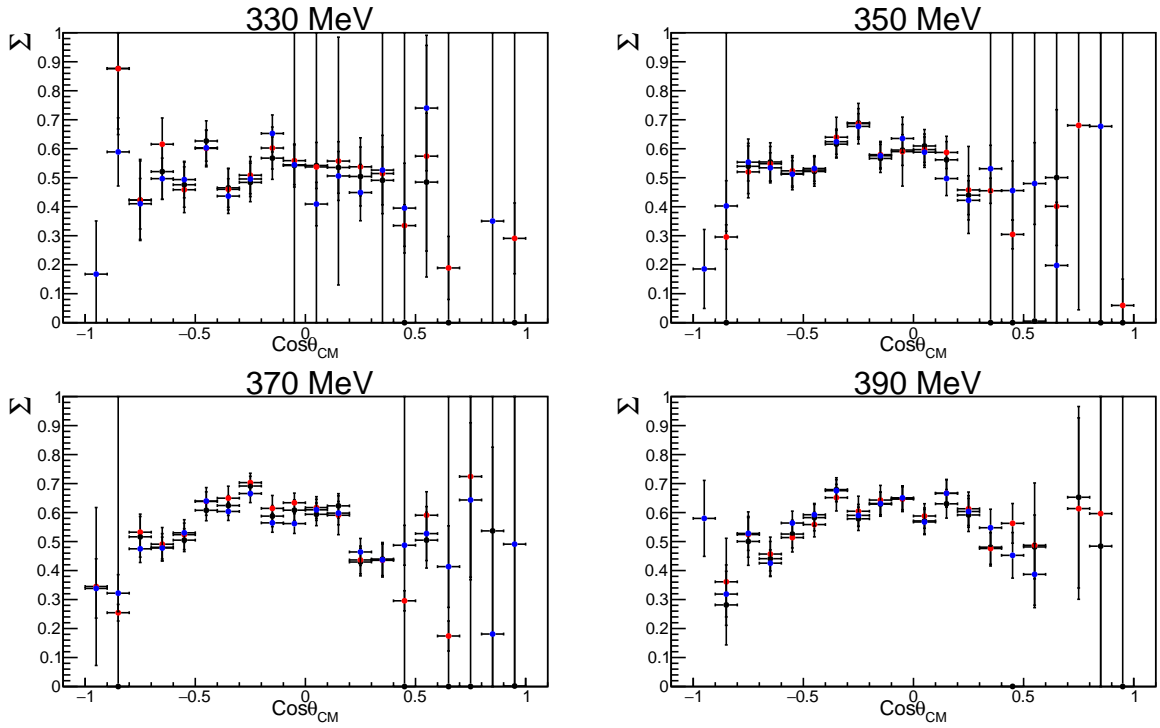
Figure 7.16: A comparison of the different event selection and observable extractions techniques used in this work for the $n\pi^0$ channel for E_γ bins of 330-390 MeV. The CutsHist analysis results are shown in blue. The WeightsHist method is represented by black and the WeightsML by red.
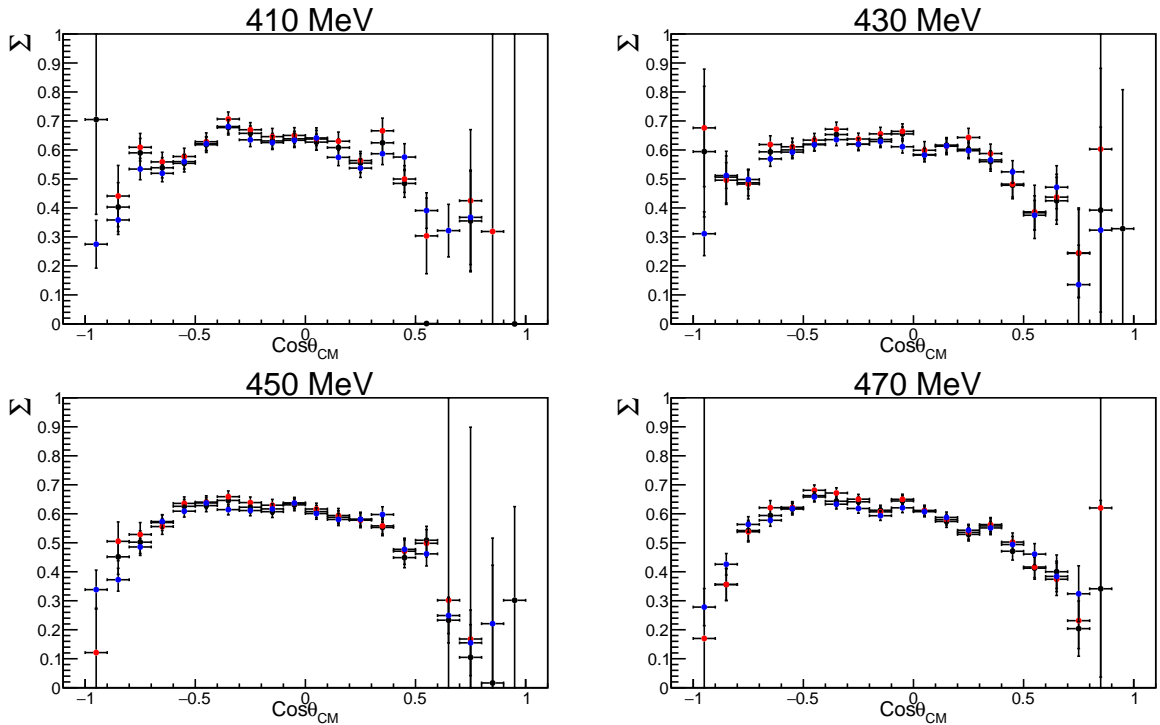
Figure 7.17: A comparison of the different event selection and observable extractions techniques used in this work for the $n\pi^0$ channel for E_γ bins of 410-470 MeV. The CutsHist analysis results are shown in blue. The WeightsHist method is represented by black and the WeightsML by red.
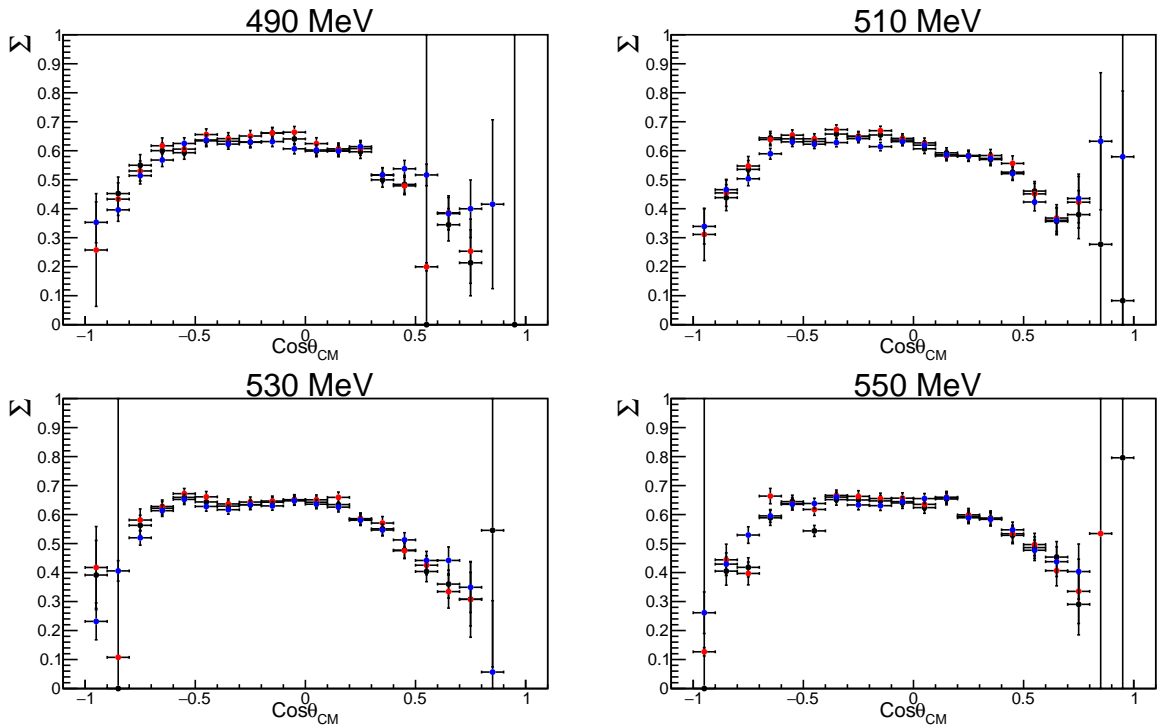
Figure 7.18: A comparison of the different event selection and observable extractions techniques used in this work for the $n\pi^0$ channel for E_γ bins of 490-550 MeV. The CutsHist analysis results are shown in blue. The WeightsHist method is represented by black and the WeightsML by red.
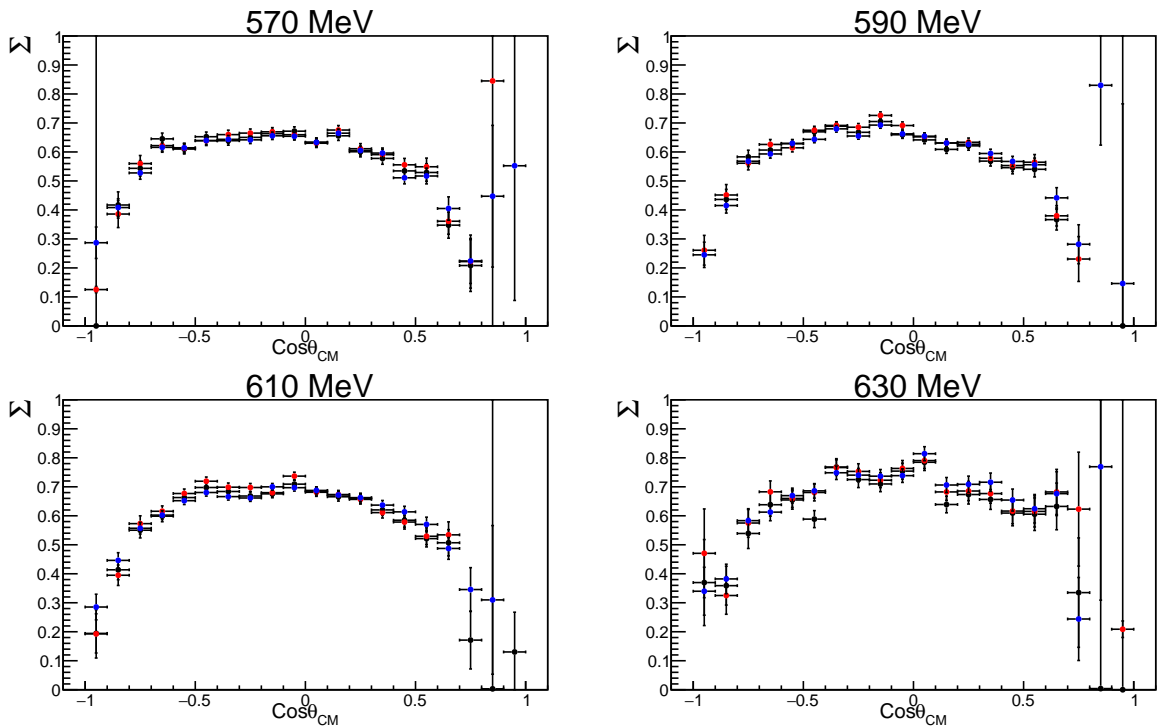
Figure 7.19: A comparison of the different event selection and observable extractions techniques used in this work for the $n\pi^0$ channel for E_γ bins of 570-630 MeV. The CutsHist analysis results are shown in blue. The WeightsHist method is represented by black and the WeightsML by red.
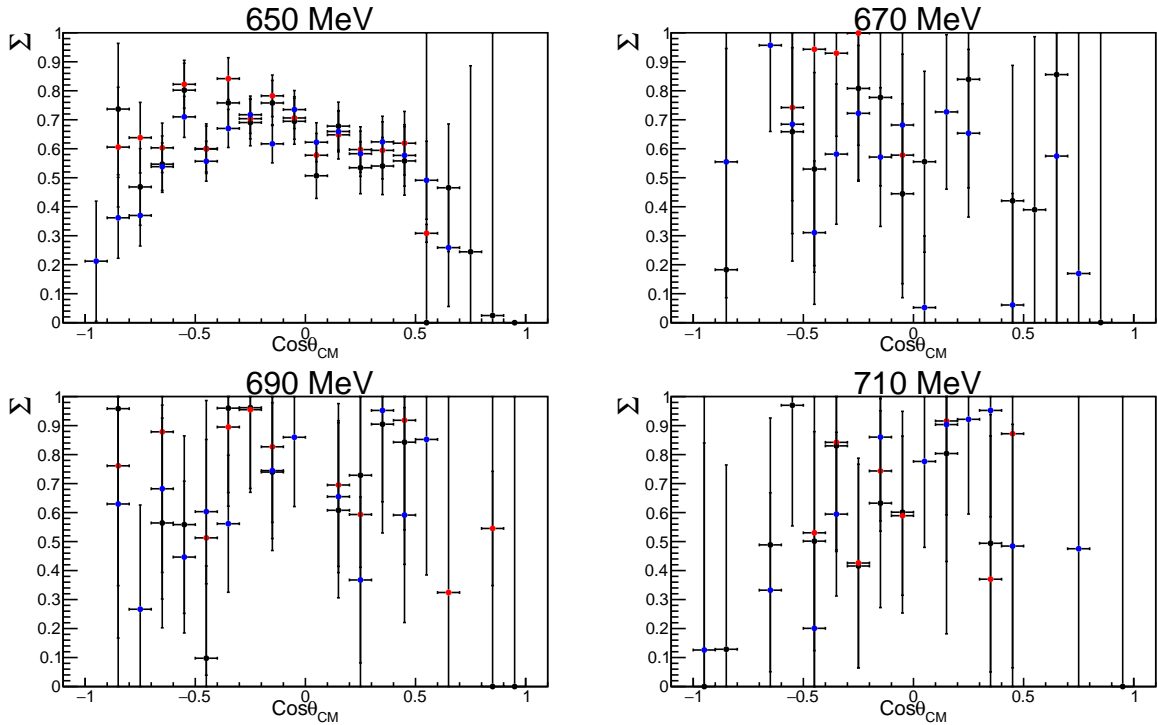
Figure 7.20: A comparison of the different event selection and observable extractions techniques used in this work for the $n\pi^0$ channel for E_γ bins of 650-710 MeV. The CutsHist analysis results are shown in blue. The WeightsHist method is represented by black and the WeightsML by red.
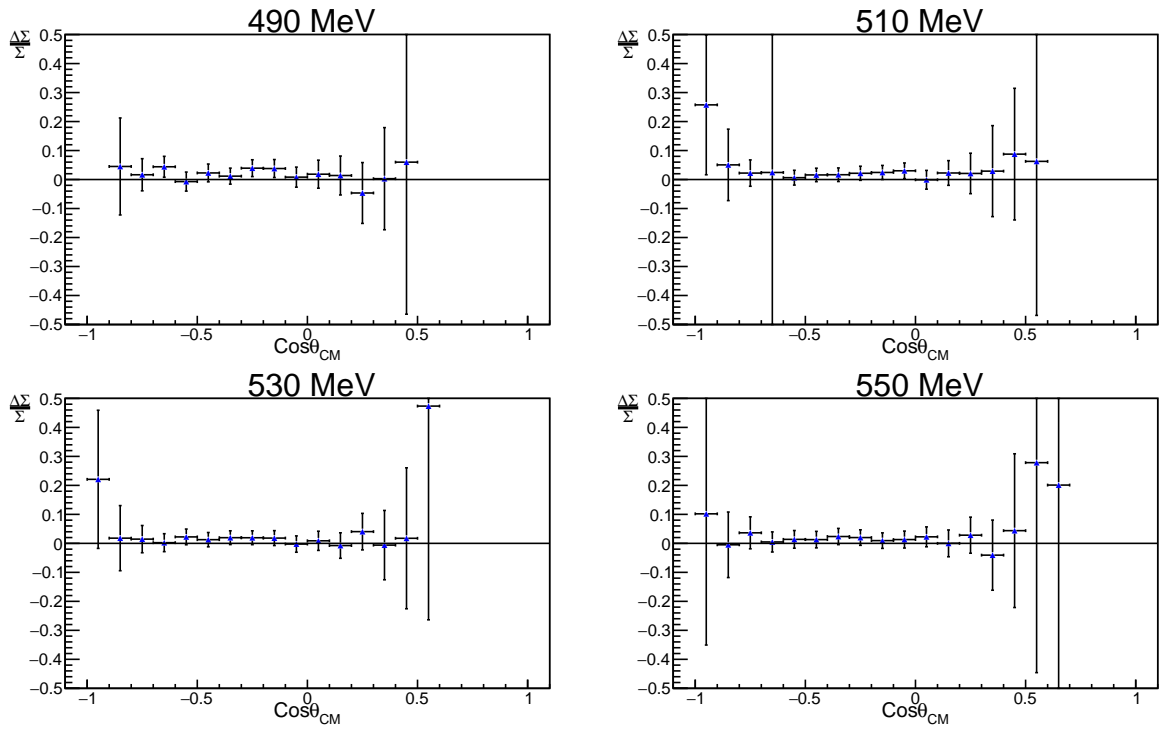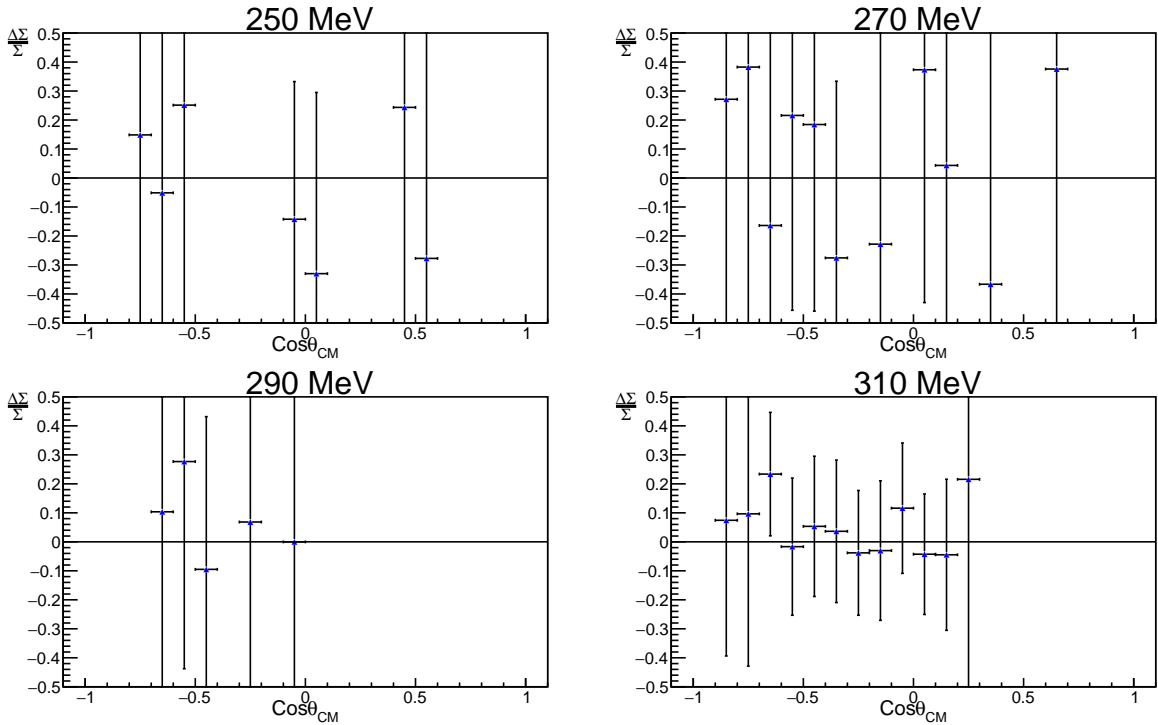

Figure 7.21: Systematic uncertainty from observable extraction method. The differences between the WeightsHist and WeightsML methods used for this analysis for the $n\pi^0$ channel for E_γ bins of 250-310 MeV. The difference between each method is divided by the weighted mean of the results of the two methods involved.
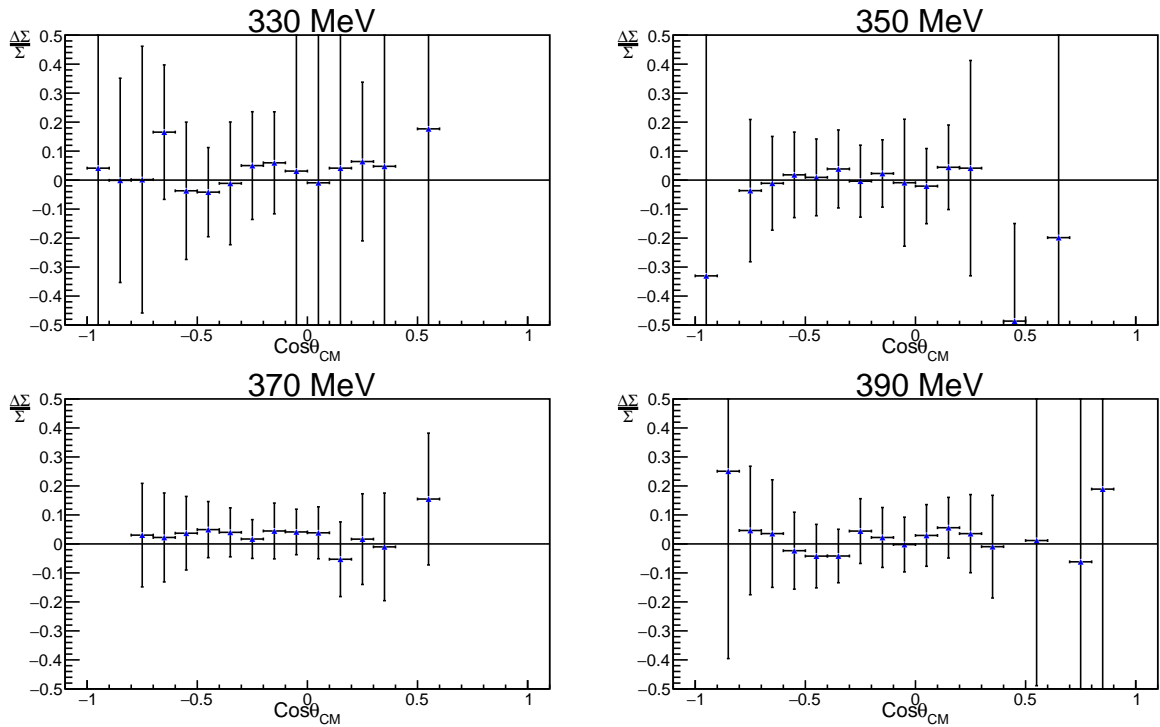
Figure 7.22: Systematic uncertainty from observable extraction method. The differences between the WeightsHist and WeightsML methods used for this analysis for the $n\pi^0$ channel for E_γ bins of 330-390 MeV.
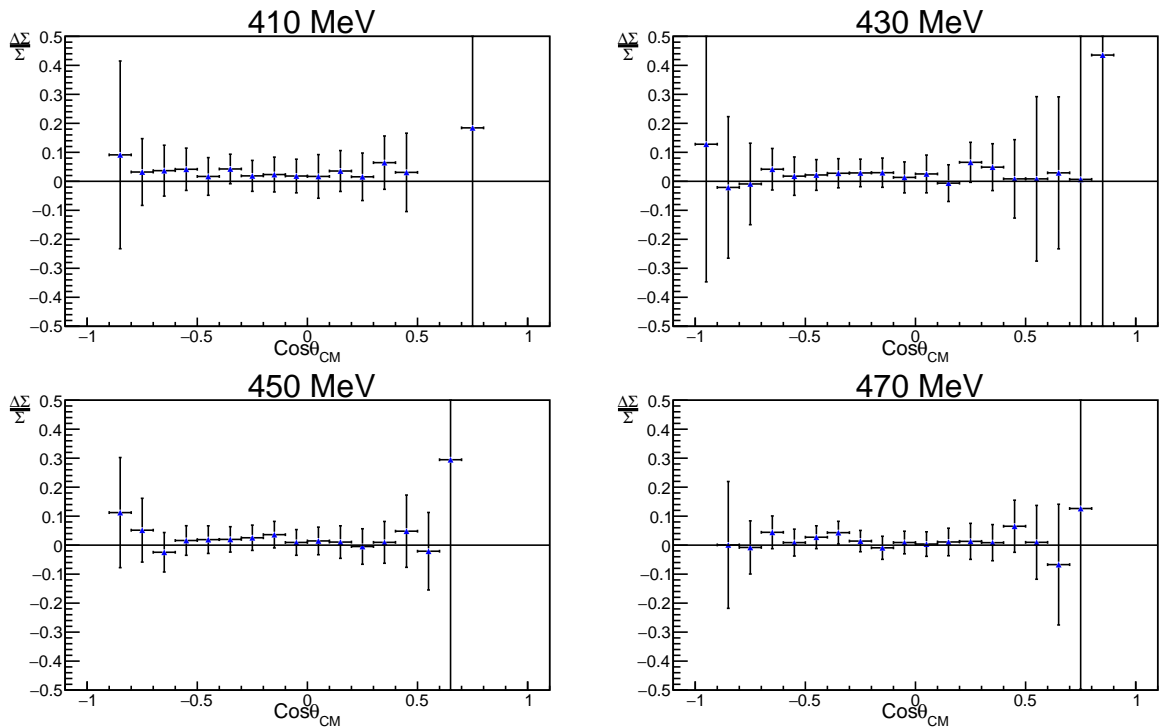
Figure 7.23: Systematic uncertainty from observable extraction method. The differences between the WeightsHist and WeightsML methods used for this analysis for the $n\pi^0$ channel for E_γ bins of 410-470 MeV.
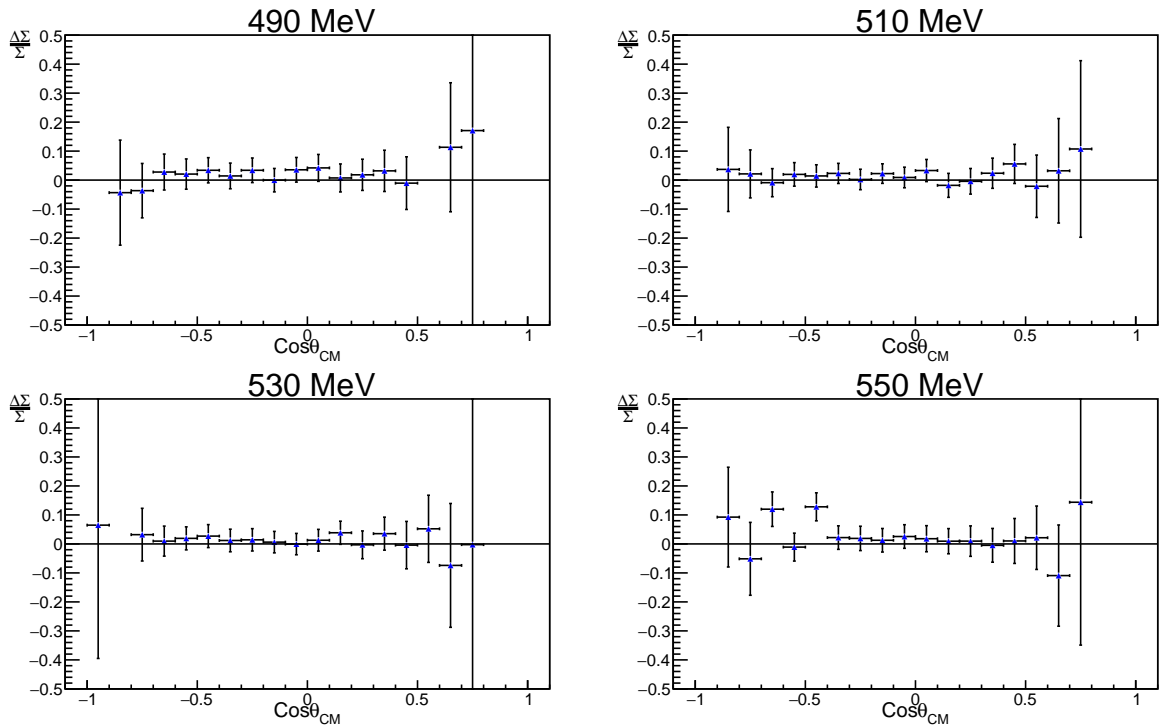
Figure 7.24: Systematic uncertainty from observable extraction method. The differences between the WeightsHist and WeightsML methods used for this analysis for the $n\pi^0$ channel for E_γ bins of 490-550 MeV.
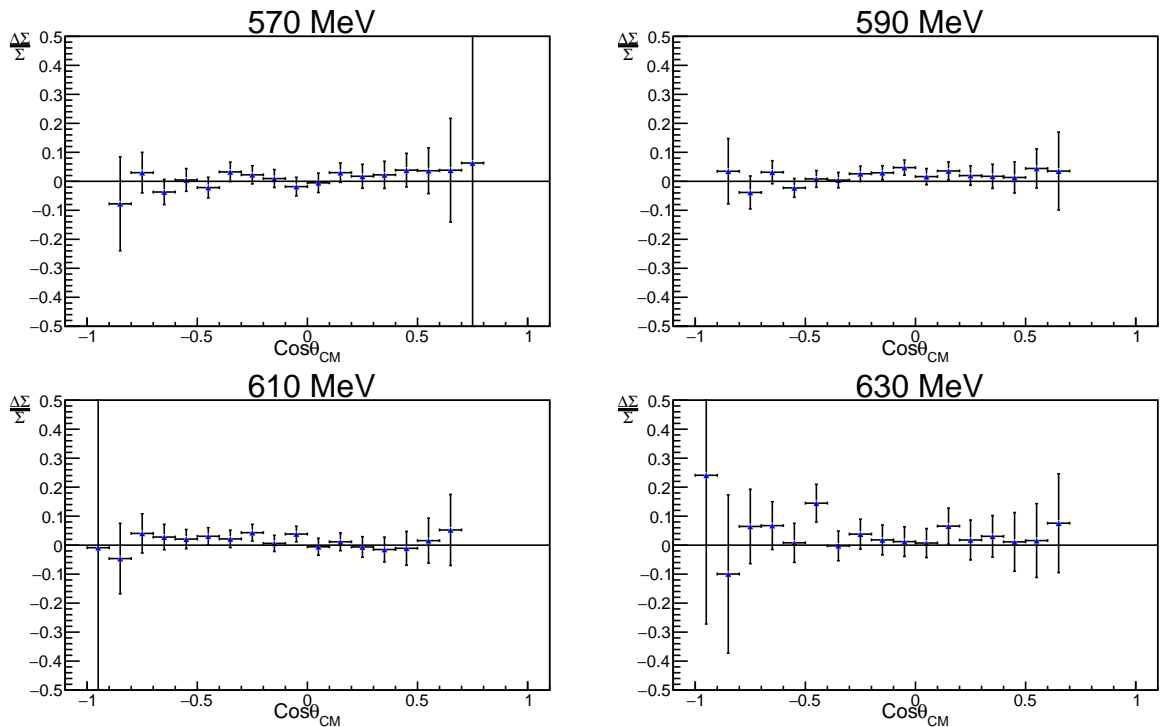
Figure 7.25: Systematic uncertainty from observable extraction method. The differences between the WeightsHist and WeightsML methods used for this analysis for the $n\pi^0$ channel for E_γ bins of 570-630 MeV.
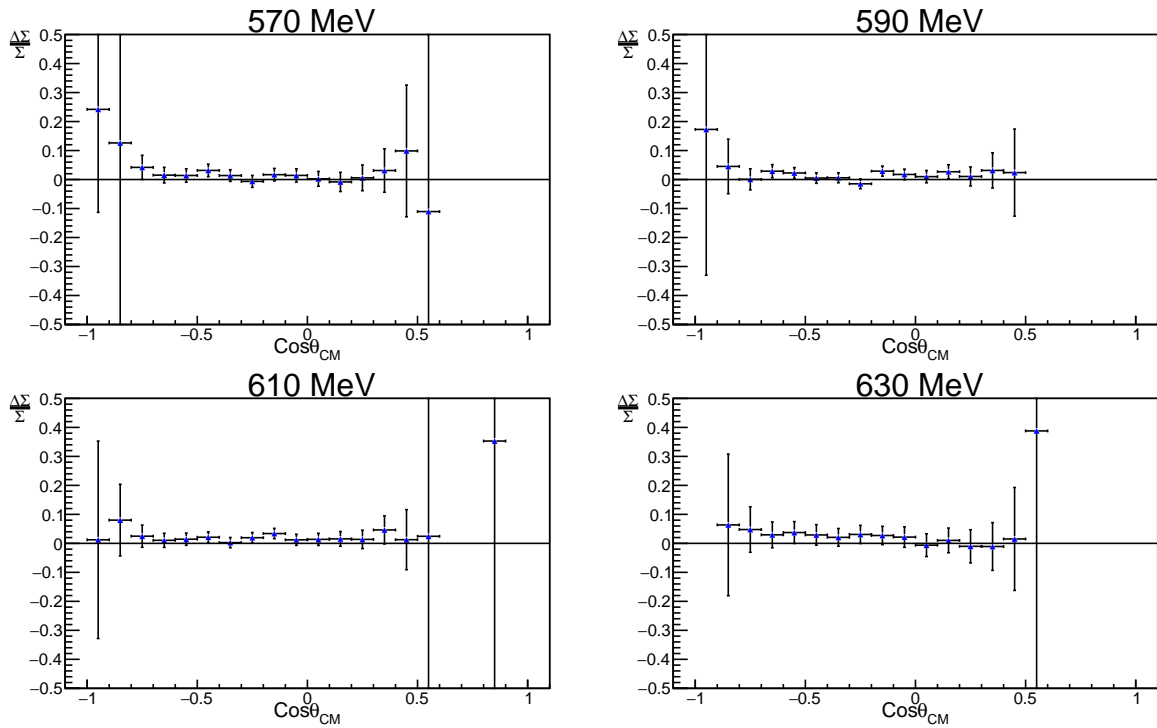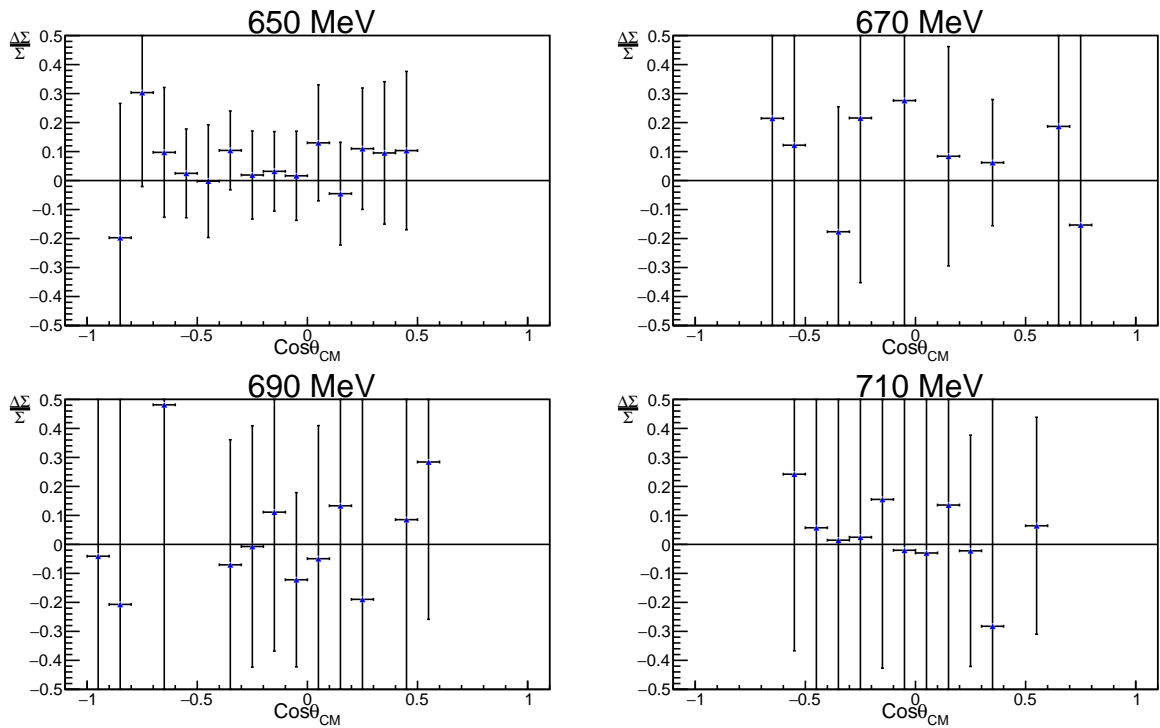
Figure 7.26: Systematic uncertainty from observable extraction method. The differences between the WeightsHist and WeightsML methods used for this analysis for the $n\pi^0$ channel for E_γ bins of 650-710 MeV.
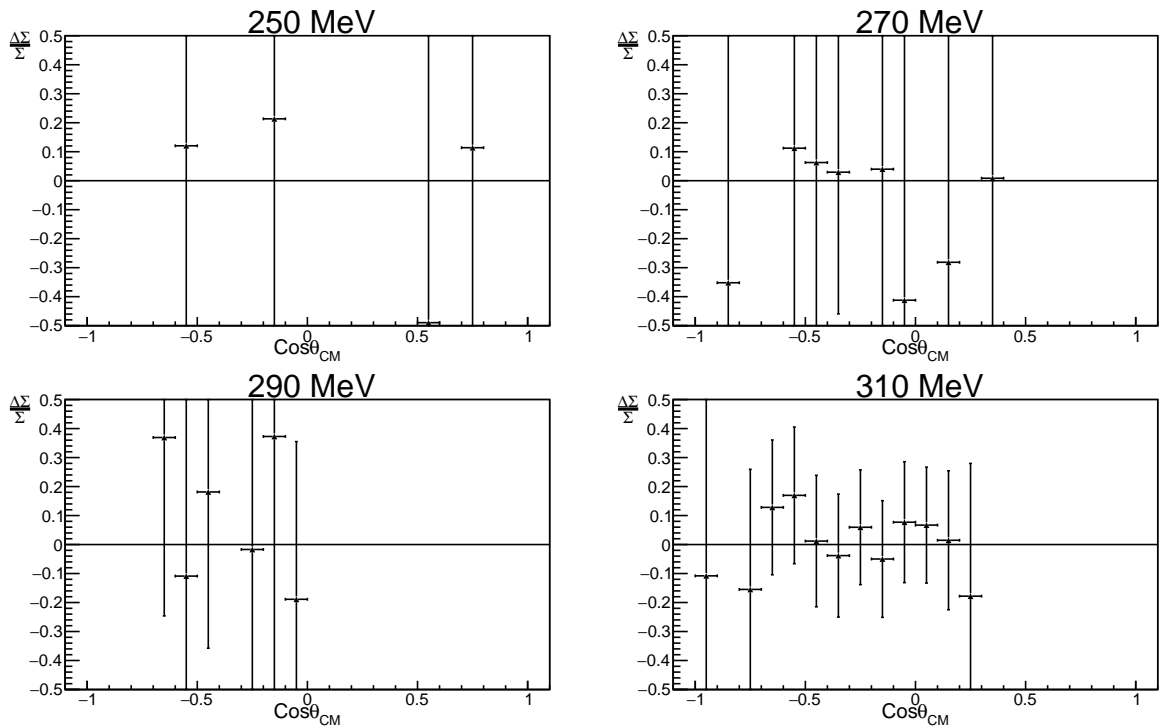
Figure 7.27: Systematic uncertainty from background extraction method. The differences between the WeightsHist and CutsHist methods used for this analysis for the $n\pi^0$ channel for E_γ bins of 250-310 MeV.
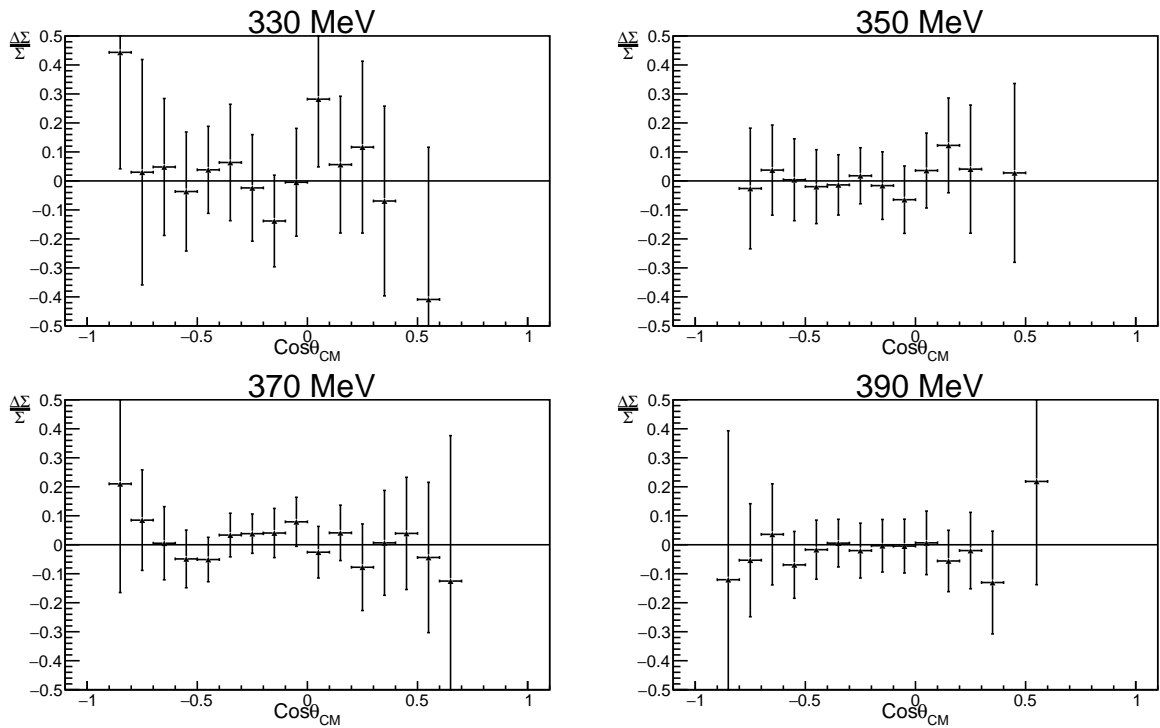
Figure 7.28: Systematic uncertainty from background extraction method. The differences between the WeightsHist and CutsHist methods used for this analysis for the $n\pi^0$ channel for E_γ bins of 330-390 MeV.
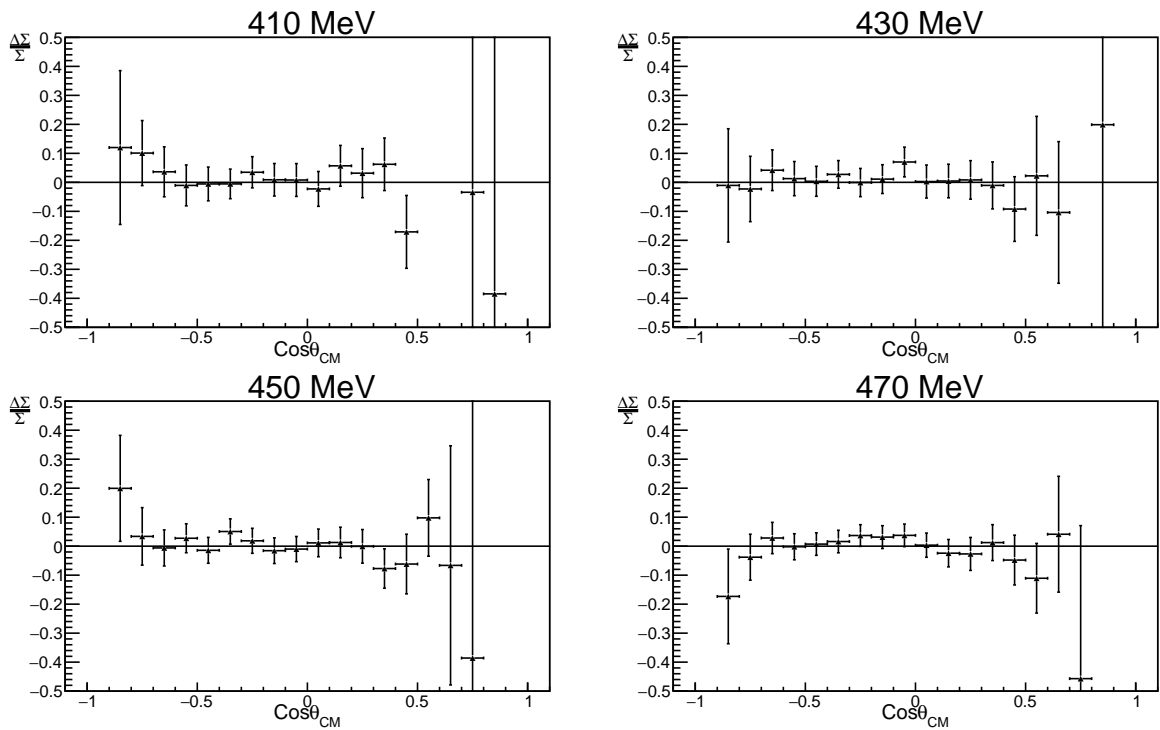
Figure 7.29: Systematic uncertainty from background extraction method. The differences between the WeightsHist and CutsHist methods used for this analysis for the $n\pi^0$ channel for E_γ bins of 410-470 MeV.
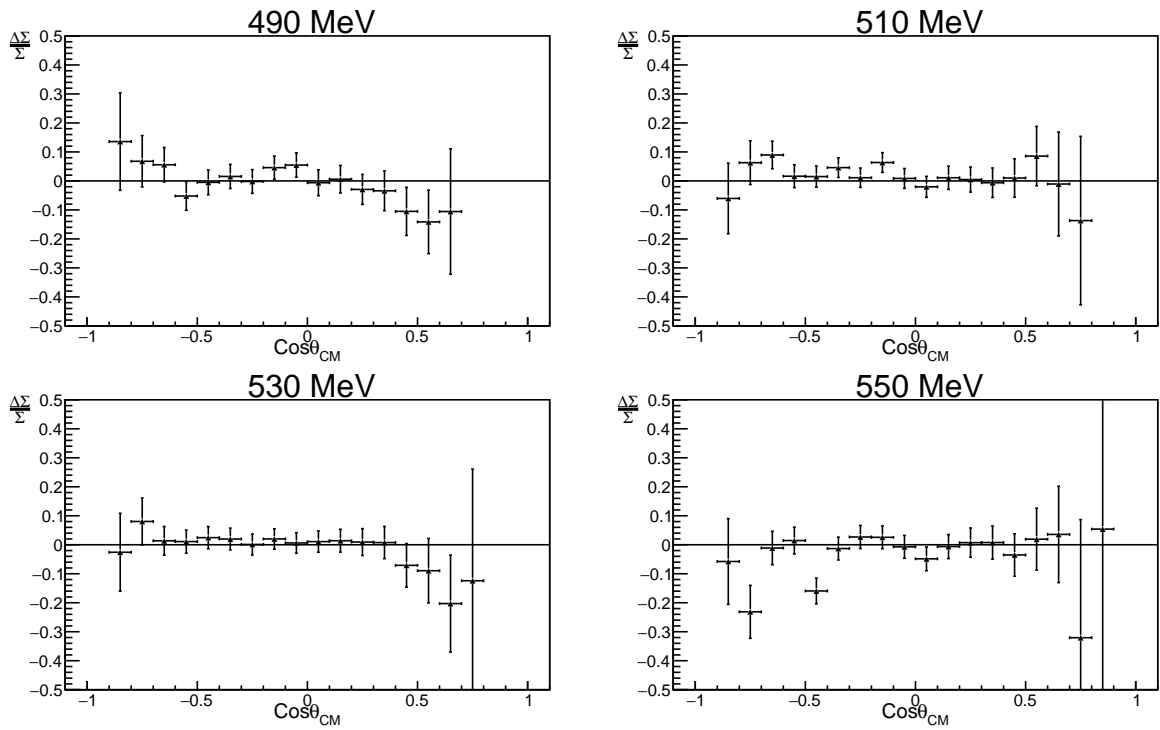
Figure 7.30: Systematic uncertainty from background extraction method. The differences between the WeightsHist and CutsHist methods used for this analysis for the $n\pi^0$ channel for E_γ bins of 490-550 MeV.
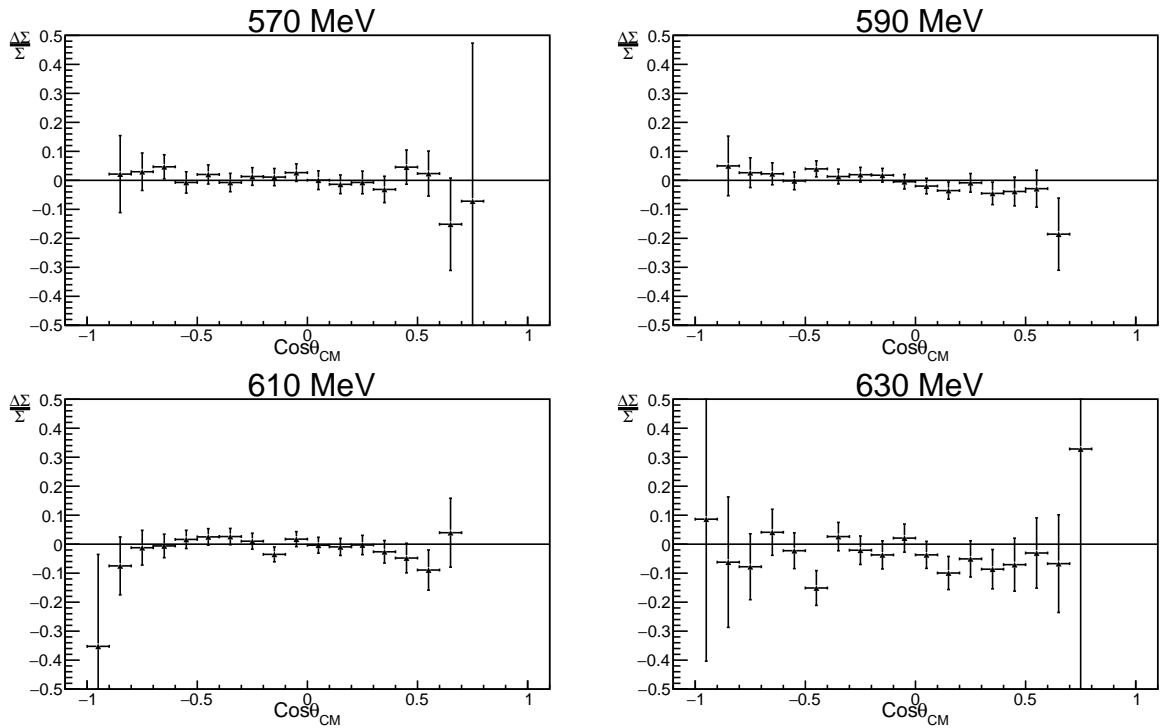
Figure 7.31: Systematic uncertainty from background extraction method. The differences between the WeightsHist and CutsHist methods used for this analysis for the $n\pi^0$ channel for E_γ bins of 570-630 MeV.
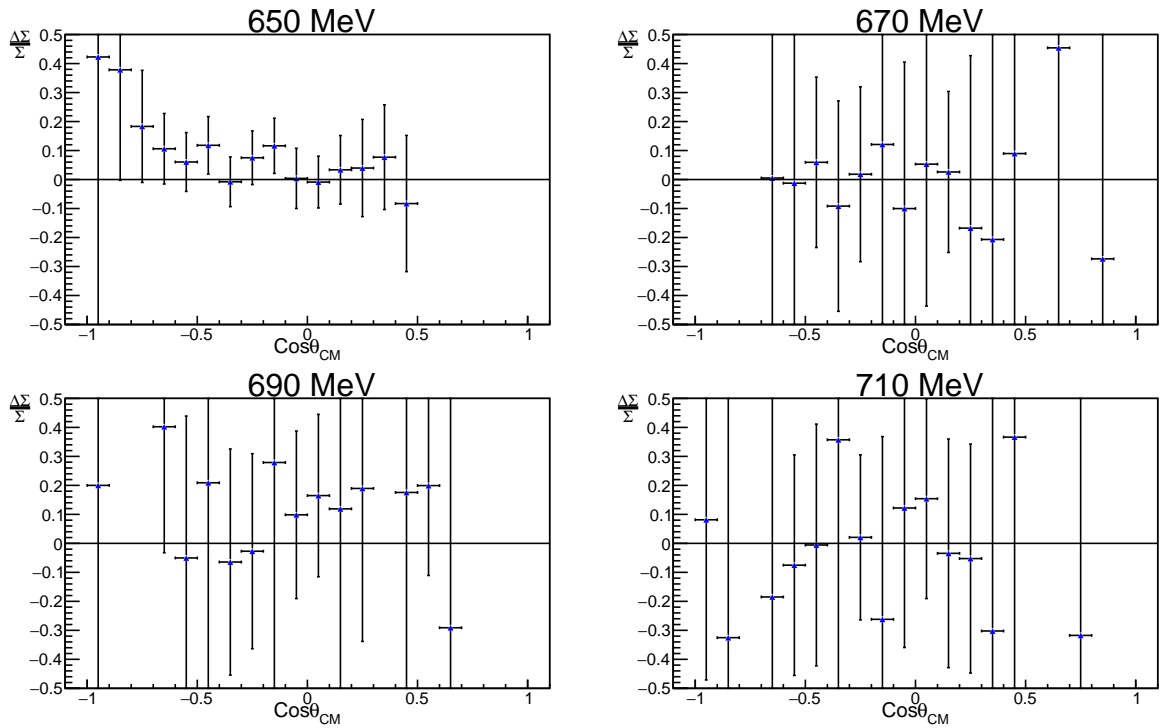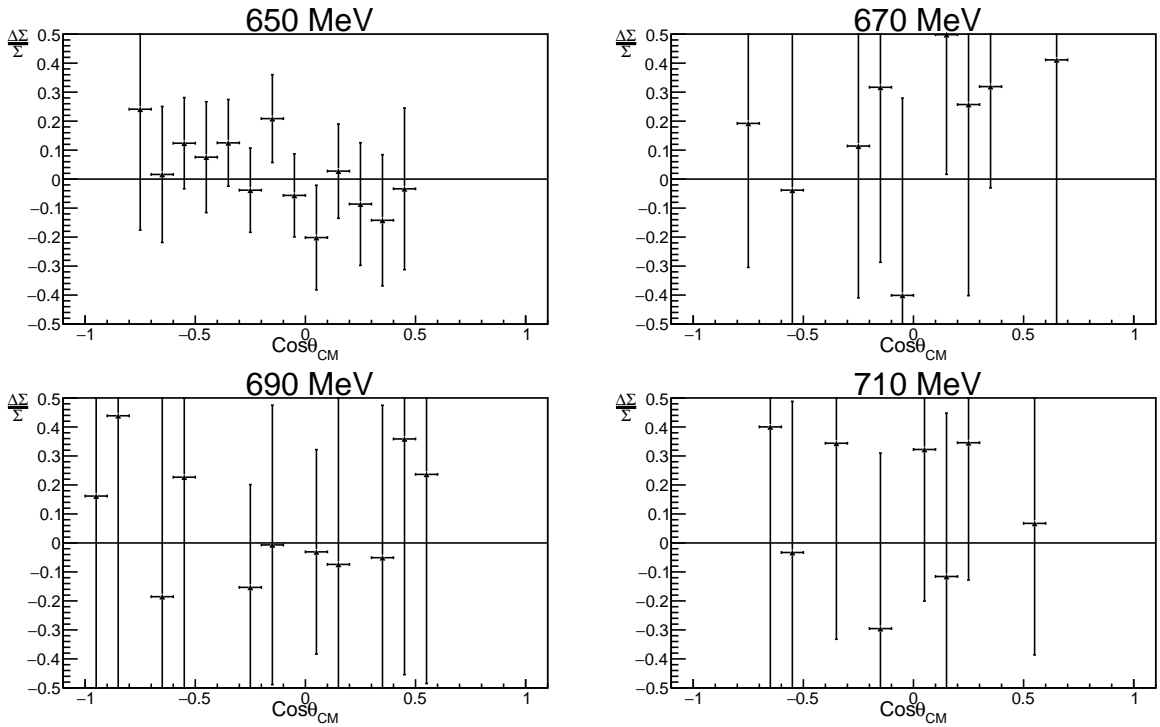
Figure 7.32: Systematic uncertainty from background extraction method. The differences between the WeightsHist and CutsHist methods used for this analysis for the $n\pi^0$ channel for E_γ bins of 650-710 MeV.
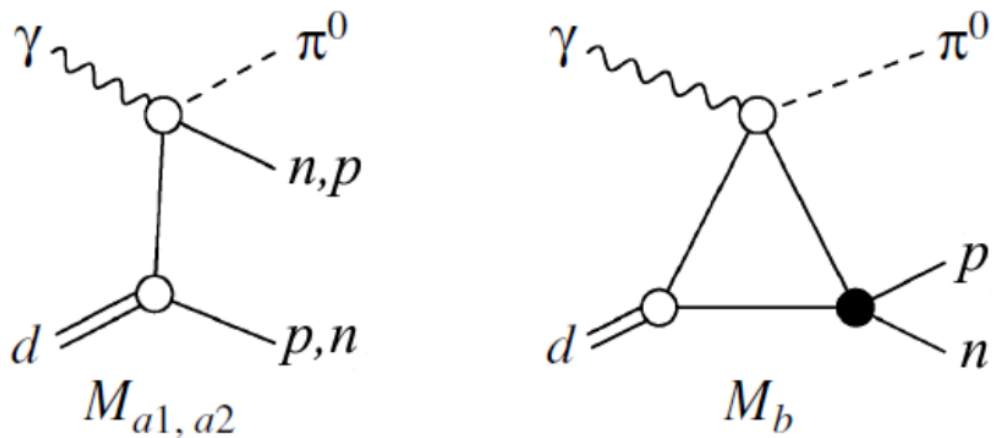
Figure 7.33: Feynman diagrams for the impulse approximation(left) and the NN-FSI(right) for the reaction $\gamma d \rightarrow \pi^0 np$. The wavy, dashed, solid and double lines correspond to the photons, pions, nucleons, and deuterons respectively. Taken from [130].
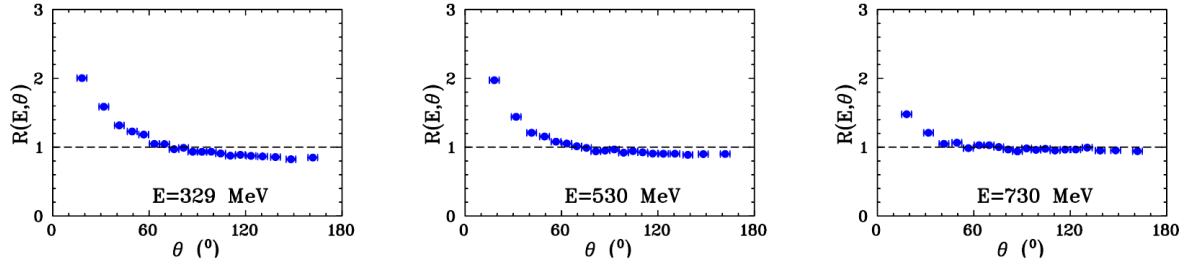
Figure 7.34: The correction factor R(E,Θ) due to final state interactions for the reaction γ d $\rightarrow \pi^0$ np at different energies of incident photon beam. Taken from [130].
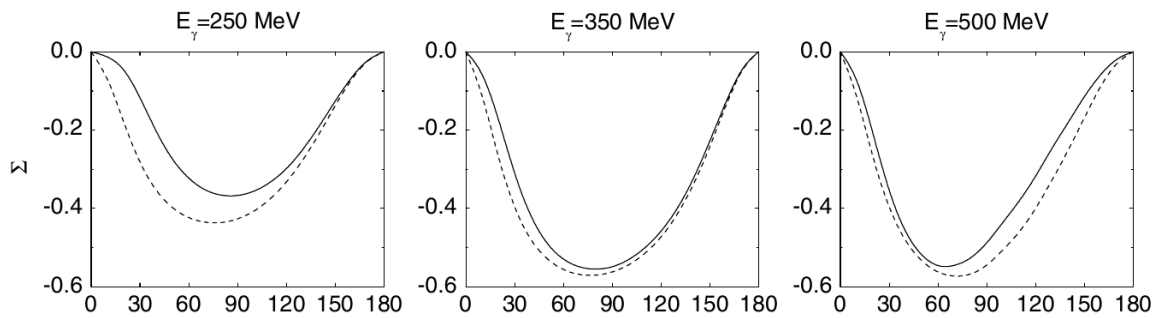
Figure 7.35: Angular distribution of the photon beam asymmetry for the reaction γ d $\rightarrow \pi^0$ np. The dotted(solid) curves are predictions without(with) FSI corrections. Taken from [129]. Note the convention in [129] gives a different sign for Σ.

E_γ	Correction Factor	Statistical Uncertainty
410	0.98	0.03
430	0.92	0.02
450	0.93	0.01
470	0.91	0.01
490	0.87	0.01
510	0.88	0.01
530	0.87	0.01
550	0.90	0.01
570	0.90	0.01
590	0.90	0.01
610	0.89	0.01
630	0.86	0.01
650	0.96	0.03
670	0.93	0.13
690	1.11	0.12
710	1.16	0.13

Table 7.3: Table of the values of the correction factor appled to the data for the August 2016 beamtime.
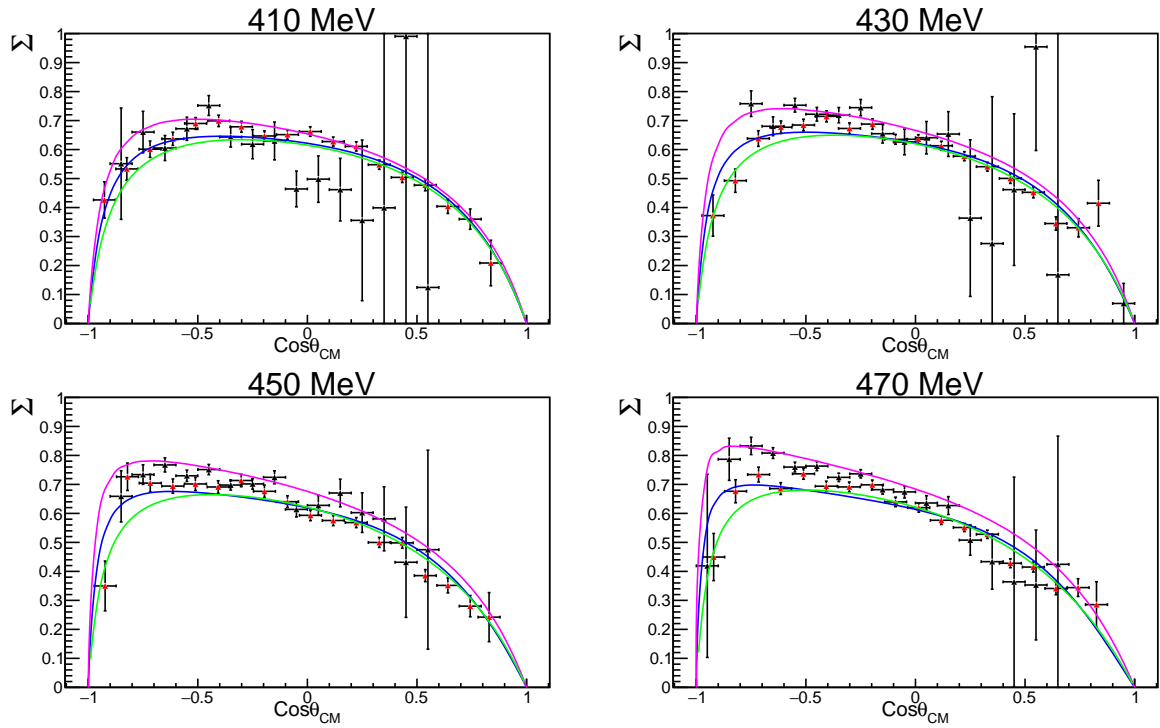
Figure 7.36: Uncorrected results of the photon asymmetry as a function of $\cos\theta$ for the reaction $p\pi^0$. The results from the WeightsML analysis is shown in black and is significantly above previous results showing the need for a correction factor. The photon energy bin is shown at the top of each plot with a width $\pm 10\,\mathrm{MeV}$ and ranges from 410-470 MeV for this plot. Previous data for the reaction is shown in red from Gardner et al. PWA predictions from SAID(blue), MAID(pink) and BnGa(green) are also shown.
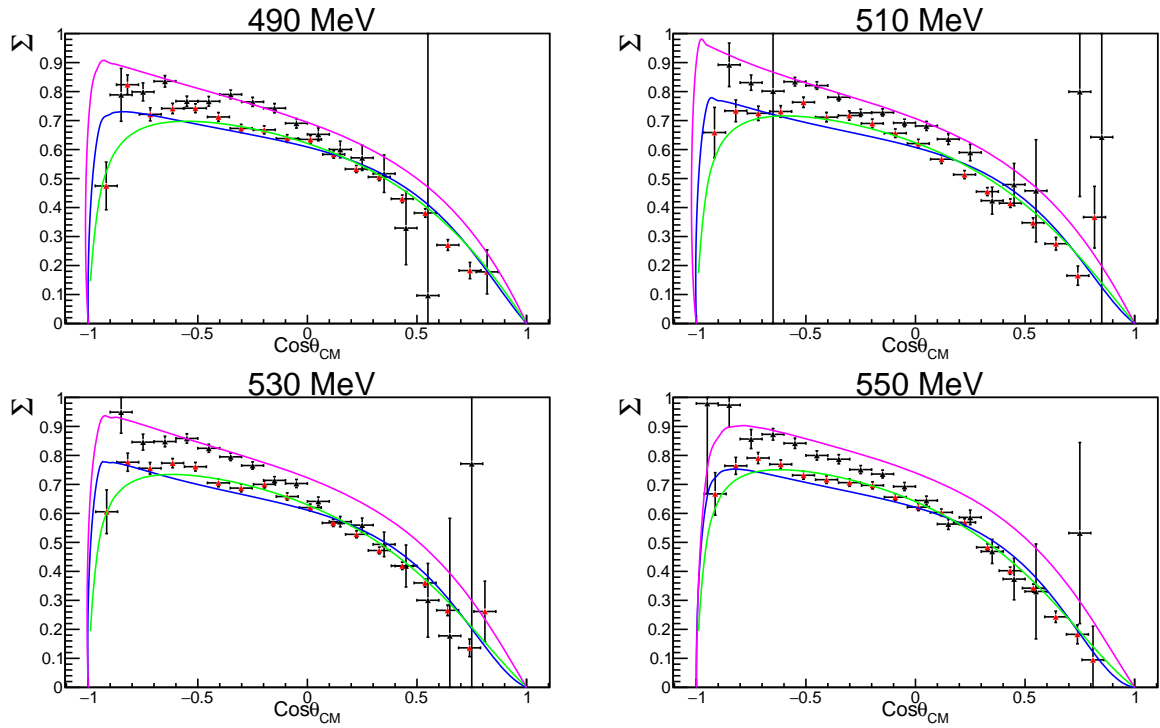
Figure 7.37: Uncorrected results of the photon asymmetry as a function of $\cos\theta$ for the reaction $p\pi^0$. The results from the WeightsML analysis is shown in black and is significantly above previous results showing the need for a correction factor. The photon energy bin is shown at the top of each plot with a width $\pm 10\,\text{MeV}$ and ranges from 490-550$\,$MeV for this plot. Previous data for the reaction is shown in red from Gardner et al. PWA predictions from SAID(blue), MAID(pink) and BnGa(green) are also shown.
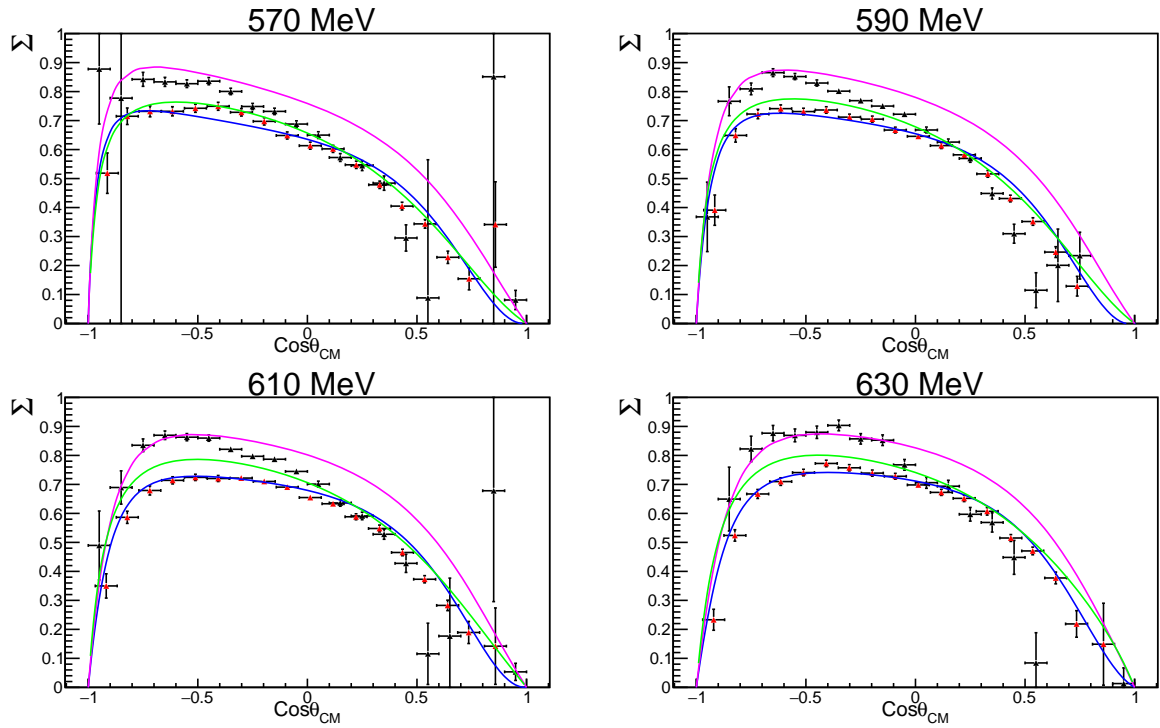
Figure 7.38: Uncorrected results of the photon asymmetry as a function of $\cos\theta$ for the reaction $p\pi^0$. The results from the WeightsML analysis is shown in black and is significantly above previous results showing the need for a correction factor. The photon energy bin is shown at the top of each plot with a width $\pm 10\,\text{MeV}$ and ranges from 570-630 MeV for this plot. Previous data for the reaction is shown in red from Gardner et al. PWA predictions from SAID(blue), MAID(pink) and BnGa(green) are also shown.
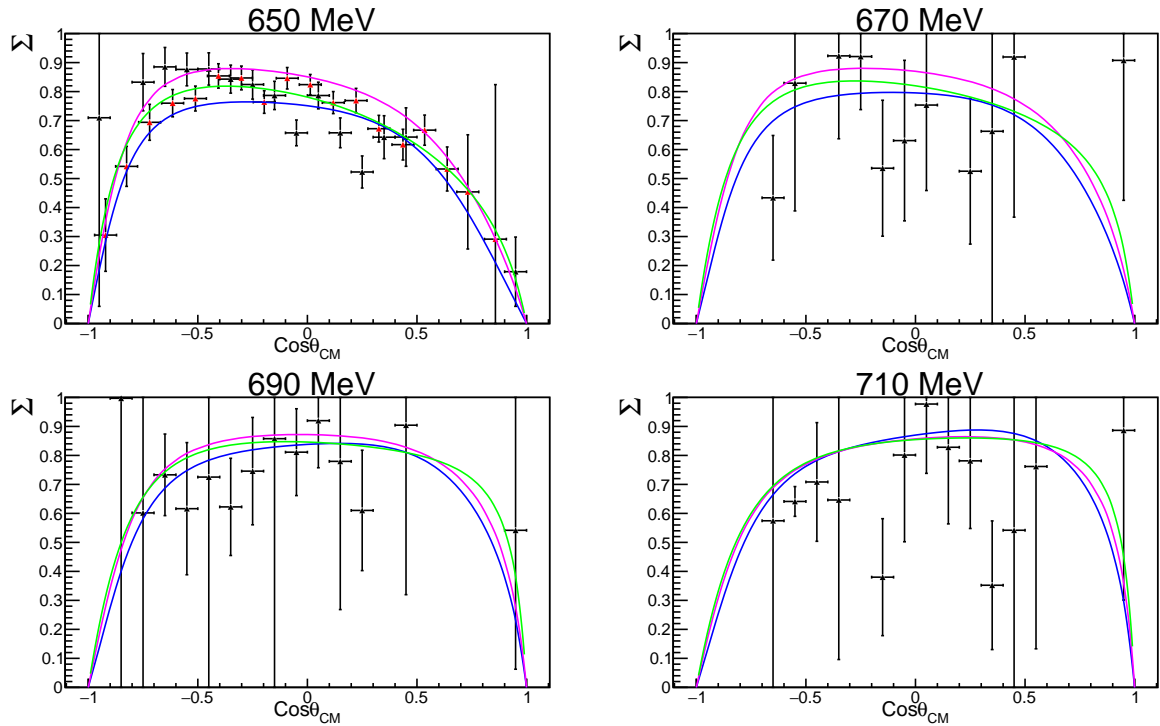
Figure 7.39: Uncorrected results of the photon asymmetry as a function of $\cos\theta$ for the reaction $p\pi^0$. The results from the WeightsML analysis is shown in black and is significantly above previous results showing the need for a correction factor. The photon energy bin is shown at the top of each plot with a width $\pm 10\,\mathrm{MeV}$ and ranges from 650-710 MeV for this plot. Previous data for the reaction is shown in red from Gardner et al. PWA predictions from SAID(blue), MAID(pink) and BnGa(green) are also shown.
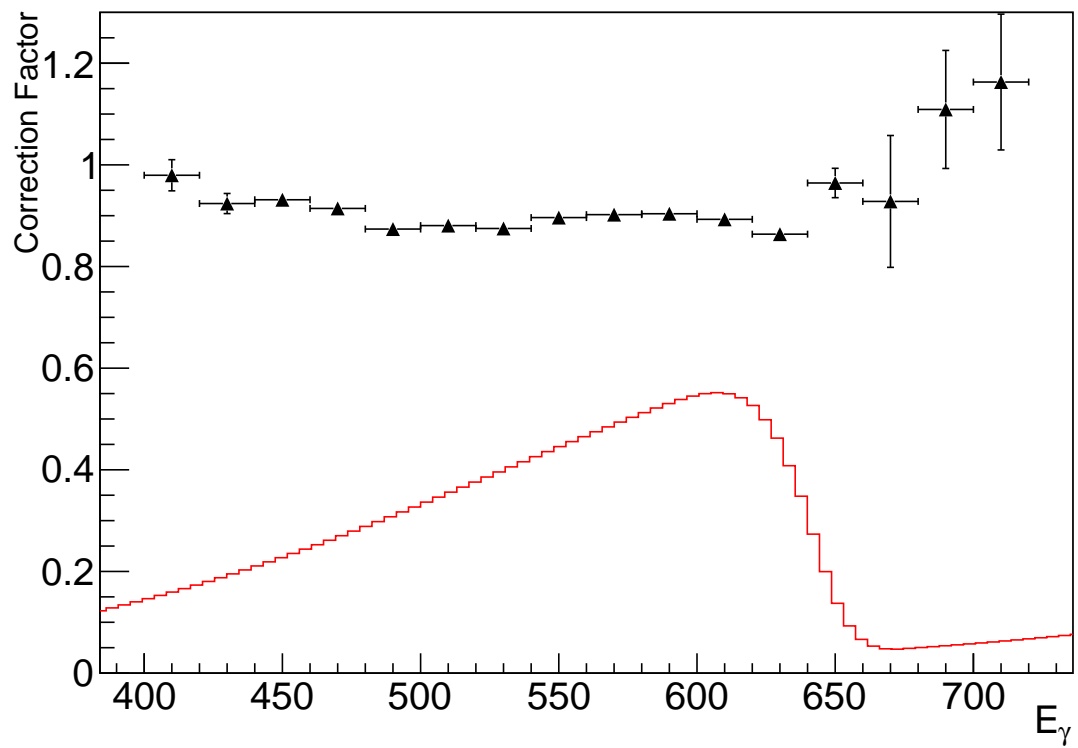
Figure 7.40: The correction factor as a function of photon beam energy calculated from the SAID PWA predictions. The magnitude of the linear polarisation is shown in red.

Chapter 8

Results

Measurements of the beam asymmetry polarisation observables, Σ, are presented in this thesis for single π^0 photoproduction off the proton and neutron. By comparing these results to predictions from partial wave analyses, as discussed in Section 3.2, we get a strong indictation of how well their analysis can describe the photoproduction process. The neutron channel in particular provides the first data in this energy range providing a test for the predicative power of the partial wave analyses and in particular indicating where values of resonance decay couplings could be improved.

8.1 Beam Asymmetry:- γp $\rightarrow$ p π^0

The beam asymmetry polarisation observable Σ has been measured for the final state γp$\rightarrow$pπ^0 across a wide range of photon beam energies, E_γ, and $\cos\theta_{CM}$ angles. Previous measurements of the channel by Gardner et al [67] on a hydrogen target allow for a comparison of free proton results with quasi-free proton measurements on the deuteron presented here. The results span the photon beam energy range of 400-720 MeV in bins of 20 MeV with 15 $\cos\theta_{CM}$ bins from -1 to 0.5. These are compared to a series of predictions from PWAs from SAID [79, 92], MAID [80, 91] and Bonn Gatchina [81, 95]. The full results are presented in Figures 8.1 to 8.4. They are compared with the results from Gardner et al. Overall a good agreement between the two data sets is seen. Results from Gardner et al. on a hydrogen target benefited from higher acceptance at
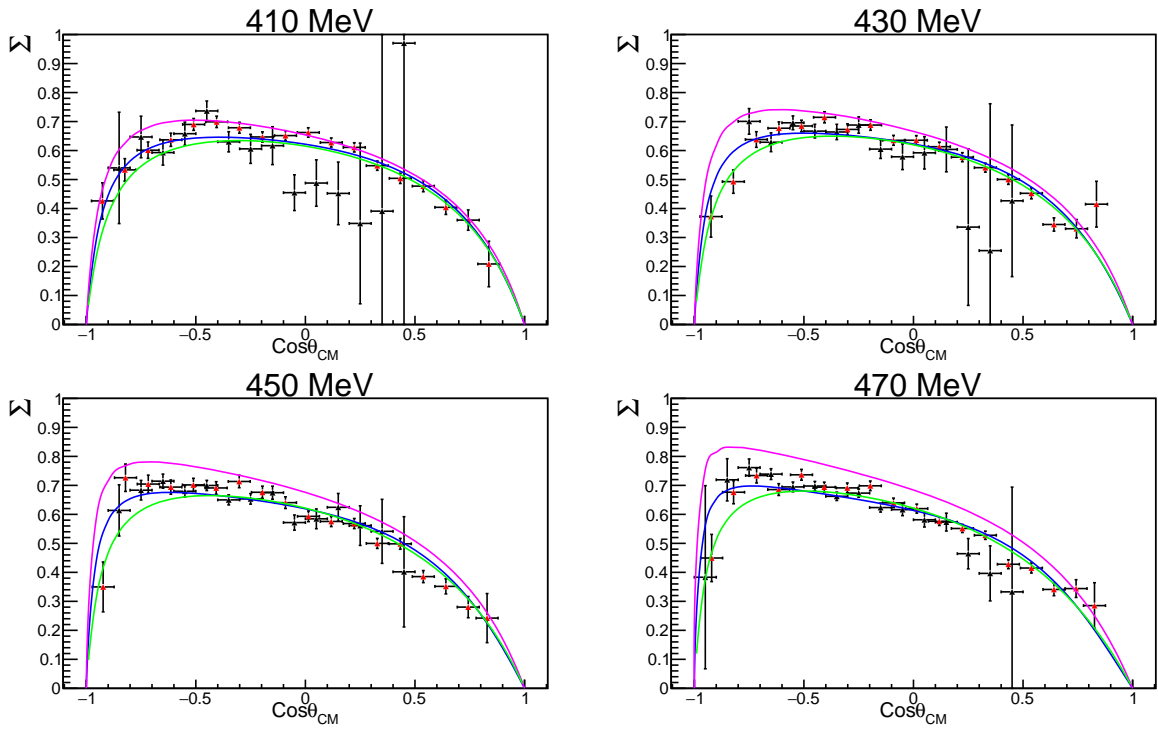
Figure 8.1: Photon asymmetry as a function of $\cos\theta$ for the reaction $p\pi^0$. The results from the WeightsML analysis is shown in black. The photon energy bin is shown at the top of each plot with a width ± 10 MeV. Previous data for the reaction is shown in red from Gardner et al. PWA predictions from SAID(blue), MAID(pink) and BnGa(green) are also shown.

forward angles as they were not required to measure the low energy proton recoiling at backward angles. The current analysis required this to distinguish between π^0s produced on the proton and neutron. A good agreement is also observed between these results and the SAID PWA predictions. There is some discrepancies with SAID at higher energies and forward angles. This could be due to a combination of the proton acceptance at forward angles and the Fermi motion from the deuterium target resulting in a shift in $\cos\theta$ angle since we are more likely to detect protons having a higher boost from Fermi motion. This could also stem from FSI effects as discussed in Section 7.4. The MAID PWA has not been updated since 2007 and so does not take the significant new data in recent years into account. This is the reason the PWA is significantly different than the other two.

A correction to the linear polarisation was required to obtain these results as outlined in Section 7.5. As the Σ observable for this channel has been extensively measured in this energy region previously, it was used as a polarimeter to correct for the systematic shift in the linear polarisation.
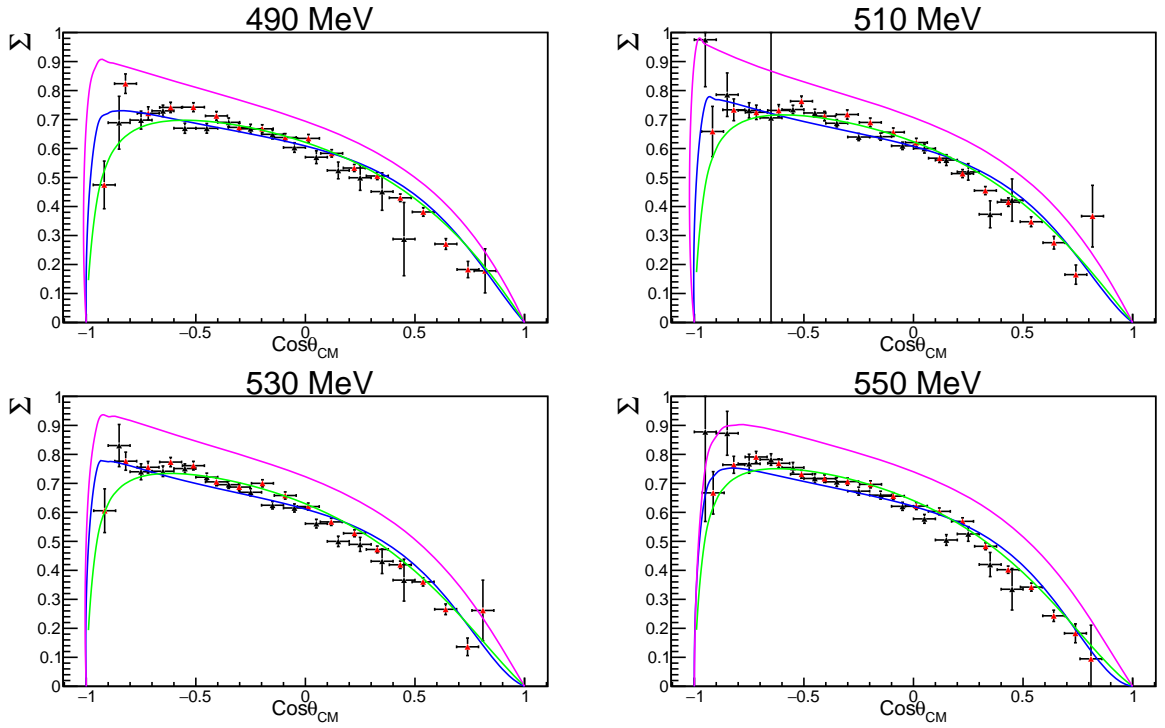
Figure 8.2: Photon asymmetry as a function of $\cos\theta$ for the reaction $p\pi^0$. The results from the WeightsML analysis is shown in black. The photon energy bin is shown at the top of each plot with a width $\pm 10\,\text{MeV}$. Previous data for the reaction is shown in red from Gardner et al. PWA predictions from SAID(blue), MAID(pink) and BnGa(green) are also shown.

8.2   Beam Asymmetry:- $\gamma n \rightarrow n\ \pi^0$

The beam asymmetry polarisation observable Σ has been measured for the final state $\gamma\,n\rightarrow n$ π^0 across the full $\cos\theta_{CM}$ range and a wider photon beam energy than the proton channel. The results span a photon beam energy range of 240-720 MeV in bins of 20 MeV with 20 $\cos\theta_{CM}$ bins from 1 to -1. These measurements are extended to lower photon beam energies due to the uncharged neutron not losing energy as it travels to the calorimeter. The protons at lower energies lose all their energy in the material between the target and calorimeter and are not detected. There are no previous neutron channel measurements in this energy region for comparison. However, the results are compared to PWA predictions from MAID [80, 91], SAID [79, 92] and Bonn Gatchina [81, 95].

The results are shown in Figures 8.5 to 8.10 with comparison to the relevant PWA predictions. An overall good agreement between the results and the PWA predictions from SAID is observed. The latest SAID model labelled ma19 includes fits to neutron cross-section data in
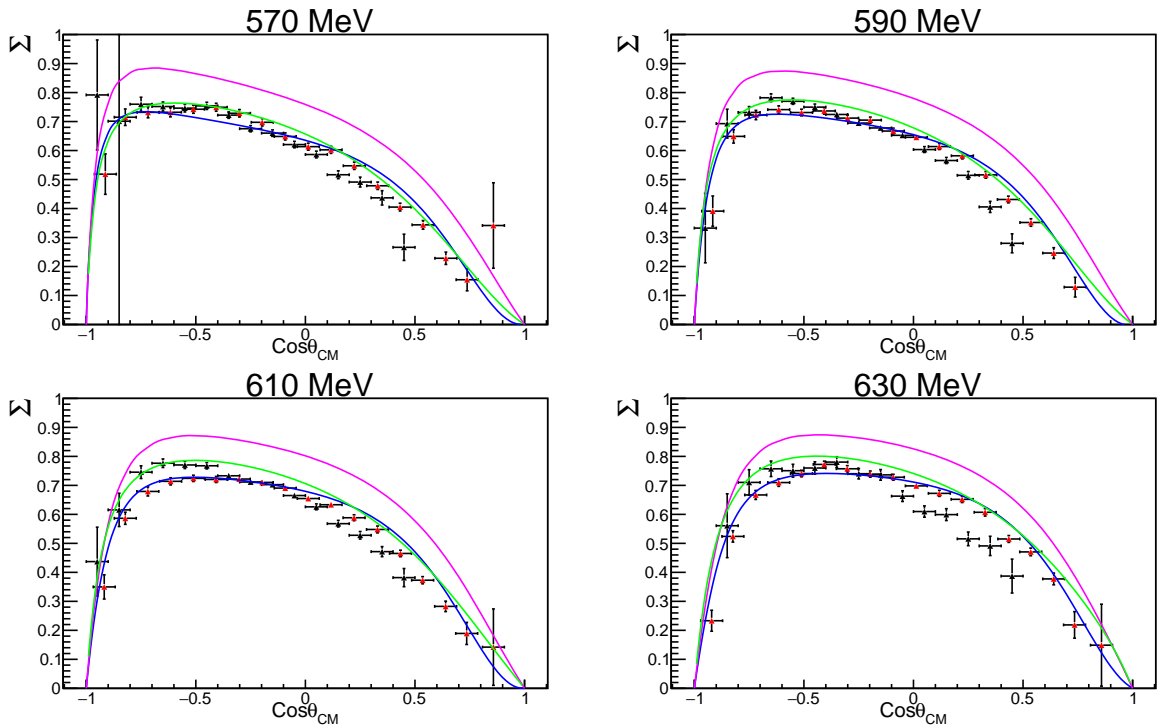
Figure 8.3: Photon asymmetry as a function of $\cos\theta$ for the reaction $p\pi^0$. The results from the WeightsML analysis is shown in black. The photon energy bin is shown at the top of each plot with a width $\pm 10\,\mathrm{MeV}$. Previous data for the reaction is shown in red from Gardner et al. PWA predictions from SAID(blue), MAID(pink) and BnGa(green) are also shown.

the region 290-813 MeV from [130]. Interestingly at higher energies the results presented here favour the older SAID model CM12. This may be due to changes to the photon decay amplitudes at the pole for neutron couplings $A_{1/2}(n)$ and $A_{3/2}(n)$ for the Roper resonance and the $N(1535)1/2^-$ and the introduction of the $N(1520)$ $1/2^-$ and $3/2^-$ to the latest SAID predictions.

8.3   Systematic Uncertainties

Two main sources of systematic uncertainty on the results presented here have been examined. The method of background subtraction and the effect of applying the correction factor have all been investigated.

The uncertainty from the background subtraction is discussed in Section 7.3. The fractional difference between the CutsHist and WeightsHist methods give an estimate of the systematic uncertainty in background subtraction method for each point. The CutsHist method is expected to
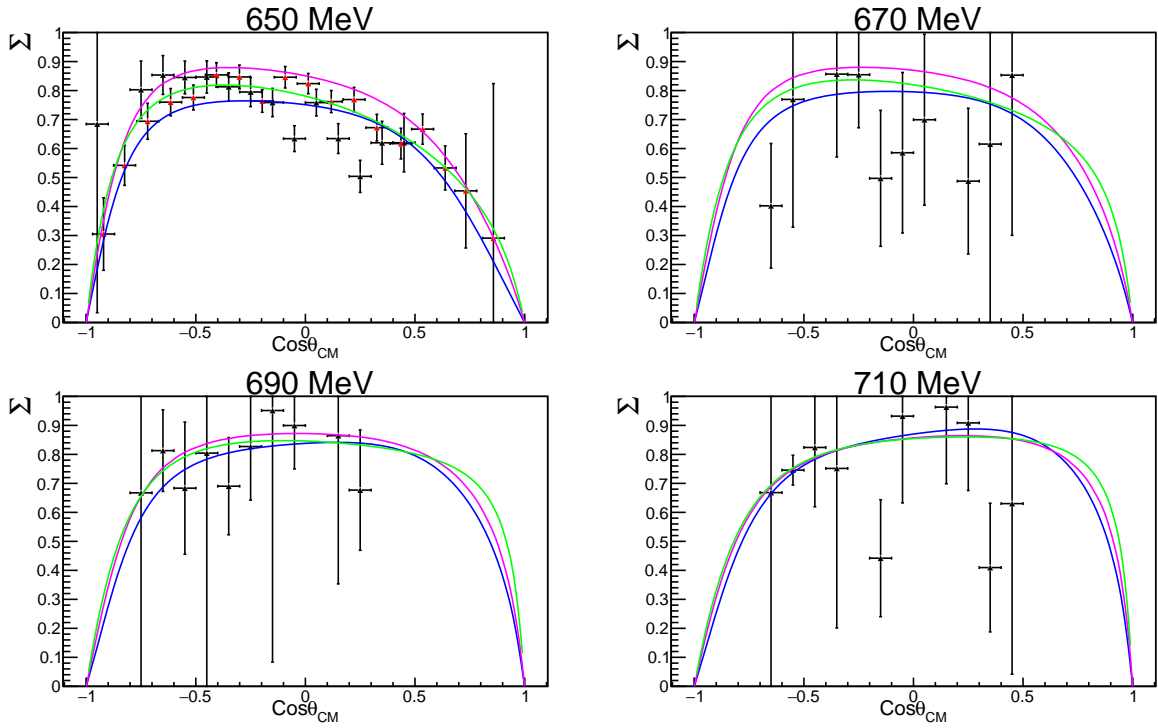
Figure 8.4: Photon asymmetry as a function of $\cos\theta$ for the reaction $p\pi^0$. The results from the WeightsML analysis is shown in black. The photon energy bin is shown at the top of each plot with a width $\pm 10\,\mathrm{MeV}$. Previous data for the reaction is shown in red from Gardner et al. PWA predictions from SAID(blue), MAID(pink) and BnGa(green) are also shown.

retain some small amount of background as outlined in Table 6.2 while the WeightsHist method is expected to remove all the background. Any error in the subtraction of the background by the weights based method is expected to be less than the effect of not subtracting the background. Hence, the difference between the non-subtracted and subtracted results is used as a conservative estimate of this uncertainty. Typically the amount of background subtracted using the coplanarity weights was around 14%. The mean for each E_γ bin is given in Tables 7.1 and 7.2 and is typically around 4% for the proton channel and 3% for the $n\pi^0$ channel. For bins greater than $630\,\mathrm{MeV}$ the uncertainty increases due to low statistics and relatively greater background coming from two pion production channels. This effect is also evident in the $n\pi^0$ bins below $300\,\mathrm{MeV}$. The full list of systematic uncertainties from the background subtraction can be found in Appendix A for both channels.

The correction factor applied to the data introduces a systematic uncertainty to each E_γ bin. Each factor was calculated using the statistical uncertainties of the five experimental data points used in the weighted mean(see Section 7.5) to determine an uncertainty for the correction
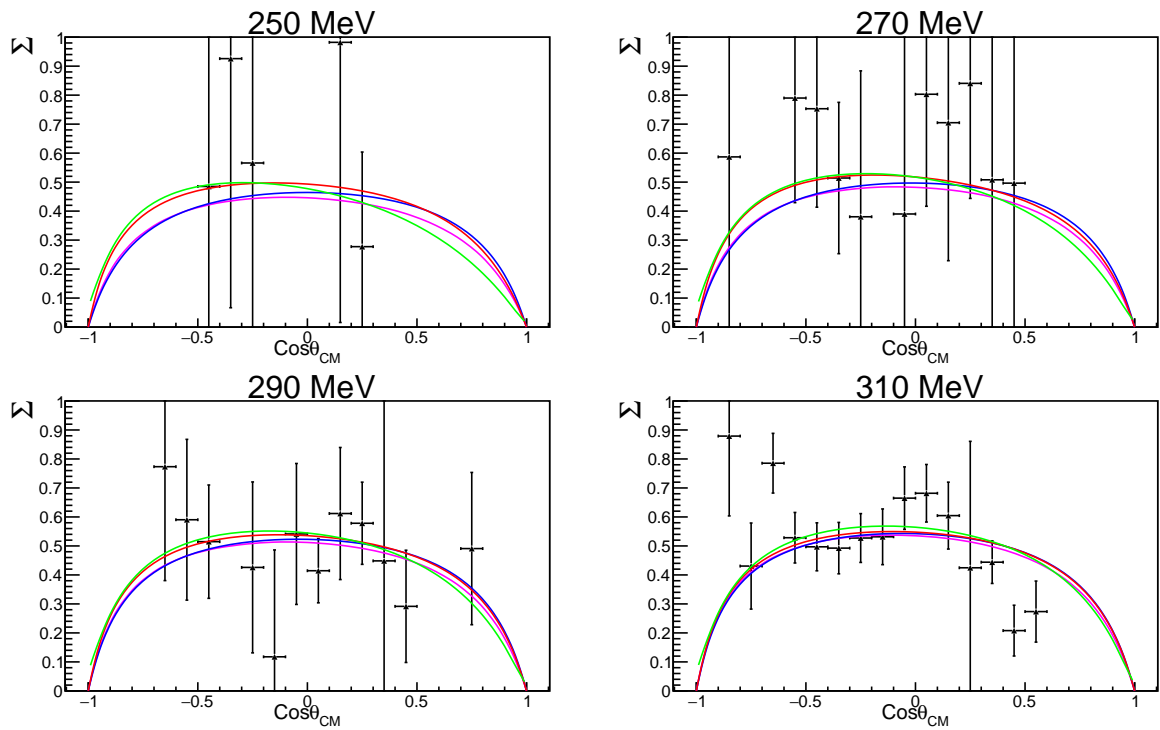
Figure 8.5: Photon asymmetry as a function of $\cos\theta$ for the reaction $n\pi^0$. The results from the WeightsML analysis are shown in black. The photon energy bin is shown at the top of each plot with a width $\pm 10\,\text{MeV}$. PWA predictions from SAID(blue), MAID(pink) and BnGa(green) are also shown. The latest SAID prediction taking account of new cross section data for the neutron channel is shown in red.
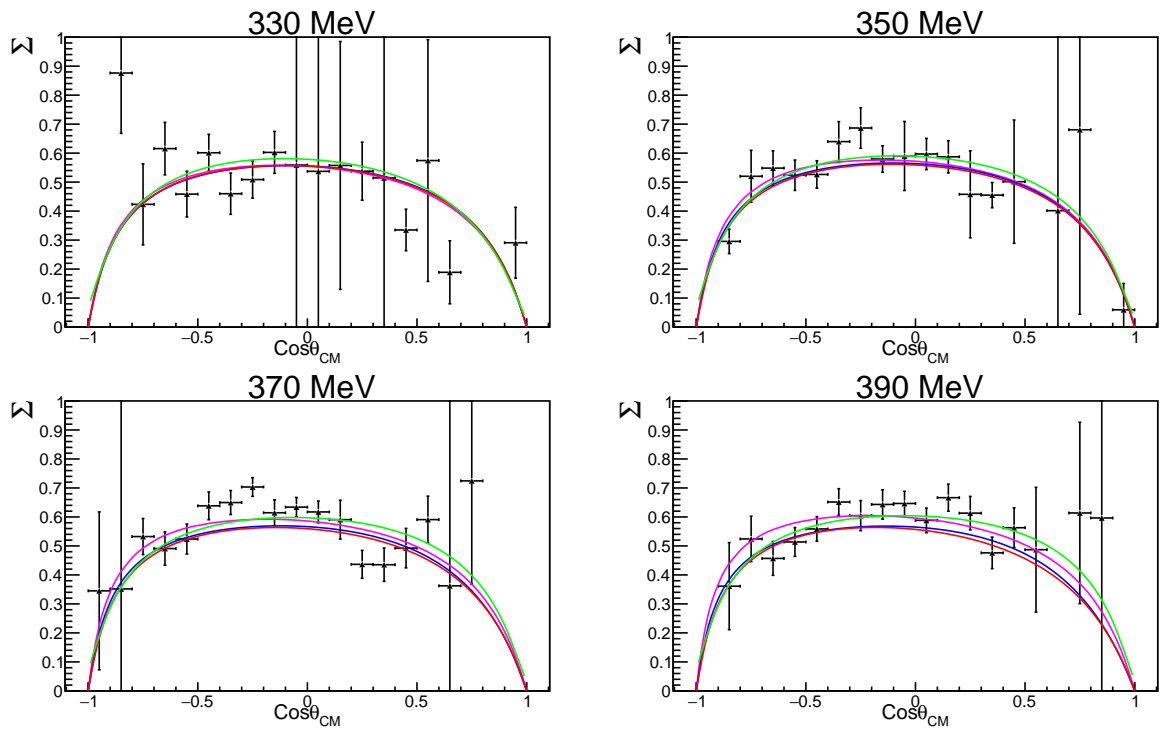
Figure 8.6: Photon asymmetry as a function of $\cos\theta$ for the reaction $n\pi^0$. The results from the WeightsML analysis are shown in black. The photon energy bin is shown at the top of each plot with a width $\pm10\,$MeV. PWA predictions from SAID(blue), MAID(pink) and BnGa(green) are also shown. The latest SAID prediction taking account of new cross section data for the neutron channel is shown in red.
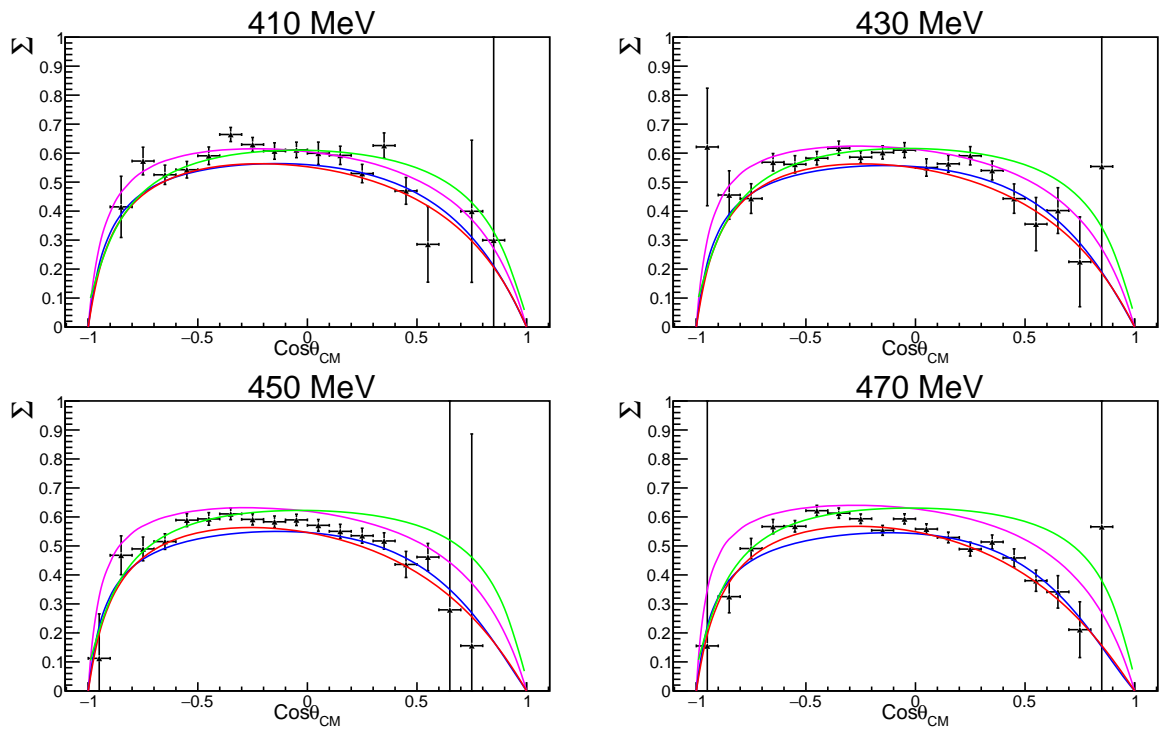
Figure 8.7: Photon asymmetry as a function of $\cos\theta$ for the reaction $n\pi^0$. The results from the WeightsML analysis are shown in black. The photon energy bin is shown at the top of each plot with a width $\pm 10\,\text{MeV}$. PWA predictions from SAID(blue), MAID(pink) and BnGa(green) are also shown. The latest SAID prediction taking account of new cross section data for the neutron channel is shown in red.
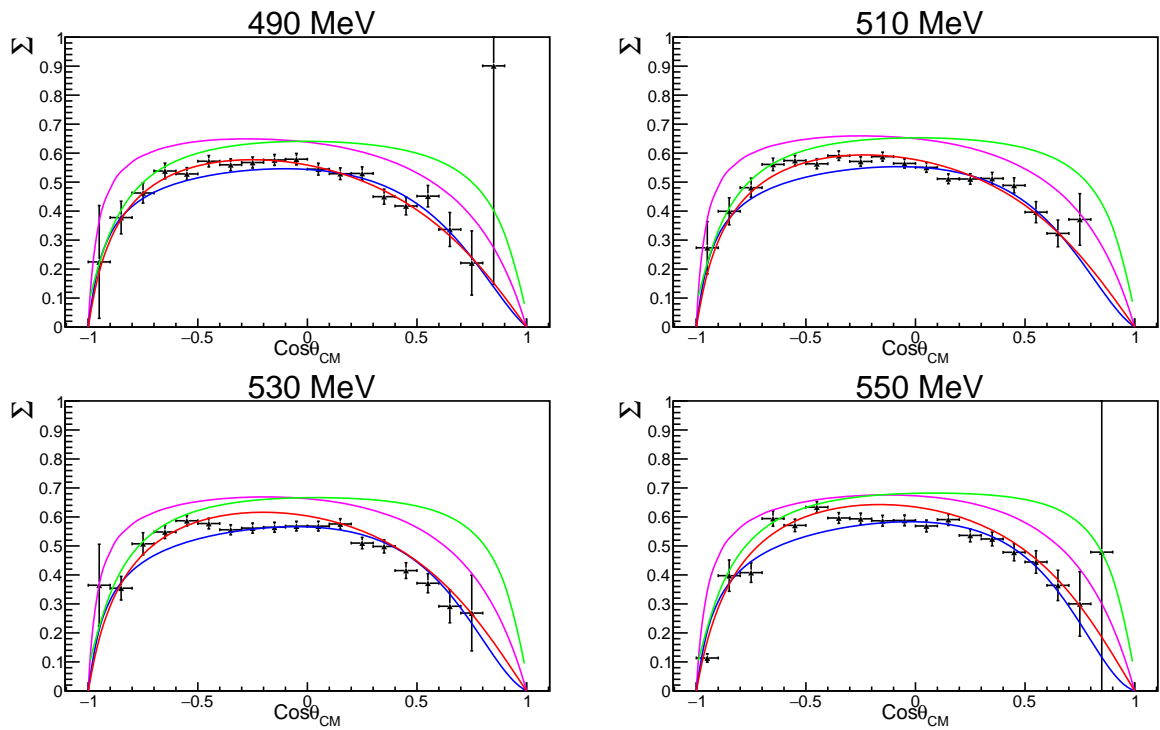
Figure 8.8: Photon asymmetry as a function of $\cos\theta$ for the reaction $n\pi^0$. The results from the WeightsML analysis are shown in black. The photon energy bin is shown at the top of each plot with a width $\pm10\,$MeV. PWA predictions from SAID(blue), MAID(pink) and BnGa(green) are also shown. The latest SAID prediction taking account of new cross section data for the neutron channel is shown in red.
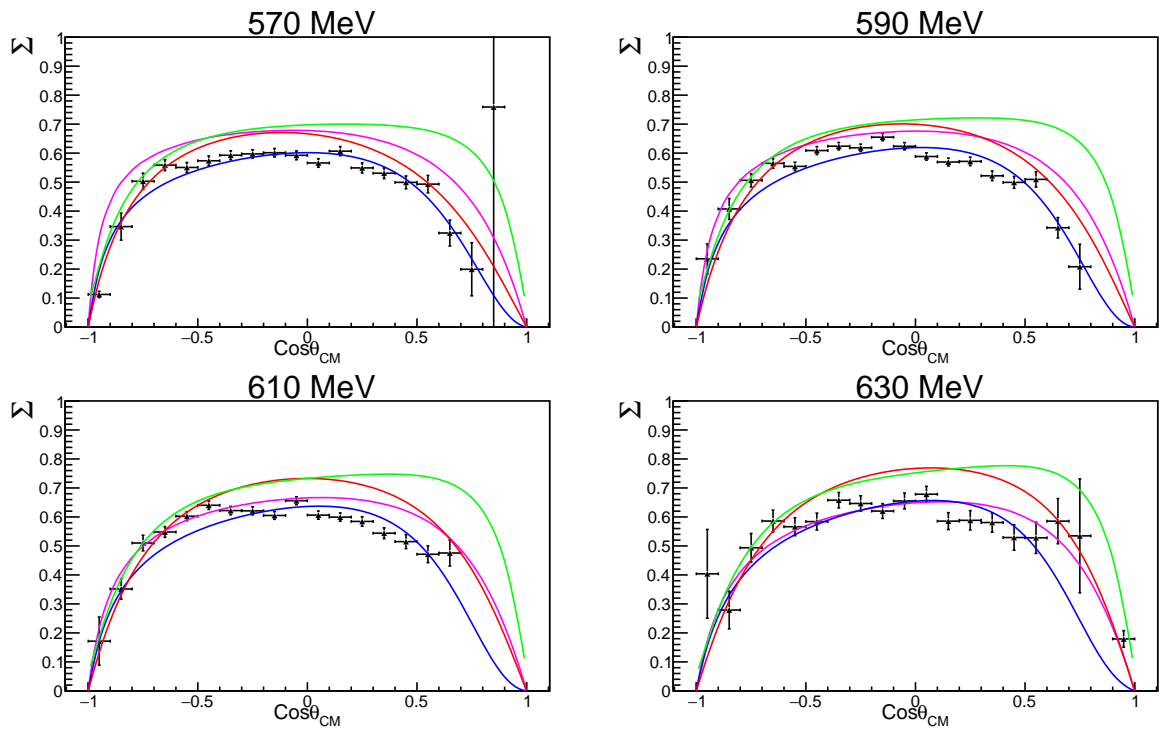
Figure 8.9: Photon asymmetry as a function of $\cos\theta$ for the reaction $n\pi^0$. The results from the WeightsML analysis are shown in black. The photon energy bin is shown at the top of each plot with a width $\pm 10\,\text{MeV}$. PWA predictions from SAID(blue), MAID(pink) and BnGa(green) are also shown. The latest SAID prediction taking account of new cross section data for the neutron channel is shown in red.
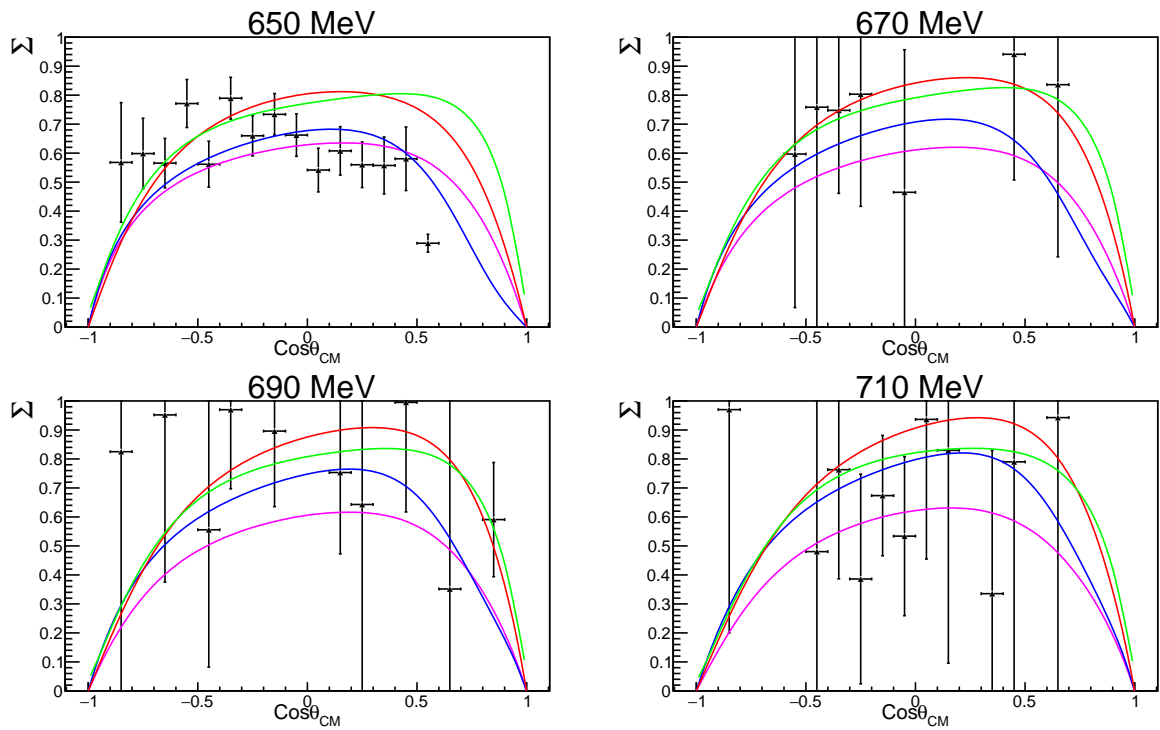
Figure 8.10: Photon asymmetry as a function of $\cos\theta$ for the reaction $n\pi^0$. The results from the WeightsML analysis are shown in black. The photon energy bin is shown at the top of each plot with a width ± 10 MeV. PWA predictions from SAID(blue), MAID(pink) and BnGa(green) are also shown. The latest SAID prediction taking account of new cross section data for the neutron channel is shown in red.
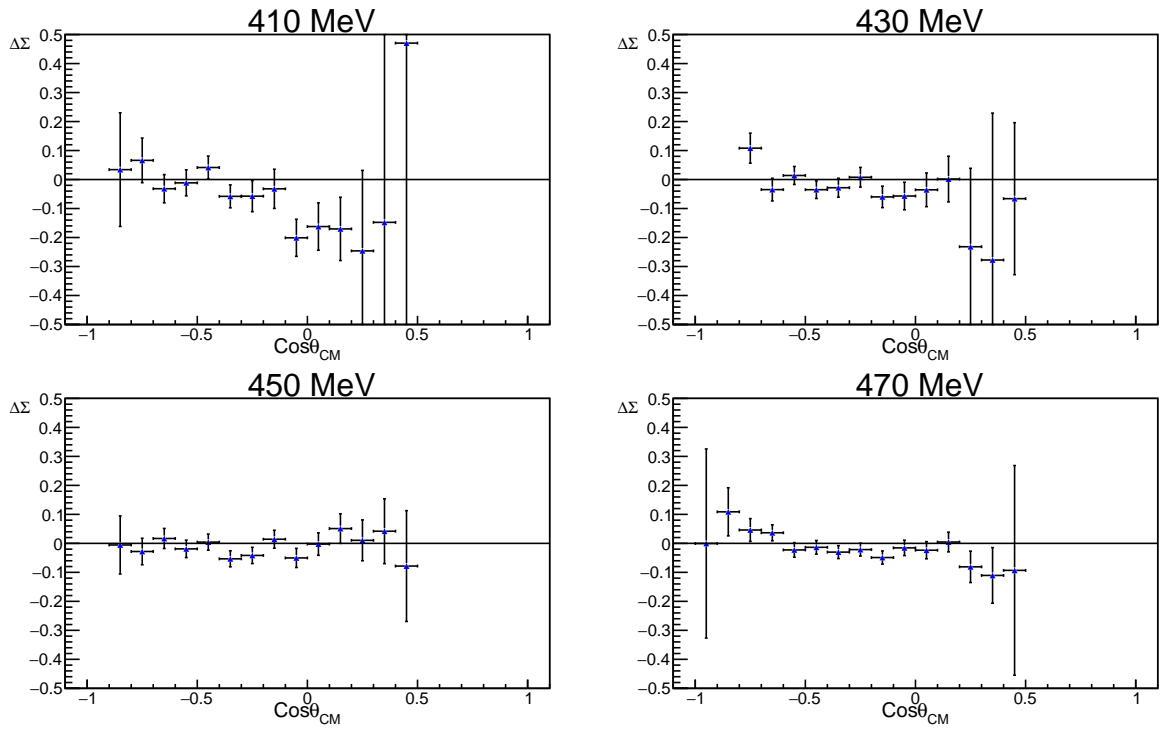
Figure 8.11: A comparison of the difference between WeightsML results presented here to Gardner et al.

factor. The statistical uncertainty on the points in this region is less than 2% so the systematic is taken from SAID to be 2%. We can observe the efficacy of such a correction by examining the difference between the corrected results and the previous results from Gardner et al. as these results are of significant input to the PWAs in this region. This difference is shown in Figures 8.11 to 8.14.   In general a reasonable agreement is shown but with significant deviations at higher energies and forward angles are observed. Forward angles are more likely to have larger effects from final state interactions due to the deuterium target as discussed in Section 7.4. The cross sections are expected to be significantly(50-100%) reduced with polarisation observables less so, but the 10% reduction observed is consistent with [129].

8.4   Conclusion

This thesis presents results of the photon beam asymmetry polarisation observable Σ for π^0 photoproduction from a liquid deuterium target. The results from the $\gamma p \rightarrow \pi^0 p$ reaction channel are in good agreement with previous measurements and PWA predictions after application of a
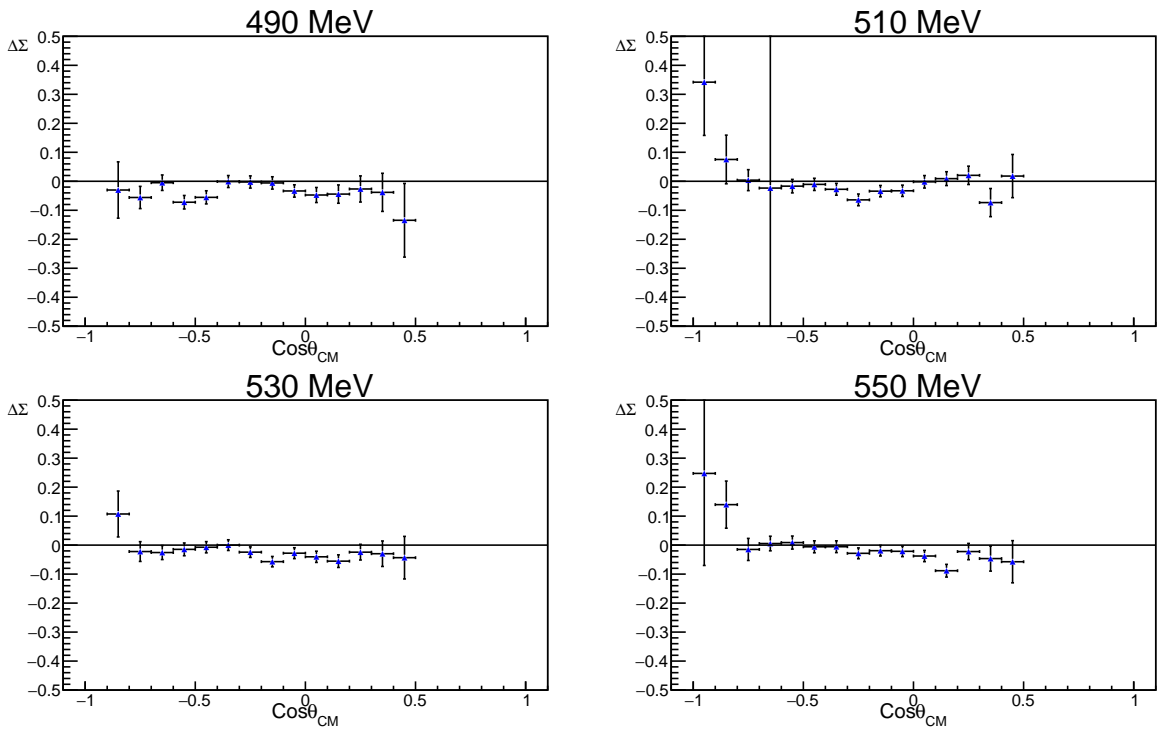
Figure 8.12: A comparison of the difference between WeightsML results presented here to Gardner et al.
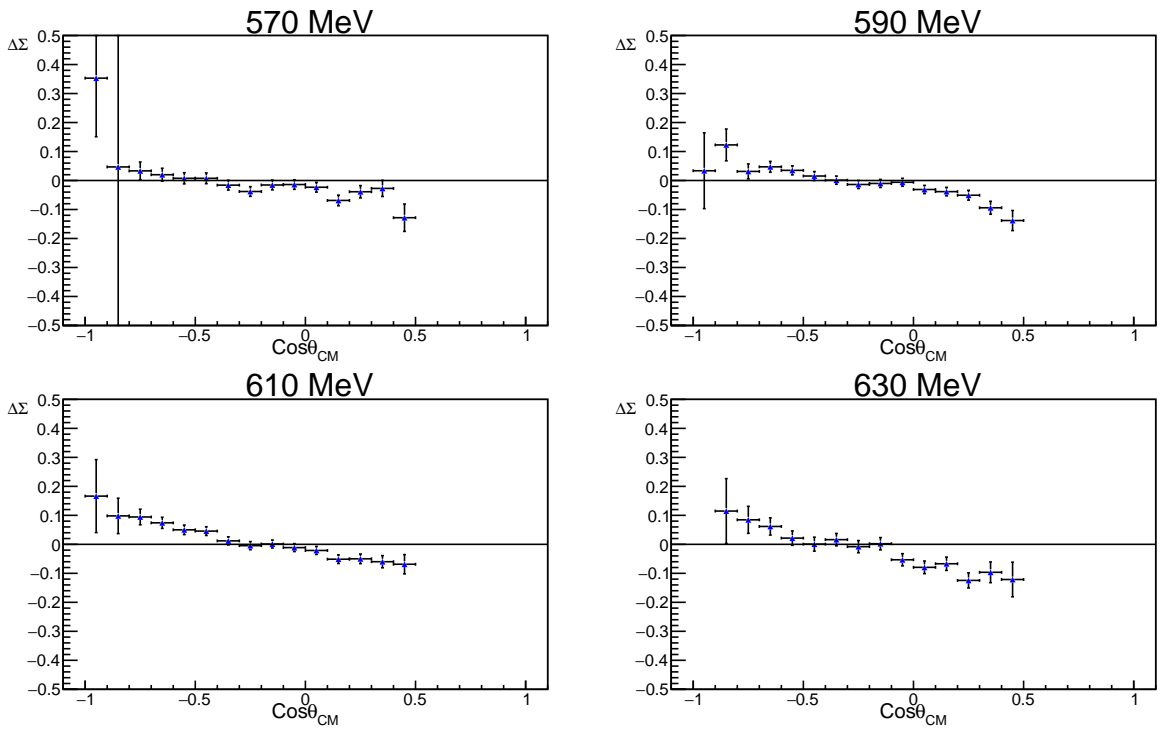
Figure 8.13: A comparison of the difference between WeightsML results presented here to Gardner et al.
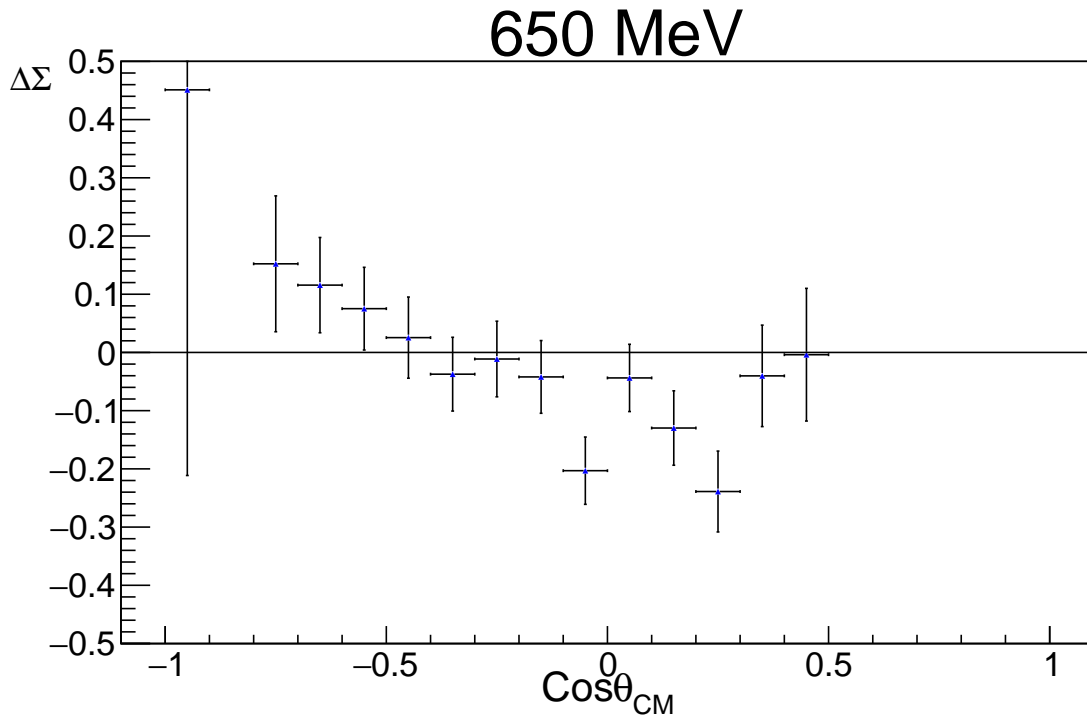
Figure 8.14: A comparison of the difference between WeightsML results presented here to Gardner et al.

correction factor. A large pool of measurements in this region are available for comparison and can be used as a quality check for these results. A correction factor due to the systematic shift from the linear polarisation determination was calculated from the SAID PWA predictions in the region and applied. This brought the results into good agreement with previous measurements and predictions.

The results for the $\gamma n \rightarrow \pi^0 n$ reaction channel represent the first measurements in this energy regime spanning a range of $240 < E_\gamma < 720$ MeV. The application of the correction factor to these measurements resulted in a good agreement with PWA predictions. A more favourable agreement was found with the older SAID model which did not include the new cross section data ([130]) for this channel in this energy range.

The different analysis methods applied to both channels all resulted in good agreement with each other suggesting that the sPlots technique and extended maximum likelihood fitting reliably extracted the observable in question. The systematic uncertainties associated with these event selection methods are small. The calibration of the degree of linear polarisation via the coherent bremsstrahlung enhancement fitting method was subject to a large systematic uncertainty due

to the technical constraints of the experiment. The use of the proton channel as a polarimeter to scale the polarisation resulted in a good agreement with previous data and provided a more reliable degree of polarisation with a systematic uncertainty of 2%.

The recently measured new cross-section data available on the neutron channel will allow a moment analysis to be carried out where the angular distributions of the profile function of the beam asymmetry are fitted with Legendre polynomials. The fitted coefficients can then be compared to model predictions to draw conclusions about the contributing partial waves. A similar analysis has been completed on proton data from a hydrogen target [67]. It showed that up to $430\,\mathrm{MeV}$ the data could be described by using only S- and P-waves. However, above this energy the introduction of D-waves were necessary for a good fit and a slight improvement was made with the inclusion of F-waves. This indicates an interference between the small F-waves and the resonances of the $\mathrm{N}(1520)\frac{3}{2}^-$, $\mathrm{N}(1535)\frac{1}{2}^-$ and $\mathrm{N}(1440)\frac{1}{2}^+$. The recent cross section data allowed determination of the photon decay amplitudes for the neutron $A_{\frac{1}{2}}(\mathrm{n})$ and $A_{\frac{3}{2}}(\mathrm{n})$ for five N* resonances. These results, particularly the π^0 n channel, provide current models attempting to describe the nucleon resonance spectrum with important input. The first measurements on the neutron are essential to determine isospin amplitudes of the nucleon resonance spectrum. Refitting with the first measurements of the beam asymmetry for neutron π^0 photoproduction in the region of these resonances will allow for a more reliable extraction of the photon decay amplitudes.

Appendix A

Tabulated Results

Values for the full results of the photon beam asymmetry Σ for the reactions $\gamma d \to \pi^0\, p(n_{spec})$ and $\gamma d \to \pi^0\, n(p_{spec})$. All results are reproducecd here including bins in which fits failed due to insufficient statistics. A large statistical uncertainty is an indicator of this.

Table A.1: The p π^0 channel results covering an E_γ range of 410 Mev to 710 MeV and a $\cos\theta$ range of -1 to 0.5. The statistical uncertainty is listed as σ_{stat} with σ_{pol} the uncertainty in the polarisation correction and σ_{bg} the uncertainty in the background subtraction.

Cos(θ)	Energy(MeV)	Σ	σ_{stat}	σ_{pol}	σ_{bg}
-1→-0.9	410	1.38	2	0.028	0.055
-0.9→-0.8	410	0.54	0.192	0.011	0.021
-0.8→-0.7	410	0.65	0.071	0.013	0.026
-0.7→-0.6	410	0.59	0.043	0.012	0.024
-0.6→-0.5	410	0.66	0.040	0.013	0.026
-0.5→-0.4	410	0.74	0.034	0.015	0.029
-0.4→-0.3	410	0.63	0.035	0.013	0.025
-0.3→-0.2	410	0.61	0.050	0.012	0.024
-0.2→-0.1	410	0.62	0.065	0.012	0.025

-0.1→0.0	410	0.45	0.062	0.009	0.018
0.0→0.1	410	0.49	0.080	0.010	0.019
0.1→0.2	410	0.45	0.108	0.009	0.018
0.2→0.3	410	0.35	0.277	0.007	0.014
0.3→0.4	410	0.39	2.673	0.008	0.015
0.4→0.5	410	0.97	7.376	0.019	0.039
-1→-0.9	430	-0.55	2.88	0.011	0.02
-0.9→-0.8	430	-0.90	1.68	0.018	0.03
-0.8→-0.7	430	0.70	0.044	0.014	0.029
-0.7→-0.6	430	0.63	0.032	0.013	0.026
-0.6→-0.5	430	0.70	0.024	0.014	0.029
-0.5→-0.4	430	0.67	0.024	0.013	0.027
-0.4→-0.3	430	0.66	0.026	0.013	0.027
-0.3→-0.2	430	0.69	0.028	0.014	0.028
-0.2→-0.1	430	0.60	0.032	0.012	0.025
-0.1→0.0	430	0.58	0.044	0.012	0.024
0.0→0.1	430	0.59	0.056	0.012	0.024
0.1→0.2	430	0.60	0.077	0.012	0.025
0.2→0.3	430	0.34	0.270	0.007	0.014
0.3→0.4	430	0.25	0.507	0.005	0.010
0.4→0.5	430	0.43	0.262	0.009	0.017
-1→-0.9	450	1.05	0.350	0.021	0.027
-0.9→-0.8	450	0.61	0.088	0.012	0.015
-0.8→-0.7	450	0.68	0.034	0.014	0.017
-0.7→-0.6	450	0.71	0.024	0.014	0.018
-0.6→-0.5	450	0.68	0.020	0.014	0.017
-0.5→-0.4	450	0.70	0.018	0.014	0.018

-0.4→-0.3	450	0.65	0.017	0.013	0.016
-0.3→-0.2	450	0.65	0.018	0.013	0.016
-0.2→-0.1	450	0.67	0.022	0.013	0.017
-0.1→0.0	450	0.57	0.026	0.011	0.014
0.0→0.1	450	0.58	0.034	0.012	0.015
0.1→0.2	450	0.62	0.048	0.012	0.016
0.2→0.3	450	0.56	0.068	0.011	0.014
0.3→0.4	450	0.54	0.110	0.011	0.014
0.4→0.5	450	0.40	0.190	0.008	0.010
-1→-0.9	470	0.38	0.316	0.008	0.010
-0.9→-0.8	470	0.72	0.073	0.014	0.020
-0.8→-0.7	470	0.76	0.030	0.015	0.021
-0.7→-0.6	470	0.74	0.019	0.015	0.020
-0.6→-0.5	470	0.69	0.017	0.014	0.019
-0.5→-0.4	470	0.70	0.016	0.014	0.019
-0.4→-0.3	470	0.66	0.014	0.013	0.018
-0.3→-0.2	470	0.67	0.014	0.013	0.019
-0.2→-0.1	470	0.62	0.016	0.012	0.017
-0.1→0.0	470	0.62	0.021	0.012	0.017
0.0→0.1	470	0.58	0.025	0.012	0.016
0.1→0.2	470	0.57	0.031	0.011	0.016
0.2→0.3	470	0.46	0.052	0.009	0.013
0.3→0.4	470	0.40	0.095	0.008	0.011
0.4→0.5	470	0.33	0.361	0.007	0.009
-1→-0.9	490	-0.55	0.229	0.011	0.01
-0.9→-0.8	490	0.69	0.091	0.014	0.022
-0.8→-0.7	490	0.70	0.031	0.014	0.023

-0.7→-0.6	490	0.73	0.020	0.015	0.024
-0.6→-0.5	490	0.67	0.017	0.013	0.022
-0.5→-0.4	490	0.67	0.017	0.013	0.022
-0.4→-0.3	490	0.69	0.015	0.014	0.022
-0.3→-0.2	490	0.67	0.016	0.013	0.022
-0.2→-0.1	490	0.65	0.016	0.013	0.021
-0.1→0.0	490	0.60	0.017	0.012	0.020
0.0→0.1	490	0.57	0.022	0.011	0.018
0.1→0.2	490	0.52	0.029	0.010	0.017
0.2→0.3	490	0.50	0.043	0.010	0.016
0.3→0.4	490	0.45	0.065	0.009	0.015
0.4→0.5	490	0.29	0.126	0.006	0.009
-1→-0.9	510	0.98	0.162	0.020	0.042
-0.9→-0.8	510	0.79	0.075	0.016	0.034
-0.8→-0.7	510	0.73	0.026	0.015	0.032
-0.7→-0.6	510	0.71	0.017	0.014	0.031
-0.6→-0.5	510	0.73	0.015	0.015	0.032
-0.5→-0.4	510	0.72	0.013	0.014	0.031
-0.4→-0.3	510	0.69	0.013	0.014	0.030
-0.3→-0.2	510	0.64	0.012	0.013	0.028
-0.2→-0.1	510	0.64	0.012	0.013	0.028
-0.1→0.0	510	0.61	0.013	0.012	0.026
0.0→0.1	510	0.60	0.016	0.012	0.026
0.1→0.2	510	0.56	0.019	0.011	0.024
0.2→0.3	510	0.52	0.028	0.010	0.022
0.3→0.4	510	0.37	0.046	0.007	0.016
0.4→0.5	510	0.42	0.073	0.008	0.018

-1→-0.9	530	1.20	0.185	0.024	0.058
-0.9→-0.8	530	0.83	0.073	0.017	0.040
-0.8→-0.7	530	0.74	0.028	0.015	0.036
-0.7→-0.6	530	0.74	0.018	0.015	0.036
-0.6→-0.5	530	0.75	0.016	0.015	0.036
-0.5→-0.4	530	0.72	0.014	0.014	0.035
-0.4→-0.3	530	0.70	0.013	0.014	0.034
-0.3→-0.2	530	0.67	0.013	0.013	0.032
-0.2→-0.1	530	0.62	0.013	0.012	0.030
-0.1→0.0	530	0.62	0.014	0.012	0.030
0.0→0.1	530	0.56	0.015	0.011	0.027
0.1→0.2	530	0.50	0.018	0.010	0.024
0.2→0.3	530	0.49	0.024	0.010	0.023
0.3→0.4	530	0.43	0.042	0.009	0.021
0.4→0.5	530	0.37	0.072	0.007	0.017
-1→-0.9	550	0.88	0.309	0.018	0.035
-0.9→-0.8	550	0.87	0.076	0.017	0.035
-0.8→-0.7	550	0.77	0.033	0.015	0.031
-0.7→-0.6	550	0.78	0.020	0.016	0.032
-0.6→-0.5	550	0.75	0.018	0.015	0.030
-0.5→-0.4	550	0.72	0.016	0.014	0.029
-0.4→-0.3	550	0.71	0.016	0.014	0.028
-0.3→-0.2	550	0.67	0.014	0.013	0.027
-0.2→-0.1	550	0.66	0.014	0.013	0.027
-0.1→0.0	550	0.62	0.014	0.012	0.025
0.0→0.1	550	0.58	0.015	0.012	0.023
0.1→0.2	550	0.50	0.018	0.010	0.020

0.2→0.3	550	0.53	0.025	0.011	0.021
0.3→0.4	550	0.42	0.042	0.008	0.017
0.4→0.5	550	0.33	0.072	0.007	0.013
-1→-0.9	570	0.79	0.190	0.016	0.028
-0.9→-0.8	570	0.70	0.074	0.014	0.025
-0.8→-0.7	570	0.76	0.024	0.015	0.027
-0.7→-0.6	570	0.75	0.016	0.015	0.026
-0.6→-0.5	570	0.75	0.013	0.015	0.026
-0.5→-0.4	570	0.75	0.012	0.015	0.026
-0.4→-0.3	570	0.72	0.011	0.014	0.025
-0.3→-0.2	570	0.68	0.011	0.014	0.024
-0.2→-0.1	570	0.66	0.011	0.013	0.023
-0.1→0.0	570	0.62	0.011	0.012	0.022
0.0→0.1	570	0.59	0.012	0.011	0.020
0.1→0.2	570	0.52	0.014	0.010	0.018
0.2→0.3	570	0.49	0.017	0.010	0.017
0.3→0.4	570	0.44	0.025	0.009	0.015
0.4→0.5	570	0.27	0.045	0.005	0.009
-1→-0.9	590	0.33	0.120	0.007	0.013
-0.9→-0.8	590	0.69	0.050	0.014	0.028
-0.8→-0.7	590	0.73	0.020	0.015	0.030
-0.7→-0.6	590	0.78	0.013	0.016	0.032
-0.6→-0.5	590	0.77	0.011	0.015	0.031
-0.5→-0.4	590	0.75	0.011	0.015	0.031
-0.4→-0.3	590	0.72	0.010	0.014	0.030
-0.3→-0.2	590	0.69	0.009	0.014	0.028
-0.2→-0.1	590	0.68	0.009	0.014	0.028

-0.1→0.0	590	0.65	0.009	0.013	0.027
0.0→0.1	590	0.60	0.010	0.012	0.025
0.1→0.2	590	0.57	0.011	0.011	0.023
0.2→0.3	590	0.51	0.013	0.010	0.021
0.3→0.4	590	0.41	0.019	0.008	0.016
0.4→0.5	590	0.28	0.033	0.005	0.011
-1→-0.9	610	0.44	0.119	0.009	0.016
-0.9→-0.8	610	0.62	0.057	0.012	0.023
-0.8→-0.7	610	0.75	0.022	0.015	0.028
-0.7→-0.6	610	0.78	0.015	0.016	0.030
-0.6→-0.5	610	0.77	0.012	0.015	0.029
-0.5→-0.4	610	0.77	0.011	0.015	0.029
-0.4→-0.3	610	0.73	0.010	0.015	0.028
-0.3→-0.2	610	0.71	0.010	0.014	0.027
-0.2→-0.1	610	0.70	0.010	0.014	0.027
-0.1→0.0	610	0.66	0.010	0.013	0.025
0.0→0.1	610	0.63	0.010	0.013	0.024
0.1→0.2	610	0.57	0.011	0.011	0.022
0.2→0.3	610	0.53	0.013	0.011	0.020
0.3→0.4	610	0.47	0.017	0.009	0.018
0.4→0.5	610	0.38	0.031	0.008	0.014
-1→-0.9	630	1.06	0.338	0.021	0.041
-0.9→-0.8	630	0.56	0.110	0.011	0.022
-0.8→-0.7	630	0.71	0.044	0.014	0.028
-0.7→-0.6	630	0.76	0.027	0.015	0.030
-0.6→-0.5	630	0.75	0.022	0.015	0.029
-0.5→-0.4	630	0.76	0.021	0.015	0.030

-0.4→-0.3	630	0.78	0.018	0.016	0.030
-0.3→-0.2	630	0.74	0.018	0.015	0.029
-0.2→-0.1	630	0.74	0.018	0.015	0.029
-0.1→0.0	630	0.66	0.018	0.013	0.026
0.0→0.1	630	0.61	0.019	0.012	0.024
0.1→0.2	630	0.60	0.020	0.012	0.023
0.2→0.3	630	0.52	0.024	0.010	0.020
0.3→0.4	630	0.49	0.033	0.010	0.019
0.4→0.5	630	0.39	0.058	0.008	0.015
-1→-0.9	650	0.68	0.651	0.014	0.062
-0.9→-0.8	650	1.02	0.230	0.020	0.092
-0.8→-0.7	650	0.80	0.099	0.016	0.073
-0.7→-0.6	650	0.85	0.067	0.017	0.077
-0.6→-0.5	650	0.85	0.057	0.017	0.076
-0.5→-0.4	650	0.85	0.056	0.017	0.077
-0.4→-0.3	650	0.81	0.048	0.016	0.074
-0.3→-0.2	650	0.80	0.050	0.016	0.072
-0.2→-0.1	650	0.76	0.049	0.015	0.069
-0.1→0.0	650	0.63	0.044	0.013	0.057
0.0→0.1	650	0.76	0.046	0.015	0.069
0.1→0.2	650	0.63	0.051	0.013	0.057
0.2→0.3	650	0.50	0.055	0.010	0.045
0.3→0.4	650	0.62	0.074	0.012	0.056
0.4→0.5	650	0.62	0.101	0.012	0.056
-1→-0.9	670	-0.42	1.929	0.008	0.10
-0.9→-0.8	670	-1.86	1.477	0.037	0.45
-0.8→-0.7	670	1.35	1.816	0.027	0.329

-0.7→-0.6	670	0.40	0.215	0.008	0.098
-0.6→-0.5	670	0.77	0.441	0.015	0.187
-0.5→-0.4	670	1.01	0.208	0.020	0.245
-0.4→-0.3	670	0.86	0.286	0.017	0.209
-0.3→-0.2	670	0.85	0.183	0.017	0.208
-0.2→-0.1	670	0.50	0.234	0.010	0.121
-0.1→0.0	670	0.59	0.277	0.012	0.142
0.0→0.1	670	0.70	0.295	0.014	0.170
0.1→0.2	670	1.02	0.205	0.020	0.247
0.2→0.3	670	0.49	0.251	0.010	0.118
0.3→0.4	670	0.62	3.188	0.012	0.150
0.4→0.5	670	0.85	0.553	0.017	0.208
-1→-0.9	690	-2.08	0.686	0.042	0.24
-0.9→-0.8	690	1.11	1.291	0.022	0.128
-0.8→-0.7	690	0.67	0.825	0.013	0.077
-0.7→-0.6	690	0.81	0.141	0.016	0.094
-0.6→-0.5	690	0.68	0.228	0.014	0.079
-0.5→-0.4	690	0.80	1.095	0.016	0.093
-0.4→-0.3	690	0.69	0.168	0.014	0.080
-0.3→-0.2	690	0.83	0.185	0.017	0.095
-0.2→-0.1	690	0.95	0.868	0.019	0.110
-0.1→0.0	690	0.90	0.150	0.018	0.104
0.0→0.1	690	1.02	0.162	0.020	0.118
0.1→0.2	690	0.86	0.511	0.017	0.100
0.2→0.3	690	0.68	0.208	0.014	0.078
0.3→0.4	690	-0.95	1.498	0.019	0.10
0.4→0.5	690	1.00	0.585	0.020	0.116

-1→-0.9	710	2.33	1.953	0.0474	0.462
-0.9→-0.8	710	1.20	1.046	0.024	0.238
-0.8→-0.7	710	-1.07	0.309	0.021	0.21
-0.7→-0.6	710	0.67	1.241	0.013	0.132
-0.6→-0.5	710	0.75	0.051	0.015	0.148
-0.5→-0.4	710	0.82	0.205	0.016	0.163
-0.4→-0.3	710	0.75	0.550	0.015	0.149
-0.3→-0.2	710	1.21	0.218	0.024	0.240
-0.2→-0.1	710	0.44	0.202	0.009	0.087
-0.1→0.0	710	0.93	0.299	0.019	0.185
0.0→0.1	710	1.14	0.239	0.023	0.226
0.1→0.2	710	0.96	0.264	0.019	0.191
0.2→0.3	710	0.91	0.233	0.018	0.180
0.3→0.4	710	0.41	0.222	0.008	0.081
0.4→0.5	710	0.63	0.588	0.013	0.125

Table A.2: The $n\pi^0$ channel results covering an E_γ range of 410 Mev to 710 MeV and a $\cos\theta$ range of -1 to 1. The statistical uncertainty is listed as σ_{stat} with σ_{pol} the uncertainty in the polarisation correction and σ_{bg} the uncertainty in the background subtraction.

Cos(θ)	Energy(MeV)	Σ	σ_{stat}	σ_{pol}	σ_{bg}
-1→-0.9	250	2	2	0.04	1.656
-0.9→-0.8	250	-0.79	7.29	0.016	0.656
-0.8→-0.7	250	-2	2	0.04	1.656
-0.7→-0.6	250	1.82	0.576	0.036	1.5049
-0.6→-0.5	250	1.75	1.318	0.035	1.4502

-0.5→-0.4	250	0.49	0.879	0.010	0.4016
-0.4→-0.3	250	0.93	0.859	0.019	0.7666
-0.3→-0.2	250	0.57	1.968	0.011	0.4686
-0.2→-0.1	250	-2	2	0.04	1.655
-0.1→0.0	250	2	2	0.040	1.6559
0.0→0.1	250	1.74	0.606	0.035	1.4429
0.1→0.2	250	0.98	0.966	0.020	0.8131
0.2→0.3	250	0.28	0.326	0.006	0.2296
0.3→0.4	250	-2	2	0.04	1.656
0.4→0.5	250	-2	2	0.04	1.656
0.5→0.6	250	2	2	0.040	1.6558
0.6→0.7	250	2	2	0.04	1.656
0.7→0.8	250	2	2	0.04	1.656
0.8→0.9	250	-2	2	0.04	1.656
0.9→1.0	250	-2	2	0.04	1.656
-1→-0.9	270	2	2	0.04	0.51
-0.9→-0.8	270	0.59	1.299	0.012	0.1496
-0.8→-0.7	270	1.07	0.606	0.021	0.2736
-0.7→-0.6	270	-0.22	0.983	0.005	0.057
-0.6→-0.5	270	0.79	0.368	0.016	0.2014
-0.5→-0.4	270	0.75	0.339	0.015	0.1920
-0.4→-0.3	270	0.51	0.260	0.010	0.1311
-0.3→-0.2	270	0.38	0.503	0.008	0.0970
-0.2→-0.1	270	-0.23	0.774	0.005	0.058
-0.1→0.0	270	0.39	0.943	0.008	0.0994
0.0→0.1	270	0.80	0.386	0.016	0.2047
0.1→0.2	270	0.70	0.475	0.014	0.1797

0.2→0.3	270	0.84	0.396	0.017	0.2143
0.3→0.4	270	0.51	2.968	0.010	0.1295
0.4→0.5	270	0.50	0.884	0.010	0.1265
0.5→0.6	270	1.06	0.771	0.021	0.2697
0.6→0.7	270	-2	2	0.04	0.51
0.7→0.8	270	-0.30	0.252	0.006	0.076
0.8→0.9	270	-2	2	0.04	0.51
0.9→1.0	270	-2	2	0.04	0.509
-1→-0.9	290	-2	2	0.04	0.594
-0.9→-0.8	290	-0.32	1.171	0.01	0.094
-0.8→-0.7	290	-0.49	1.609	0.01	0.148
-0.7→-0.6	290	0.77	0.392	0.02	0.2296
-0.6→-0.5	290	0.59	0.277	0.012	0.1753
-0.5→-0.4	290	0.51	0.195	0.011	0.1528
-0.4→-0.3	290	-0.30	0.237	0.013	0.089
-0.3→-0.2	290	0.43	0.294	0.014	0.1265
-0.2→-0.1	290	0.12	0.368	0.002	0.0349
-0.1→0.0	290	0.54	0.243	0.01	0.1607
0.0→0.1	290	0.41	0.110	0.011	0.1231
0.1→0.2	290	0.61	0.227	0.012	0.1817
0.2→0.3	290	0.58	0.141	0.013	0.1717
0.3→0.4	290	0.45	2.082	0.013	0.1331
0.4→0.5	290	0.29	0.193	0.01	0.0866
0.5→0.6	290	-1.17	0.612	0.023	0.347
0.6→0.7	290	1.90	0.946	0.038	0.5636
0.7→0.8	290	0.49	0.2626	0.001	0.1457
0.8→0.9	290	-2	2	0.04	0.594

0.9→1.0	290	-2	2	0.04	0.594
-1→-0.9	310	1.03	1.064	0.0212	0.0860
-0.9→-0.8	310	0.88	0.275	0.018	0.0733
-0.8→-0.7	310	0.433	0.148	0.009	0.0359
-0.7→-0.6	310	0.79	0.102	0.016	0.0655
-0.6→-0.5	310	0.53	0.087	0.011	0.0440
-0.5→-0.4	310	0.50	0.082	0.010	0.0414
-0.4→-0.3	310	0.49	0.088	0.010	0.0410
-0.3→-0.2	310	0.53	0.084	0.011	0.0439
-0.2→-0.1	310	0.53	0.096	0.011	0.0443
-0.1→0.0	310	0.66	0.107	0.013	0.0554
0.0→0.1	310	0.68	0.099	0.014	0.0568
0.1→0.2	310	0.60	0.115	0.012	0.0504
0.2→0.3	310	0.42	0.436	0.008	0.0354
0.3→0.4	310	0.44	0.073	0.009	0.0370
0.4→0.5	310	0.21	0.087	0.004	0.0173
0.5→0.6	310	0.27	0.105	0.005	0.0228
0.6→0.7	310	-0.25	1.575	0.005	0.021
0.7→0.8	310	2	2	0.04	0.1668
0.8→0.9	310	2	2	0.04	0.1668
0.9→1.0	310	-2	2	0.04	0.166
-1→-0.9	330	2	2	0.04	0.0314
-0.9→-0.8	330	0.88	0.208	0.018	0.0137
-0.8→-0.7	330	0.42	0.139	0.008	0.0066
-0.7→-0.6	330	0.62	0.090	0.012	0.0096
-0.6→-0.5	330	0.46	0.078	0.009	0.0071
-0.5→-0.4	330	0.60	0.063	0.012	0.0094

-0.4→-0.3	330	0.46	0.071	0.009	0.0072
-0.3→-0.2	330	0.51	0.063	0.010	0.0079
-0.2→-0.1	330	0.60	0.072	0.012	0.0094
-0.1→0.0	330	0.56	2	0.011	0.0087
0.0→0.1	330	0.54	0.543	0.011	0.0084
0.1→0.2	330	0.55	0.427	0.011	0.0087
0.2→0.3	330	0.54	0.100	0.011	0.0084
0.3→0.4	330	0.51	0.527	0.010	0.0080
0.4→0.5	330	0.33	0.071	0.007	0.0052
0.5→0.6	330	0.57	0.416	0.011	0.0090
0.6→0.7	330	0.19	0.108	0.004	0.0029
0.7→0.8	330	-0.54	2.956	0.01	0.008
0.8→0.9	330	-2	2	0.04	0.031
0.9→1.0	330	0.29	0.122	0.006	0.0045
-1→-0.9	350	-0.29	0.531	0.0065	0.009
-0.9→-0.8	350	0.30	0.042	0.006	0.0094
-0.8→-0.7	350	0.52	0.089	0.010	0.0166
-0.7→-0.6	350	0.55	0.059	0.011	0.0175
-0.6→-0.5	350	0.52	0.052	0.010	0.0167
-0.5→-0.4	350	0.53	0.047	0.011	0.0168
-0.4→-0.3	350	0.64	0.068	0.013	0.0204
-0.3→-0.2	350	0.69	0.069	0.014	0.0219
-0.2→-0.1	350	0.58	0.045	0.012	0.0185
-0.1→0.0	350	0.59	0.118	0.012	0.0188
0.0→0.1	350	0.60	0.053	0.012	0.0191
0.1→0.2	350	0.59	0.055	0.012	0.0187
0.2→0.3	350	0.46	0.150	0.009	0.0146

0.3→0.4	350	0.46	0.043	0.009	0.0145
0.4→0.5	350	0.50	0.21	0.010	0.0160
0.5→0.6	350	-0.38	2	0.008	0.012
0.6→0.7	350	0.40	2.003	0.008	0.0128
0.7→0.8	350	0.68	0.636	0.0140	0.0217
0.8→0.9	350	-0.66	1.786	0.013	0.021
0.9→1.0	350	0.064	0.090	0.001	0.0019
-1→-0.9	370	0.35	0.272	0.007	0.0150
-0.9→-0.8	370	0.35	0.92	0.007	0.0153
-0.8→-0.7	370	0.53	0.062	0.011	0.0232
-0.7→-0.6	370	0.49	0.057	0.010	0.0214
-0.6→-0.5	370	0.52	0.051	0.010	0.0228
-0.5→-0.4	370	0.64	0.047	0.013	0.0278
-0.4→-0.3	370	0.65	0.041	0.013	0.0283
-0.3→-0.2	370	0.70	0.032	0.014	0.0306
-0.2→-0.1	370	0.61	0.044	0.012	0.0267
-0.1→0.0	370	0.63	0.033	0.013	0.0276
0.0→0.1	370	0.62	0.037	0.012	0.0269
0.1→0.2	370	0.59	0.066	0.012	0.0257
0.2→0.3	370	0.44	0.048	0.009	0.0190
0.3→0.4	370	0.49	0.068	0.009	0.0189
0.4→0.5	370	0.30	0.034	0.010	0.0214
0.5→0.6	370	0.36	0.71	0.012	0.0257
0.6→0.7	370	0.17	0.051	0.007	0.0158
0.7→0.8	370	0.72	0.356	0.014	0.0315
0.8→0.9	370	-0.53	0.896	0.01	0.022
0.9→1.0	370	-2	2	0.04	0.087

-1→-0.9	390	1.724	2	0.034	0.0533
-0.9→-0.8	390	0.362	0.150	0.007	0.0111
-0.8→-0.7	390	0.52	0.078	0.010	0.0162
-0.7→-0.6	390	0.46	0.058	0.009	0.0141
-0.6→-0.5	390	0.51	0.049	0.010	0.0159
-0.5→-0.4	390	0.56	0.042	0.011	0.0173
-0.4→-0.3	390	0.65	0.046	0.013	0.0201
-0.3→-0.2	390	0.60	0.051	0.012	0.0187
-0.2→-0.1	390	0.64	0.050	0.012	0.0199
-0.1→0.0	390	0.65	0.042	0.013	0.0200
0.0→0.1	390	0.59	0.042	0.012	0.0182
0.1→0.2	390	0.67	0.046	0.013	0.0206
0.2→0.3	390	0.61	0.057	0.012	0.0190
0.3→0.4	390	0.48	0.054	0.010	0.0147
0.4→0.5	390	0.56	0.068	0.011	0.0174
0.5→0.6	390	0.49	0.215	0.010	0.0150
0.6→0.7	390	-0.07	0.137	0.001	0.002
0.7→0.8	390	0.61	0.312	0.012	0.0190
0.8→0.9	390	0.60	2	0.012	0.0184
0.9→1.0	390	2	2	0.04	0.062
-1→-0.9	410	1.20	0.363	0.024	0.0330
-0.9→-0.8	410	0.41	0.105	0.008	0.0114
-0.8→-0.7	410	0.57	0.047	0.011	0.0158
-0.7→-0.6	410	0.53	0.033	0.011	0.0144
-0.6→-0.5	410	0.54	0.028	0.011	0.0149
-0.5→-0.4	410	0.59	0.030	0.012	0.0163
-0.4→-0.3	410	0.66	0.024	0.013	0.0183

-0.3→-0.2	410	0.63	0.024	0.013	0.0173
-0.2→-0.1	410	0.61	0.028	0.012	0.0167
-0.1→0.0	410	0.61	0.026	0.012	0.0168
0.0→0.1	410	0.60	0.038	0.012	0.0165
0.1→0.2	410	0.59	0.031	0.012	0.0163
0.2→0.3	410	0.53	0.031	0.011	0.0146
0.3→0.4	410	0.63	0.043	0.013	0.0172
0.4→0.5	410	0.47	0.046	0.009	0.0129
0.5→0.6	410	0.29	0.130	0.006	0.0078
0.6→0.7	410	-0.27	2	0.005	0.007
0.7→0.8	410	0.40	0.245	0.008	0.0110
0.8→0.9	410	0.30	2	0.006	0.0082
0.9→1.0	410	-0.11	2	0.002	0.003
-1→-0.9	430	0.62	0.202	0.012	0.0127
-0.9→-0.8	430	0.46	0.083	0.009	0.0093
-0.8→-0.7	430	0.44	0.051	0.009	0.0091
-0.7→-0.6	430	0.57	0.030	0.011	0.0117
-0.6→-0.5	430	0.56	0.029	0.011	0.0115
-0.5→-0.4	430	0.58	0.023	0.012	0.0119
-0.4→-0.3	430	0.62	0.024	0.012	0.0127
-0.3→-0.2	430	0.59	0.020	0.012	0.0120
-0.2→-0.1	430	0.60	0.022	0.012	0.0124
-0.1→0.0	430	0.61	0.025	0.012	0.0125
0.0→0.1	430	0.55	0.029	0.011	0.0113
0.1→0.2	430	0.56	0.029	0.011	0.0116
0.2→0.3	430	0.59	0.031	0.012	0.0121
0.3→0.4	430	0.54	0.032	0.011	0.0111

0.4→0.5	430	0.44	0.050	0.009	0.0091
0.5→0.6	430	0.36	0.091	0.007	0.0073
0.6→0.7	430	0.40	0.078	0.008	0.0082
0.7→0.8	430	0.23	0.154	0.005	0.0046
0.8→0.9	430	0.55	0.561	0.011	0.0114
0.9→1.0	430	1.84	2	0.037	0.0378
-1→-0.9	450	0.11	0.153	0.002	0.0027
-0.9→-0.8	450	0.47	0.066	0.009	0.0113
-0.8→-0.7	450	0.49	0.040	0.010	0.0119
-0.7→-0.6	450	0.51	0.026	0.010	0.0125
-0.6→-0.5	450	0.59	0.022	0.012	0.0143
-0.5→-0.4	450	0.59	0.021	0.012	0.0144
-0.4→-0.3	450	0.61	0.019	0.012	0.0148
-0.3→-0.2	450	0.59	0.019	0.012	0.0143
-0.2→-0.1	450	0.58	0.019	0.012	0.0141
-0.1→0.0	450	0.59	0.019	0.012	0.0143
0.0→0.1	450	0.57	0.020	0.011	0.0138
0.1→0.2	450	0.55	0.024	0.011	0.0133
0.2→0.3	450	0.54	0.025	0.011	0.0130
0.3→0.4	450	0.52	0.028	0.010	0.0125
0.4→0.5	450	0.44	0.045	0.009	0.0105
0.5→0.6	450	0.46	0.047	0.009	0.0112
0.6→0.7	450	0.284	0.870	0.006	0.0067
0.7→0.8	450	0.16	0.730	0.003	0.0037
0.8→0.9	450	-0.28	4.364	0.006	0.006
0.9→1.0	450	1.85	2	0.037	0.0450
-1→-0.9	470	0.16	4.639	0.003	0.0038

-0.9→-0.8	470	0.33	0.055	0.007	0.0080
-0.8→-0.7	470	0.49	0.035	0.010	0.0121
-0.7→-0.6	470	0.57	0.024	0.011	0.0139
-0.6→-0.5	470	0.57	0.019	0.011	0.0140
-0.5→-0.4	470	0.62	0.018	0.012	0.0153
-0.4→-0.3	470	0.61	0.017	0.012	0.0151
-0.3→-0.2	470	0.59	0.016	0.012	0.0146
-0.2→-0.1	470	0.55	0.017	0.011	0.0136
-0.1→0.0	470	0.59	0.017	0.012	0.0146
0.0→0.1	470	0.56	0.017	0.011	0.0137
0.1→0.2	470	0.53	0.018	0.011	0.0130
0.2→0.3	470	0.49	0.024	0.010	0.0120
0.3→0.4	470	0.51	0.024	0.010	0.0126
0.4→0.5	470	0.46	0.031	0.009	0.0113
0.5→0.6	470	0.38	0.036	0.008	0.0093
0.6→0.7	470	0.34	0.055	0.007	0.0084
0.7→0.8	470	0.21	0.096	0.004	0.0052
0.8→0.9	470	0.57	1.397	0.011	0.0139
0.9→1.0	470	-1.82	2	0.037	0.045
-1→-0.9	490	0.22	0.194	0.004	0.0065
-0.9→-0.8	490	0.38	0.056	0.008	0.0109
-0.8→-0.7	490	0.46	0.034	0.009	0.0134
-0.7→-0.6	490	0.54	0.027	0.011	0.0156
-0.6→-0.5	490	0.53	0.021	0.011	0.0153
-0.5→-0.4	490	0.57	0.019	0.011	0.0166
-0.4→-0.3	490	0.56	0.020	0.011	0.0162
-0.3→-0.2	490	0.57	0.019	0.011	0.0165

-0.2→-0.1	490	0.58	0.018	0.012	0.0167
-0.1→0.0	490	0.58	0.019	0.012	0.0168
0.0→0.1	490	0.54	0.020	0.011	0.0158
0.1→0.2	490	0.53	0.020	0.011	0.0153
0.2→0.3	490	0.53	0.022	0.011	0.0154
0.3→0.4	490	0.45	0.025	0.009	0.0130
0.4→0.5	490	0.42	0.030	0.008	0.0121
0.5→0.6	490	0.45	0.037	0.009	0.0131
0.6→0.7	490	0.34	0.058	0.007	0.0097
0.7→0.8	490	0.22	0.110	0.004	0.0064
0.8→0.9	490	0.90	0.753	0.018	0.0262
0.9→1.0	490	1.74	2	0.035	0.0507
-1→-0.9	510	0.27	0.090	0.005	0.0076
-0.9→-0.8	510	0.40	0.046	0.008	0.0111
-0.8→-0.7	510	0.48	0.032	0.010	0.0133
-0.7→-0.6	510	0.56	0.021	0.011	0.0155
-0.6→-0.5	510	0.57	0.018	0.011	0.0159
-0.5→-0.4	510	0.56	0.017	0.011	0.0156
-0.4→-0.3	510	0.59	0.016	0.012	0.0164
-0.3→-0.2	510	0.57	0.016	0.011	0.0158
-0.2→-0.1	510	0.59	0.015	0.012	0.0163
-0.1→0.0	510	0.56	0.015	0.011	0.0156
0.0→0.1	510	0.55	0.016	0.011	0.0153
0.1→0.2	510	0.51	0.016	0.010	0.0142
0.2→0.3	510	0.51	0.018	0.010	0.0141
0.3→0.4	510	0.51	0.020	0.010	0.0142
0.4→0.5	510	0.49	0.025	0.010	0.0135

0.5→0.6	510	0.40	0.036	0.008	0.0110
0.6→0.7	510	0.32	0.046	0.006	0.0089
0.7→0.8	510	0.37	0.088	0.007	0.0103
0.8→0.9	510	-0.41	2	0.008	0.011
0.9→1.0	510	1.76	2	0.035	0.0488
-1→-0.9	530	0.36	0.141	0.007	0.0056
-0.9→-0.8	530	0.35	0.040	0.007	0.0055
-0.8→-0.7	530	0.51	0.038	0.010	0.0079
-0.7→-0.6	530	0.55	0.022	0.011	0.0085
-0.6→-0.5	530	0.59	0.017	0.012	0.0091
-0.5→-0.4	530	0.58	0.018	0.012	0.0090
-0.4→-0.3	530	0.56	0.017	0.011	0.0086
-0.3→-0.2	530	0.56	0.017	0.011	0.0087
-0.2→-0.1	530	0.56	0.017	0.011	0.0088
-0.1→0.0	530	0.57	0.016	0.011	0.0088
0.0→0.1	530	0.57	0.016	0.011	0.0088
0.1→0.2	530	0.58	0.018	0.012	0.0089
0.2→0.3	530	0.51	0.019	0.010	0.0079
0.3→0.4	530	0.50	0.02	0.010	0.0077
0.4→0.5	530	0.42	0.027	0.008	0.0064
0.5→0.6	530	0.37	0.032	0.007	0.0057
0.6→0.7	530	0.29	0.056	0.006	0.0045
0.7→0.8	530	0.27	0.130	0.005	0.0041
0.8→0.9	530	-0.39	2	0.007	0.006
0.9→1.0	530	-1.75	2	0.035	0.027
-1→-0.9	550	0.11	0.014	0.002	0.0039
-0.9→-0.8	550	0.40	0.053	0.008	0.0138

-0.8→-0.7	550	0.41	0.034	0.008	0.0141
-0.7→-0.6	550	0.59	0.026	0.012	0.0206
-0.6→-0.5	550	0.57	0.021	0.011	0.0198
-0.5→-0.4	550	0.63	0.019	0.013	0.0220
-0.4→-0.3	550	0.60	0.018	0.012	0.0207
-0.3→-0.2	550	0.59	0.019	0.012	0.0206
-0.2→-0.1	550	0.59	0.018	0.012	0.0204
-0.1→0.0	550	0.59	0.018	0.012	0.0204
0.0→0.1	550	0.57	0.020	0.011	0.0197
0.1→0.2	550	0.59	0.020	0.012	0.0205
0.2→0.3	550	0.54	0.022	0.011	0.0186
0.3→0.4	550	0.52	0.023	0.010	0.0182
0.4→0.5	550	0.48	0.029	0.010	0.0166
0.5→0.6	550	0.44	0.038	0.009	0.0154
0.6→0.7	550	0.36	0.052	0.007	0.0126
0.7→0.8	550	0.30	0.111	0.006	0.0104
0.8→0.9	550	0.48	2	0.010	0.0166
0.9→1.0	550	-1.79	2	0.036	0.062
-1→-0.9	570	0.11	0.010	0.002	0.0019
-0.9→-0.8	570	0.35	0.046	0.007	0.0059
-0.8→-0.7	570	0.50	0.027	0.010	0.0086
-0.7→-0.6	570	0.56	0.018	0.011	0.0096
-0.6→-0.5	570	0.55	0.016	0.011	0.0094
-0.5→-0.4	570	0.57	0.016	0.011	0.0098
-0.4→-0.3	570	0.59	0.015	0.012	0.0101
-0.3→-0.2	570	0.60	0.014	0.012	0.0102
-0.2→-0.1	570	0.60	0.014	0.012	0.0103

-0.1→0.0	570	0.59	0.015	0.012	0.0101
0.0→0.1	570	0.57	0.014	0.011	0.0097
0.1→0.2	570	0.61	0.015	0.012	0.0104
0.2→0.3	570	0.55	0.017	0.011	0.0094
0.3→0.4	570	0.53	0.018	0.011	0.0091
0.4→0.5	570	0.50	0.022	0.010	0.0085
0.5→0.6	570	0.49	0.029	0.010	0.0084
0.6→0.7	570	0.32	0.044	0.006	0.0055
0.7→0.8	570	0.20	0.091	0.004	0.0034
0.8→0.9	570	0.76	2	0.015	0.0130
0.9→1.0	570	-0.63	2	0.013	0.010
-1→-0.9	590	0.24	0.051	0.005	0.0054
-0.9→-0.8	590	0.41	0.035	0.008	0.0094
-0.8→-0.7	590	0.51	0.022	0.010	0.0117
-0.7→-0.6	590	0.56	0.017	0.011	0.0131
-0.6→-0.5	590	0.55	0.014	0.011	0.0128
-0.5→-0.4	590	0.61	0.013	0.012	0.0141
-0.4→-0.3	590	0.62	0.012	0.012	0.0144
-0.3→-0.2	590	0.61	0.012	0.012	0.0143
-0.2→-0.1	590	0.66	0.012	0.013	0.0151
-0.1→0.0	590	0.62	0.012	0.012	0.0144
0.0→0.1	590	0.59	0.012	0.012	0.0136
0.1→0.2	590	0.57	0.013	0.011	0.0132
0.2→0.3	590	0.57	0.014	0.011	0.0132
0.3→0.4	590	0.52	0.016	0.010	0.0121
0.4→0.5	590	0.50	0.020	0.010	0.0115
0.5→0.6	590	0.51	0.026	0.010	0.0118

0.6→0.7	590	0.34	0.035	0.007	0.0079
0.7→0.8	590	0.21	0.077	0.004	0.0048
0.8→0.9	590	-1.60	2	0.032	0.037
0.9→1.0	590	-1.61	2	0.032	0.037
-1→-0.9	610	0.17	0.083	0.003	0.0034
-0.9→-0.8	610	0.35	0.035	0.007	0.0069
-0.8→-0.7	610	0.51	0.026	0.010	0.0101
-0.7→-0.6	610	0.55	0.018	0.011	0.0109
-0.6→-0.5	610	0.60	0.015	0.012	0.0119
-0.5→-0.4	610	0.64	0.014	0.013	0.0127
-0.4→-0.3	610	0.62	0.014	0.012	0.0123
-0.3→-0.2	610	0.62	0.013	0.012	0.0123
-0.2→-0.1	610	0.61	0.013	0.012	0.0120
-0.1→0.0	610	0.66	0.013	0.013	0.0130
0.0→0.1	610	0.61	0.014	0.012	0.0120
0.1→0.2	610	0.60	0.014	0.012	0.0119
0.2→0.3	610	0.58	0.016	0.012	0.0116
0.3→0.4	610	0.54	0.018	0.012	0.0108
0.4→0.5	610	0.51	0.024	0.010	0.0102
0.5→0.6	610	0.47	0.028	0.009	0.0093
0.6→0.7	610	0.48	0.044	0.010	0.0094
0.7→0.8	610	-0.25	2	0.005	0.004
0.8→0.9	610	-1.61	2	0.032	0.031
0.9→1.0	610	-1.61	2	0.032	0.031
-1→-0.9	630	0.40	0.153	0.008	0.0203
-0.9→-0.8	630	0.28	0.064	0.006	0.0140
-0.8→-0.7	630	0.49	0.049	0.010	0.0248

-0.7→-0.6	630	0.59	0.037	0.012	0.0295
-0.6→-0.5	630	0.57	0.030	0.011	0.0285
-0.5→-0.4	630	0.58	0.029	0.012	0.0294
-0.4→-0.3	630	0.66	0.026	0.013	0.0331
-0.3→-0.2	630	0.65	0.026	0.013	0.0325
-0.2→-0.1	630	0.62	0.025	0.012	0.0312
-0.1→0.0	630	0.66	0.027	0.013	0.0330
0.0→0.1	630	0.68	0.027	0.014	0.0341
0.1→0.2	630	0.59	0.029	0.012	0.0295
0.2→0.3	630	0.59	0.033	0.012	0.0296
0.3→0.4	630	0.58	0.033	0.012	0.0292
0.4→0.5	630	0.53	0.043	0.011	0.0266
0.5→0.6	630	0.53	0.053	0.011	0.0266
0.6→0.7	630	0.59	0.077	0.012	0.0295
0.7→0.8	630	0.53	0.196	0.011	0.0269
0.8→0.9	630	-0.79	2	0.016	0.039
0.9→1.0	630	0.18	2	0.004	0.0090
-1→-0.9	650	-0.09	0.035	0.002	0.010
-0.9→-0.8	650	0.57	0.206	0.011	0.0612
-0.8→-0.7	650	0.60	0.121	0.012	0.0645
-0.7→-0.6	650	0.57	0.085	0.011	0.0609
-0.6→-0.5	650	0.77	0.082	0.015	0.0831
-0.5→-0.4	650	0.56	0.079	0.011	0.0605
-0.4→-0.3	650	0.79	0.072	0.016	0.0850
-0.3→-0.2	650	0.66	0.069	0.013	0.0711
-0.2→-0.1	650	0.73	0.071	0.015	0.0790
-0.1→0.0	650	0.66	0.073	0.013	0.0713

0.0→0.1	650	0.54	0.075	0.011	0.0583
0.1→0.2	650	0.61	0.083	0.012	0.0655
0.2→0.3	650	0.56	0.078	0.011	0.0603
0.3→0.4	650	0.56	0.098	0.011	0.0600
0.4→0.5	650	0.58	0.109	0.012	0.0625
0.5→0.6	650	0.29	0.0307	0.006	0.0311
0.6→0.7	650	-0.50	2	0.010	0.054
0.7→0.8	650	-1.21	2	0.024	0.131
0.8→0.9	650	1.88	2	0.038	0.2021
0.9→1.0	650	-1.88	2	0.038	0.202
-1→-0.9	670	-1.56	2	0.031	0.592
-0.9→-0.8	670	-0.43	2	0.009	0.163
-0.8→-0.7	670	-1.34	2	0.027	0.507
-0.7→-0.6	670	1.56	2	0.031	0.5918
-0.6→-0.5	670	0.60	0.529	0.012	0.2260
-0.5→-0.4	670	0.76	0.768	0.015	0.2872
-0.4→-0.3	670	0.75	0.286	0.015	0.2831
-0.3→-0.2	670	0.80	0.386	0.016	0.3042
-0.2→-0.1	670	-0.78	2	0.016	0.295
-0.1→0.0	670	0.46	0.491	0.009	0.1760
0.0→0.1	670	-0.49	0.352	0.010	0.185
0.1→0.2	670	1.035	0.327	0.021	0.3902
0.2→0.3	670	-0.79	0.389	0.016	0.298
0.3→0.4	670	1.48	0.106	0.030	0.5618
0.4→0.5	670	0.94	0.433	0.019	0.3564
0.5→0.6	670	-1.61	2	0.032	0.609
0.6→0.7	670	0.84	0.593	0.017	0.3167

0.7→0.8	670	1.61		0.032	0.6092
0.8→0.9	670	-1.56	0.848	0.031	0.591
0.9→1.0	670	-0.33	0.268	0.007	0.125
-1→-0.9	690	-1.12	2	0.022	0.299
-0.9→-0.8	690	0.83	3.386	0.017	0.2204
-0.8→-0.7	690	-1.13	2.73	0.023	0.302
-0.7→-0.6	690	0.95	0.576	0.019	0.2543
-0.6→-0.5	690	-0.71	2	0.014	0.188
-0.5→-0.4	690	0.56	0.473	0.011	0.1484
-0.4→-0.3	690	0.97	0.272	0.019	0.2591
-0.3→-0.2	690	1.03	0.27	0.021	0.2764
-0.2→-0.1	690	0.90	0.260	0.018	0.2394
-0.1→0.0	690	1.40	0.304	0.028	0.3757
0.0→0.1	690	1.10	0.382	0.022	0.2938
0.1→0.2	690	0.75	0.280	0.015	0.2012
0.2→0.3	690	0.64	0.901	0.013	0.1718
0.3→0.4	690	-1.07	0.315	0.021	0.285
0.4→0.5	690	0.99	0.377	0.020	0.2659
0.5→0.6	690	1.56	0.465	0.031	0.4171
0.6→0.7	690	0.35	3.933	0.007	0.0939
0.7→0.8	690	2.17	2	0.043	0.5790
0.8→0.9	690	0.59	0.196	0.012	0.1578
0.9→1.0	690	-2.17	2	0.043	0.579
-1→-0.9	710	-0.72	1.56	0.014	0.246
-0.9→-0.8	710	0.97	0.770	0.019	0.3333
-0.8→-0.7	710	1.19	1.55	0.024	0.4085
-0.7→-0.6	710	-1.01	2	0.020	0.347

-0.6→-0.5	710	1.12	0.500	0.022	0.3831
-0.5→-0.4	710	0.48	2.475	0.010	0.1650
-0.4→-0.3	710	0.76	0.376	0.015	0.2621
-0.3→-0.2	710	0.39	0.361	0.008	0.1326
-0.2→-0.1	710	0.67	0.207	0.013	0.2314
-0.1→0.0	710	0.53	0.274	0.011	0.1834
0.0→0.1	710	0.94	0.481	0.019	0.3217
0.1→0.2	710	0.83	0.734	0.017	0.2851
0.2→0.3	710	1.14	0.336	0.023	0.3941
0.3→0.4	710	0.34	0.494	0.007	0.1152
0.4→0.5	710	0.79	1.009	0.016	0.2714
0.5→0.6	710	1.76	0.404	0.035	0.6040
0.6→0.7	710	0.94	2	0.019	0.3238
0.7→0.8	710	1.81	2	0.036	0.6225
0.8→0.9	710	1.81	2	0.036	0.6225
0.9→1.0	710	-0.33	0.321	0.007	0.114

Bibliography

[1] J. Chadwick. Possible existence of a neutron. *Nature*, 129(3252):312, 1932. DOI: 10.1038/129312a0.

[2] E. Rutherford. Collision of α particles with light atoms. IV. An anomalous effect in nitrogen. *The London, Edinburgh, and Dublin Philosophical Magazine and Journal of Science*, 37(222):581–587, 1919. DOI: 10.1080/14786431003659230.

[3] E. Wigner. On the Consequences of the Symmetry of the Nuclear Hamiltonian on the Spectroscopy of Nuclei. *Physical Review*, 51(2):106, 1937. DOI: 10.1103/PhysRev.51.106.

[4] W. Heisenberg. On the structure of atomic nuclei. *Z. Phys.*, 77:1–11, 1932. DOI: 10.1007/BF01342433.

[5] M. Gell-Mann. Isotopic spin and new unstable particles. *Physical Review*, 92(3):833, 1953. DOI: 10.1103/PhysRev.92.833.

[6] K. Nishijima. Charge independence theory of V particles. *Progress of Theoretical Physics*, 13(3):285–304, 1955. DOI: 10.1143/PTP.13.285.

[7] M. Gell-Mann. California Institute of Technology Report No. CTSL-20, 1961 (unpublished). *Phys. Rev*, 125:1067, 1962.

[8] M. Gell-Mann and Y. Ne'eman. *The eightfold way*. WA Benjamin, 1964. DOI: 10.1016/0029-5582(66)90165-9.

[9] W. B. Fowler and N. P. Samios. The omega-minus experiment. *Scientific American*, 211(4):36–45, 1964.

[10] M. Gell-Mann. *The Quark and the Jaguar: Adventures in the Simple and the Complex*. Macmillan, 1995.

[11] M. Breidenbach et al. Observed behavior of highly inelastic electron-proton scattering. *Physical Review Letters*, 23(16):935, 1969. DOI: 10.1103/PhysRevLett.23.935.

[12] O. W. Greenberg. Spin and unitary-spin independence in a paraquark model of baryons and mesons. *Physical Review Letters*, 13(20):598, 1964. DOI: 10.1103/PhysRevLett.13.598.

[13] R. L. Jaffe. Quark confinement. *Nature*, 268(5617):201, 1977. DOI: 10.1038/268201a0.

[14] E. Noether. Invariante Variationsprobleme, Math-phys. *Klasse, pp235-257*, 1918.

[15] M. Peskin and D. Schroeder. *An introduction to quantum field theory*. Westview Press Inc, 1995. DOI: 10.1201/9780429503559.

[16] F. J. Ynduráin. *The theory of quark and gluon interactions*. Springer Science & Business Media, 2007. DOI: 10.1007/978-3-662-02940-4.

[17] E. Klempt and A. Zaitsev. Glueballs, hybrids, multiquarks: Experimental facts versus QCD inspired concepts. *Physics Reports*, 454(1):1–202, 2007. DOI: 10.1016/j.physrep.2007.07.006.

[18] J. M. Cornwall and A. Soni. Glueballs as bound states of massive gluons. *Physics Letters B*, 120(4):431–435, 1983. DOI: 10.1016/0370-2693(83)90481-1.

[19] R. Mann. *An introduction to particle physics and the Standard Model*. CRC Press, 2011. DOI: 10.1201/9781420083002.

[20] J. Ashman et al. An investigation of the spin structure of the proton in deep inelastic scattering of polarised muons on polarised protons. *Nuclear Physics B*, 328(1):1–35, 1989. DOI: 10.1016/0550-3212(89)90089-8.

[21] M. S. Bhagwat, I. C. Cloët, and C. D. Roberts. Covariance, dynamics and symmetries, and Hadron form factors. In *Exclusive Reactions at High Momentum Transfer*, pages 112–120. World Scientific, 2008. DOI: 10.1142/97898127969500010.

[22] http://boson.physics.sc.edu/∼gothe/summer-school-12/lectures/craig-1a.pdf.

[23] D. J. Gross and F. Wilczek. Ultraviolet behavior of non-abelian gauge theories. *Physical Review Letters*, 30(26):1343, 1973. DOI: 10.1103/PhysRevLett.30.1343.

[24] H. D. Politzer. Reliable perturbative results for strong interactions? *Physical Review Letters*, 30(26):1346, 1973. DOI: 10.1103/PhysRevLett.30.1346.

[25] K. G. Wilson. Confinement of quarks. *Physical review D*, 10(8):2445, 1974. DOI: 10.1103/PhysRevD.10.2445.

[26] S. Dürr et al. Ab initio determination of light hadron masses. *Science*, 322(5905):1224–1227, 2008. DOI: 10.1126/science.1163233.

[27] A. S. Kronfeld. Twenty-First Century Lattice Gauge Theory: Results from the Quantum Chromodynamics Lagrangian. *Annual Review of Nuclear and Particle Science*, 62:265–284, 2012. DOI: 10.1146/annurev-nucl-102711-094942.

[28] C. D. Roberts and A. G. Williams. Dyson-Schwinger equations and their application to hadronic physics. *Progress in Particle and Nuclear Physics*, 33:477–575, 1994. DOI: 10.1016/0146-6410(94)90049-3.

[29] J. C. R. Bloch et al. Nucleon form factors and a nonpointlike diquark. *Physical Review C*, 60(6):062201, 1999. DOI: 10.1103/PhysRevC.60.062201.

[30] G. Eichmann and C. S. Fischer. Baryon Structure and Reactions from Dyson–Schwinger Equations. *Few-Body Systems*, 60(1):2, 2019. DOI: 10.1007/s00601-018-1469-5.

[31] A. O. Chodos et al. Baryon structure in the bag theory. *Physical Review D*, 10(8):2599, 1974. DOI: 10.1103/PhysRevD.10.2599.

[32] A. O. Chodos et al. New extended model of hadrons. *Physical Review D*, 9(12):3471, 1974. DOI: 10.1103/PhysRevD.9.3471.

[33] S. O. Théberge, A. W. Thomas, and G. A. Miller. Pionic corrections to the MIT bag model: The (3, 3) resonance. *Physical Review D*, 22(11):2838, 1980. DOI: 10.1103/PhysRevD.22.2838.

[34] D. Faiman and A. W. Hendry. Harmonic-oscillator model for baryons. *Physical Review*, 173(5):1720, 1968. DOI: 10.1103/PhysRev.173.1720.

[35] N. Isgur and G. Karl. Positive-parity excited baryons in a quark model with hyperfine interactions. *Physical Review D*, 19(9):2653, 1979. DOI: 10.1103/PhysRevD.19.2653.

[36] N. Isgur and G. Karl. Ground-state baryons in a quark model with hyperfine interactions. *Physical Review D*, 20(5):1191, 1979. DOI: 10.1103/PhysRevD.20.1191.

[37] S. Capstick and W. Roberts. Quark models of baryon masses and decays. *Progress in Particle and Nuclear Physics*, 45:S241–S331, 2000. DOI: 10.1016/S0146-6410(00)0019-5.

[38] M. Sikora. Recoil polarimetery in meson photoproduction reactions. *Ph.D thesis*, The University of Edinburgh, 2011.

[39] E. Santopinto. Interacting quark-diquark model of baryons. *Physical Review C*, 72(2):022201, 2005. DOI: 10.1103/PhysRevC.72.022201.

[40] M. Anselmino et al. Diquarks. *Reviews of Modern Physics*, 65(4):1199, 1993. DOI: 10.1103/RevModPhys.65.1199.

[41] D. B. Leinweber. Do quarks really form diquark clusters in the nucleon? *Physical Review D*, 47(11):5096, 1993. DOI: 10.1103/PhysRevD.47.5096.

[42] C. P. Forsyth and R. E. Cutkosky. Evidence against diquarks from baryon resonance decays. *Nuclear Physics B*, 178(1):35–44, 1981. DOI: 10.1016/0550-3213(81)90496-X.

[43] S. Gardner. Polarisation Observables in Neutral Pion Photoproduction with MAMI. *Ph.D thesis*, University of Glasgow, 2016.

[44] G. Höhler et al. Handbook of pion-nucleon scattering. 1979.

[45] W. Meyer et al. Polarized H, D and 3He targets for particle physics experiments. *Progress in Particle and nuclear Physics*, 49(2):403–489, 2002. DOI: 10.1016/S0146-6410(02)00159-X.

[46] M. Tanabashi et al. Review of particle physics. *Physical Review D*, 98(3):030001, 2018. DOI: 10.1103/PhysRevD.98.030001.

[47] P. Bareyre, C. Bricman, and G. Villet. Phase-Shift Analysis of Pion-Nucleon Elastic Scattering below 1.6 GeV. *Physical Review*, 165(5):1730, 1968. DOI: 10.1103/PhysRev.165.1730.

[48] P. Auvil, A. T. Lea, C. Lovelace, and A. Donnachie. Pion-nucleon phase shifts and resonances. 1964. DOI: 10.1016/0031-9163(64)91184-9.

[49] B. H. Bransden, P. J. O'Donnell, and R. G. Moorhouse. Pion-Nucleon Scattering Amplitudes in the Range 300-700 MeV. *Physical Review*, 139(6B):B1566, 1965. DOI: 10.1103/PhysRev.139.B1566.

[50] B. H. Brandsen, P. J. O'Donnell, and R.G. Moorhouse. Pion-nucleon scattering and resonant states near 900 MeV. *Physics Letters*, 19:420–421, 1965. DOI: 10.1016/0031-9163(65)90925-X.

[51] K. M. Watson. Some general relations between the photoproduction and scattering of π mesons. *Physical Review*, 95(1):228, 1954. DOI: 10.1103/PhysRev.95.228.

[52] S. D. Drell, M. H. Friedman, and F. Zachariasen. Theory of S-Wave Pion Scattering and Photoproduction at Low Energies. *Physical Review*, 104(1):236, 1956. DOI: 10.1103/PhysRev.104.236.

[53] T. A. Armstrong et al. Total hadronic cross section of γ rays in hydrogen in the energy range 0.265-4.215 GeV. *Physical Review D*, 5(7):1640, 1972. DOI: 10.1103/PhysRevD.5.1640.

[54] H. Meyer et al. Total cross section for photoproduction of hadrons on hydrogen and deuterium between 1.0 and 6.4 GeV. *Physics Letters B*, 33(2):189–192, 1970. DOI: 10.1016/0370-2693(70)90298-4.

[55] H. G. Hilpert et al. Total cross section for photoproduction of hadrons on protons up to 5 GeV. *Physics Letters B*, 27(7):474–476, 1968. DOI: 10.1016/0370-2693(68)90244-X.

[56] F. A. Berends, A. Donnachie, and D. L. Weaver. Photoproduction and electroproduction of pions (I) dispersion relation theory. *Nuclear Physics B*, 4(1):1–53, 1967. DOI: 10.1016/0550-3213(67)90196-4.

[57] H. Tanabe and K. Ohta. Dynamical model for pion photoproduction in the Δ region. *Physical Review C*, 31(5):1876, 1985. DOI: 10.1103/PhysRevC.31.1876.

[58] I. S. Barker, A. Donnachie, and J. K. Storrow. Analysis of π^0 photoproduction at intermediate and high energies. *Nuclear Physics B*, 79(3):431–460, 1974. DOI: 10.1016/0550-3213(74)90561-6.

[59] G. F. Chew, M. L. Goldberger, F. E. Low, and Y. Nambu. Relativistic dispersion relation approach to photomeson production. *Physical Review*, 106(6):1345, 1957. DOI: 10.1103/PhysRev.106.1345.

[60] I. S. Barker, A. Donnachie, and J. K. Storrow. Complete experiments in pseudoscalar photoproduction. *Nuclear Physics B*, 95(2):347–356, 1975. DOI: 10.1016/0550-3213(75)90049-814786431003659230.

[61] R. A. Adelseck and B. Saghai. Kaon photoproduction: Data consistency, coupling constants, and polarization observables. *Physical Review C*, 42(1):108, 1990. DOI: 10.1103/PhysRevC.42.108.

[62] A. M. Sandorfi, S. Hoblit, H. Kamano, and T. S. H. Lee. The determination of pseudoscalar meson photoproduction amplitudes from complete experiments. In *AIP Conference Proceedings*, volume 1388, pages 99–105. AIP, 2011. DOI: 10.1063/1.3647357.

[63] W. Chiang and F. Tabakin. Completeness rules for spin observables in pseudoscalar meson photoproduction. *Physical Review C*, 55(4):2054, 1997. DOI: 10.1103/PhysRevC.55.2054.

[64] G. Keaton and R. Workman. Amplitude ambiguities in pseudoscalar meson photoproduction. *Physical Review C*, 53(3):1434, 1996. DOI: 10.1103/PhysRevC.53.1434.

[65] T. Vrancx et al. Incompleteness of complete pseudoscalar-meson photoproduction. *Physical Review C*, 87(5):055205, 2013. DOI: 10.1103/PhysRevC.87.055205.

[66] B. Dey et al. Polarization observables in the longitudinal basis for pseudo-scalar meson photoproduction using a density matrix approach. *Physical Review C*, 83(5):055208, 2011. DOI: 10.1103/PhysRevC.83.055208.

[67] S. Gardner et al. Photon asymmetry measurements of $\gamma\, p \rightarrow \pi^0\, p$ for E_{gamma}= 320-650 MeV. *The European Physical Journal A*, 52(11):333, 2016. DOI: 10.1140/epja/i2016-16333-5.

[68] R. L. Walker. Phenomenological analysis of single-pion photoproduction. *Physical Review*, 182(5):1729, 1969. DOI: 10.1103/PhysRev.182.1729.

[69] D. J. Drickey and R. F. Mozley. Neutral Meson Production with Polarized X Rays. *Physical Review*, 136(2B):B543, 1964. DOI: 10.1103/PhysRec.136.B543.

[70] R. Beck et al. Measurement of the E2/M1 Ratio in the N->Δ Transition using the reaction p $(\gamma, p)\, \pi^0$. *Physical review letters*, 78(4):606, 1997. DOI: 10.1103/PhysRevLett.78.606.

[71] R. Beck et al. Determination of the E2/M1 ratio in the γ N-> Δ (1232) transition from a simultaneous measurement of p $(\gamma, p)\, \pi^0$ and p (γ, π^+) n. *Physical Review C*, 61(3):035204, 2000. DOI: 10.1103/PhysRevC.61.035204.

[72] D. Hornidge et al. Accurate Test of Chiral Dynamics in the $\gamma p \rightarrow \pi^0 p$ Reaction. *Physical review letters*, 111(6):062004, 2013. DOI: 10.1103/PhysRevLett.111.062004.

[73] G. Audit et al. DAPHNE: a large-acceptance tracking detector for the study of photoreactions at intermediate energies. *Nuclear Instruments and Methods in Physics Research Section A: Accelerators, Spectrometers, Detectors and Associated Equipment*, 301(3):473–481, 1991. DOI: 10.1016/0168-9002(91)90013-G.

[74] R. Crawford et al. Two-body photodisintegration of the deuteron from 100 to 800 MeV. *Nuclear Physics A*, 603(3-4):303–325, 1996. DOI: 10.1016/0375-9474(96)80004-B.

[75] R. Beck. Experiments with photons at MAMI. *The European Physical Journal A-Hadrons and Nuclei*, 28(1):173–183, 2006. DOI: 10.1140/epja/i2006-09-018-1.

[76] G. Blanpied et al. Polarized Compton scattering from the Proton. *Physical review letters*, 76(7):1023, 1996. DOI: 10.1103/PhysRevLett.76.1023.

[77] O Hanstein, D Drechsel, and L Tiator. The position and the residues of the delta resonance pole in pion photoproduction. *Physics Letters B*, 385(1-4):45–51, 1996.

[78] O Hanstein, D Drechsel, and L Tiator. Multipole analysis of pion photoproduction based on fixed t dispersion relations and unitarity. *Nuclear Physics A*, 632(4):561–606, 1998.

[79] I. Strakovsky, W. Briscoe, A. Kudryavtsev, V. Tarasov, and R. Workman. SAID analysis of meson photoproduction: Determination of neutron and proton EM couplings. In *EPJ Web of Conferences*, volume 73, page 04003. EDP Sciences, 2014. DOI: 10.1051/epjconf/20147304003.

[80] D. Drechsel, S. S. Kamalov, and L. Tiator. Unitary isobar model–MAID2007. *The European Physical Journal A*, 34(1):69–97, 2007. DOI: 10.1140/epja/i2007-10490-6.

[81] A. V. Anisovich et al. Properties of baryon resonances from a multichannel partial wave analysis. *The European Physical Journal A*, 48(2):1–13, 2012. DOI: 10.1140/epja/i2012-12015-8.

[82] J.P. Bocquet et al. GRAAL: a polarized γ-ray beam at ESRF. *Nuclear Physics A*, 622(1-2):c124–c129, 1997. DOI: 10.1016/S0375-9474(97)00337-0.

[83] O. Bartalini et al. Measurement of π photoproduction on the proton from 550 to 1500 MeV at GRAAL. *The European Physical Journal A-Hadrons and Nuclei*, 26(3):399–419, 2005. DOI: 10.1140/epja/i2005-10191-2.

[84] R. Di Salvo et al. Measurement of Σ beam asymmetry in π^0 photoproduction off the neutron in the second and third resonances region. *The European Physical Journal A*, 42(2):151, 2009. DOI: 10.1140/epja/i2009-10870-x.

[85] F. V. Adamian et al. Measurement of the cross section asymmetry of the reaction γ p->π^0 p in the resonance energy region E_γ= 0.5->1.1 GeV. *Physical Review C*, 63(5):054606, 2001. DOI: 10.1103/PhysRevC.63.054606.

[86] The Crystal Barrel Detector at ELSA.

[87] E. Gutz et al. High statistics study of the reaction $\gamma p \to p\pi^0 \eta$. *The European Physical Journal A*, 50(4):74, 2014. DOI: 10.1140/epja/i2014-14074-1.

[88] D. Elsner et al. Linearly polarised photon beams at ELSA and measurement of the beam asymmetry in π^0 photoproduction off the proton. *The European Physical Journal A*, 39(3):373–381, 2009. DOI: 10.1140/epja/i2008-10708-1.

[89] N. Sparks et al. Measurement of the beam asymmetry Σ in the forward direction for γ p$\to$ p π^0. *Physical Review C*, 81(6):065210, 2010. DOI: 10.1103/PhysRevC.81.065210.

[90] G. Blanpied et al. N->Δ Transition from simultaneous measurements of p(γ, π) and p (γ, γ). *Physical review letters*, 79(22):4337, 1997. DOI: 10.1103/PhysRevC.64.025203.

[91] D. Drechsel, O. Hanstein, S.S. Kamalov, and L. Tiator. A unitary isobar model for pion photo-and electroproduction on the proton up to 1 GeV. *Nuclear Physics A*, 645(1):145–174, 1999. DOI: 10.1016/S0375-9474(98)00572-7.

[92] R. L. Workman, M. W. Paris, W. J. Briscoe, and I. I. Strakovsky. Unified Chew-Mandelstam SAID analysis of pion photoproduction data. *Physical Review C*, 86(1):015202, 2012. DOI: 10.1103/PhysRevC.86.015202.

[93] K. M. Watson. The effect of final state interactions on reaction cross sections. *Physical Review*, 88(5):1163, 1952. DOI: 10.1103/PhysRev.88.1163.

[94] P. Adlarson et al. Measurement of π^0 photoproduction on the proton at MAMI C. *Physical Review C*, 92(2):024617, 2015. DOI: 10.1103/PhysRevC.92.024617.

[95] A. V. Anisovich, E. Klempt, V. A. Nikonov, M.A. Matveev, A. V. Sarantsev, and U. Thoma. Photoproduction of pions and properties of baryon resonances from a Bonn-Gatchina partial-wave analysis. *The European Physical Journal A*, 44(2):203–220, 2010. DOI: 10.1140/epja/i2010-10950-x.

[96] S. J. D. Kay. First investigation of electromagnetic coupling of the d*(2380) hexaquark . *Ph.D thesis*, University of Edinburgh, 2018.

[97] K. Aulenbacher et al. The MAMI source of polarized electrons. *Nuclear Instruments and Methods in Physics Research Section A: Accelerators, Spectrometers, Detectors and Associated Equipment*, 391(3):498–506, 1997. DOI: 10.1016/S0168-9002(97)00528-7.

[98] W. Hartmann, D. Conrath, et al. A source of polarized electrons based on photoemission of GaAsP. *Nuclear Instruments and Methods in Physics Research Section A: Accelerators, Spectrometers, Detectors and Associated Equipment*, 286(1-2):1–8, 1990. DOI: 10.1016/0168-9002(90)90200-P.

[99] K. D. Paschke. Controlling helicity-correlated beam asymmetries in a polarized electron source. *The European Physical Journal A*, 32(4):549–553, 2007.

[100] H. Herminghaus et al. The design of a cascaded 800 MeV normal conducting CW race track microtron. *Nuclear Instruments and Methods*, 138(1):1–12, 1976. DOI: 10.1016/0029-554X(76)90145-2.

[101] H. Herminghaus. The polytron as a cw electron accelerator in the 10 GeV range. *Nuclear Instruments and Methods in Physics Research Section A: Accelerators, Spectrometers, Detectors and Associated Equipment*, 305(1):1–9, 1991. DOI: 10.1016/0168-9002(91)90511-N.

[102] A. Jankowiak. The Mainz Microtron MAMI –Past and future. *The European Physical Journal A - Hadrons and Nuclei*, 28(1):149–160, 2006. DOI: 10.1140/epja/i2006-09-016-3.

[103] D. Werthmueller. Experimental study of nucleon resonance contributions to eta-photoproduction on the neutron. *Ph.D thesis*, Universität Basel, 2014.

[104] D. Howdle. Measurement of Polarisation Observables using Linearly Polarised Photons with the Crystal Ball at MAMI. *Ph.D thesis*, University of Glasgow, 2012.

[105] K. Livingston. The Stonehenge technique. A method for aligning coherent bremsstrahlung radiators. *Nuclear Instruments and Methods in Physics Research Section A: Accelerators, Spectrometers, Detectors and Associated Equipment*, 603(3):205–213, 2009. DOI: 10.1016/j.nima.2009.02.010.

[106] D. Lohmann et al. Linearly polarized photons at MAMI (Mainz). *Nuclear Instruments and Methods in Physics Research Section A: Accelerators, Spectrometers, Detectors and Associated Equipment*, 343(2-3):494–507, 1994. DOI: 10.1016/0168-9002(94)90230-5.

[107] S. J. Hall et al. A focal plane system for the 855 MeV tagged photon spectrometer at MAMI-B. *Nuclear Instruments and Methods in Physics Research Section A: Accelerators, Spectrometers, Detectors and Associated Equipment*, 368(3):698–708, 1996. DOI: 10.1016/0168-9002(95)00661-3.

[108] J.C. McGeorge et al. Upgrade of the Glasgow photon tagging spectrometer for Mainz MAMI-C. *The European Physical Journal A*, 37.1:129–137, 2008. DOI: 10.1140/epja/i2007-10606-0.

[109] C. Collicott. PROBING PROTON STRUCTURE THROUGH SINGLE POLARISA-TION OBSERVABLES OF COMPTON SCATTERING AND π^0 PHOTOPRODUC-TION WITHIN THE $\Delta(1232)$ REGION. *Ph.D thesis*, Dalhousie University, 2015.

[110] J. Mancell. A Study of η Photoproduction on the Proton at MAMI. *Ph.D thesis*, University of Glasgow, 2012.

[111] D. Glazier, D. Watts, and J. Annand. Proposal for Experiment: Polarisation observables using the Nucleon polarimeter with the Crystal Ball at MAMI.

[112] M. H. Sikora et al. Measurement of the ^{1}H (γ, P) π^0 Reaction Using a Novel Nucleon Spin Polarimeter. *Physical review letters*, 112(2):022501, 2014. DOI: 10.1103/Phys-RevLett.112.022501.

[113] Geant4: A toolkit for the simulation of the passage of particles through matter.

[114] M. E. Röbig. *Eichung des TAPS-Detektorsystems mit Höhenstrahlung*. PhD thesis, 1991.

[115] K.Livingston. Polarization from Coherent Bremsstrahlung Enhancement 2011 URL: http://nuclear.gla.ac.uk/ clasg8/CbremJlab/enhFitting.html.

[116] R. Macrae. Polarisation observables in π0 photoproduction at MAMI. *Ph.D thesis*, University of Glasgow, 2018.

[117] H. Olsen and L. C. Maximon. Electron and Photon Polarization in Bremsstrahlung and Pair Production. *Physical Review*, 110:589–590, 1958. DOI: 10.1103/PhysRev.110.589.

[118] K. Aulenbacher, V. Tioukine, and E. Riehn. A Mott polarimeter operating at MeV electron beam energies. *Review of Scientific Instruments*, 82:033303, 2011. DOI: 10.1063/1.3556593.

[119] R. Brun and F. Rademakers. ROOT-an object oriented data analysis framework. *Nuclear Instruments and Methods in Physics Research Section A: Accelerators, Spectrometers, Detectors and Associated Equipment*, 389(1):81–86, 1997. DOI: 10.1016/S0168-9002(97)00048-X.

[120] J.R.M. Annand. Data analysis within an AcquRoot Framework. 2005. url: http://www.nuclear.gla.ac.uk/ acqusys/doc/AcquRoot.11.08.pdf.

[121] A2 Collaboration. Generation of analysis trees. https://github.com/A2-Collaboration-dev/a2GoAT.

[122] D. I. Glazier. Hadron Spectroscopy Data Analysis: https://github.com/dglazier/HASPECT6.

[123] Parallel ROOT Facility: https://root.cern.ch/proof.

[124] L. Moneta et al. The roostats project. *arXiv preprint arXiv:1009.1003*, 2010.

[125] M. Pivk and F. R. Le Diberder. Plots: A statistical tool to unfold data distributions. *Nuclear Instruments and Methods in Physics Research Section A: Accelerators, Spectrometers, Detectors and Associated Equipment*, 555(1-2):356–369, 2005. DOI: 10.1016/j.nima.2005.08.106.

[126] M. Dieterle. *Comparison of the Experimental Resolution in Case of Using a 1.76 and 4.76 cm LD2 Target, Master project work, Universitat Basel.* PhD thesis, 2009.

[127] T. Cao, Y. Ilieva, N. Zachariou, CLAS Collaboration, et al. Determination of the Polarization Observables Determination of the Polarization Observables C_x, C_z, and P_y for the Quasi-Free Mechanism in the Reaction $\gamma \, d \rightarrow K^+ \Lambda n$. *Few-Body Systems*, 59(6):110, 2018. DOI: 10.1007/s00601-018-1430-7.

[128] R. Barlow. Extended maximum likelihood. *Nuclear Instruments and Methods in Physics Research Section A: Accelerators, Spectrometers, Detectors and Associated Equipment*, 297(3):496–506, 1990. DOI: 10.1016/0168-9002(90)91334-8.

[129] M. I. Levchuk et al. Incoherent pion photoproduction on the deuteron in the first resonance region. *Physical Review C*, 74(1):014004, 2006. DOI: 10.1103/PhysRevC.74.014004.

[130] W. J. Briscoe et al. Cross Section for γ n$\rightarrow \pi^0$ n measured at Mainz/A2. *arXiv preprint arXiv:1908.02730*, 2019.

[131] V. E. Tarasov et al. On the extraction of cross sections for π^0 and η photoproduction off neutrons from deuteron data. *Physics of Atomic Nuclei*, 79(2):216–227, 2016. DOI: 10.1134/S1063778816020186.